Universitat Autònoma de Barcelona

Cholesterol and Compressed CO2: a Smart Molecular Building Block and Advantageous Solvent to Prepare Stable Self-assembled Colloidal Nanostructures

Lidia Priscila Ferrer Tasies

ADVERTIMENT. L'accés als continguts d'aquesta tesi doctoral i la seva utilització ha de respectar els drets de la persona autora. Pot ser utilitzada per a consulta o estudi personal, així com en activitats o materials d'investigació i docència en els termes establerts a l'art. 32 del Text Refós de la Llei de Propietat Intel·lectual (RDL 1/1996). Per altres utilitzacions es requereix l'autorització prèvia i expressa de la persona autora. En qualsevol cas, en la utilització dels seus continguts caldrà indicar de forma clara el nom i cognoms de la persona autora i el títol de la tesi doctoral. No s'autoritza la seva reproducció o altres formes d'explotació efectuades amb finalitats de lucre ni la seva comunicació pública des d'un lloc alliè al servei TDX. Tampoc s'autoritza la presentació del seu contingut en una finestra o marc aliè a TDX (framing). Aquesta reserva de drets afecta tant als continguts de la tesi com als seus resums i índexs.

ADVERTENCIA. El acceso a los contenidos de esta tesis doctoral y su utilización debe respetar los derechos de la persona autora. Puede ser utilizada para consulta o estudio personal, así como en actividades o materiales de investigación y docencia en los términos establecidos en el art. 32 del Texto Refundido de la Ley de Propiedad Intelectual (RDL 1/1996). Para otros usos se requiere la autorización previa y expresa de la persona autora. En cualquier caso, en la utilización de sus contenidos se deberá indicar de forma clara el nombre y apellidos de la persona autora y el título de la tesis doctoral. No se autoriza su reproducción u otras formas de explotación efectuadas con fines lucrativos ni su comunicación pública desde un sitio ajeno al servicio TDR. Tampoco se autoriza la presentación de su contenido en una ventana o marco ajeno a TDR (framing). Esta reserva de derechos afecta tanto al contenido de la tesis como a sus resúmenes e índices.

WARNING. The access to the contents of this doctoral thesis and its use must respect the rights of the author. It can be used for reference or private study, as well as research and learning activities or materials in the terms established by the 32nd article of the Spanish Consolidated Copyright Act (RDL 1/1996). Express and previous authorization of the author is required for any other uses. In any case, when using its content, full name of the author and title of the thesis must be clearly indicated. Reproduction or other forms of for profit use or public communication from outside TDX service is not allowed. Presentation of its content in a window or frame external to TDX (framing) is not authorized either. These rights affect both the content of the thesis and its abstracts and indexes.

Universitat Autònoma de Barcelona

Cholesterol and Compressed CO_2: a Smart Molecular Building Block and Advantageous Solvent to Prepare Stable Self-assembled Colloidal Nanostructures

Lidia Priscila Ferrer Tasies

Tesi doctoral

Programa de Doctorat de Química

Directores

Dr. Susagna Ricart Miró

Dr. Nora Ventosa Rull

Tutora

Prof. Roser Pleixats Rovira

Departament de Química
Facultat de Ciències

2016

La present memòria es presenta per aspirar al Grau de Doctor per:

Lidia Priscila Ferrer Tasies,

Vist i plau:

Dr. Susagna Ricart Miró

Dr. Nora Ventosa Rull

Prof. Roser Pleixats Rovira

Bellaterra, 18 de gener de 2016

NORA VENTOSA RULL, Scientific Research and **SUSAGNA RICART MIRÓ** Tenured Scientist, of the Spanish Council of Research at the Materials Science Institute of Barcelona (ICMAB-CSIC)

CERTIFY

That **Lidia Priscila Ferrer Tasies**, Masters in Molecular Nanoscience and Nanotechnology, has performed, under their management, the research work entitled **"Cholesterol and Compressed CO_2: a Smart Molecular Building Block and Advantageous Solvent to Prepare Stable Self-assembled Colloidal Nanostructures"**. This work has been performed under the mark of the Chemistry Ph.D. program of the Chemistry Department of the Autonomous University of Barcelona.

And in witness whereof this is signed by

Directors

Dr. Susagna Ricart Miró Dr. Nora Ventosa Rull

DATE

“La frase más excitante que se puede oír en ciencia, la que anuncia nuevos descubrimientos, no es "¡Eureka!" (¡Lo encontré!) sino ’Es extraño...’.”

Isaac Asimov

Agraïments

En aquesta vida, mai caminem sols, així que aquestes paraules d'agraïment van dirigides a totes aquelles persones que en el transcurs d'aquest viatge m'han acompanyat, m'han ensenyat i han deixat una petjada en mi i en aquesta tesi.

Primer de tot vull agrair al Prof. Jaume Veciana i a la Prof. Concepció Rovira per donar-me l'oportunitat de realitzar la tesi doctoral al seu grup d'investigació, on he pogut endinsar-me al món científic sempre en un ambient molt agradable. També vull donar les gràcies a les meves dues directores de tesi, la Dra. Nora Ventosa i la Dra. Susagna Ricart. Us agraeixo moltíssim la confiança dipositada en mi i tots els bons consells que sempre m'heu donat. Moltes gràcies per el vostre esforç, per animar-me sempre a assolir nous reptes i sobretot per la vostra humanitat. Gràcies de tot cor!

Vull agrair també al Ministeri d'Economia i Competitivitat (beca predoctoral FPI-MICINN i ajuda mobilitat - 2013), al CIBER-BBN (ajuda mobilitat - 2013), a l'Associació d'Experts en Fluïts Comprimits FLUCOMP (ajuda assistència a congressos - 2015) i al CSIC per el finançament econòmic rebut en el transcurs de la tesi.

El treball que es presenta en aquesta tesi no hagués estat possible sense les col·laboracions establertes amb científics experts en diferents camps. I would like to thank to all the people that have contributed to the research done in this thesis.

First, I would like to thank to Prof. Brian A. Korgel, who gave me the opportunity to learn about nanocrystals during my stay in his Research Group at the University of Texas at Austin. Thanks also to all the group members, who made me feel as part of their team since the beginning. I would like to expand my gratitude to Dorothy Silbaugh for all the help in the laboratory and for sharing her knowledge about nanocrystals. I also would like to express my gratitude to Dr. Dwight Romanovicz for his technical assistance in the Electron Microscopy Service. Thanks to Vikas, Adrien, Yixuan, Richard, Kyle, Cherrelle and Jon, I spent there a very wonderful period of my thesis.

M'agradaria donar les gràcies al Dr. Jordi Faraudo per totes les simulacions realitzades, han sigut peces clau per entendre molt millor els nostres sistemes experimentals. Gràcies per sempre estar disposat a resoldre els meus dubtes i per tot el que he aprés en les nostres converses científiques.

Quiero agradecer al Prof. Francisco Santoyo y al Prof. José Manuel Domínguez, de la Universidad de Granada, el suministro de diferentes moléculas sintetizadas, su calidad científica, y sus excelentes ideas. Quiero agradecer al Prof. José Manuel Domínguez por haberme dado la oportunidad de hacer una estancia breve en su grupo. También quiero agradecer al Dr. Mariano Ortega y al Dr. Fernando Carmona, de esa misma universidad, toda la ayuda prestada.

Moltes gràcies a la Dra. Imma Ratera i al Dr. Witold Tatkiewicz per la excel·lent col·laboració en la investigació de les propietats mecàniques dels quatsomes. Gràcies a la Dra. Núria Crivillers per les mesures de voltametria cíclica i tot el seu suport. També vull agrair a la Silvia Illa totes les simulacions que va fer en el seu treball de màster d'una part del meu treball experimental.

Vull donar les gràcies a la Dra. Evelyn Moreno per tot el treball de SWAXS i per haver-me iniciat en el món dels sincrotrons. I would like to expand my gratitude to Prof. Jan Skov Pedersen, from Aarhus University in Denmark, for the conducted analysis of the SAXS data of quatsomes.

M'agradaria agrair a les persones que em van iniciar al increïble món de les vesícules i han fet que realment estimi molt la meva feina. Han sigut les persones que em van ensenyar al laboratori i m'han ajudat en tot moment, vull donar les meves sinceres gràcies a la Dra. Ingrid Cabrera, a la Dra. Elisa Elizondo i a la Dra. Evelyn Moreno.

Moltes gràcies al Servei de Microscòpia de la UAB, i principalment moltes gràcies al Dr. Pablo Castro que ha sigut un tècnic excel·lent amb una gran qualitat científica. Muchas gracias por tu esfuerzo incondicional, por compartir siempre tus conocimientos y por las extensas conversaciones en las largas sesiones de cryo-TEM, ¡muchas gracias de verdad!

Moltes gràcies al Servei d'Anàlisi Química de la UAB per totes les mesures realitzades. També m'agradaria agrair a la Dra. Alba Eustaquio la seva gran disposició per resoldrem dubtes analítics i sobretot per presentar-me l'ICMAB, tot va començar amb una trucada... gràcies!

Vull recalcar també tot el valuós treball desenvolupat per diferents estudiants que han realitzat estades breus al grup i ens ajudat en la nostra recerca. Especialment vull agrair al Marwane Chlyeh, al David Piña i a l'Alejandro R. Pérez.

Moltes gràcies al personal tècnic i d'administració del ICMAB. Sobretot moltes gràcies a l'Amable per totes les caracteritzacions realitzades. Gracias Amable por ayudarme siempre y sobre todo por tu alegría.

També vull agrair a la professora Rosemary Thwaite, del Servei de llengües de la UAB, tot el suport que m'ha donat per la redacció d'aquesta tesi en anglès.

En un ambit més personal, vull donar les gràcies a tots els meus companys de NANOMOL, tots els que han passat des de el primer dia que vaig posar un peu al laboratori. Heu sigut tots grans companys i amics i heu fet que tot fos més fàcil. També vull agrair a tots els companys del ICMAB tot els bons moments que hem passat. Vull agrair a la Laura Cabana tots els ànims que sempre m'ha transmès i l'ajuda amb l'anglès, i a la Marta Vilardell que em descobrís el món del LyX per escriure aquesta tesi.

Vull donar les gràcies a tots els *supercrítics* que han treballat més estretament amb mi, Santi, Alba, Elisa, César, Ingrid, Elena, Evelyn, Marc, Queralt, Eva, Maria, Antonio, Dolores, David i Ariadna. Gràcies per ser uns companys immillorables i excepcionals. També vull agrair a les *supers* tot el que m'han aportat durant aquests anys. Gracias por vuestro amor y sabiduría, gracias por todos los momentos vividos y sobre todo gracias por estar siempre ahí. Solo por conoceros, todo esto ya ha valido la pena.

Aprofito per agrair a tots els amics més propers que sempre s'han interessat per la meva feina i m'han donat molta força.

Vull agrair molt especialment als meus pares i germans tot l'amor i recolzament que sempre m'han donat. GRÀCIES en majúscules per tot, aquesta tesi també és vostra! També vull donar les gràcies a tota la meva família Ferrer-Tasies per tots els ànims i suports. I vull agrair als meus avis, els que ja no estan, tot el que em van ensenyar, vau ser persones molt fortes que vau lluitar molt a la vida i per això m'agradaria dedicar-vos aquesta tesi.

Per últim vull agrair-te Rafa tot el teu suport, la teva força, el teu pensament crític i la teva valentia. M'has animat sempre a assolir nous reptes i sobretot, m'has ensenyat a ser feliç. Aquesta tesi la vaig començar i la he acabat gràcies a tu. Ho saps, no? jo també.

A TOTS VOSALTRES... MOLTÍSSIMES GRÀCIES!

Lidia

Preamble

Great part of this PhD Thesis has been performed under the frame of collaborative projects. This is why besides the results obtained by the author, it has been decided to include some experiments performed by other scientists which complete and reinforce the work presented in this manuscript.

Contents

1

Introduction and Objectives

1.1. Introduction

1.1.1. What is supramolecular chemistry?

Supramolecular chemistry, which dates back to the late 1960s, has been described as "chemistry beyond the molecule", whereby a "supermolecule" is a species that is held together by non-covalent interactions between two or more covalent molecules or ions. It can also be described as "lego™ chemistry" in which each lego™ brick represents a molecular building block and these blocks are held together by intermolecular interactions (bonds), of a reversible nature, to form a supramolecular aggregate [1]. These intermolecular bonds include electrostatic interactions, hydrogen bonding, $\pi-\pi$ interactions, dispersion interactions and hydrophobic or solvophobic effects. These non-covalent interactions are considerably weaker than covalent interactions, which can range between ca. 150 kJ mol^{-1} to 450 kJ mol^{-1} for single bonds. Non-covalent bonds range from 2 kJ mol^{-1} for dispersion interactions to 300 kJ mol^{-1} for 'ion-ion' interactions [1].

Supramolecular chemistry can be split into two broad categories; *host–guest chemistry* and *self-assembly*. The difference between these two areas is a question of size and shape. If one molecule is significantly larger than another and can wrap around it then it is termed the 'host' and the smaller molecule is its 'guest', which becomes enveloped by the host. In that case the supramolecular assembling phenomena is qualified as *host–guest chemistry*. Where there is no significant difference in size and no species is acting as a host for another, the non-covalent joining of two or more species is termed *self-assembly* [1].

1.1.2. Molecular self-assembly principles

Molecular self-assembly can be defined as the spontaneous and reversible association of molecular species to form larger, more complex supramolecular entities according to the intrinsic information contained in the components (chemical building blocks) [1–4]. The formation of molecular crystals [5], colloids [6], lipid bilayers [7], phase-separated polymers [8], and self-assembled monolayers [9] are all examples of molecular self-assembly, as in Nature are the folding of polypeptide chains into proteins [10] and the folding of nucleic acids into their functional forms [11]. The concepts of self-assembly historically have come from studying molecular processes and, as it occurs in the majority of fields, the inspiration for many supramolecular species designed and developed by scientists has come from biological systems (Figure 1.1).

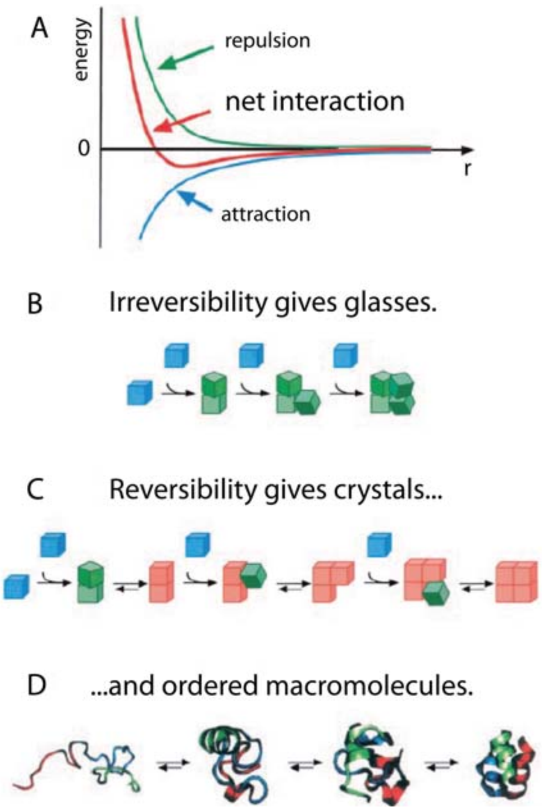

Figure 1.1.: (A) Aggregation occurs when there is a net attraction and an equilibrium separation between the components. The equilibrium separation normally represents a balance between attraction and repulsion. (B and C) Schematic illustration of the essential differences between irreversible aggregation and ordered self-assembly. (B) Components (shown in blue) that interact with one another irreversibly form disordered glasses (shown in green). (C) Components that can equilibrate, or adjust their positions once in contact, can form ordered crystals if the ordered form is the lowest-energy form (shown in red). (D) Biology provides many examples of self-assembly (here, the formation of a protein, an asymmetric, catalytically active nanostructure); these examples will stimulate the design of biomimetic processes. Obtained from [3].

The success of self-assembly in a molecular system is determined by five characteristics of such systems [3]:

- **Components**. A self-assembling system consists of a group of molecules or segments of a macromolecule that interact with one another. Their interaction leads from some less ordered state (a solution, disordered aggregate or random coil) to a final state (a crystal or folded macromolecule) that is more ordered.

- **Interactions.** Self-assembly occurs when molecules interact with one another through a balance of attractive and repulsive interactions. These interactions are generally weak (that is, comparable to thermal energies) and non-covalent (van der Waals and Coulomb interactions, hydrophobic interactions, and hydrogen bonds).

- **Reversibility (or adjustability).** For self-assembly to generate ordered structures, the association either must be reversible or must allow the components to adjust their positions within an aggregate once it has formed. The strength of the bonds between the components, therefore, must be comparable to the forces tending to disrupt them. For molecules, the forces are generated by thermal motion.

- **Environment.** The self-assembly of molecules is carried out normally in solution or at an interface to allow the required motion of the components. The interaction of the components with their environment can strongly influence the course of the process.

- **Mass transport and agitation.** For self-assembly to occur, the molecules must be mobile. In solution, thermal motion provides the major part of the energy required to bring the molecules into contact.

1.1.3. Self-assembled colloidal nanostructures

Most of the self-assembling molecules possess amphiphilic character. Amphiphiles, or surfactants, are molecules with two distinct regions that have very different solubilities. They are constituted or are formed by a hydrophilic (water-soluble) end and a lipophilic (organic-soluble) end that is highly hydrophobic. The hydrophilic part will be referred to as the head group and the hydrophobic part as the tail.

Amphiphilic molecules are common in everyday life, for example, soaps, which contain sodium dodecyl sulfate, and phospholipids, like phosphatidyl choline, which are the basis of biological cell membranes. Other lipids, such as cholesterol and fatty acids, are also part of this category. The lipophilic region is made up of long aliphatic organic chains, such as alkanes, fluorocarbons or aromatic or other non-polar groups. The head group is made up of highly solvated hydrophilic functionalities, such as sulfonates, carboxylates, phosphonates and ammonium derivatives. It is this hydrophilic functionality that gives rise to the different classes of surfactants. Examples include anionic (i.e., sulfonate) groups, cationic (i.e., quaternary ammonium salts), amphoteric (i.e., zwitterionic betaines) and non-ionic (i.e., fatty acids) [1].

When amphiphilic molecules are under aqueous conditions, their hydrophobic-hydrophilic dual character promotes their association through weak, non-covalent interactions to form ordered assemblies with different morphologies and sizes that range from nanometers to microns [12–15]. The thermodynamic driving force of this molecular self-assembly is provided by the desolvation, collapse, and intermolecular association of the hydrophobic part of monomers. This tendency of the hydrophobic tail to minimize contact with water, called *hydrophobic effect*, is mainly due to the entropic gain of the water structure by not being in contact with the hydrophobic part [16]. Intermolecular polar interactions, such as electrostatics and hydrogen bonding, can also occur and help define the structural specificity. A variety of different aggregate shapes are observed that range from spherical and rod-like micelles to amphiphilic bilayers.

The actual form assumed by a colloidal aggregate depends on the molecular structure and geometry of the constituent amphiphiles. In a first-order approximation, the geometry of an amphiphile is described by the classical packing parameter concept developed by Israelachvili [17, 18]. For dilute solutions in which interactions between aggregates are not important, the packing parameter is defined as $p = v/a_0 l_c$, where v is the volume of the hydrocarbon chain(s) of the molecule, which are assumed to be fluid and incompressible, the critical chain length l_c is the maximum effective length that the chains can assume, and a_0 is the optimal cross-sectional area per headgroup at the polar hydrocarbon/water interface of the assembly. So, the packing parameter of an amphiphilic molecule determines the preferred curvature of the aggregates formed: $p < 1/3$ spherical micelles; $1/3 < p < 1/2$, cylindrical micelles; $1/2 < p < 1$, vesicles; $p = 1$, planar bilayers; $p > 1$, reverse phases (see Figure 1.2).

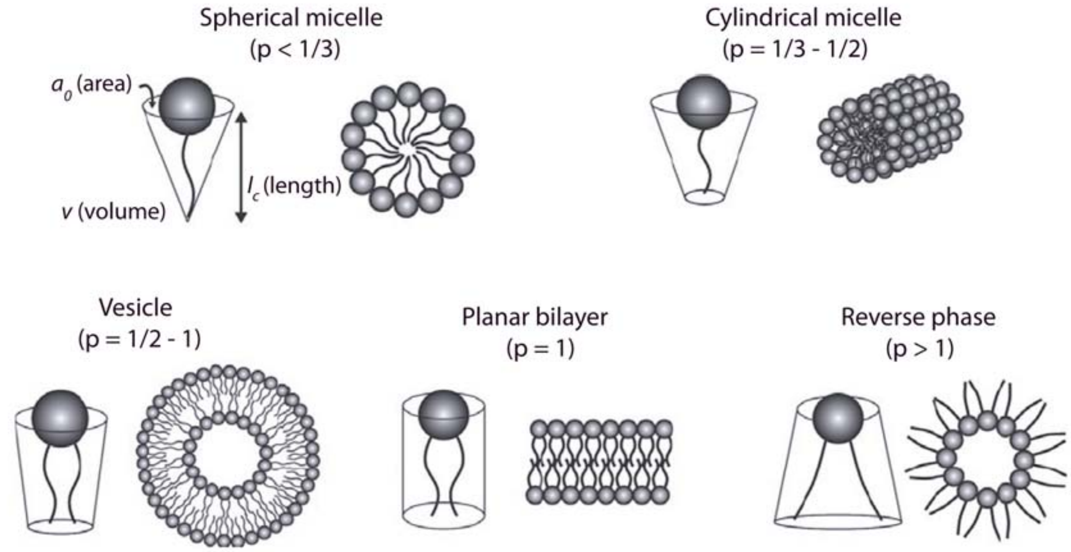

Figure 1.2.: Relationship between the packing parameter $(p = v/a_0 l_c)$ and the self-assembled morphology of amphiphilic molecules under aqueous conditions. Obtained from [19].

The morphology of the final assembled structure is dependent not only on the geometry of the monomer but also on the external environment in which self-assembly occurs [3, 20, 21]. The temperature, pH and ionic strength of the aqueous phase, as well as the concentration of the monomer and the preparation method, can dictate the formation of a variety of structures formed by a single, distinct amphiphile. Thus, the prediction of the supramolecular structure is difficult due to the spatial complexity and relative weakness of the intermolecular interactions (for example, electrostatic forces, hydrogen bonding, π-π stacking and hydrophobic effects). Therefore the ability to design and arrange individual molecular building blocks into well-defined architectures in aqueous solutions remains a challenge [22].

1.1.4. Cholesterol as molecular building block

Cholesterol, an essential component of mammalian cells, has been described by Michael S. Brown and Joseph L. Goldstein as “the most highly decorated small molecule in biology” [23, 24], and has excellent properties such as biocompatibility, biodegradability, and low toxicity [25, 26]. Cholesterol’s predominant characteristic is its ability to modulate the physicochemical properties (e.g. fluidity and permeability) of the cell membrane. Due to this, cholesterol affects a number of cellular processes [24].

Cholesterol is an amphiphatic molecule, a compound possessing both hydrophilic and lipophilic properties. It contains both a polar hydroxyl group on one side and a non-polar tetracylic steroidal ring structure with a branched hydrocarbon tail on the other (Figure 1.3). Further, cholesterol is comprised of a rigid planar subunit due to the *trans*-configuration of the rings and a flexible iso-octyl side chain 'tail'. The combination of this rigidity and flexibility gives cholesterol the property of orientational ordering and display of liquid crystalline behavior in combination with amphiphilic lipid membrane binding capabilities [24]. Therefore, cholesterol is structurally composed of different sections which play a role in its interesting self-assembly behavior in a variety of multi-component solutions [27–30].

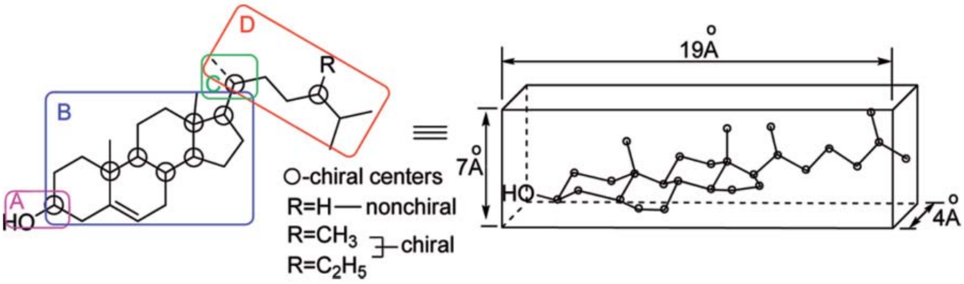

Figure 1.3.: A structural depiction of a cholesterol molecule highlighting the four domains of functional importance ((A) important for polarity and hydrogen bonding, (B) sterol rings, its conformation is important as it provides a rigid planar skeleton, (C) controls the conformation of the side chain, and (D) branched aliphatic side chain) (left) to function in membranes as a flat elongated compound. The structure presumed to form in cellular membranes (right). Obtained from [31].

Helical ribbons were first discovered in human gallbladder bile, and it was found that these structures form as a precursor of gallstones upon dilution of bile [29]. Konikoff *et al.* confirmed that cholesterol is the major constituent of these helical ribbons by various experimental techniques including density gradient centrifugation or X-ray diffraction. They also found that the helical ribbons themselves are precursors of stable cholesterol monohydrate crystals [28, 29]. Chung *et al.* used several model bile systems which consisted of a mixture of three types of chiral molecules in water: a bile salt, a phosphatidylcholine, and cholesterol. They demonstrated that helical ribbons formed with two distinctive pitch angles, 11.1 ± 0.5° and 53.7 ± 0.8° [27]. Zastavker *et al.* then showed that the self-assembly of the helical ribbons with these two distinct pitch angles was not unique to model bile, but was a general phenomenon for a variety of four-component systems composed of a bile salt or non-ionic surfactants, a phosphatidylcholine or fatty acids, a steroid analogue of cholesterol, and water [32]. Additionally, in almost all systems, they found small amounts of intermediate pitch helices (Figure 1.4). It was found that in undiluted solutions containing cholesterol, surfactants, and fatty acids or phospholipids, cholesterol is solubilised by micelles, i.e.

cholesterol was contained in the core. These solutions contain both the free surfactants and the surfactants contained in micelles in equilibrium. Upon dilution, the equilibrium shifts from primarily micelles to primarily free surfactants. The micelles break up and release the cholesterol, causing the solution to become supersaturated with cholesterol. Subsequent dilution leads to the formation of large cholesterol monohydrate crystals. However, the exact structures that are formed and the sequence in which they form depend on the composition of the solution and the concentration of its components as shown in Figure 1.5 [24]. Therefore, it is clear that aqueous mixtures of cholesterol with other components can lead the formation of different structures.

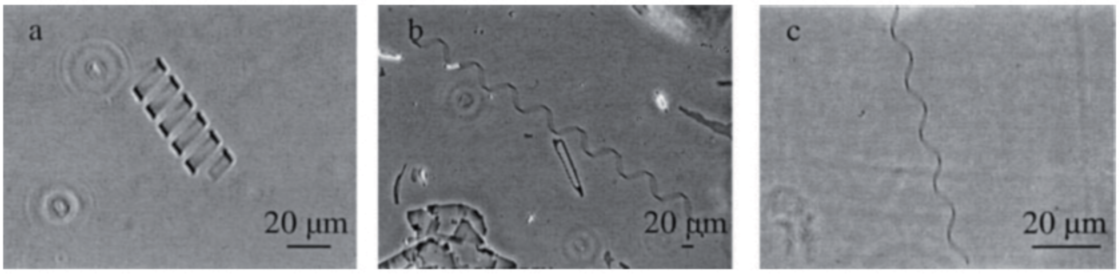

Figure 1.4.: Helical ribbons observed in an aqueous mixture of a non-ionic surfactant, fatty acid and cholesterol. Three different helical pitches were detected, (a) 11 ± 2° (low pitch angle), (b) 54 ± 2° (high pitch angle), and (c) 40.8 ± 3.8° (intermediate pitch angle). Obtained from [32].

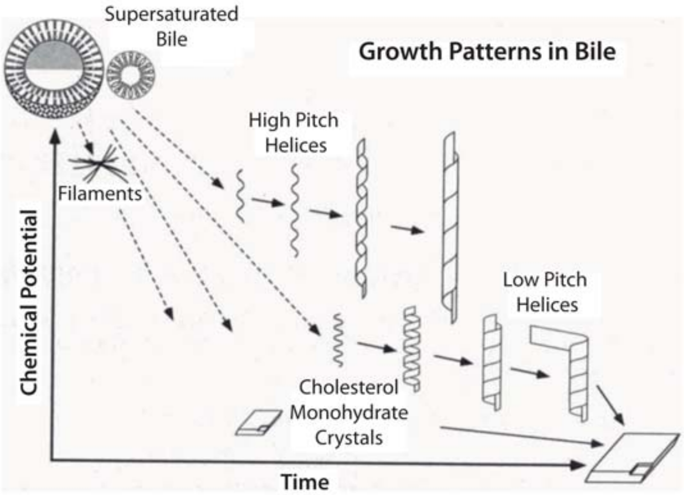

Figure 1.5.: Sequence and relative stability of metastable intermediates plotted as a functions of time after supersaturation of bile. Obtained from [27].

On the other hand, the majority of conjugation strategies used to conjugate cholesterol onto molecules, biomolecules, or macromolecules of interest rely on the hydroxyl group of the cholesterol ‘A’ domain (see Figure 1.3). The most common are esterification, carbamate, and carbonate bond formation using chloroformate derivatives [24]. Self-assembly of amphiphilic cholesterol-modified molecules, such as cholesterol-modified polymers, has been a subject of great interest for the past few decades [33, 34]. Cholesterol units attached onto macromolecules as pendant(s) or as end-group(s) can induce formation of structures of well-defined morphology in water as a result of specific interactions among the cholesterol moieties [24, 35]. Besides, there are several reports that also use these cholesterol moieties as the driving force for biasing the organization of chromophores through different packing modes, leading to control over nanoscopic properties of the resultant hierarchical self-assembly [36].

Cholesterol incorporated into liposomes also plays an important role in biomedical applications. Its ability to modulate the physicochemical properties of lipid bilayer has been employed to stabilize liposomes for their application in drug delivery or analytical science. Further, vesicle membranes can be modified with cholesterol molecules bearing different groups, where functionalized vesicles can be easily formed. Therefore, the small molecule cholesterol has contributed significantly to the field of bionanotechnology and its many applications, such as biosensing, analytical sciences, drug delivery, and cell mimicry [24].

1.1.5. Cholesterol-rich nanovesicles

The bottom-up fabrication of supramolecular architectures with controlled three-dimensional arrangements is key to the design of novel functional materials. In this regard, vesicles are one of the most studied self-assembled structures due to their diverse and important applications, which among others cover their use as cell membrane models [37], reaction vessels [38, 39] and drug delivery systems (DDS) [40–43].

Vesicles are spherical objects enclosing a liquid compartment (lumen), with a diameter ranging from 20 nm to a few thousand of nanometers, separated from its surroundings by at least one thin membrane consisting of a bilayer (unilamellar) or several layers (multilamellar) of amphiphilic molecules [17]. Depending on the number of bilayers formed (lamellarity) and the size of the vesicles, they are broadly classified into small unilamellar vesicles (SUVs, size < 200 nm and single bilayer), large unilamellar vesicles (LUVs, size ranging from 200 - 1000 nm and single bilayer), giant unilamellar vesicles (GUVs, size > 1000 nm and single bilayer), multilamellar vesicles (MLVs, consisting of several concentric bilayers) and multivesicular vesicles (MVVs, composed by several small vesicles entrapped into larger ones) (Figure 1.6).

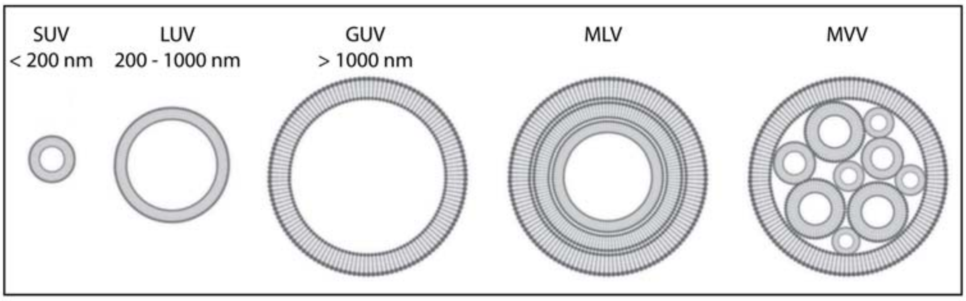

Figure 1.6.: Types of vesicles depending on size and lamellarity. SUV: small unilamellar vesicle; LUV: large unilamellar vesicle; GUV: giant unilamellar vesicle; MLV: multilamellar vesicle; MVV: multivesicular vesicle.

Size and lamellarity are important structural parameters that need to be controlled, since they are crucial factors affecting the properties and performance of vesicles. Furthermore, their unique structure enables them to trap hydrophobic compounds within their bilayers and hydrophilic compounds within their lumen, makes vesicles excellent candidates to be used as nanocarriers for the protection and delivery of active ingredients in pharmaceutical and cosmetic formulations [40–46].

Liposomes, vesicles constituted mainly by phospholipids, are the most studied vesicular systems since Dr. Alec Bangham *et al.* first reported their discovery in 1964 [47, 48]. Over the last 50 years, liposomal nanotechnology has significantly evolved, and now liposomes have found applications in many fields including nanopharmaceutics [49], cosmetics [50], food [51], and textile [52] industries. Liposomes are essentially used as nanocontainers for protecting, transporting, and targeting solutes [53] and are the most common and well-investigated nanocarriers for targeted drug delivery [54]. They have improved therapies for a range of biomedical applications by stabilizing therapeutic compounds, overcoming obstacles to cellular and tissue uptake, and improving biodistribution of compounds to target sites *in vivo* [55, 56]. The diversity in the design of the composition, structure, and size of liposomes makes possible to tailor liposome-based systems for different applications in drug delivery and for diagnosis purpose. Vesicle membranes can be modified with different targeting or protective units, that promote specific and increased accumulation of the drug or the bioactive molecule in the target cells. Figure 1.7 summarizes most of the modifications or improvements that a liposome can experience for different applications in drug delivery and diagnosis.

As a drug delivery system, liposomes offer several advantages including biocompatibility, capacity for self-assembly, ability to carry large drug payloads, and a wide range of physicochemical and biophysical properties that can be modified to control their biological characteristics [54–56]. Encapsulation within liposomes protects compounds from early inactivation, degradation and dilution in the circulation [57].

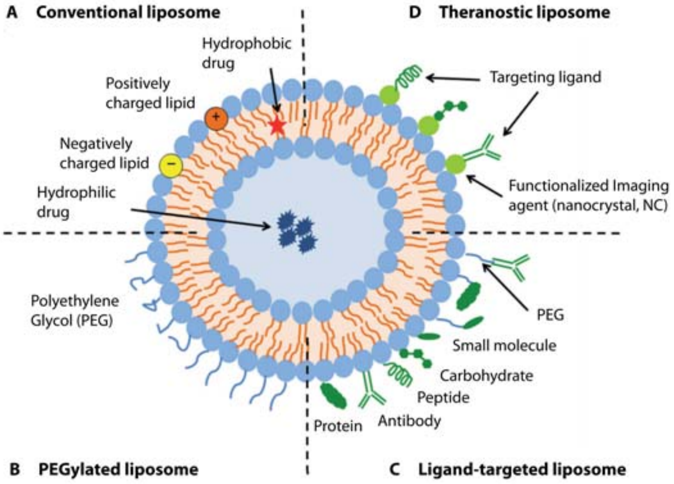

Figure 1.7.: Schematic representation of the different types of liposomal drug delivery systems. (A) Conventional liposome - Liposomes consist of a lipid bilayer that can be composed of cationic, anionic, or neutral (phospho)lipids, which encloses an aqueous core. Both the lipid bilayer and the aqueous space can incorporate hydrophobic or hydrophilic compounds, respectively. (B) PEGylated liposome - Liposome characteristics and behavior *in vivo* can be modified by addition of a hydrophilic polymer coating, polyethylene glycol (PEG), to the liposome surface to confer steric stabilization. (C) Ligand-targeted liposome - Liposomes can be used for specific targeting by attaching ligands (e.g., antibodies, peptides, and carbohydrates) to its surface or to the terminal end of the attached PEG chains. (D) Theranostic liposome - A single system consist of a nanoparticle, a targeting element, an imaging component, and a therapeutic component. Obtained from [54].

The great potential and felicitous properties of liposomes has prompted their use in the treatment of some major health threats for humans including cancer, infections, metabolic and autoimmune diseases, and has even led to the first marketed products [58]. For example liposomal formulations of anticancer drugs have already been approved for human use. This is the case of Doxil®, a liposomal formulation of doxorubicin, which is an anthracycline drug, used to treat cancer in AIDS-related Kaposi’s sarcoma, leukemia, and ovarian, breast, bone, lung, and brain cancers [54]. Its advantages over the free doxorubicin are a greater efficacy and a lower cardio toxicity [59].

Important pharmacological specifications like stability, loading capability and leakage kinetics of entrapped substances, are determined by the structural characteristics (e.g. size, morphology, supramolecular organization, structural homogeneity) of these nanocarriers [60]. This is why the control of their structural features is a very important issue for drug delivery purposes. For instance small unilamellar vesicles (SUVs) have attracted great attention in the drug delivery field since these vesicles are large enough to avoid the first-pass elimination through the kidneys but sufficiently small to present a minimal uptake by the mononuclear phagocytic system (MPS), facilitating their longer circulation lifetime in the body and hence a higher possibility to reach the target cells [61]. Moreover, due to their nanoscale size SUVs can accumulate within tumours through the so-called enhanced permeability and retention (EPR) effect and thereby be applied in cancer therapy [62, 63]. This latter effect is produced by the anomalous enhancement of vascularisation around the tumours and the weakening of vascular endothelial cells. On the other hand SUVs, compared to MLVs or MVVs, allow a more robust membrane functionalization (Figure 1.8) and also these unilamellar systems can have a sharper response to an external stimulus (Figure 1.9).

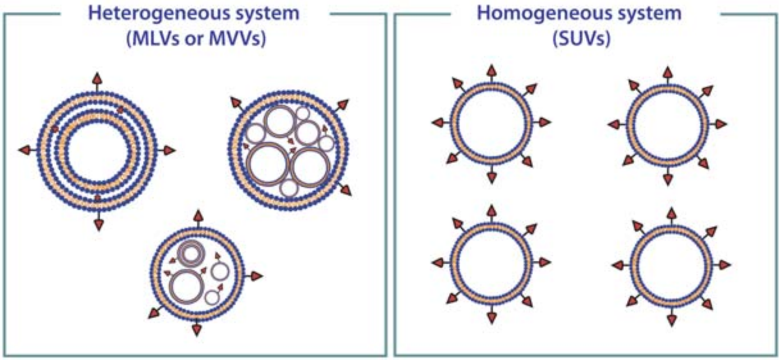

Figure 1.8.: Schematic illustration of the membrane functionalization of homogeneous (right) and heterogeneous (left) vesicle-like systems.

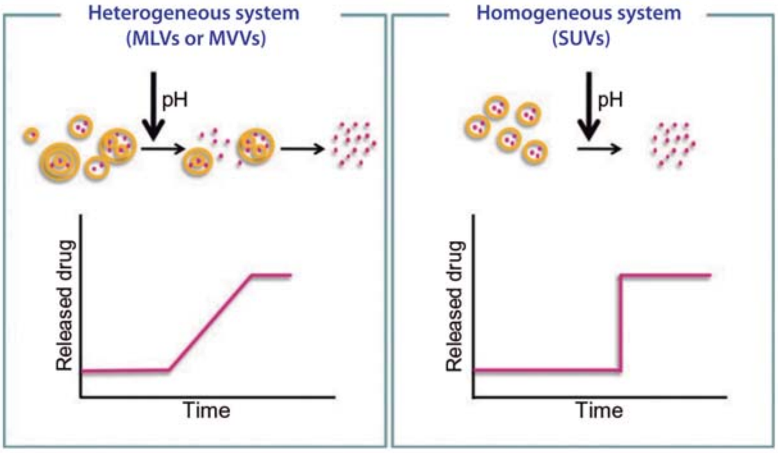

Figure 1.9.: Schematic illustration of the response to an external stimulus presented by a vesicular DDS with homogeneous (right) and heterogeneous (left) vesicle-to-vesicle structural characteristics in terms of size and lamellarity. Obtained from [19].

Despite their versatility and biocompatibility, the translation to the clinic of liposomal formulations could be hindered by the tendency of these lipid self-assemblies to aggregate and by their low degree of structural homogeneity, which are critical quality attributes with a major impact on the pharmacological properties [64]. Liposomes correspond to metastable kinetically trapped states, which are formed by the input of external energy on a planar lamellar phase (e.g., sonication or mechanical filtration). The stability of these structures is kinetically limited because their phospholipid building blocks are highly insoluble, and therefore, the collapsed planar lamellar is the equilibrium state of aggregation [65, 66]. Additionally, liposomes suffer chemical and physical alterations, which shorten their shelf-life and limit, as a consequence, drug stability and conditions of storage [67]. Liposomes' physical instability leads to problems of high permeability which induce undesired or too fast leakage rates. As previously mentioned, the addition of cholesterol is often required for modulating membrane rigidity and stability [57, 68, 69]. Their chemical instability is related to hydrolysis, oxidation, or peroxidation of the constitutive lipid molecules and is normally prevented by adding antioxidants and low-temperature storage.

Due to these special conditions of preparation and storage together with the elevated price of phospholipids, there is a great interest in finding nonphospholipid building blocks or tectons, which self-assemble into stable vesicles and which satisfy the quality standards required in pharmaceutical formulations [64, 70]. For instance, it has been reported that certain amphiphilic polymers, such as blockcopolymers, and some polypeptides organize themselves into vesicular-like architectures, giving rise to *polymersomes* [71–73] and *peptosomes* [74], respectively [75–77]. Other chemical structures such as rod-coil polymers, dendrimers, and amphiphilic fullerene derivatives have also shown to form vesicles [70]. Furthermore, the use of surfactants as cheaper and more stable substitutive molecules than phospholipids has emerged as a really interesting choice for the industrial production of vesicular systems in pharmaceutical and cosmetic applications. The combination of cationic and anionic surfactants generates the so-called *catanionic* vesicles [78–80], which are spontaneous, single-walled, equilibrium vesicles of controlled size and surface charge, and these vesicles are used for drug and gene delivery [81–83]. *Niosomes*, nonionic surfactant vesicles, are widely studied as an inexpensive alternative of nonbiological origin [84–86]. As their name indicates, niosomes are constituted by nonionic surfactants, which, depending on their nature, require the addition of a certain percentage of cholesterol to form vesicle-like supramolecular assemblies [85, 87]. As explained before, cholesterol is added to many formulations, as is the case with liposomes, to modulate the bilayer fluidity, reduce the leakage, and enhance the encapsulation efficiency (EE) of drugs [85].

Therefore in the finding of stable non-liposomal vesicle-like assemblies, it is considerably interesting the formation of cholesterol-based supramolecular vesicles.

1.1.6. Preparation of colloidal nanostructures

In order to achieve optimal performance of supramolecular architectures as functional materials, a tight control over the structural characteristics of the resulting self-assembled system is desired. Beside environmental conditions, such as temperature, pH, and ionic strength of the dispersing medium or type and concentration of components, the path followed for the self-assembly of the monomer units exerts an important influence on the structural properties of the obtained colloidal system and its homogeneity.

Methods for the preparation of homogeneous vesicular formulations that present controlled size, morphology, and supramolecular organization are required for fully exploiting the potential of these self-assembled structures.

Apart from controlling the structural characteristics of the final material, an adequate manufacturing process for pharmaceutical products (i.e., vesicles) should be easily compliant with the regulations imposed by the Food and Drug Administration (FDA) in the United States or the European Medicines Agency (EMA) in Europe. These regulations involve the development and implementation of good manufacturing practices (GMPs), which are rules that ensure the quality, safety, and traceability of the obtained product [88]. Regarding this, it is important to note that the majority of vesicle preparation methods use organic solvents and that, depending on the application, they should be reduced below the allowed limits [89].

1.1.6.1. Conventional methods

Current methodologies for vesicle formation such as *the thin film hydration* (TFH) [47, 48, 90, 91] or the *reverse-phase evaporation* [92], render systems with low structural homogeneity. For instance, the thin-film hydration (TFH) of vesicles, yields systems with large heterogeneity in terms of size and lamellarity. For that reason modifications after production are required in order to obtain a vesicle population with specific characteristics and properties (Figure 1.10). When preparing SUVs using these methodologies, post-formation steps, such as *freeze-thawing* [93, 94], *sonication* [95], *extrusion* [96–98] and *high pressure homogenization* [99, 100] are necessary for their size reduction and homogenization (Figure 1.11). Besides, those preparation methods involving a solvent-free state, like the TFH method (Figure 1.10), where a lipid film is formed, may favor demixing of membrane components [101]. For instance, by this method, it can be difficult to obtain stable cholesterol-based supramolecular vesicles due to the formation of cholesterol-rich domains [101, 102]. On the other hand, the use of large amounts of organic solvents, which are toxic in many cases, and particularly its incomplete post processing removal are other major issues not only at lab scale but also at large scale production [103]. In addition these multi-step and time-consuming procedures have a high risk of damaging the functionality of bioactive molecules, if they are added in the system, and of oxidizing the vesicle membrane components. All these drawbacks are particularly relevant for the preparation of stable cholesterol-based supramolecular vesicles, and if these vesicles are forming bioconjugates with expensive and/or fragile active biomolecules such as proteins, peptides, enzymes or hormones. Thus, it is crucial to develop simple and mild processes for controlling the structure at the micro-, nano- and supramolecular levels that are also amenable to be scalable [104].

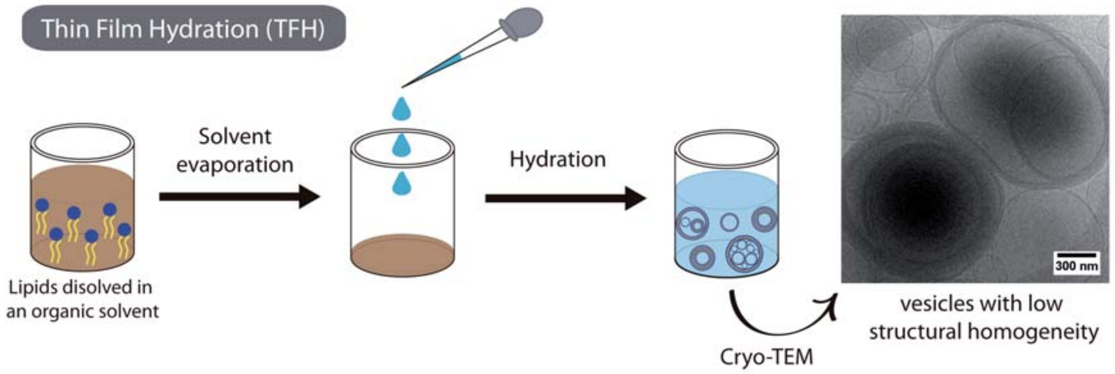

Figure 1.10.: Schematic illustration of vesicle formation using thin-film hydration (TFH) method and cryo-transmission electron microscopy (cryo-TEM) image corresponding to the obtained systems with low structural homogeneity.

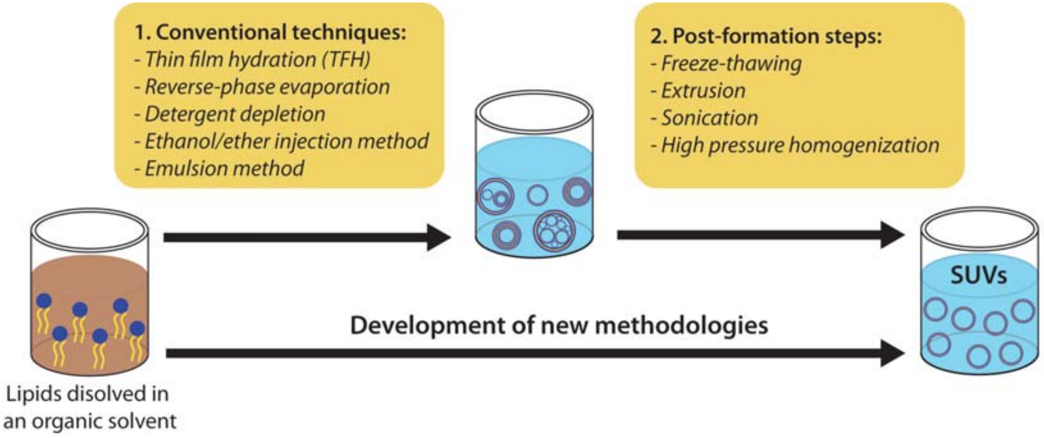

Figure 1.11.: Conventional methodologies for the preparation of vesicles and the most common post-formation steps for their homogenization.

1.1.6.2. DELOS-SUSP method using compressed CO_2

Compressed fluid (CFs)-based methodologies, also named as dense gas technologies, have been gaining ground during the last 25 years as promising alternatives to conventional methodologies for the preparation of nanostructured materials [105–109]. CFs are defined as a substance that at normal conditions of pressure *(P)* and temperature *(T)* exist as gases but with increased *P* can be converted into liquids or supercritical fluids. The supercritical region is achieved when the substance is exposed to conditions above its critical pressure *(Pc)* and temperature *(Tc)*. The most important feature, within the supercritical region, is that there is no phase boundary between the gas and liquid phases. The consequence is that supercritical fluids have properties which are "hybrids" of those normally associated with liquids and gases and which are continuously adjustable from gas to liquid with small pressure and temperature variations (Figure 1.12). Thus, the viscosities and diffusivities are similar to those of the gas phase while the density is closer to that of a liquid one. The possibility of obtaining such special behavior at conditions below or near the critical point (subcritical region), allow working at mild conditions of *T* and *P*, reducing the cost related to the use of elevated pressures and decreasing the risk of damaging the structure and properties of the molecules to be processed.

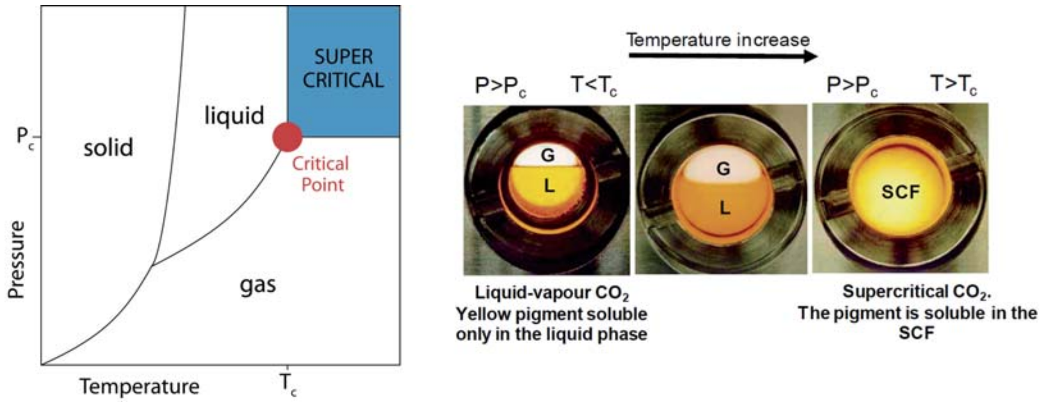

Figure 1.12.: Phase diagram of a compressed fluid (left) and images illustrating the different solvating power of CO_2 as a function of its state (right).

The solvent power of a CF, either in the liquid or supercritical state, is proportional to its density, which is extremely responsive to changes in temperature and pressure around the critical point. Solvation power of CFs can therefore be tuned by pressure changes, which propagates much more quickly than temperature and composition solvent changes. This can offer a better control over the morphology of the materials on the microscopic scale than most of conventional processing techniques. This combination of properties makes compressed or supercritical fluids particularly attractive and has led to the current scientific and industrial interests on them for material processing [110, 111]. The most widely used dense gas is carbon dioxide (CO_2) since it is non-flammable, non-toxic, noncorrosive, inexpensive, non-polluting and has easily accessible critical parameters of 31.1 °C and 73.8 bar [112]. Due to these interesting properties, CO_2 has gained great attention as a "green substitute" to organic solvents in the preparation of lipid-based nanocarriers such as liposomes. Several methodologies involving compressed CO_2 have recently been investigated to improve the processing of vesicles because they provide the potential to reduce the amount of organic solvent required by conventional methods and allow a better control over the final vesicle structural characteristics [113–115]. Moreover processing with compressed CO_2 offers sterile operating conditions and the potential for one-step production processes, which is convenient in transferring the technology to larger scale operations [116].

Several CFs methodologies have been developed to generate vesicles [103], however some problems related with the elevated pressures and temperatures required during the processing are still a drawback for some of them.

1.1.7. DELOS-SUSP method for the preparation of cholesterol-rich vesicles

In the year 2000 the *Nanomol* group, where this Thesis has been done, developed a new procedure based on the use of compressed CO_2 called *Depressurization of an Expanded Organic Solution (DELOS)* for the production of micron-sized and submicron-sized crystalline particles with high polymorphic purity [117, 118]. As novelty the process used the CO_2 as co-solvent being completely miscible at a given pressure and temperature with an organic solution containing the solute to be crystallized [117, 119, 120]. The process uses milder conditions of pressure (< 10 MPa) and temperature (< 308 K) than the previously mentioned methodologies based on CFs [103], allowing the processing of heat labile compounds and reducing the investment cost of a high pressure plant when the process is scaled-up. In order to take full advantage of compressed fluid processing without using severe working conditions, a novel and improved procedure based on DELOS process was developed latter on for the preparation of colloidal suspensions. This method, named as *Depressurization of an Expanded Organic Solution-Suspension (DELOS-SUSP)*, enabled the one-step preparation of cholesterol-rich nanovesicles [121]. Moreover it has been already demonstrated that this method allows the preparation of several nanovesicle-bioactive hybrids [122]. α-Galactosidase A (GLA)-nanovesicle and epidermal growth factor (EGF)-nanovesicle hybrids prepared using DELOS-SUSP, have shown higher efficacy, in relation to the free proteins, in pre-clinical *in-vitro* and *in-vivo* tests and in compasionate treatments with humans, respectively [123, 124].

Briefly, the DELOS-SUSP method (Figure 1.13) consists in loading a solution of the membrane lipid components and the desired hydrophobic bioactives in an organic solvent (e.g., ethanol) into a high-pressure autoclave previously driven to the working temperature (Figure 1.13a). The reactor is then pressurized, in a second stage, with a large amount of compressed CO_2 until reach the working pressure (10 MPa) (Figure 1.13b). Finally in the third stage, the vesicular conjugates are formed by depressurizing the resulting CO_2-expanded solution over an aqueous phase, which might contain water soluble surfactants and hydrophilic bioactives (Figure 1.13c).

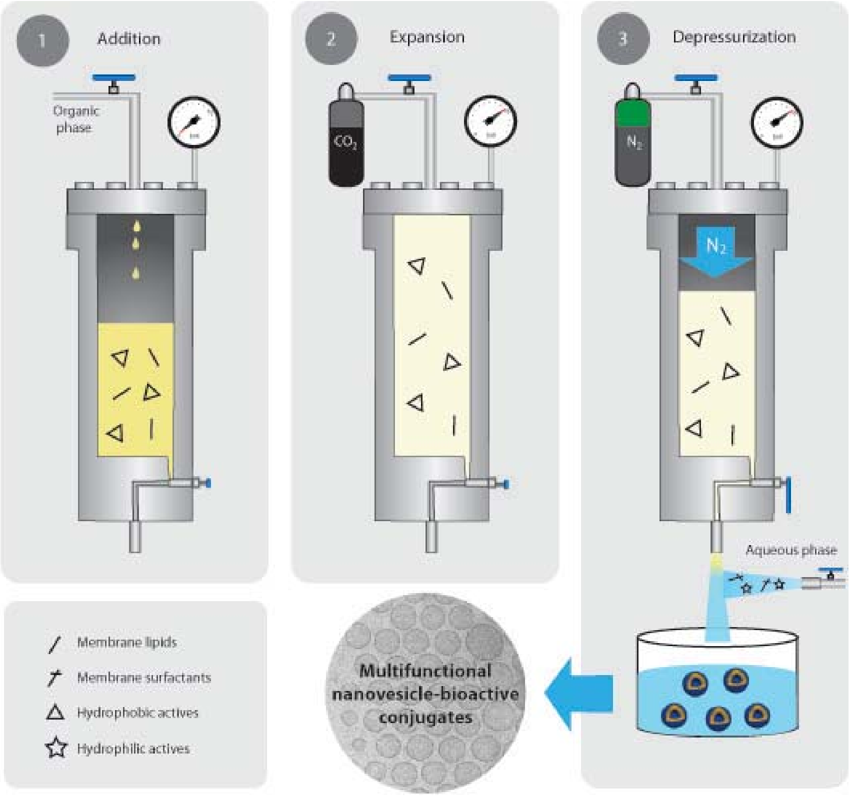

Figure 1.13.: Schematic representation of the DELOS-SUSP method for the efficient preparation of multifunctional nanovesicle-bioactive hybrids. The whole procedure includes the loading (a) of an organic solution of the lipidic membrane components and the desired hydrophobic active compounds/molecules into an autoclave at a working temperature (T_w) and atmospheric pressure; the addition of CO_2 (b) to produce a CO_2- expanded solution, at a given X_{CO_2}, working pressure (P_w), and T_w, where the hydrophobic active and membrane components remain dissolved; and finally, the depressurization (c) of the expanded solution over an aqueous solution, which might contain membrane surfactants and hydrophilic biomolecules, to produce an aqueous dispersion of the nanovesicle-bioactive(s) hybrids with vesicle-to-vesicle homogeneity regarding size and morphology.

In the final step a flow of N_2 at the working pressure is used in order to push down the CO_2-expanded solution and to keep constant the pressure inside the reactor. During the depressurization step, the expanded organic solution experiences a large, abrupt and extremely homogeneous temperature decrease produced by the CO_2 evaporation from the expanded solution, and this is probably the reason that explains the obtaining of homogeneous vesicles regarding size, lamellarity and morphology. No further energy input is required for achieving the desired SUVs structural characteristics, neither for increasing the loading or functionalization efficiencies.

By using DELOS-SUSP non-liposomal nanovesicular structures, composed of non-soluble cholesterol and the cationic surfactant hexadecyltrimethylammonium bromide (CTAB) were prepared (Figure 1.14). Specifically, these structures were prepared by depressurizing a volumetric expanded organic solution containing cholesterol in ethanol over a flow of an aqueous solution containing the CTAB surfactant. These nanovesicles show a high vesicle-to-vesicle homogeneity regarding size, morphology and supramolecular organization [102], which make them extremely attractive for their use as nanocarriers in drug delivery or as templates in material synthesis, among others.

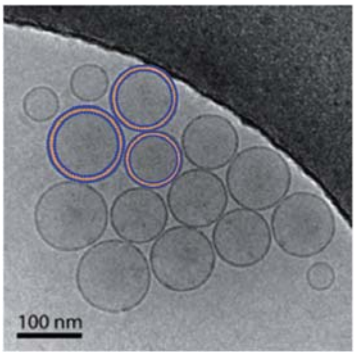

Figure 1.14.: Cryo-transmission electron microscopy (cryo-TEM) image corresponding to the non-liposomal vesicular system composed of cholesterol and CTAB in water.

The present Thesis is devoted to deep study the self-assembling phenomena and phase behavior related to these new nanostructures, and to their exploitation for the formation of other nanocolloids.

1.2. Objectives

Nowadays, there is a great interest in finding non-lipid building blocks or tectons, which self-assemble into stable vesicles and which satisfy the quality standards required in pharmaceutical formulations. Within this framework, *Nanomol* group discovered the formation of novel stable non-liposomal nanovesicles using aqueous mixtures of cholesterol and hexadecyltrimethylammonium bromide (CTAB), a cationic surfactant. This vesicle formation was achieved by a compressed fluid (CF)-based technology, the DELOS-SUSP method. In view of the high stability that these cholesterol-based supramolecular vesicles exhibited, the aims of this Thesis were to provide further insight into their physicochemical features and expand their range of application.

We have investigated these novel non-liposomal nanovesicles at different levels, from their formation up to their applications in bioimaging, among others. Furthermore, we also studied the formation of other cholesterol-based supramolecular assemblies with non-vesicular morphology by the DELOS-SUSP process. The following three main objectives have been addressed, each as a Thesis chapter:

- Objective 1: To characterize in depth the formation and properties of stable non-liposomal nanovesicles formed using aqueous mixtures of cholesterol and ionic surfactants.

- Objective 2: To study the self-assembling of aqueous mixtures of cholesterol derivatives with ionic surfactants by the DELOS-SUSP process.

- Objective 3: To develop new nanovesicle-nanocrystal hybrids for biomedical imaging applications.

2

Quatsomes, new vesicular system

2.1. Background

As stated in the general Introduction (Chapter 1), there is a great interest in finding non-lipid building blocks or tectons, which self-assemble into stable vesicles. In this context, the *Nanomol* group, under the framework of the PhD Thesis of Dr. Mary Cano-Sarabia [125], obtained non-liposomal nanoscopic vesicles using cholesterol and CTAB in water by DELOS-SUSP method. Dynamic light scattering (DLS) and cryogenic transmission electron microscopy (cryo-TEM) (Figure 2.1) revealed that this vesicular system has an outstanding vesicle to vesicle homogeneity regarding size and lamellarity.

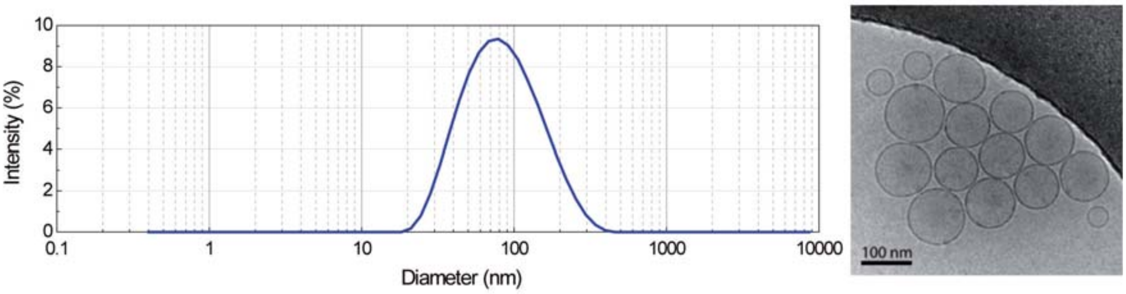

Figure 2.1.: Particle size distribution (left) and cryo-TEM image (right) corresponding to a vesicular system composed of cholesterol and CTAB in water.

Figure 2.2 shows the molecular structures of quaternary ammonium surfactant CTAB and cholesterol, and their corresponding supramolecular assemblies (micelles and crystals, respectively) formed in the presence of water. Therefore, the self-organization of cholesterol and CTAB into exceptionally homogeneous bilayer vesicles has to be attributed to a synergy between both molecular entities.

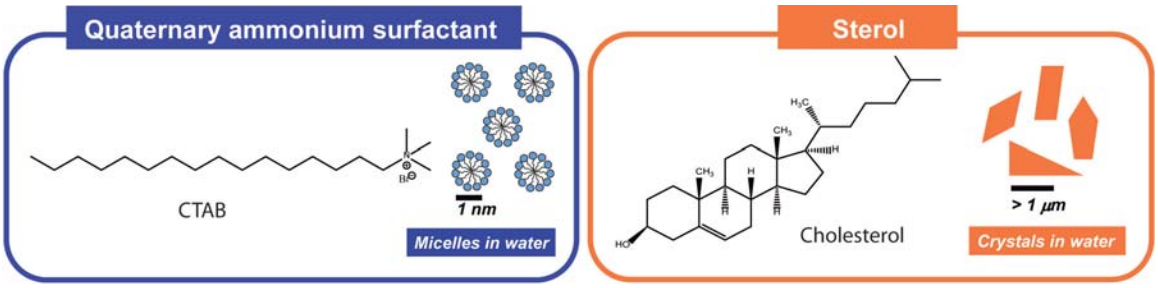

Figure 2.2.: Molecular structures of CTAB and cholesterol showing that in water CTAB forms micelles [126, 127] and cholesterol forms crystals.

In this Chapter we have studied in depth the self-assembling of cholesterol and CTAB molecules in aqueous medium in order to rationalize the nature of their exceptional non-covalent interactions and the driving force of assembling them into nanovesicles.

2.2. Self-assembling of cholesterol and CTAB in aqueous medium

To investigate the cooperative behavior between cholesterol (Chol) and CTAB molecules, different aqueous mixtures of both molecules at different Chol/CTAB molar ratio (Q value) were prepared by a sonication process. The different colloidal phases formed were characterized by optical density measurements (OD), dynamic light scattering (DLS), and cryo-TEM. Experimental observations were complemented by theoretical studies using Molecular Dynamics (MD) simulations.

According to the literature and as explained in the Introduction of this Thesis, systems composed of one or more amphiphilic molecules can form different types of colloidal phases depending on their geometry, the molar ratio between them, the concentration and the temperature [128–137]. Using different characterization techniques, we can elucidate the structure of the different colloidal supramolecular structures formed and study the transition between them. For example, as shown in Figure 2.3, the transition of a micellar phase to a vesicular phase can involve the formation of intermediate supramolecular organizations with rodlike or disklike-shaped micelles. Understanding the pathways of self-assembly is the key to achieving control and predictive capabilities in order to fabricate well-defined nanostructures.

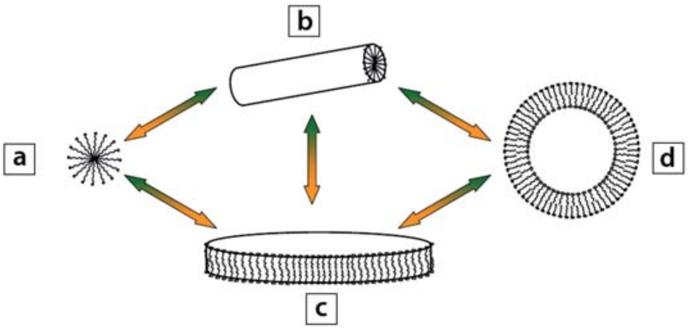

Figure 2.3.: A schematic representation of the pathways that may be involved in the transition from micelles to unilamellar vesicles. (a) Micelle, (b) rodlike micelle, (c) disklike micelle and (d) vesicle. Adapted from [128].

2.2.1. Preparation of cholesterol/CTAB mixtures by sonication

Desired amounts of cholesterol and CTAB were weighted in glass bottles and suspended in 10 ml of Milli-Q water in order to prepare the different mixtures detailed in Table 2.1 (see Section 6.4.1 of the Experimental Part). For all preparations, the CTAB concentration was kept constant 10 times above its critical micelle concentration (cmc), at a value of 10 mM. The resulting dispersion was sonicated at 298 K, using a Vibracell Sonifier titanium probe working at 20 kHz (Sonic and Materials Corporation) for 4 min until homogeneous dispersions were achieved. Sonication methodology was chosen among the distinct colloidal phases preparation routes that avoid any solvent-free state and are easily handled and commonly used in the literature. Before analysis, all mixtures were left to stabilize at 298 K for 1 week.

Table 2.1.: Concentration of cholesterol and Chol/CTAB molar ratio *(Q)* of the different mixtures prepared and further characterized. *Note: for all preparations water was used as dispersant medium at 298 K. The CTAB concentration was kept constant 10 times above its critical micelle concentration (cmc), at a value of 10 mM. In order to facilitate the description of each Chol/CTAB mixture, it has been used a nominal Q value.*

Chol concentration (mM)	***Q* = Chol/CTAB (mol/mol)**
0	0
0.01	1×10^{-3}
0.11	1×10^{-2}
0.96	0.1
5.0	0.5
10	1
15	1.5
30	3

The visual aspect of the different mixtures is shown in Figure 2.4. When Q is near to 0, so there is a small amount of cholesterol in the mixtures, the samples exhibit transparent aspect, however when Q progressively increases, the samples become increasingly turbid.

2.2.2. Supramolecular phases characterization

2.2.2.1. Characterization by optical density (OD) measurements

Optical density (OD) is the absorbance per unit length, i.e., the absorbance divided by the thickness of the sample. Optical density is given as:

$$OD_{\lambda} = \frac{A_{\lambda}}{l} \tag{2.1}$$

where *(l)* is the distance that light travels through the sample (the sample thickness), measured in cm, and (A_{λ}) the absorbance at wavelength (λ). The wavelength selected to measure the optical density should be one in which the system does not absorb. A measurement of optical density is like a measurement of the turbidity of the system, i.e., it is a measure of light diffracted by the sample. Through optical density measurements, it is possible to detect phase changes in liquid systems to micro- and nanoscopic level [137, 138].

Following the procedure described in Section 6.3.6 of the Experimental Part, the changes in the supramolecular organization of the mixtures as a function of *Q* were monitored by optical density (OD). The wavelength selected to measure the optical density of the Chol/CTAB systems was $\lambda = 500$ nm, at which neither cholesterol nor CTAB absorb.

The dependence of the optical density at $\lambda = 500$ nm with the *Q* value is shown in Figure 2.4, together with an image of the macroscopic aspect of the different Chol/CTAB mixtures. At $Q = 0$, the dispersed system presents homogeneous and transparent aspect (Figure 2.4a). The optical density has a value near 0, typical of micelle solutions that do not scatter light at the investigated wavelength. When *Q* progressively increases from 0 to 1, the dispersion system starts to exhibit a more turbid aspect, which is usual for vesicular and liposomal organizations. Correspondingly, a modest increase in the optical density plot is observed. At $Q > 1$ solid particles precipitate in the dispersed systems and, consequently, the optical density abruptly increases due to the more intensive light scattering produced by these larger aggregates.

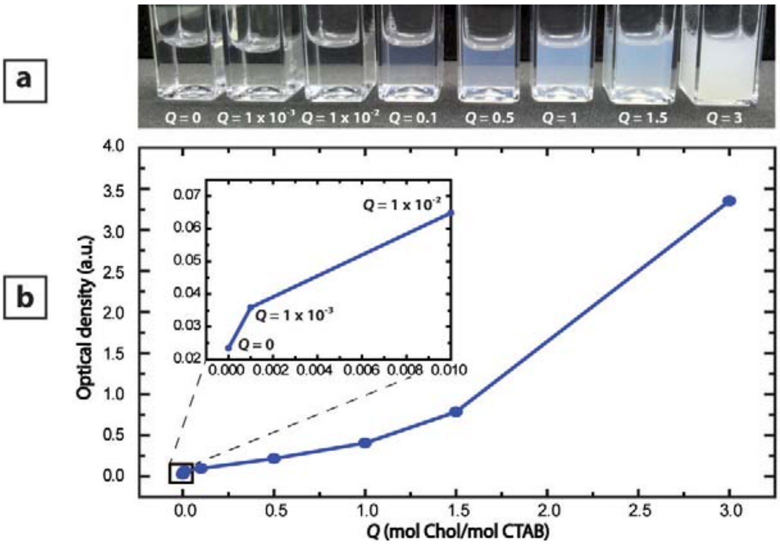

Figure 2.4.: (a) Images showing the visual appearance of Chol/CTAB mixtures prepared by sonication. (b) Optical density variation, measured at $\lambda = 500$ nm, of the self-assembled objects present in Chol/CTAB mixtures in water at different *Q* values.

The optical density evolution shows that the Chol/CTAB system in aqueous media forms larger supramolecular organizations as the concentration of cholesterol increases.

The size and morphology of such supramolecular structures are studied in the following Section.

2.2.2.2. Size distribution and morphology

The size distribution and morphology of each Chol/CTAB mixture were characterized by dynamic light scattering (DLS) and cryogenic transmission electron microscopy (cryo-TEM). DLS gives statistical measurements, however an individual inspection of the different assemblies can be performed by cryo-TEM.

Dynamic light scattering (DLS) (sometimes referred to as photon correlation spectroscopy or quasi-elastic light scattering) (see Section 6.3.3 of the Experimental Part) is a technique for measuring the size of particles typically in the sub micron region. DLS measures Brownian motion and relates this to the size of the particles. Brownian motion is the random movement of particles due to the bombardment by the solvent molecules that surround them. Therefore, the diameter that is measured in DLS is a value that refers to how a particle diffuses within a fluid so it is referred to as a hydrodynamic diameter. Besides, the diameter that is obtained by this technique is the diameter of a sphere that has the same translational diffusion coefficient as the particle. Normally DLS is concerned with measurement of particles suspended within a liquid and gives us a bulk measurement.

Cryo-transmission electron microscopy (cryo-TEM) (see Section 6.3.1 of the Experimental Part) is a powerful method for uncovering the structure of soft nanostructured materials. The method is based on ultra-fast cooling and conversion of a liquid sample to a vitrified (glassy) specimen that can be examined in the TEM. Direct-imaging cryo-TEM discloses both the global supramolecular structure and local aggregate-specific details, at the hydrated state, and at a nanometer resolution. This placed the method as a central characterization tool in colloid, material, bio- and nano-related technologies in academia and industry [129].

The size distribution obtained for each Q value is summarized in Table 2.2. Both DLS and cryo-TEM (Figure 2.5, Figure 2.6) evidenced the formation of distinct supramolecular phases. In the course of the formation of different supramolecular assemblies induced by increasing the cholesterol content in the system, five distinct phase domains can be pictured. Each one governed by a predominant supramolecular assembly morphology.

Table 2.2.: Size distribution of the supramolecular aggregates formed by Chol/CTAB mixtures at different molar ratios in water measured by DLS. The size distribution reported is based on intensity of light scattered.

Chol/CTAB molar ratio (*Q*)[a]	**Peak 1**		**Peak 2**		**Peak 3**		**Peak 4**	
	***d*(nm)**[b]	***I%***[c]	***d*(nm)**[b]	***I%***[c]	***d*(nm)**[b]	***I%***[c]	***d*(nm)**[b]	***I%***[c]
0	1	82	11	5	143	13	-	-
1×10^{-3}	1	27	-	-	157	73	-	-
1×10^{-2}	-	-	-	-	128	100	-	-
0.1	-	-	-	-	119	100	-	-
0.5	-	-	-	-	115	100	-	-
1	-	-	37	21	159	79	-	-
1.5	-	-	20	6	191	90	4144	4
3	-	-	19	6	232	86	5322	8

[a] Molar ratio between Chol and CTAB (mol/mol) in the system.
[b] *d* is the mean diameter.
[c] *I*% is calculated as the percentage area under the curve.

In accordance with DLS and cryo-TEM images, the first domain defined at $Q = 0$ is governed by CTAB micelles with their hydrocarbon core sizing 1 nm (peak 1 in Table 2.2 and in Figure 2.5a). Minor populations at 11 and 143 nm (peaks 2 and 3 of Table 2.2 and Figure 2.5a) may correspond to larger CTAB micelles or to emergent and unstable CTAB vesicles that we have generically denoted as mixed micelles (MM) [139]. As the light scattering intensity *(I)* in DLS is proportional to d^6, in which d means the particle diameter, even small populations of the 11 and 143 nm sized nano-objects are detected.

The second domain comprises Q values between 1×10^{-3} and 0.1. At $Q = 1 \times 10^{-3}$, the micellar population (peak 1 of Figure 2.5b) coexists with a growing population of objects between 70 and 295 nm (peak 3 of Figure 2.5b). The cryo-TEM images of Figure 2.6b show the presence of large micelles of elongated flexible shapes also called wormlike micelles (B1). At $Q = 1 \times 10^{-2}$, the cryo-TEM images (Figure 2.6c) evidenced the presence of wormlike mixed micelles (C1) thicker and more curved than the wormlike structures observed at $Q = 1 \times 10^{-3}$. The size of the nano-objects detected at $Q = 1 \times 10^{-2}$ is centered at 128 nm (Figure 2.5c). The progressive incorporation of cholesterol to the mixture until $Q = 0.1$, (Figure 2.5d and Figure 2.6d) appears to provoke, according to cryo-TEM, the thickening, folding, and partial self-closing of the worm membrane, generating open bilayer fragments (D1). On close inspection of Figure 2.6d, the presence of disklike mixed micelles (D2) and a closed vesicle (D3) is also revealed. However, analysis of several cryo-TEM images confirms the wormlike phase, as the predominant morphology in the second domain. The average size of the colloidal systems generated

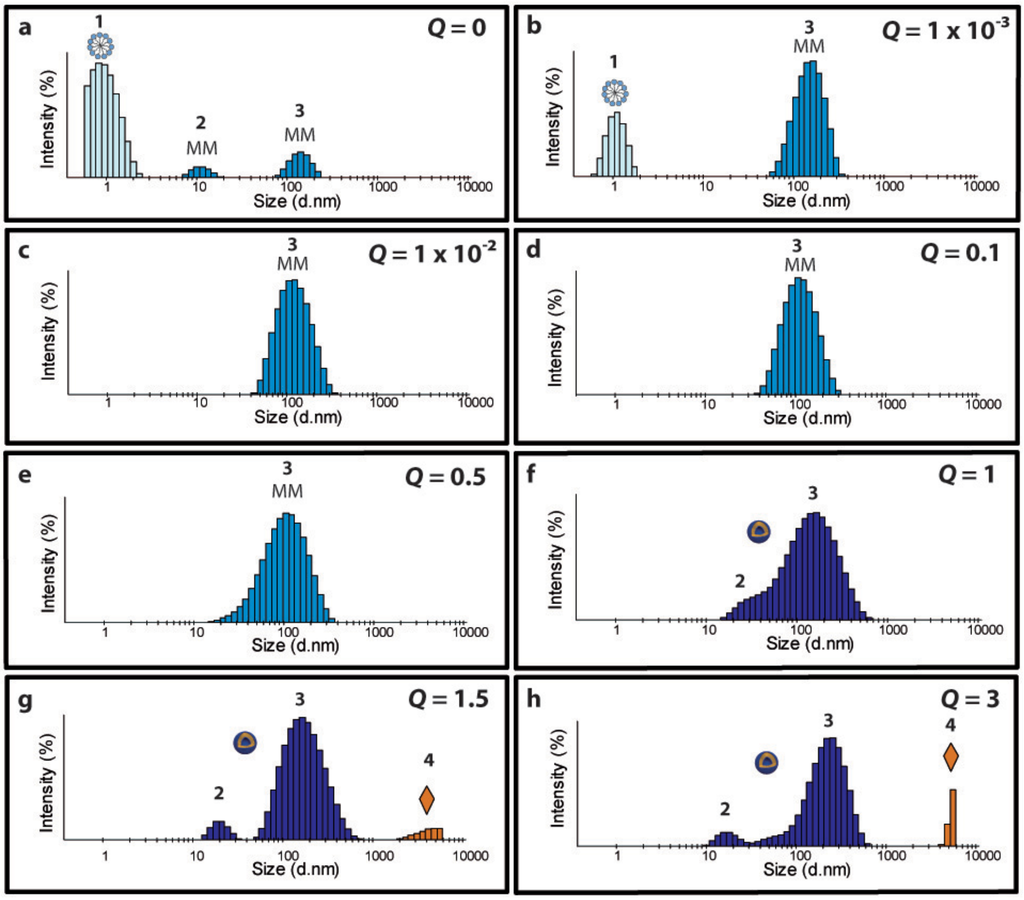

Figure 2.5.: Particle size distributions measured by DLS of supramolecular assemblies present in Chol/CTAB mixtures in water at different Chol/surfactant molar ratios: (a) $Q = 0$, (b) $Q = 1 \times 10^{-3}$, (c) $Q = 1 \times 10^{-2}$, (d) $Q = 0.1$, (e) $Q = 0.5$, (f) $Q = 1$, (g) $Q = 1.5$, and (h) $Q = 3$.

at $Q = 0.1$ lies at 119 nm.

The third domain is pictured at $Q = 0.5$. The cryo-TEM images (Figure 2.6e) evidenced a change in the primary morphology from worm to disklike mixed micelles (E1) with a particle size mean of 115 nm (Figure 2.5e). In this domain, disklike micelles coexist with a considerable amount of closed vesicles (E3). Upon addition of cholesterol to the mixture, the destabilizing edge energies of the disklike phase can be minimized either by growth of the floppy bilayers to reduce the overall edge length relative to the membrane area or by bending of the bilayer to form hemisphere caplike structures (E2) with smaller peripheries, which eventually close up on themselves to form vesicles [75, 76, 132, 140].

The equimolar assembling of cholesterol and CTAB ($Q = 1$) defined the fourth phase domain. At such a molar ratio, the dispersed system contains a pure phase of spherical and unilamellar vesicles (F1 of Figure 2.6f) with diameter sizes around 40 and 160 nm (peaks 2 and 3 of Figure 2.5f).

Finally, the fifth domain is defined at Q values larger than 1 ($Q > 1$), where it was found

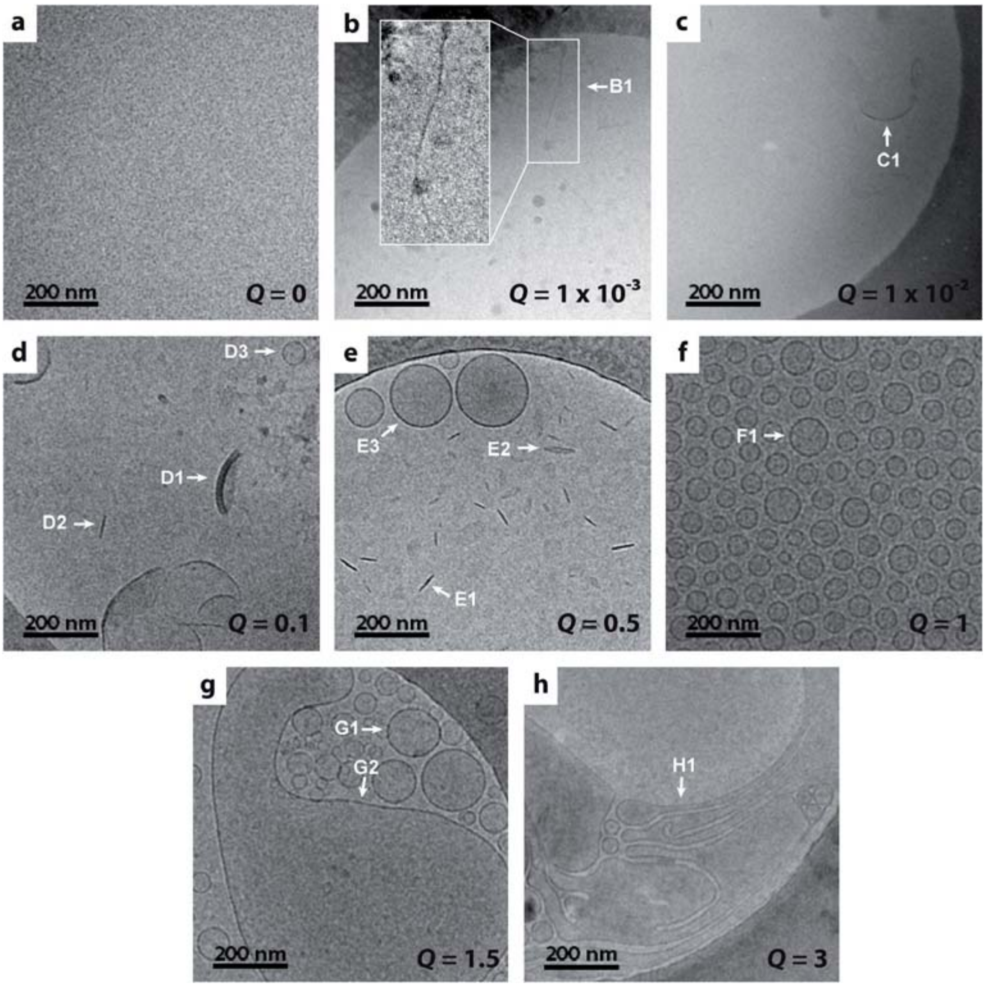

Figure 2.6.: Nanostructures observed by cryo-transmission electron microscopy in aqueous mixtures of Chol and CTAB at different Chol/CTAB molar ratios ranging from 0 to 3: (a) Q = 0, (b) $Q = 1 \times 10^{-3}$, (c) $Q = 1 \times 10^{-2}$, (d) Q = 0.1, (e) Q = 0.5, (f) Q = 1, (g) Q = 1.5, and (h) Q = 3. Inset of (b) shows the wormlike micelle aggregates detected at $Q = 1 \times 10^{-3}$. B1: worm, C1: worm, D1: nascent bilayer, D2: disk, D3: vesicle, E1: disk, E2: cap, E3: vesicle, F1: vesicle, G1: vesicle, G2: distorted vesicle and H1: distorted vesicle.

the coexistence between self-assembled colloidal nano-objects and solid. At Q = 1.5, the particle size plot (Figure 2.5g) shows the presence of three populations with diameters centered at 20 (peak 2), 191 (peak 3) and 4144 nm (peak 4). According to cryo-TEM analysis (Figure 2.6g) the peaks 2 and 3 correspond to vesicles (G1) and distorted vesicles (G2). In order to characterize the larger structures, TEM without cryofixation was used showing the presence of some solid particles (Figure 2.7a and peak 4 in Figure 2.5g). At Q = 3, cryo-TEM (Figure 2.6h) shows more distorted vesicles (H1) and TEM reveal again the presence of solid particles (Figure 2.7b and peak 4 in Figure 2.5h).

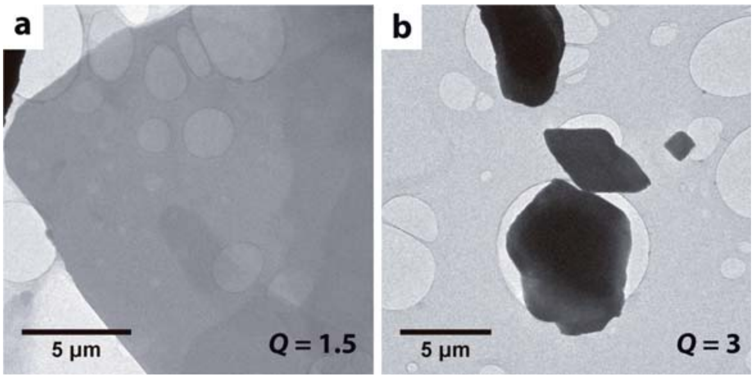

Figure 2.7.: Solid particles observed by transmission electron microscopy in aqueous mixtures of Chol and CTAB at Chol/CTAB molar ratio (a) $Q = 1.5$ and (b) $Q = 3$.

The morphology, size and nature of the solid phase obtained at $Q > 1$ was further examined by optical microscopy, light scattering and powder X-ray diffraction, respectively. The optical microscopy images (Figure 2.8) (Section 6.3.7 of the Experimental Part) confirmed that the solid phase correspond to a crystalline phase with plate-like morphology typical of lipid systems. Moreover, the presence of crystals is more pronounced at $Q = 3$. By means of light scattering (Section 6.3.5 of the Experiment Part) it was determined that at $Q = 1.5$ (Figure 2.9) the crystals formed have sizes between 2.2 and 80 µm and at $Q = 3$ (Figure 2.9) between 300 nm and 150 µm.

In order to characterize the nature of the solid phase obtained at $Q > 1$, the solid material at $Q = 1.5$ was filter out and their powder X-ray diffraction pattern was measured (Figure 2.10) (see Section 6.3.10 of the Experimental Part). The results show that the solid is a crystalline phase of cholesterol. It corresponds to the most common polymorph of cholesterol as evidenced by the perfect match between the powder X-ray diffraction pattern of the filtered crystals with the powder diffraction pattern simulated from the crystal structure of the most common polymorph of cholesterol, with Cambridge structural database code CHOEST20.

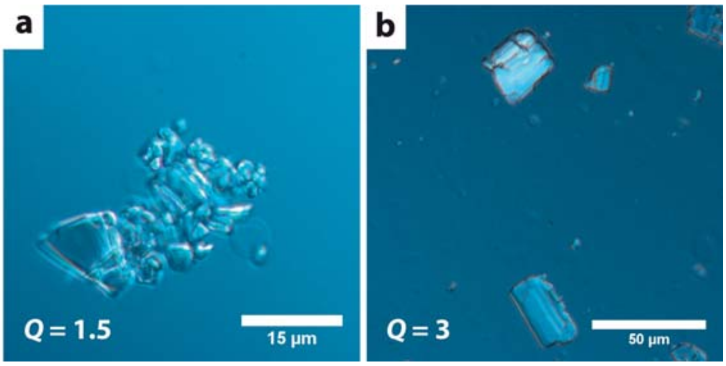

Figure 2.8.: Optical microscopy of solid particles observed at Chol/CTAB molar ratio (a) $Q = 1.5$ and (b) $Q = 3$.

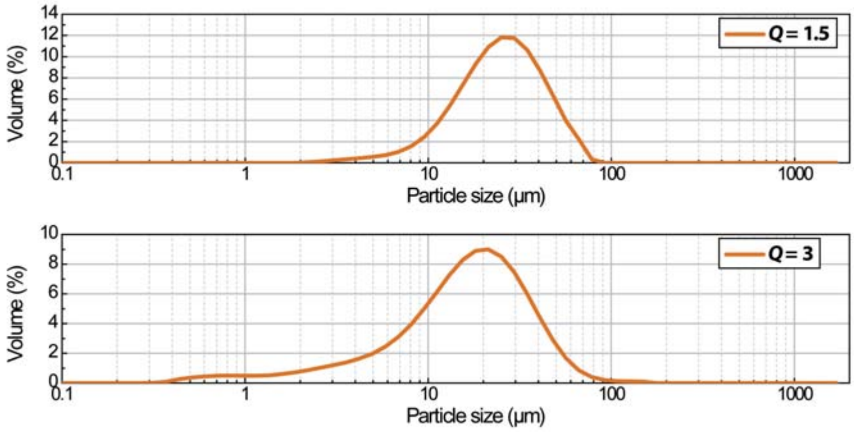

Q	**Light Scattering (μm)**		
	D10	**D50**	**D90**
1.5	12.5	27.2	51.2
3	4.45	18.4	41.9

Figure 2.9.: Volumetric particle size distribution measured with light scattering of Chol/CTAB self-assembly nanodispersions prepared in water at Chol/CTAB molar ratio $Q = 1.5$ and 3. Table presents the size distributions expressed in percentiles of 10, 50 and 90% of accumulated volume, corresponding respectively to D10, D50 and D90 values. D50 value corresponds to the median volumetric particle size distribution.

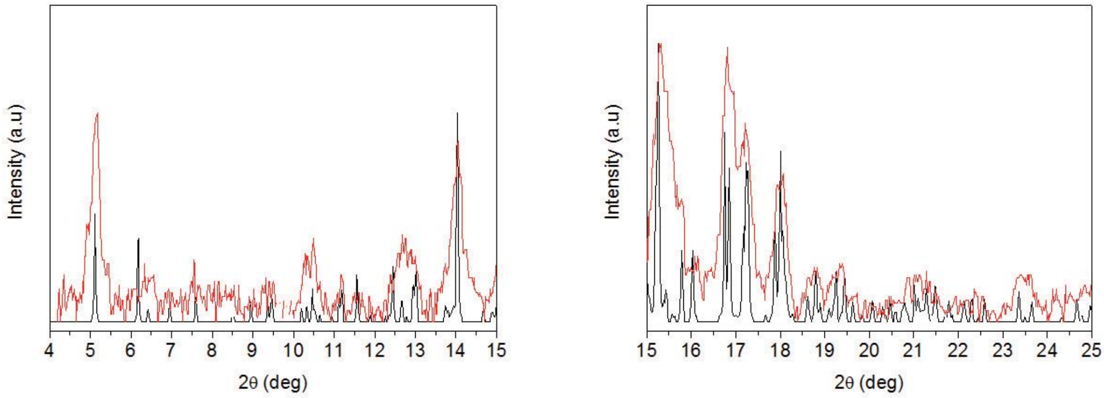

Figure 2.10.: Overlay between the experimental (red) PXRD pattern obtained from the solid phase of $Q = 1.5$ and the PXRD pattern simulated (black) from the crystal structure of the most common polymorph of cholesterol (Cambridge structure database code: CHOEST20).

Considering all of the above, it can be concluded that at the fifth domain ($Q > 1$) the solubility limit of cholesterol in these bilayers was reached and plate-like cholesterol crystals were observed. Hence, the progressive addition of cholesterol in this domain promotes an increase of the cholesterol crystalline particles, which co-exist with vesicles like colloidal phase.

Upon the above described study, the phase behavior of cholesterol/CTAB mixtures at 298 K can be summarized with the scheme depicted in Figure 2.11. As shown, a pure vesicular phase is only formed at equimolar proportions of both components, whereas coexistence of vesicular structures with other types of colloidal and crystalline phases is observed when one moves away from the equimolar ratio.

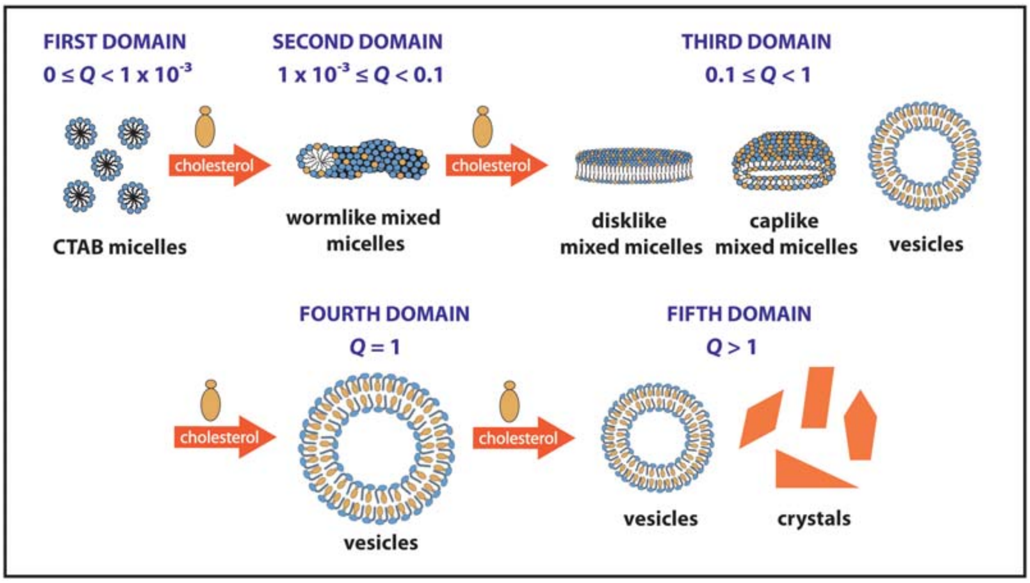

Figure 2.11.: Schematic illustration of the different supramolecular organizations observed using mixtures of cholesterol and CTAB in water. The *Q* value is the molar ratio between Chol and CTAB (mol/mol) in the system.

2.2.3. Molecular Dynamics Simulations of cholesterol/CTAB mixtures in water

To have a molecular picture of the process and the supramolecular structures underlying this transition, all-atomic Molecular Dynamics (MD) simulations were performed of mixtures of cholesterol and CTAB in water. All simulations were conducted by Dr. Jordi Faraudo from the Institut de Ciència de Materials de Barcelona, (ICMAB-CSIC).

The cholesterol/surfactant/water molar ratios used are described in Table 2.3, and the parameters and protocols of the MD simulations can be found in Section A.1 of the Appendix of this Thesis.

Table 2.3.: Composition for each simulation described in the text (number of molecules of each species and total number of atoms) and equilibrium size of the simulation box (averaged over production runs). *Note: For bilayer simulations, it was considered a bilayer patch in the XY plane in its tensionless state in contact with water maintained at a pressure of 1 in the Z direction (perpendicular to the bilayer). For bulk simulations, it was considered diluted bulk conditions (certain amount of molecules inside a large water box).*

Simulation	**Number of molecules Chol/CTAB/water**	**Atoms (total)**	**Eq. box size**
S1 (Bilayer)	54/54/5,443	23,727	15.7 $\text{nm}^2 \times 14.5$ nm
S2 (Bilayer)	30/60/5,443	22,329	11.9 $\text{nm}^2 \times 18.0$ nm
S3 (Bilayer)	10/60/5,443	20,849	14.4 $\text{nm}^2 \times 14.0$ nm
S4 (Bulk)	1/72/11,109	37,937	369.7 nm^3
A1 (Bulk)	1/1/6,434	19,445	194.0 nm^3
A2 (Bulk)	60/0/1,063	7,629	70.43 nm^3
A3 (Bulk)	0/72/21,176	68,064	667.3 nm^3

The MD method is based on the numerical solution of the Newton equations of motion for all atoms of a molecular system constrained to the thermodynamic conditions (T, p, and so forth). All the MD simulations were performed using the NAMD 2.9 and VMD programs [141, 142].

In Figure 2.12 are depicted the molecular structures of cholesterol and CTAB used in the MD simulations. As shown, the length of the molecule is around 1.8 nm for cholesterol and 2.4 nm for CTAB.

Let us consider first the conceptually simplest case of a simulation with only one cholesterol and one CTAB molecule in water (simulation A1 of Table 2.3). The equilibrium state obtained in the simulations corresponds to an association of the cholesterol molecule to the hydrocarbon chain of the surfactant, as can be expected from the hydrophobic character of the sterol unit. The mismatch in size between the two molecular entities and the rigidity of the cholesterol molecule produces a deformation of the polar ammonium headgroup of the surfactant around the polar oxygen group of cholesterol with a separation between N in CTAB and O of the hydroxyl group in cholesterol of 0.58 nm (snapshot of Figure 2.13). In the simulations, it was obtained a free energy of $\Delta G = -4.7$ kcal/mol, corresponding to this association. This value for the free energy is large enough to consider that this noncovalent molecular union works as a unique supramolecular synthon or tecton, providing a new building block unit for complex structure formation (Figure 2.13).

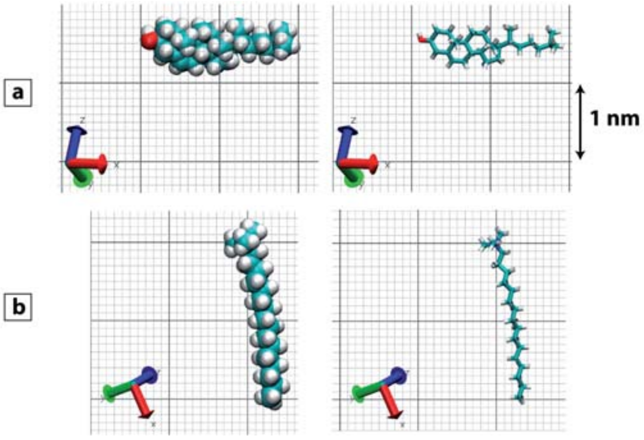

Figure 2.12.: Depiction of (a) cholesterol and (b) CTAB molecules using the van der Waals atomic radius (left) and with bonds-only format (right).

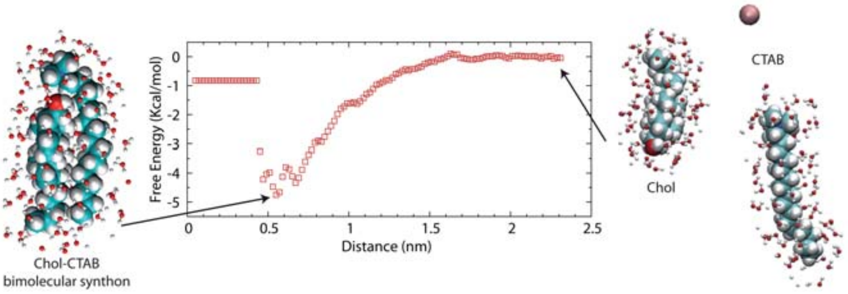

Figure 2.13.: Evolution of the Gibbs free energy of interaction (ΔG) between a single CTAB and a single cholesterol molecule (simulation A1) in water as a function of the intermolecular distance. A snapshot from MD simulations, showing on the right, the initial state of the simulation, and on the left, the structure of the Chol/CTAB supramolecular synthon at the free-energy minimum state.

As mentioned in the Introduction of the present dissertation, the actual form assumed by a colloidal aggregate depends on the molecular structure and geometry of the constituent amphiphiles (see Figure 2.14). In a first-order approximation, the geometry of an amphiphile is described by the classical packing parameter concept [17, 18]. For a single amphiphilic molecule, the packing parameter is defined as $p = v/a_0 l_c$, where v is the volume of the hydrocarbon chains of the molecule, l_c is the length of the hydrocarbon chain, and a_0 is the optimal cross-sectional area per headgroup at the polar hydrocarbon/water interface of the assembly. So, the packing parameter of an amphiphilic molecule determines the preferred curvature of the aggregates formed: $p < 1/3$ spherical micelles; $1/3 < p < 1/2$, cylindrical micelles; $1/2 < p < 1$, vesicles; $p = 1$, planar bilayers; $p > 1$, reverse phases.

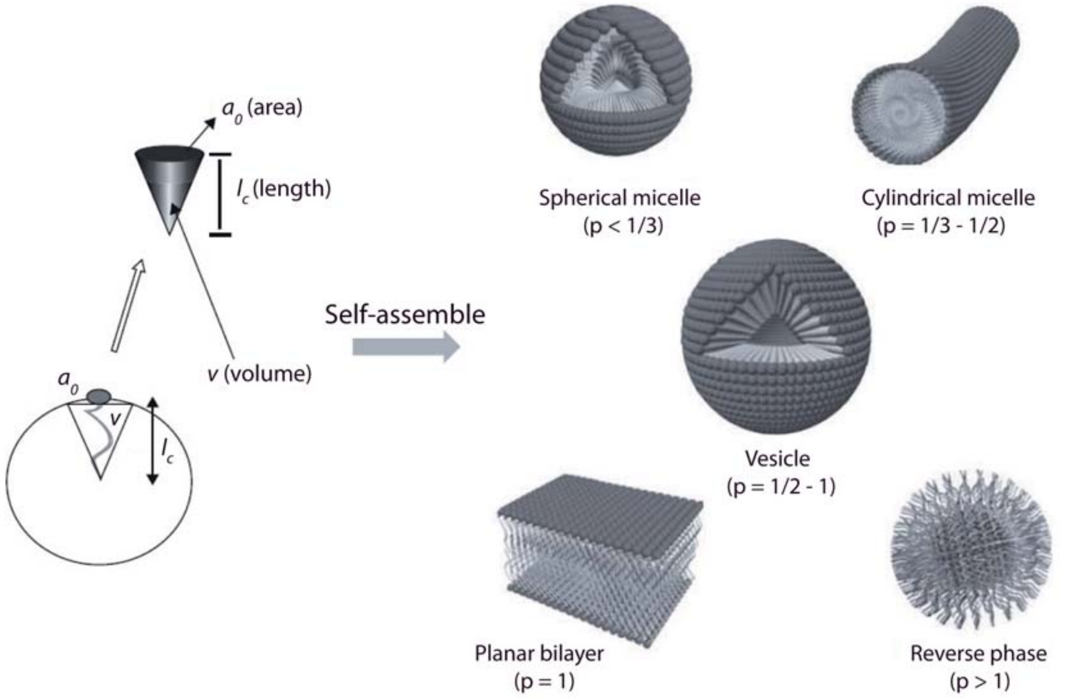

Figure 2.14.: Relationship between the packing parameter *(p)* and the self-assembled morphology of amphiphilic molecules under aqueous conditions. Adapted from [143].

Table 2.4 presents the molecular and structural parameters used to estimate the individual packing parameter of CTAB and cholesterol. The parameters a_0, v and l_c were taken directly from the simulations (also they can be calculated using approximated equations described in [6]). As seen in Table 2.4, the packing parameter *(p)* is 0.42 for CTAB and 1.22 for cholesterol, so it can be predicted that CTAB molecule has a conical shape, typical of micelle-forming surfactants, whereas cholesterol has an inverted conical shape (Figure 2.15a).

Table 2.4.: Molecular and packing parameters for CTAB and cholesterol. *Note: l_c is the length of the hydrocarbon chain, v is the volume of the hydrocarbon chain and a_0 is the optimal cross-sectional area per headgroup at the polar hydrocarbon/water interface of the assembly. The packing parameter is calculated by $p = v/a_0 l_c$.*

Amphiphile	**CTAB**	**Cholesterol**
l_c(nm)	1.93	1.73
v(nm^3)	0.54	0.40
a_0(nm^2)	0.64	0.19
p	0.42	1.22

The packing parameter of the cholesterol-CTAB bimolecular synthon was also calculated. As seen in the snapshot of Figure 2.13, the length of the hydrocarbon tail of this supramolecular synthon *(l_c)* was taken as that of the cholesterol molecule (1.73 nm) and its volume *(v)* as the sum of both ($0.54 + 0.40 = 0.94$ nm^3). The value of a_0 for the synthon can be taken as equal to its value for pure CTAB ($a_0 = 0.64$ nm^2) since the headgroup of the synthon is that of the CTAB surfactant (see again the snapshot of Figure 2.13). Using these values, the obtained packing parameter *(p)* for the Chol-CTAB synthon is 0.85 (Figure 2.15b). As Figure 2.14 shows, the necessary condition for the formation of bilayers is $1/2 < p \leq 1$ [17, 143], thus this new supramolecular system will form bilayers, as double-chained amphiphiles do. The synthon, formed by the assembly of a conical molecule and an inverted conical molecule, has a cylindrical shape, which is the required shape for the formation of bilayers (see Figure 2.15c).

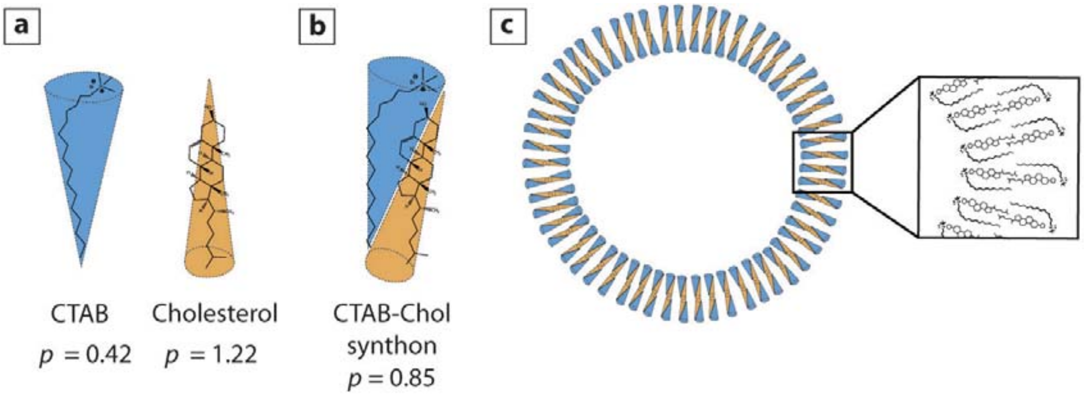

Figure 2.15.: Schematic illustration of (a) the shape of CTAB and cholesterol molecules, (b) the formation of a Chol-CTAB bimolecular amphiphile and (c) their self-assembling into bilayer vesicles based on the packing parameter concept.

The atomistic structure of such a bilayer is investigated in the simulation of a mixture containing equal numbers of CTAB and cholesterol molecules in water (simulation S1 of Table 2.3). In the simulations (see snapshots of Figure 2.16a and Figure 2.17a), it was obtained a homogeneous bilayer in which cholesterol molecules are incorporated in the hydrophobic region of the bilayer (avoiding contact with water) and surfactant molecules are deformed in a way similar to that described in the previous simulation. A more quantitative description of the bilayer structure is given by the atomic density profile, shown in Figure 2.16a. The headgroup and chain distribution of CTAB across the bilayer has the typical shape observed in a two-chain phospholipid bilayer [6, 144, 145].

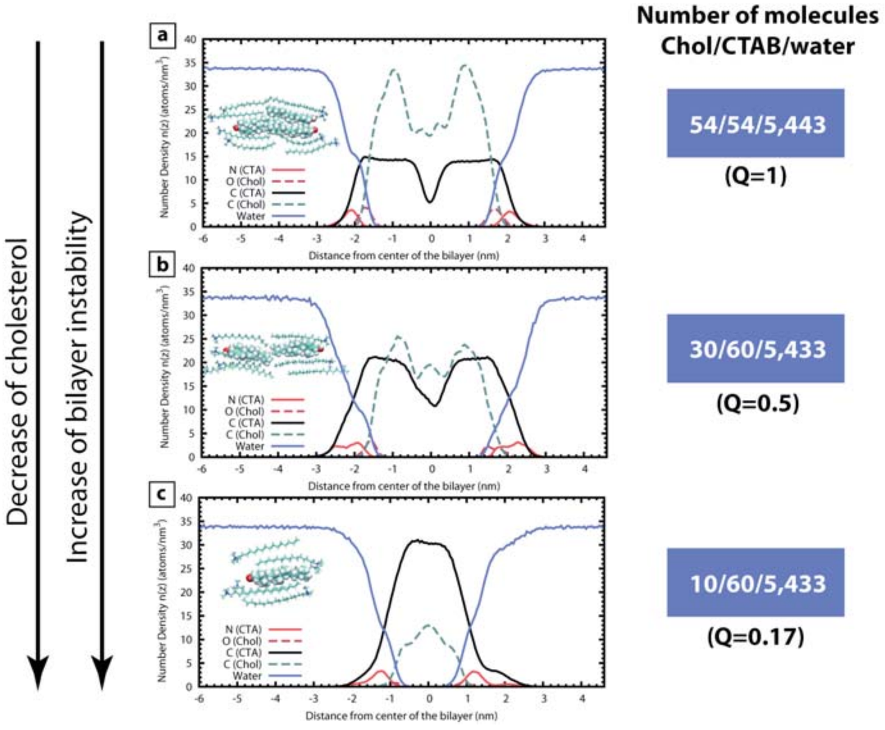

Figure 2.16.: Average density profile of distinct sterol/surfactant mixtures as a function of the z coordinate (perpendicular to the membrane) obtained from MD simulations. (a) S1 ($Q = 1$), (b) S2 ($Q = 0.5$), and (c) S3 ($Q = 0.17$). The Q value is the molar ratio between Chol and CTAB. Solid red line: nitrogen atom from CTAB molecule (atoms/nm^3), dashed red line: oxygen atom from cholesterol molecule (atoms/nm^3), black solid line: carbon atom from CTAB molecule (atoms/nm^3), black dashed line: carbon atom from cholesterol molecule (atoms/nm^3), blue line: water density (molecules/nm^3). Snapshots from MD simulations showing a small portion of the bilayer accompany each atomic density profile (surfactant molecules are shown with bonds-only format, whereas cholesterol molecules are shown using the van der Waals atomic radius).

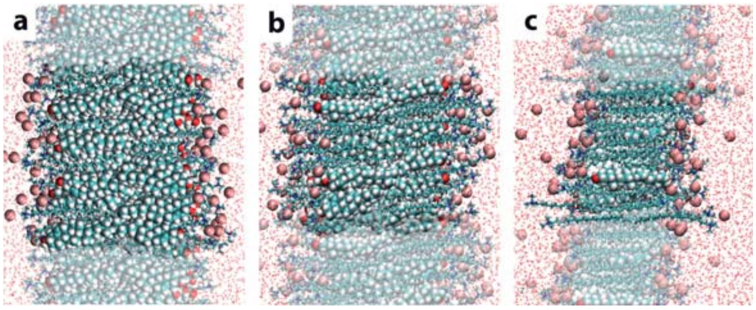

Figure 2.17.: Snapshots corresponding to the full bilayer of simulations (a) S1 ($Q = 1$), (b) S2 ($Q = 0.5$) and (c) S3 ($Q = 0.17$) of Table 2.3. For the sake of clarity, only cholesterol molecules and Br^- counterions are shown with their actual van der Waals radius.

As seen in Figure 2.16a, the CTAB molecules arrange into two-layered leaflets with the headgroups in contact with water (red lines) and the tails in the interior of the bilayer (black lines). Water molecules (blue line) scarcely penetrate into the bilayer, and the interaction with the membrane components is limited to the solvation of the surfactant polar headgroups. The total bilayer thickness (measured from the peaks in the surfactant headgroup distribution) is about 4.4 nm, and the hydrocarbon region has a thickness about 3.6 nm. These values are in agreement with the average thickness between 4.0 and 5.0 nm, estimated from cryo-TEM images (Figure 2.18) of Chol-CTAB vesicles formed at $Q = 1$ (see Table 2.1 and Section 6.4.2 of the Experimental Part).

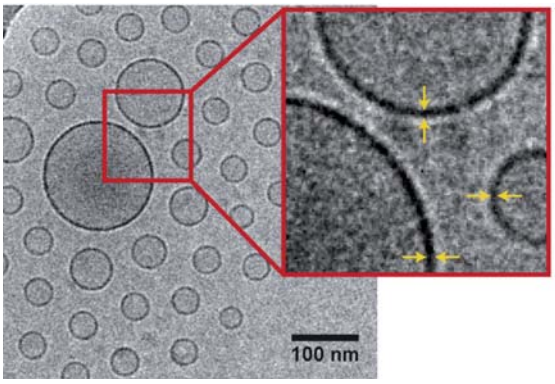

Figure 2.18.: Scheme of the procedure followed to estimate the membrane thickness of Chol-CTAB vesicles at $Q = 1$ by cryo-TEM. The Q value is the molar ratio between Chol and CTAB (mol/mol) in the system.

Concerning the Figure 2.16, note also that the atomic distribution of carbon atoms from the surfactant tails (black lines) has a small density depletion in the center, as observed in typical two-tail phospholipid bilayers (see for example Figure 2 in reference [145]). Cholesterol molecules (black dashed lines) accommodate themselves, including the hydroxyl groups (red dashed lines) in the hydrophobic region generated by the CTAB tails to avoid any contact with the water (blue line) medium. As seen in Figure 2.16a, the size of this region is enough to accommodate two nonoverlapping layers of cholesterol molecules (note the central minima in the density profile of cholesterol molecules). The cholesterol density profile shows a maximum at 1 nm associated to the overlapping of the rigid carbocyclic moieties of the sterol molecules, as represented in the molecular scheme of Figure 2.16a. The obtained equilibrium area per polar headgroup is 58 Å^2, similar to that obtained for certain anionic phospholipids (for example, values among 53–55 Å^2 were obtained in MD simulations for anionic phosphatidylserine (PS) lipids) [146, 147].

Starting from these MD results, further ABF–MD simulations have been performed (Section A.1.3 of the Appendix) in order to investigate the thermodynamic stability of this bilayer system. All free energy calculations are summarized in Figure 2.19. The calculations give $\Delta G = -35$ kcal/mol for the transfer of a surfactant molecule from water to a Chol-CTAB bilayer at equimolar ratio. This quantity has to be compared with the free energy gain of $\Delta G = -30$ kcal/mol for the transfer of a surfactant molecule from water to a CTAB micelle (see flowchart of Figure 2.19e,f). Similar results are obtained for the cholesterol molecule. A free energy change of $\Delta G = -55$ kcal/mol was obtained for the transfer of a cholesterol molecule into a 1:1 Chol-CTAB bilayer and $\Delta G = -50$ kcal/mol for incorporation into a cholesterol nanocrystal (see flowchart of Figure 2.19b,c). Therefore, the simulations predict a thermodynamic preference for both CTAB and cholesterol molecules for the mixed environment of an equimolar Chol-CTAB bilayer as compared with a homogeneous environment. The free energy associated with this preference of individual molecules (of about 5 kcal/mol) is almost identical to the binding free energy (4.7 kcal/mol) calculated for the association of a single surfactant with a cholesterol molecule, calculated in simulation A1 (see Figure 2.13). Consequently, all the calculations indicate that the pair Chol-CTAB works as a unique supramolecular architecture for the formation of more complex colloidal phases, such as vesicles.

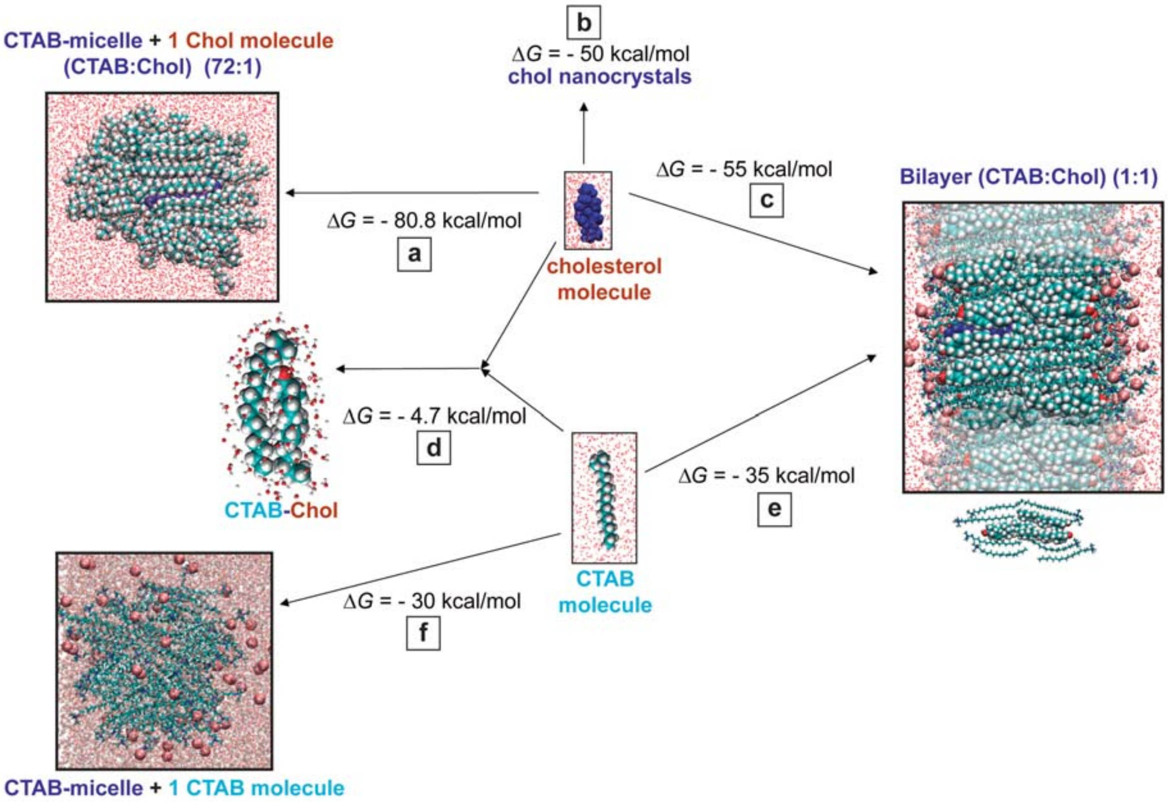

Figure 2.19.: Diagram showing the free energies of interaction of the pairs (a) cholesterol molecule/CTAB-micelle, (b) cholesterol molecule/cholesterol nanocrystal, (c) cholesterol molecule/Chol-CTAB bilayer (1:1), (d) cholesterol molecule/CTAB molecule, (e) CTAB molecule/Chol-CTAB bilayer (1:1) and (f) CTAB molecule/CTAB-micelle.

It is clear that the structure of the bilayer depends crucially on its equimolar composition. In order to understand the dependence with composition, further simulations of bilayers with different compositions were performed (simulations S2 and S3). The atomic density profiles and snapshots of these simulations (Figure 2.16b,c and Figure 2.17b,c) reveal that the bilayer becomes unstable as the cholesterol/CTAB ratio decreases and suggests the formation of distinct intermediate colloidal phases. In simulation S2 ($Q = 0.5$), a bilayer as in the S1 ($Q = 1$) case was observed again. However, the atomic density profiles show a less-defined structure, with a broader distribution of the surfactant headgroups and a decrease in the thickness of the hydrocarbon core of the bilayer (3.2 nm in this case). The accommodation of cholesterol molecules inside the bilayer is now more difficult. There is now a strong overlap of cholesterol in the center of the bilayer, indicated by the unusual central peak of cholesterol in the middle of the bilayer of the atomic density profile (see Figure 2.16b). The origin of this peak is also evident in the snapshots of Figure 2.16b and Figure 2.17b; it is due to the tail–tail contact between cholesterol molecules located in opposite leaflets.

In the case of simulation S3 ($Q = 0.17$), a completely different structure was obtained. The initial configuration (bilayer) becomes unstable and the system equilibrates at a different structure, made of interdigitated molecules with alternate orientations (see Figure 2.16c and Figure 2.17c). The atomic density profiles no longer have the typical structure of a bilayer. Instead, Figure 2.16c shows a central hydrophobic region of about 2 nm containing the hydrocarbon tails of CTAB and the cholesterol molecules and an external hydrophilic region containing the surfactant headgroups and solvation water. Overall, the density profiles of Figure 2.16c are compatible with the worms and disks morphologies detected by cryo-TEM (Figure 2.6). However, the exact, supramolecular structure cannot be identified from these simulations due to the unavoidable small size of the simulated system.

Finally, it will be briefly discussed how a CTAB micelle is altered by the addition of a small quantity of cholesterol. To this end, a simulation in which a cholesterol molecule is added to a CTAB micelle in water (simulation S4 of Table 2.3) was performed. The cholesterol molecule is rapidly incorporated into the micelle and protected from water inducing a certain degree of ordering in an inherently disordered micelle. Starting from these MD simulations, ABF calculations were also performed in order to determine the free energy involved in the process (see the flowchart of Figure 2.19a and Figure 2.20). It was obtained a free energy of $\Delta G = -80.8$ kcal/mol for the transfer of a cholesterol molecule from water to the micelle, which is more favorable than the transfer from water into a pure cholesterol nanocrystal system (–50 kcal/mol). Therefore, thermodynamics dictate the preferential incorporation of cholesterol into the surfactant micelles.

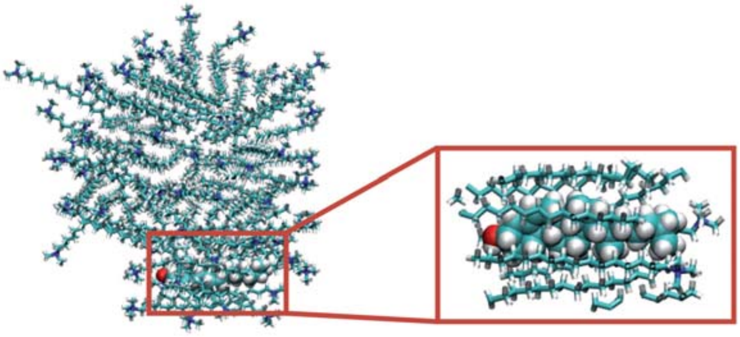

Figure 2.20.: Snapshot of a cholesterol molecule incorporated into a CTAB micelle (simulation S4). Surfactant molecules are shown in bond representation and cholesterol molecule is shown with their actual van der Waals radius. The color code employed is the standard crystallographic convention (i.e., red corresponds to oxygen, blue to nitrogen, cyan to carbon and white to hydrogen).

It is interesting to compare recent simulation results for the behavior of cholesterol inside phospholipid bilayers with that observed in Chol-CTAB vesicles at equimolar ratio. Molecular dynamics simulations employing the coarse-grained MARTINI methodology [148, 149], which allows the sampling of large time and length scales, have identified a rich phenomenology.

In general, there is no evidence for a possible association between cholesterol and phospholipid molecules. Specifically, a flip-flop of cholesterol between the two layers of a phospholipid bilayer has been observed [148], being faster for unsaturated phospholipids and even a preference for the membrane interior (with an orientation perpendicular to that of the phospholipids) is obtained for polyunsaturated phospholipids [149]. Figure 2.21 shows an example of a cholesterol flip-flop in a coarse-grained dipalmitoylphosphatidylcholine (DPPC) bilayer during an equilibrium simulation reported by Bennett *et al.* in [148]. The proportion used in that simulations was 64 molecules of DPPC and 2 molecules of cholesterol.

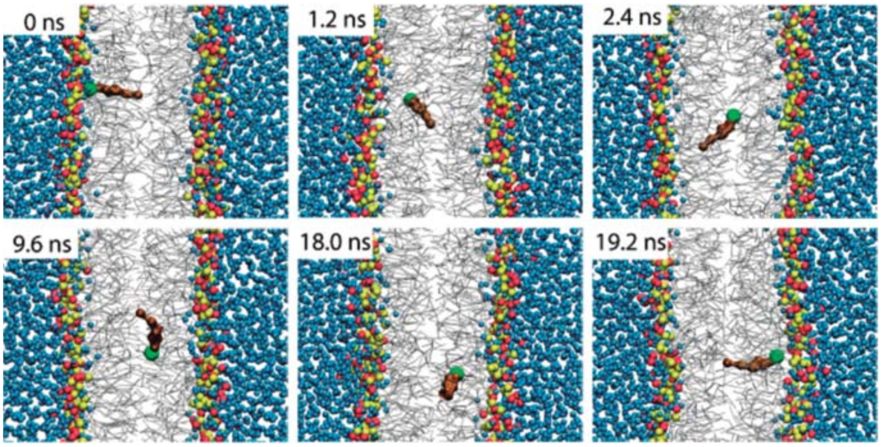

Figure 2.21.: Example of cholesterol flip-flop reported by Bennett *et al.* in [148]. Snapshots illustrating cholesterol flip-flop in a coarse-grained dipalmitoylphosphatidylcholine (DPPC) bilayer during an equilibrium simulation (it was simulated 64 molecules of DPPC and 2 molecules of cholesterol). Water molecules are blue spheres, the DPPC cholines are red spheres, their phosphates are yellow spheres, and their tails are grey lines. The body of cholesterol is brown licorice, and its hydroxyl is a green sphere. Time equal to 0 ns corresponds to right before the hydroxyl of cholesterol enters the hydrophobic interior, at 1.2 μs of simulation.

Regarding the Chol-CTAB vesicles, the interaction between the two layers of 1:1 Chol-CTAB bilayer from ongoing large-scale coarse-grained simulations [148, 149] was estimated by Dr. Jordi Faraudo analyzing the distance fluctuations between synthons of two different layers using the methodology described in [150]. These fluctuations, induced by thermal energy, are compensated by the bilayer elastic energy, thus the elastic parameters can be estimated. The obtained interaction was 215 $K_B T/nm^4$, 7.8 times higher than the interaction between the layers of a DPPC or POPC bilayer (27.7 $K_B T/nm^4$) [150]. Such a high value shows a cohesive interaction between the two layers of a Chol-CTAB vesicles, thus it is expected that cholesterol flip-flop events (which involve the rupture of a cholesterol–surfactant synthon) should be rarer than in phospholipid bilayers. Also, cholesterol mobility inside the bilayers is expected to be extremely low and this fact can predict that these systems will have a great stability in comparison to typical phospholipid formulations. The supramolecular synthon formed by one CTAB and one cholesterol molecule can be considered, to a good extent, as a single entity which self-assembles in particularly stable vesicles.

2.2.4. Comparison with self assembling of cationic and anionic surfactants

The transition pathway and transient morphologies induced by the addition of cholesterol to a micellar solution of CTAB observed in this work are similar to those found in previous studies of the micelle-to-vesicle transition that occurs on mixing cationic and anionic surfactants [75, 128, 130, 133, 135, 136]. However, the mechanism for which a mixture composed of a cationic surfactant, like CTAB, and a sterol, like cholesterol, self-assemble into a vesicle is rather different and does not have any precedent explanation.

In water, cationic and anionic surfactants individually self-assemble in micelles, but their mixtures are able to self-assemble in more complex structures (including vesicles) due to the electrostatic complexation between cationic and anionic surfactant molecules. Comparison of the sequence of events described here with the results in mixtures of cationic and anionic surfactants also suggests the complexation between CTAB and cholesterol molecules as the molecular origin for formation of vesicles with improved nanostructure and physicochemical properties. MD simulations confirm that it is the synergy between the CTAB and the sterol entities that generates a bimolecular synthon that at certain proportions behaves as a single building block with adequate structural characteristics to self-assemble into vesicles. This behavior cannot be expected in a heterogeneous mixture of two dissimilar, noninteracting components [17, 136].

In view of the structural results, it is worth emphasizing here the profound, conceptual differences with previous works on transitions from multicomponent membrane vesicles to micelles studied for mixed anionic–cationic surfactants and two-chain lipid systems [75, 128, 130–137, 151]. In these systems, both molecular types have head groups at the water–hydrocarbon interface [131]. In the mixed cationic-anionic surfactant systems, both polar groups electrostatically interact, modifying the geometry of the system and causing the bilayer and vesicle formation. Instead, in the quatsome system, the sterol does not live at the surface but in the interior of the bilayer (snapshot of Figure 2.16a). Such particular arrangement of the sterol unit makes the volume of the hydrophobic region of the CTAB molecule apparently increase, leading to the formation of a bimolecular synthon with a structural architecture similar to that of a double-tailed amphiphile, whose spontaneous aggregation geometry is that of a vesicle. Therefore for cholesterol-CTAB systems, it is the synergy between one sterol and one single-tail quaternary ammonium surfactant that allows the self-assembling into multicomponent membrane vesicles in aqueous media only at the equimolar proportion. Using the cholesterol-CTAB system as a model, the formation of non-liposomal vesicles using mixtures of sterols and ionic surfactants have been called *Quatsomes.*

2.2.5. Summary

- Phase-behavior analysis of different aqueous mixtures of the quaternary ammonium surfactant CTAB and cholesterol, using optical density, dynamic light scattering, and cryo-TEM, have shown that a pure vesicular phase is only formed at equimolar proportions of both components, whereas coexistence of these vesicular structures with other types of colloidal and crystalline phases is observed when one moves away from the equimolar ratio.

- Molecular dynamic (MD) simulations with atomistic detail revealed that the cholesterol and CTAB pair works as a unique supramolecular architecture for the formation of more complex vesicular colloidal phases. This bimolecular synthon can be considered, to a good extent, a single entity which self-assembles in particularly stable vesicles.

- The new non-liposomal vesicles formed by sterols and ionic surfactants have been called *Quatsomes*.

2.3. Characterization of Chol-CTAB quatsomes

The qualitative observation of a great stability over time and a high structural homogeneity of Chol-CTAB quatsomes, has driven to a deeper quantitative characterization of this new vesicular phase.

2.3.1. Thermodynamic stability

2.3.1.1. Introduction: classification of vesicles upon their thermodynamic stability

Vesicles can be either thermodynamically and non-thermodynamically stable. The vast majority of liposomes (phospholipids in water) are thermodynamically nonstable, they are not the equilibrium aggregation state for the system, but they can be considered as metastable structures of high kinetic stability.

In 2000, Marques [78] reported the distinct properties that are to be displayed by thermodynamically stable vesicles [79, 152, 153]. (i) The vesicles are to be generated spontaneously (simple mixing of components), i.e., without the input of energy be it mechanical, chemical, electrochemical, or any other. (ii) There should be stability in time with respect to average size and polydispersity once equilibrium is attained. (iii) The formation and properties of the vesicles have to be reversible upon change of an external factor and independent of the method of preparation. (iv) The vesicles are to appear in equilibrium with neighboring single phase regions in phase diagrams, namely micellar and lamellar phases, in appropriate heterogeneous regions.

There are, in principle, two scenarios for vesicles to be in thermodynamic equilibrium; they can either be stabilized by entropy on a mesoscopic scale (undulations, translation, polydispersity) [154–158], or they can have a nonzero spontaneous curvature [159]. Both stabilization mechanisms give rise to vesicles of a particular size and size distribution. Membranes composed of a single lipid species are generally not believed to exhibit a spontaneous curvature, as the two monolayers that make up the bilayer are oppositely curved. Vesicles composed of a single lipid species can therefore only be stabilized against the formation of lamellar phases by entropic contributions on mesoscopic length scale [160].

The equilibrium size distribution of a population of vesicles is determined by a subtle competition between the entropy of mixing and the curvature elasticity of the bilayers [18, 157, 158]. The curvature energy per unit area of bilayer, f_c, is [154–156]

$$f_c = \frac{1}{2} k_c(\kappa_1 + \kappa_2 - 2C_o)^2 + \overline{k}\kappa_1\kappa_2 \tag{2.2}$$

where $\varkappa_1$, $\varkappa_2$ are two principal curvatures of the surface of a membrane, and the constant C_o (= *1/radius*, R_o) is called the spontaneous curvature of the membrane surface. k_c and $\overline{k}$ are the mean and Gaussian bending constants, respectively. The magnitude of k_c determines the energy needed to bend the bilayer away from its spontaneous radius of curvature, R_o, and consequently determines the magnitude of fluctuations. $\overline{k}$ influences only the topology (and hence the number) of the structures formed, and the magnitude of $\overline{k}$ has little effect at equilibrium as long as curvature fluctuations take place at constant topology or constant vesicle number [77]. Due to this little effect at equilibrium, the bending constant k_c has been considered as effective elastic constant.

Depending on C_o and k_c, three different types of stable vesicles can be formed [160]:

1. Elastically stabilized equilibrium vesicles with spontaneous curvature ($C_o \neq 0$ and large k_c): These vesicles have a nonzero spontaneous curvature ($C_o \neq 0$) that picks out a preferential vesicle radius R_o ($C_o = 1/R_o$) [159, 160]. The fluctuations around R_o follow a Gaussian distribution (Figure 2.23) [156], and these fluctuations are related with k_c by [161]

$$\frac{\sigma^2}{R_o^2} = \frac{K_B T}{4\pi k_c} \tag{2.3}$$

R_o, as the experimental vesicle radius mean, and σ, as the experimental vesicle radius standard deviation, can be calculated by fitting the particle size distribution to a Gaussian distribution (Figure 2.23). Knowing these parameters it can be calculated the bending rigidity k_c by

$$k_c = \left(\frac{R_o}{\sigma}\right)^2 \frac{1}{4\pi} K_B T \tag{2.4}$$

If the bending constant is sufficiently large ($k_c >> K_B T$, where K_B is Boltzmann's constant), variations from the spontaneous curvature are sufficiently unfavorable that multilamellar vesicles (MLVs) are prohibited. In this case, the vesicles are narrowly distributed around a preferred size set by the spontaneous curvature. Thus, a monodisperse population of unilamellar vesicles at equilibrium implies that stabilization results from a spontaneous curvature ($C_o \neq 0$) and a large bending constant

(k_c). At higher concentrations, or in the presence of attractive bilayer interactions, this mechanism can lead to stable vesicles with a quantized number of bilayers as the interaction energy can overcome the increase in curvature energy for a limited deviation away from the spontaneous curvature [159, 162].

Equilibrium vesicles with spontaneous curvature have been observed in few systems. The most relevant one are the catanionic vesicles, which are formed simply by mixing cationic and anionic surfactants [78, 155, 159, 163–166]. Several studies have revealed that catanionic spontaneous vesicle phase represents thermodynamic equilibrium and is not just a kinetically trapped metastable state [77, 159, 167]. In 1990, Safran *et al.* [155] predicted that these catanionic vesicles with spontaneous curvature need to be mixed systems with asymmetric distribution of components. The non-ideal surfactant mixing can cause the interior and exterior monolayers of the vesicle bilayer to have different compositions, leading to a spontaneous bilayer curvature (Figure 2.22) [155, 156, 168].

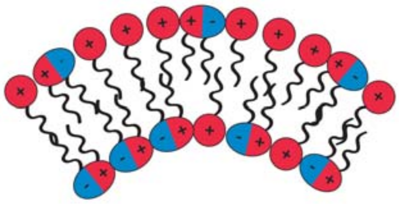

Figure 2.22.: Diagram showing excess surfactant in outer leaflet which gives rise to vesicle curvature. Adapted from [168].

The first cationic-anionic (catanionic) surfactant system reported to form unilamellar vesicles spontaneously without substantial input of energy was mixtures of cetyltrimethylammonium tosylate and sodium dodecylbenzene sulfonate (CTAT:SDBS) in aqueous solution [169].

On the other hand, previous studies have reported measurements of the bilayer elastic constant and the spontaneous curvature, C_o (= 1/ R_o), for catanionic systems. Jung *et al.* [159] presented the analysis for CTAB/sodium perfluorooctanoate (FC_7) vesicles. As shown in Figure 2.23, a histogram of the size distribution was built up by measuring the size of ≈ 3,000 spherical vesicles taken from many different samples over several weeks. They reported that the best fit to a Gaussian distribution gave R_o = 23 nm and $k_c = 6 \pm 2$ $K_B T$, suggesting stabilization by the energetic costs of deviations from the spontaneous curvature. Usually, catanionic vesicles formed by mixtures of anionic and cationic single-chain amphiphiles have modulus bendings between 0.5 - 7 $K_B T$ [159].

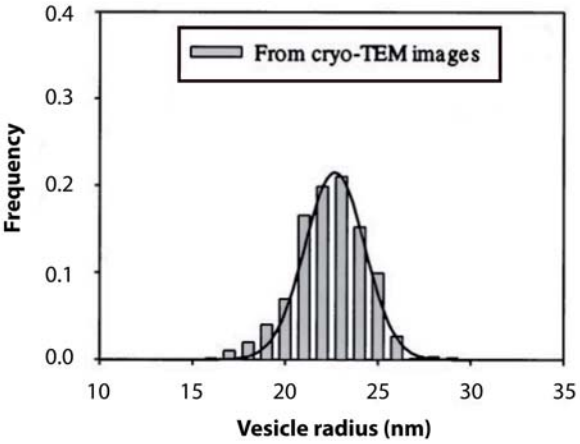

Figure 2.23.: Example of vesicle size distribution of systems with spontaneous curvature reported by Jung *et al.* in [159]. The vesicle size distribution histogram follows a Gaussian distribution; the solid line is a fit to a Gaussian distribution, giving R_o = 23 nm and $k_c = 6 \pm 2\ K_B T$. Adapted from [159].

Equilibrium vesicles with spontaneous curvature have been also observed in mixtures of components capable of electrostatic or hydrogen bond interactions between them, with strong asymmetric distribution in both leaflets [166].

2. Entropically stabilized equilibrium vesicles with non-spontaneous curvature ($C_o = 0$ and very small k_c): Vesicles can be stabilized by the gain in entropy resulting from the large number of finite sized vesicles as opposed to a few large lamellae or an intermediate number of multilamellar liposomes [162]. These equilibrium vesicles were proposed after the prediction of catanionic vesicles [158].

Entropically stabilized vesicles have a low bending constant ($k_c \sim K_B T$). The bending energy is therefore low and the population of vesicles is stabilized both by the entropy of mixing and the undulation interaction. The resulting size distribution of the vesicular system is broad and decays exponentially, thus a polydisperse population of unilamellar vesicles at equilibrium implies that stabilization results from entropy and a low bending constant [162]. Figure 2.24 shows an example of size distribution of entropy stabilized vesicles reported by Hervé *et al.* in [158].

Very few vesicle systems are stabilized entropically, specifically it has been claimed this stabilization in anionic/zwitterionic mixtures (DOPG/DOPC) without the need of asymmetry in the distribution of amphiphiles in both leaflets (very similar amphiphiles, no hydrogen bonding or electrostatic interactions between components). Lipid mixtures have an extra degree of freedom of distributing the various lipids differently between inner and outer monolayers of the curved bilayers. This redistribution does not give rise to a nonzero spontaneous curvature. The bilayers composed of a mixture of lipids typically do have a lower rigidity than expected from the rigidities of bilayers composed by the pure lipids. This relatively low rigidity results in a relatively low membrane persistence length. Claessens *et al.* [160] argued that this is the reason why the sizes of the entropically stabilized vesicles composed of DOPC/DOPG mixtures are relatively small.

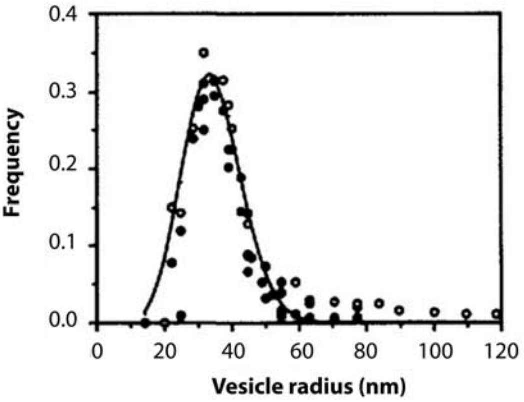

Figure 2.24.: Example of size distribution of entropy stabilized vesicles reported by Hervé *et al.* in [158]. The vesicles size distribution decays exponentially (polydisperse population) and it does not follow a Gaussian distribution. Adapted from [158].

3. Kinetically stabilized vesicles with non-spontaneous curvature ($C_o = 0$ and large k_c) and non-thermodynamically stable: These vesicles are metastable structures of a high kinetic stability [170, 171] (but not thermodynamic stability), because their formation usually requires some energy input. This kind of vesicles usually has a bending modulus between 10 - 40 $K_B T$.

Many vesicle systems are stabilized kinetically, specifically it seems clear that most phospholipid liposomes and block copolymer vesicles have non-spontaneous curvature *(C_o = 0)* and large elastic constants. The equilibrium phase is an infinite planar lamellae. In these systems, vesicles and liposomes, such the ones formed by cholesterol and phospholipids (e.g. DPPC, DOPC), have an excess of free energy over infinite lamellar phases given by

$$f_c = 4\pi R^2 \frac{k_c}{2}\left(\frac{2}{R}\right)^2 = 8\pi k_c \tag{2.5}$$

At low concentrations, vesicles can be kinetically stable because, in practice, infinite lamellar phases are impossible and the planar bilayer is finite. Consequently, it has either edges or exposure of hydrophobic core to water. The competition between the bending free energy required to create a vesicle and the cost of a planar, finite structure (instead of an infinite lamella) gives the kinetic stability criterion first proposed by Fromherz in 1983 [132, 134]. Considering the two energy factors, edge energy and bending elastic energy, Fromherz [132] introduced the *vesiculation index (V_f)* defined by Equation 2.6, which essentially is the ratio of line energy to bending energy. R_D is the radius of the central part of a flat bilayer disk (planar bilayer) and Λ is the edge tension [70].

$$V_f = \frac{R_D \Lambda}{4k_c} \tag{2.6}$$

The vesiculation index *(V_f)* [172] corresponds to the ratio of the edge energy of disk to the elastic energy of spherical shell. The flat disk is the only stable structure when V_f = 0, and the closed vesicles becomes a stable form when $V_f > 2$. For $0 < V_f < 2$, there appear energy minima at both vesicle and disk, with a transformation barrier in between; the depths of the two energy minima equal each other when $V_f = 1$, and the bilayer disk is more stable for $0 < V_f < 1$, while to closed vesicle is more stable for $1 < V_f < 2$.

2.3.1.2. Stability of Chol-CTAB (W-US) quatsomes

In this Section are described the studies performed over Chol-CTAB quatsomes in water prepared by sonication method (see Section 6.2.3 and Table 6.3 of the Experimental Part), hereinafter referred as Chol-CTAB (W-US) quatsomes. Briefly, 38.6 mg of cholesterol and 36.4 mg of CTAB were added directly to 10 ml of Milli-Q water and the resulting dispersion was sonicated at 298 K for 4 min until a homogeneous dispersion was achieved. The membrane components concentration was 7.4 mg/ml (10 mM cholesterol and 10 mM CTAB) in high purity water. The obtained vesicles were stored at 298 K until characterization.

As described in the previous Section, stability of vesicular systems depends on two parameters, the spontaneous curvature C_o (= $1/R_o$) and the bending rigidity *(k_c)* (see Equation 2.2). In the case of equilibrium vesicles with spontaneous curvature, particle size distribution of vesicle population follows a Gaussian function and C_o and k_c of these type of vesicles can be extracted from this function. So, in the present Thesis, the particle size distribution of Chol-CTAB (W-US) quatsomes was measured at equilibrium, and the goodness of fitting these experimental data to a Gaussian distribution was conducted, to determine if this new phase can be classified as equilibrium vesicles with spontaneous curvature.

In order to be sure that measurements were done using quatsomes at equilibrium, the physical stability of Chol-CTAB (W-US) quatsomes was evaluated using DLS by means of particle size evolution and zeta potential (Z-potential) (for further details see Section 6.3.3). Following size, vesicles growing or diminishing can be detected. On the other hand, Z-potential is an important and useful indicator of particle surface charges, which can be used to predict and control the stability of colloidal suspensions. The higher the Z-potential values, the more stable a suspension becomes since the system is stabilized by mean of electrostatic repulsion [173].

With the purpose of checking the Chol-CTAB (W-US) quatsome stability over time, size and Z-potential were measured after 1, 7, 14, 30 and 90 days of storage at 298 K. In Table 2.5 and in Figure 2.25 are shown the results obtained by DLS. As seen in Figure 2.25, 7 days after quatsome preparation, the size distribution of quatsomes remain constant over time. Thus, these quatsomes have stability in time with respect to average size and polydispersity once equilibrium is attained. In addition, taking into account that the light scattering intensity *(I)* in DLS is proportional to 6th power of the particle diameter, the shape of the size distribution at equilibrium indicates the presence of a large number of vesicles with smaller sizes. On the other hand, cryo-TEM pictures (Figure 2.26) revealed the coexistence of disklike micelles and vesicles 1 day after quatsome preparation, however after 7 days, only vesicles were found. Therefore, all Chol-CTAB (W-US) quatsome characterizations were performed at least 1 week after quatsome preparation. Regarding Z-potential (Table 2.5), the values remain constant with a high value during the time of the experiment, so quatsomes presented an excellent stability.

Table 2.5.: Physicochemical properties of Chol-CTAB (W-US) quatsomes prepared by sonication method in water.

Quatsome aging	Size		Z-potential (mV)
	Mean (nm) [a]	PdI [b]	
1 day	107.5 ± 0.9	0.306±0.005	81.5 ± 3.5
7 days	100.5 ± 0.5	0.417±0.008	79.2 ± 2.4
14 days	95.03 ± 1.29	0.401±0.006	82.2 ± 3.4
30 days	95.45 ± 2.15	0.348±0.050	83.2±5.8
90 days	93.59 ± 2.17	0.320±0.003	81.2±4.3

[a] Intensity weighted mean hydrodynamic size of the collection of vesicles measured by dynamic light scattering.

[b] Polidispersity index showing the width of the particle size distribution.

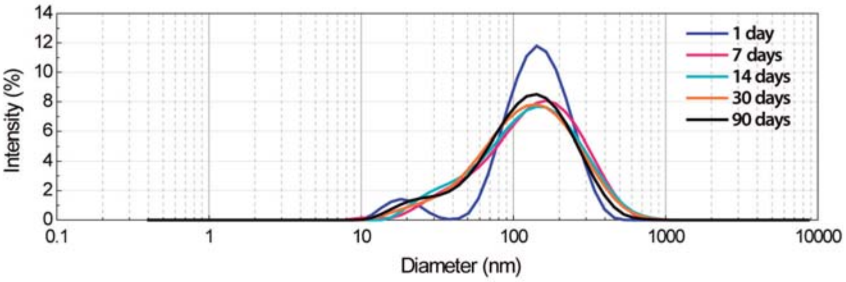

Figure 2.25.: Size evolution over time of Chol-CTAB (W-US) quatsomes prepared by sonication.

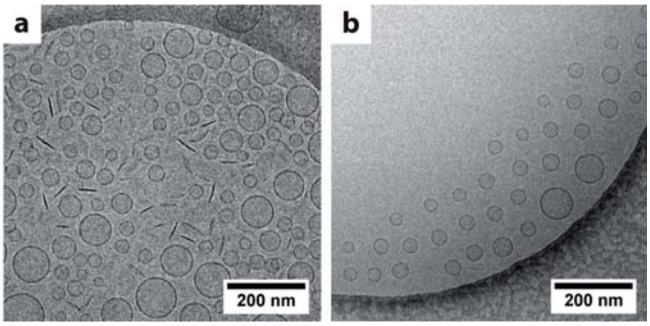

Figure 2.26.: Cryo-TEM images of Chol-CTAB (W-US) quatsomes produced by sonication taken (a) 1 day and (b) 7 days after sample prepared.

With the aim to extract R_o and k_c of Chol-CTAB (W-US) quatsomes, its particle size distribution was measured by quantitative analysis of cryo-TEM images. It should be noted that DLS and SAXS (small-angle X-ray scattering) techniques, are not appropriate for these studies because in these scattering techniques, the light from the larger particles will swamp the scattered light from the smaller ones, thus a direct imaging with cryoTEM avoids the need for model-dependent interpretation of scattering data. A histogram of the Chol-CTAB quatsome size distribution was developed by measuring the size of 8,694 spherical vesicles taken from many different samples prepared in the same way 1 week after sample preparation. The measurements were conducted by Dr. Witold Tatkiewicz from the *Nanomol* group (ICMAB-CSIC). As shown in Figure 2.27, the obtained vesicle size distribution follows a Gaussian distribution, so this excellent result allowed us to calculate the experimental vesicle radius mean (R_o), the spontaneous curvature $(C_o = 1/\ R_o)$ and the experimental vesicle radius standard deviation (σ) for Chol-CTAB (W-US) quatsomes. These parameters were approximated as R_o = 15.75 nm, σ = 1.58 nm and C_o= 0.634 nm^{-1}. Finally, we calculated from the Equation 2.4 [161] that $k_c = 7.90\ K_B T$.

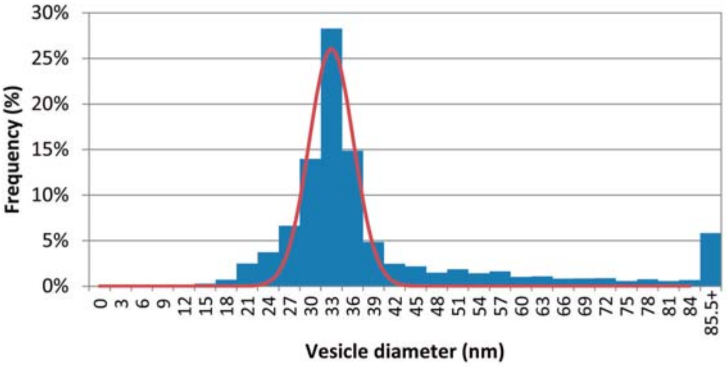

Figure 2.27.: Vesicle size distribution histogram determined from cryo-TEM images of Chol-CTAB (W-US) quatsomes prepared by sonication.

To complement this experimental study, an approximate bending modulus of Chol-CTAB (W-US) quatsomes was estimated by Dr. Jordi Faraudo using preliminary results from ongoing large-scale coarse-grained simulations [148, 149]. The distance fluctuations between Chol-CTAB synthons of two different layers were analyzed using the methodology described in [150]. These fluctuations, induced by thermal energy, are compensated by the bilayer elastic energy, thus the elastic parameters can be predicted. The bending modulus (k_c) estimated was 13 ± 2 $K_B T$, which is of the same order of magnitude as the approximated from cryo-TEM images (7.90 $K_B T$).

Therefore, the above study indicates that Chol-CTAB (W-US) quatsomes are elastically stabilized equilibrium vesicles with spontaneous curvature $(C_o \neq 0)$ and large k_c. In next Section, other evidence supporting this remarkable finding is described.

2.3.1.3. Formation of two-bilayer vesicles from Chol-CTAB quatsomes

Previous research [159] has indicated that a consequence of stabilization by spontaneous curvature is the possibility of vesicles with a discrete number of bilayers depending on the magnitude and sign of the bilayer interactions. Indeed, Jung *et al.* [159] reported that adding electrolyte to sodium perfluorooctanoate/CTAB catanionic vesicles with spontaneous curvature, leads to vesicles with two bilayers; the attractive interactions between the bilayers can overcome the cost of small deviations from the spontaneous curvature to form two-bilayer vesicles, but larger deviations to form three and more bilayer vesicles are prohibited. Therefore, vesicles with a discrete numbers of bilayers at equilibrium are possible only for bilayers with a large bending modulus coupled with a spontaneous curvature.

In order to confirm that Chol-CTAB (W-US) quatsomes are equilibrium vesicles with spontaneous curvature, electrolyte buffer was added over a Chol-CTAB quatsome sample. Specifically, 100 μl of Chol-CTAB quatsomes in water were diluted into 2900 μl of 25 mM $NaHCO_3$ buffer (pH = 8). 90 days after dilution, the sample was analyzed under cryo-TEM and the formation of two-bilayer quatsomes was observed (Figure 2.28a). To attribute this two-bilayer vesicle phenomenon to the use of electrolyte, the same dilution process was carried out diluting 100 μl of Chol-CTAB quatsomes in water into 2900 μl of its same solvent. The sample was also analyzed under cryo-TEM 90 days after dilution, and as shown in Figure 2.28b, the dilution process into water did not change the quatsome morphology, thus the formation of two-bilayer quatsomes must be associated to the presence of $NaHCO_3$ electrolyte.

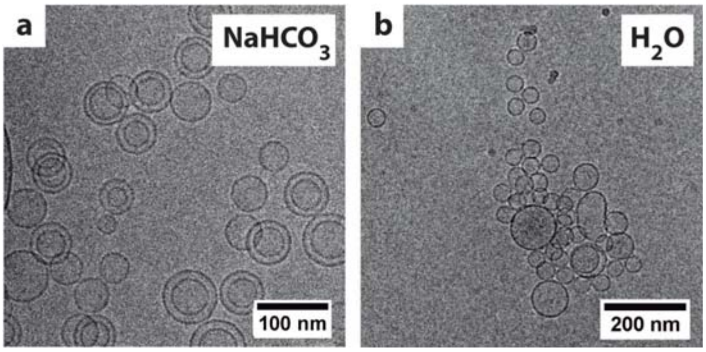

Figure 2.28.: Cryo-TEM images of the dilution of 100 μl of Chol-CTAB quatsomes in water into 2900 μl of (a) 25 mM $NaHCO_3$ buffer (pH=8) and (b) Milli-Q water. Images were taken 90 days after sample prepared.

In order to follow this procedure, we performed the same dilution process using $NaHCO_3$ buffer as in the previous sample and imaged the sample periodically with cryo-TEM. The diluted Chol-CTAB quatsome sample was analyzed 1 day, 20 days and 40 days after preparation (Figure 2.29). After 1 day (Figure 2.29a), disklike micelles inside quatsomes were observed. After 20 days (Figure 2.29b), some of these disklike micelles were transformed into vesicles and, consequently, two-bilayer quatsomes were detected. Finally, after 40 days (Figure 2.29c), all disklike micelles were transformed into vesicles and the coexistence of regular quatsomes and two-bilayer quatsomes was revealed. The evidences presented in this Section suggest that adding $NaHCO_3$ electrolyte to quatsomes leads to the formation of two-bilayer vesicles at equilibrium. Accordingly, the formation of quatsomes with a discrete numbers of bilayers at equilibrium was achieved, and this observation supports that Chol-CTAB quatsomes have a large bending modulus coupled with a spontaneous curvature [159].

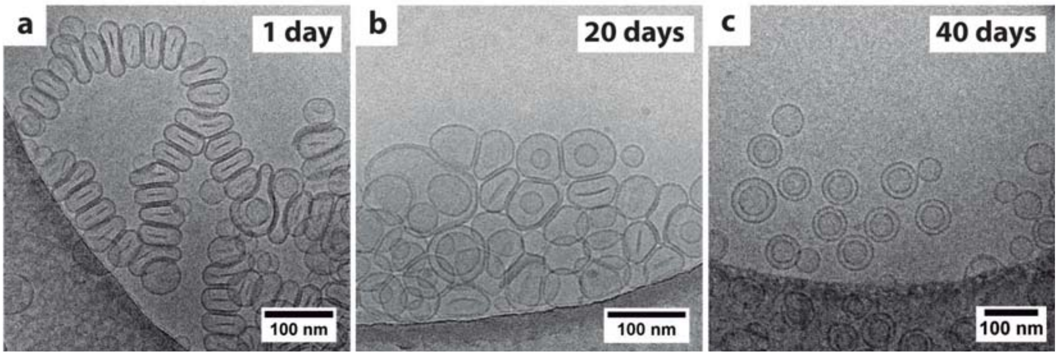

Figure 2.29.: Dilution of 100 µl of Chol-CTAB (W-US) quatsomes into 2900 µl of 25 mM $NaHCO_3$ buffer (pH=8). Cryo-TEM images taken (a) 1 day, (b) 20 days and (c) 40 days after sample prepared.

2.3.1.4. Morphological homogeneity

The homogeneity of Chol-CTAB (W-US) quatsomes was studied by SWAXS (small- and wide-angle X-ray scattering) experiments.

The development of new generation synchrotron sources has allowed the study of supramolecular assemblies such as vesicles in solution. Among the different techniques available at synchrotron sources, SWAXS is the appropriate tool to study the nanostructure of colloidal aggregates such as vesicles [174]. This technique is able to provide unique structural information with the advantage of measuring average properties of the bulk samples that can be otherwise obviated by using microscopic techniques such as cryo-TEM or confocal microscopy [133, 174, 175].

The X-ray scattering experiments devoted to study the vesicular nanostructure of quatsomes were performed at the X33 beamline of the European Molecular Biology Laboratory (EMBL, Hamburg, Germany). Data were analyzed by Dr. Evelyn Moreno from the *Nanomol* group (ICMAB-CSIC) and Prof. Jan Skov Pedersen (Aarhus University, Denmark). Two duplicate measurements of the same batch were performed at room temperature. The experimental procedures are detailed in Section 6.3.11 of the Experimental Part. Furthermore, in Section A.4 of the Appendix, is detailed the description of the theoretical model that we have used to interpret the scattering data of vesicles.

SAXS data presented in Figure 2.30a and measured at 298 K display only a broad and diffuse peak centred at q_{max} = 1.34 nm^{-1}, which indicates that the sample consist of purely unilamellar vesicles with a repeated distance *(d)* of 4.7 nm *(*$d = 2\pi/q_{max}$*)*. In the case of unilamellar vesicles this repeated distance of 4.7 nm can be assigned to the thickness of the bilayer membrane plus the ordered layer of hydration water (see

Figure 2.31) [176].

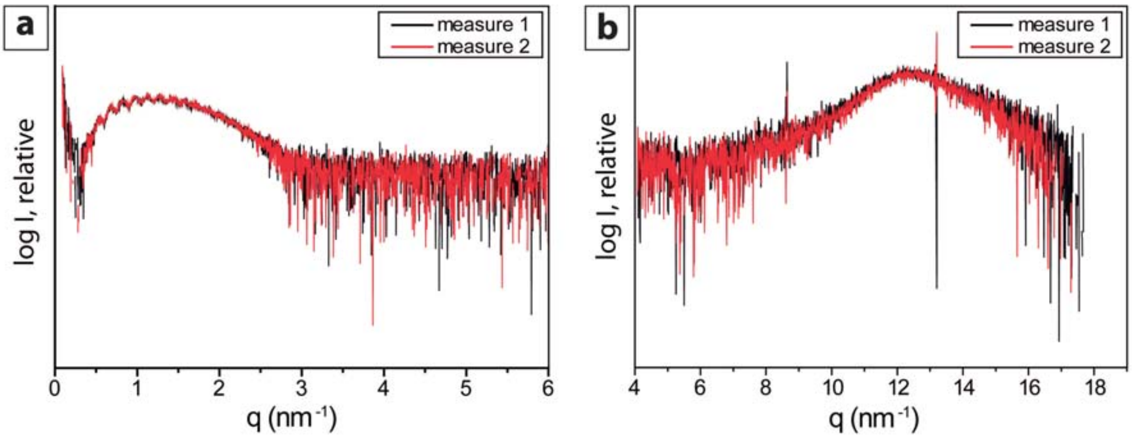

Figure 2.30.: (a) SAXS and (b) WAXS curves of cholesterol-CTAB (W-US) quatsomes prepared by sonication. Data collected at X33 beamline of the EMBL at 298 K.

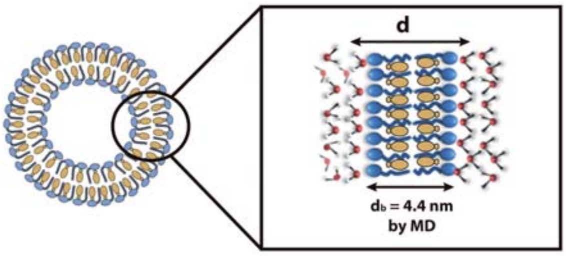

Figure 2.31.: Schematic view of the repeating distance *(d)* measured by SAXS. In the case of unilamellar vesicles the repeating distance corresponds to the bilayer thickness plus the ordered layer of hydration water. The parameter d_b represents the dimension of the bilayer thickness calculated by Molecular Dynamics (MD) simulations [177].

The polydispersity index *(p)* and the quatsome diameter have been estimated by Prof. Jan Skov Pedersen by fitting the experimental data to a vesicle model (Figure 2.32) (see Section A.4 of the Appendix). The obtained p was less than 0.02. This value represents an extremely narrow size distribution as evidenced by the well-defined high frequency oscillations observed in the scattering curve (see Figure A.7 of the Appendix). It has to be noted that, as far as we are concern, such oscillations have not been previously reported from experimental data. Therefore, these oscillations reveled that Chol-CTAB (W-US) quatsomes have a high degree of structural homogeneity. Additionally, through the position of these high frequency oscillations, Prof. Jan Skov Pedersen calculated the quatsome diameter, obtaining a value of 42 nm. These data must be interpreted with caution since SAXS could proportion larger sizes than the real ones, thus further simulations have to be carried out to extract a more accurate vesicle diameter. However, it is worth mentioning that diameter estimated using SAXS agrees with the diameter estimated by cryo-TEM images (31.49 ± 3.16 nm) (Figure 2.27).

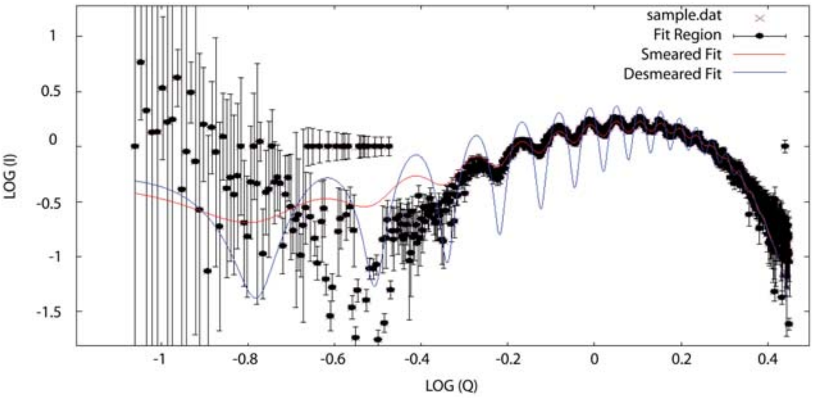

Figure 2.32.: Fit of the experimental data to a vesicle model to estimate the quatsome size and its polydispersity index *(p)*. Studies performed by Prof. Jan Skov Pedersen (Aarhus University, Denmark).

The WAXS regime is often used to determine the alkyl chain packing in lipid dispersions. The background subtracted WAXS intensities of quatsomes prepared by sonication method are shown in Figure 2.30b. At 298 K the WAXS curves only show a broad diffuse peak centered about 12.33 nm^{-1} that represents a distance of around 0.5 nm in real space that could be attributed to lateral separation of chains.

Analyzing in detail the cryo-TEM images (Figure 2.26b) and the SAXS measurements (Figure 2.30a) of Chol-CTAB (W-US) quatsomes, one might think that the well-defined high frequency oscillations observed in the scattering curves can be formed by the intervesicle distance and not by the high degree of structural homogeneity (Figure 2.33).

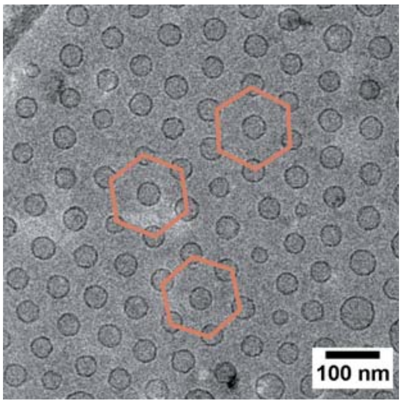

Figure 2.33.: Cryo-TEM image of Chol-CTAB (W-US) quatsomes showing the intervesicle distance.

To distinguish between these two possibilities, a dilution study was performed taking into account that when a quatsome sample is more diluted, quatsomes are more isolated in the medium and the intervesicular distance increases. Thus, the well-defined high frequency oscillations should disappear if they are produced due to intervesicular distance. Measurements were performed at the SAXS beamline of the Elettra (Trieste, Italy) and the Chol-CTAB quatsome sample was diluted from 7.4 mg/ml to 5.4, 2.7 and 2.2 mg/ml. From the SAXS data shown in Figure 2.34, it is apparent that the high frequency oscillations are observed in all diluted samples. The nanostructure is maintained upon sample dilution, thus this clear indicates that the well-defined high frequency oscillations are due to the intrinsic vesicle to vesicle great homogeneity.

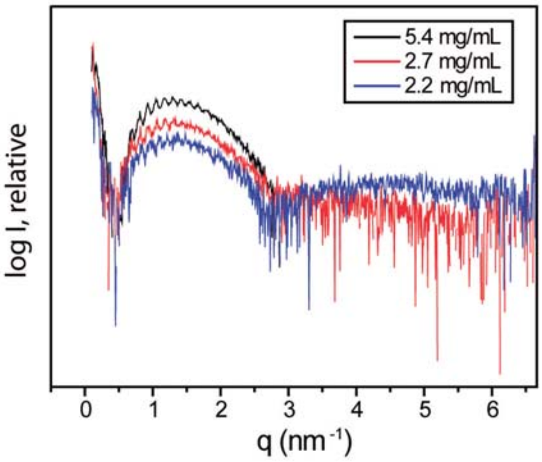

Figure 2.34.: SAXS curves of cholesterol-CTAB (W-US) quatsomes at different vesicle concentration. Data collected at SAXS beamline of the Elettra at 298 K.

2.3.1.5. Comparison with a non-thermodynamically stable vesicle system

With the purpose of comparing the SAXS scattering curves of Chol-CTAB (W-US) quatsomes (Figure 2.30a) with SAXS measurements of a non-thermodynamically stable vesicle system, phospholipid liposomes having the same cholesterol molar content were prepared. Specifically, we tried to perform cholesterol:DPPC (dipalmitoylphosphatidylcholine) (1:1 mol:mol) liposomes in water. In these studies, we attempted to prepare these liposomes with narrow size distribution to investigate the possibility to obtain again the well-defined high frequency oscillations discovered in the scattering curves of Chol-CTAB (W-US) quatsomes.

Based on the remarkable results obtained in the formation of Chol-CTAB (W-US) quatsomes by sonication method, first of all we investigated the preparation of Chol-DPPC liposomes with high content of cholesterol using this route, this liposome preparation has been called Chol-DPPC (W-US) (Table 6.4 of the Experimental Part).

Usually, liposomes are produced by Thin Film Hidration (TFH) methodology [178], where sonication could be the final step of this process, but the use of only sonication is not common in liposome production. The dry membrane components, 9.37 mg of DPPC and 4.92 mg of cholesterol, were added directly to 10 ml of Milli-Q water and sonicated 4 min at 298 K (see Section 6.2.3 of the Experimental Part). After this stage, presence of suspended solid was observed. Size measurements of this sample did not meet DLS quality criteria because of high polydispersity and presence of large aggregates in the formulation. Although only approximate, the sizes obtained are represented in Figure 2.35, where is clearly evidenced the heterogeneity of this sample. Therefore, Chol-DPPC (W-US) liposomes cannot be formed using sonication method.

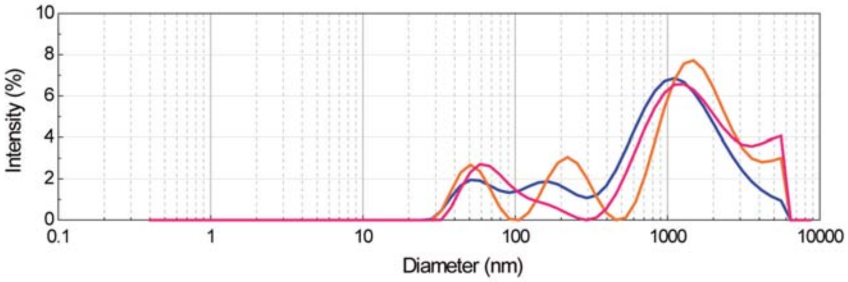

Figure 2.35.: Particle size distributions measured by DLS of cholesterol:DPPC (1:1) components sonicated in water at 298 K. 3 consecutive measurements were performed and did not meet DLS quality criteria because of high polydispersity and presence of large aggregates in the formulation.

With the still purpose of obtaining Chol-DPPC liposomes with narrow size distribution, the conventional Thin Film Hydration (TFH) method [178] was employed. It is worthy to remark that to achieve homogeneous liposomes in size, this method was followed by extrusion using a filter with a pore size of 100 nm, and the sample was passed through the extruder twenty-one times reducing the size of the vesicles by mechanical energy (see Section 6.2.2 and Section 6.5.1.2 of the Experimental Part for liposome preparation). Using this process, from now on called TFH 100x21, liposomal vesicles were obtained. These vesicles were referred as Chol-DPPC (W-TFH100x21) liposomes (Table 6.4 of the Experimental Part). It has to be noted that due to the oxidative degradation of liposomes, their were stored at 277 K and physicochemical measurements were conducted 1 day after sample preparation.

First of all, the physicochemical properties of the obtained Chol-DPPC (W-TFH100x21) liposomes were studied in terms of size and morphology. As shown in Table 2.6 and Figure 2.36a these liposomes were nanoscopic and homogeneous in size, presenting mean diameters around 120 nm and low polidispersity indexes. The morphology of this sample, studied through the cryo-TEM images, showed spherically-shaped nanovesicles with mixtures of small unilamellar vesicles (SUVs), multilamellar vesicles (MLVs) and multivesicular vesicles (MVVs). The Z-potential, with a value lower than 30 mV (in absolute value), indicated less stability than Chol-CTAB (W-US) quatsomes with values around 80 mV.

Table 2.6.: Physicochemical characteristics of Chol-DPPC (W-TFH100x21) liposomes and Chol-CTAB (W-US) quatsomes.

Vesicle sample	**Size**		**Stability**	**Morphology**[e]
	Mean(nm)[c]	**PdI**[d]	**Z-pot.(mV)**	
Chol-DPPC[a] (W-TFH100x21) liposomes	121.4 ± 1.1	0.032 ± 0.028	-17.1 ±0.2	SUVs, MLVs, MVVs
Chol-CTAB[b] (W-US) quatsomes	100.5 ± 0.5	0.417±0.008	79.2 ± 2.4	SUVs

[a] Physicochemical measurements were conducted 1 day after sample preparation. Liposomes stored at 277 K.

[b] Physicochemical measurements were conducted 7 days after sample preparation. Quatsomes stored at 298 K.

[c] Intensity weighted mean hydrodynamic size of the collection of vesicles measured by dynamic light scattering.

[d] Polidispersity index showing the width of the particle size distribution.

[e] Morphology of the vesicles observed by cryo-TEM. SUVs: Small unilamellar vesicles. MLVs: Multilamellar vesicles. MVVs: Multivesicular vesicles.

After the physicochemical characterization of such liposomes and taking into account that they were homogeneous in size, their nanostructure was investigated using SAXS. These measurements were performed at the BM16 beamline of the European Synchrotron Radiation Facility (ESRF, Grenoble, France) and were compared with the SAXS data of Chol-CTAB (W-US) quatsomes. SAXS data analysis was conducted by Dr. Evelyn Moreno (ICMAB).

As evidenced in Figure 2.36b, the obtained scattering curves of Chol-DPPC (W-TFH100x21) liposomes presented both contributions, the broad peak associated to unilamellar vesicles (Figure 2.30) and two periodical Bragg peaks ($q_1 \approx 0.96$ and $q_2 \approx 1.79$ nm^{-1}) typical of planar lamellar phases ($q_1 = q_2/2$) [179]. These Bragg peaks reveal the presence of multilamellar vesicles that behave as ordered membrane stacks. From the q-values of the Bragg peaks we can obtain the repeated distances by using the equation $d = 2\pi/q$. Accordingly, the obtained d value for Chol-DPPC (W-TFH100x21) liposomes is around 6.5 nm. As illustrated in Figure 2.37 this repeated distance accounts for the thickness of the bilayer and the hydration water between consecutive bilayers.

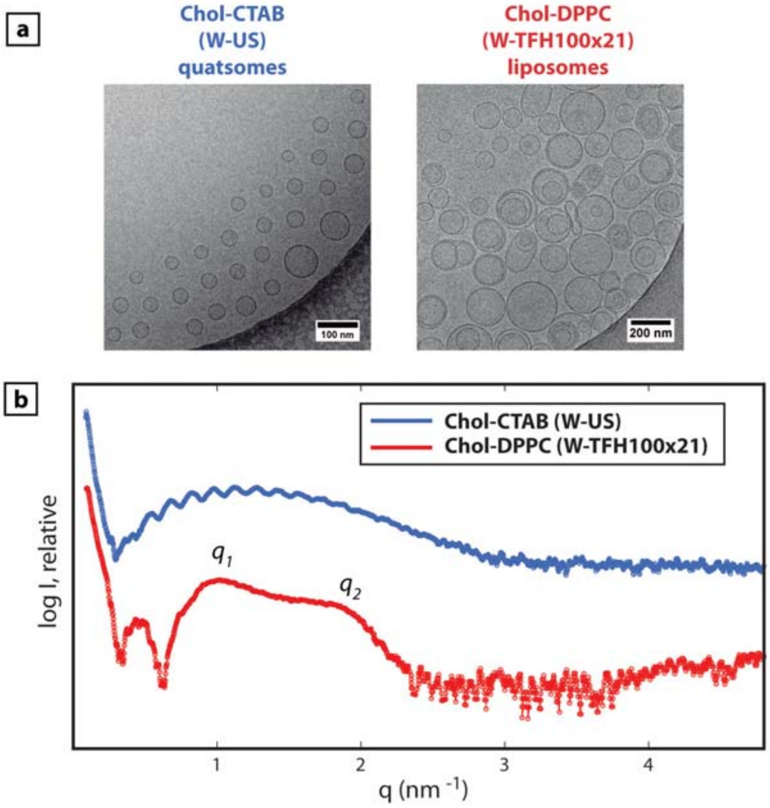

Figure 2.36.: (a) Cryo-TEM pictures and (b) SAXS measurements of Chol-DPPC (W-TFH100x21) liposomes and Chol-CTAB (W-US) quatsomes. SAXS data collected at the BM16 beamline of the ESRF and X33 beamline of the EMBL, both at 298 K. Bragg peaks due to the presence of multilamellar vesicles are indicated by q_1 and q_2.

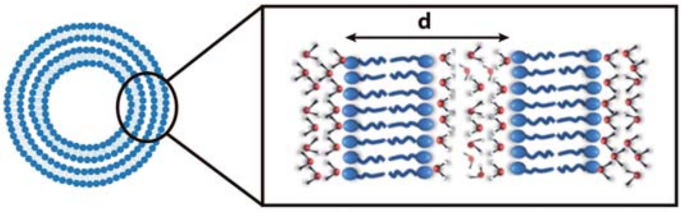

Figure 2.37.: Schematic view of the repeating distances (*d*) that is measured by SAXS. In the case of multilamellar vesicles the repeating distance corresponds to the bilayer thickness plus the full hydration layer of water.

Thus, by inspection of individual vesicles (Figure 2.36a) and as these SAXS statistical measurements revealed, the Chol-DPPC (W-TFH100x21) liposome system was formed by a mixture of unilamellar and multilamellar vesicles. Therefore, the obtained results indicated that even though the Chol-DPPC (W-TFH100x21) liposomes had a narrow size distribution (Table 2.6), the presence of multilamellar vesicles, typical in liposomal formulations, did not allow the formation of the well-defined high frequency oscillations in the scattering curves of the SAXS measurements.

2.3.1.6. Conclusions

In this Thesis we have demonstrated that Chol-CTAB (W-US) quatsomes, which show a monodisperse population of unilamellar vesicles at equilibrium, are stabilized by the energy costs of deviations from the spontaneous curvature. Consequently these quatsomes are elastically stabilized vesicles.

We have calculated the bending constant *(k_c)* of this system obtaining a large value around 7.90 $K_B T$ (k_c >> $K_B T$). This fact demonstrated that variations from the spontaneous curvature are sufficiently unfavorable that multilamellar vesicles (MLVs) are prohibited. Besides, we have determined that Chol-CTAB (W-US) quatsomes are narrowly distributed around a preferred size (31.49 ± 3.16 nm) set by the spontaneous curvature. In addition, a high degree of structural homogeneity was observed by SAXS as evidenced by the well-defined high frequency oscillations observed in the scattering curves of these quatsomes.

On the other hand, if vesicles are elastically stabilized, the presence of attractive bilayer interactions can lead to stable vesicles with a quantized number of bilayers as the interaction energy can overcome the increase in curvature energy for a limited deviation away from the spontaneous curvature. In this context, we have demonstrated that adding $NaHCO_3$ electrolyte to Chol-CTAB (W-US) quatsomes leads to the formation of two-bilayer vesicles at equilibrium, and this observation supports that Chol-CTAB quatsomes have a large bending modulus coupled with a spontaneous curvature.

In comparison with other elastically stabilized systems, where vesicles are formed simply by mixing the membrane components [78], the use of energy to Chol-CTAB (W-US) quatsome formation is needed to minimize the large size of the initial hydrophobic cholesterol crystals in water. In infinite time, Chol-CTAB quatsomes could be formed without applying energy due to the clear association between cholesterol and CTAB in water studied by MD simulations. Therefore, all the findings explained above demonstrated that Chol-CTAB (W-US) quatsomes are thermodynamically stable vesicles, however the preparation route of these vesicles can play an important role in the final nanostructure.

Finally, it is important to recall that the most common equilibrium vesicles with spontaneous curvature, the catanionic vesicles, need to be mixed systems with asymmetric distribution of components in the interior and exterior monolayers of the vesicle bilayer [155]. However, this fact is not clear for all the equilibrium vesicles with spontaneous curvature. Regarding Chol-CTAB (W-US) quatsomes, the curvatures of interior and exterior monolayers of the vesicle bilayer could be modified by the Chol-CTAB synthons. For instance, the synthons could change these monolayer curvatures changing the area per molecule with the relative position of cholesterol, leading to a spontaneous bilayer curvature without the need of asymmetric distribution of components. Nevertheless, in order to have a better comprehension of the symmetry or asymmetry of the interior and exterior monolayers of Chol-CTAB quatsomes, more detailed studies by MD simulations or by other theoretical calculations should be performed.

2.3.2. Impact of ethanol addition

In this Section, Chol-CTAB quatsomes with 10% of EtOH in volume prepared by DELOS-SUSP were studied (Figure 2.38). Hereinafter this vesicle system has referred as Chol-CTAB (W10Et-DELOS) quatsomes (see Section 6.2.1 and Table 6.3 of the Experimental Part). It is worthy to remark that this vesicle formation using that methodology has been mentioned in the Introduction of this Thesis. As mentioned, these vesicles are prepared by depressurizing a volumetric expanded organic solution containing cholesterol in ethanol over a flow of an aqueous solution containing the CTAB surfactant.

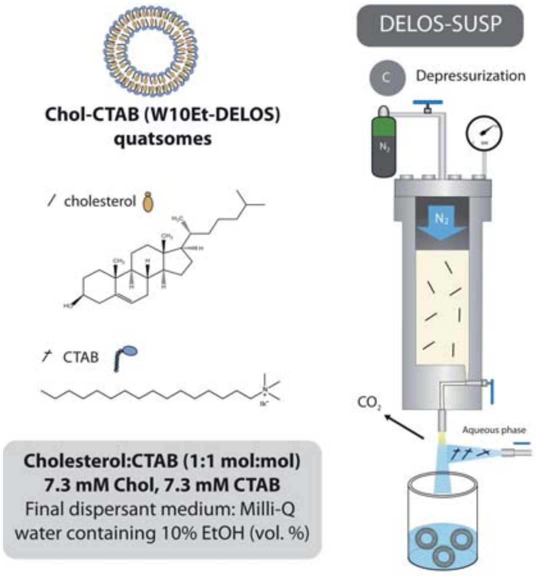

Figure 2.38.: Schematic representation of the DELOS-SUSP method to obtain Chol-CTAB (W10Et-DELOS) quatsomes.

The method to prepare these quatsomes consisted in the loading of a 7.5 ml high-pressure autoclave with a solution containing 76 mg of cholesterol in 2.88 ml of ethanol. The solution was then pressurized with compressed CO_2 at a molar fraction of $X_{CO_2}= 0.6$ until reaching a working pressure of 10 MPa, which produced a volumetric expanded organic solution of cholesterol. In Section 6.2.1.4 of the Experimental Part is shown the solubility curve of cholesterol in CO_2-expanded ethanol, as presented a co-solvent behavior of CO_2 is observed until X_i = 0.76, which means that below this molar fraction one single phase is obtained when the CO_2 is added over a saturated solution of cholesterol in pure ethanol. Finally, the expanded organic phase was depressurized over 24 ml of Milli-Q water containing 72 mg of CTAB. The membrane components concentration was 5.4 mg/ml (7.3 mM cholesterol and 7.3 mM CTAB) in high purity water containing 10% ethanol (vol. %).

It is important to recall that the presence of ethanol in vesicle formulations has been shown to be an efficient permeation enhancer. Specifically, ethosome vesicles containing ethanol in relatively high concentrations (20 - 30% w/w), have been able to allow transdermal delivery [180, 181]. Thus, the presence of a high ethanol percentage in the dispersant media makes quatsomes promising carriers for attaining good skin penetrability in topical delivery. Furthermore, it is worth highlighting that DELOS-SUSP methodology presents several advantages over the more easily implemented sonication methodology. The DELOS-SUSP route is an easily scalable preparation method that can be easily implemented under GMP regulations. In addition, it allows the straightforward integration/encapsulation of active biological species such as proteins and enzymes that could be degraded if sonication procedures are used. Therefore the DELOS-SUSP methodology is a green, robust and easy scalable productive process.

On the other hand, it has to be noted that the temperature effect in the storage of Chol-CTAB (W10Et-DELOS) quatsomes was measured previously in *Nanomol* group as described in the PhD Thesis of Dr. Ingrid Cabrera [182]. In these studies, it was observed that the Chol-CTAB quatsomes keep their physicochemical properties under 277 and 298 K. Taking into account these structures are used for the integration/encapsulation of active biological species, 277 K for Chol-CTAB (W10Et-DELOS) quatsomes storage was chosen in order to preserve such biological species over time.

The size distribution and Z-potential of Chol-CTAB (W10Et-DELOS) quatsomes 1 week after sample preparation were measured by DLS. These physicochemical characteristics were compared with the ones obtained with Chol-CTAB (W-US) quatsomes. As shown in Table 2.7 and Figure 2.39, the Chol-CTAB (W10Et-DELOS) quatsomes presented an unimodal size distribution centred around 82 nm. Additionally, its Z-potential value was higher than the obtained with Chol-CTAB (W-US) quatsomes.

Table 2.7.: Physicochemical characteristics of Chol-CTAB (W10Et-DELOS) quatsomes and Chol-CTAB (W-US) quatsomes measured 1 week after sample preparation.

Vesicle	**Size**		**Stability**
sample	**Mean(nm)**[c]	**PdI**[d]	**Z-pot.(mV)**
Chol-CTAB[a] (W10Et-DELOS) quatsomes	81.85 ± 1.79	0.319±0.020	115 ± 3
Chol-CTAB[b] (W-US) quatsomes	100.5 ± 0.5	0.417±0.008	79.2 ± 2.4

[a] Chol-CTAB (W10Et-DELOS) quatsomes were stored at 277 K.

[b] Chol-CTAB (W-US) quatsomes were stored at 298 K.

[c] Intensity weighted mean hydrodynamic size of the collection of vesicles measured by dynamic light scattering.

[d] Polidispersity index showing the width of the particle size distribution.

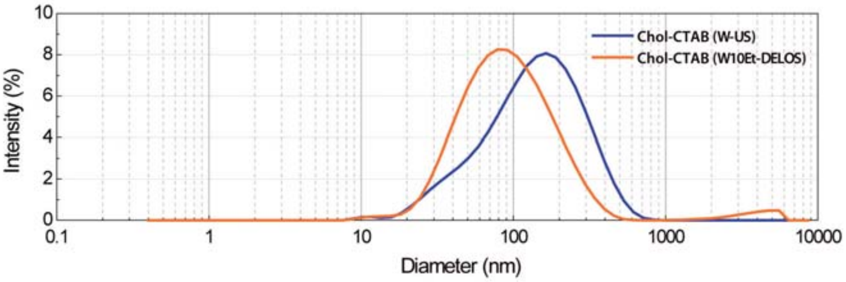

Figure 2.39.: Size distribution of Chol-CTAB (W10Et-DELOS) quatsomes and Chol-CTAB (W-US) quatsomes measured 1 week after sample preparation.

2.3.2.1. Evaluation of Chol-CTAB (W10Et-DELOS) quatsome stability with time

The physicochemical properties of Chol-CTAB (W10Et-DELOS) quatsomes were evaluated using DLS by means of particle size distribution and Z-potential after 1, 7, 14, 300 and 1,000 days of storage at 277 K. As seen in Table 2.8 and Figure 2.40, DLS measurements showed that 14 days after quatsome preparation the size distribution of these quatsomes remain constant over time at least up 1,000 days. The quatsome morphology after 14 days of aging was evaluated by cryo-TEM, and the images

(Figure 2.40) depicted unilamellar and spherical nanovesicles. The Z-potential values (Table 2.8) remained constant with a high value during the time of the experiment, thus Chol-CTAB (W10Et-DELOS) quatsomes presented an excellent stability over time.

Table 2.8.: Physicochemical properties of Chol-CTAB (W10Et-DELOS) quatsomes measured with time.

Quatsome[a] aging	Size		Z-potential (mV)
	Mean (nm) [b]	PdI [c]	
1 day	86.30 ± 0.99	0.393±0.005	110 ± 6
7 days	81.85 ± 1.79	0.319±0.020	115 ± 3
14 days	73.47 ± 0.94	0.262±0.006	110 ± 6
300 days	71.74 ± 0.57	0.275±0.003	112±5
1,000 days	72.43 ± 0.60	0.277±0.005	115±3

[a] Chol-CTAB (W10Et-DELOS) quatsomes were stored at 277 K.

[b] Intensity weighted mean hydrodynamic size of the collection of vesicles measured by dynamic light scattering.

[c] Polidispersity index showing the width of the particle size distribution.

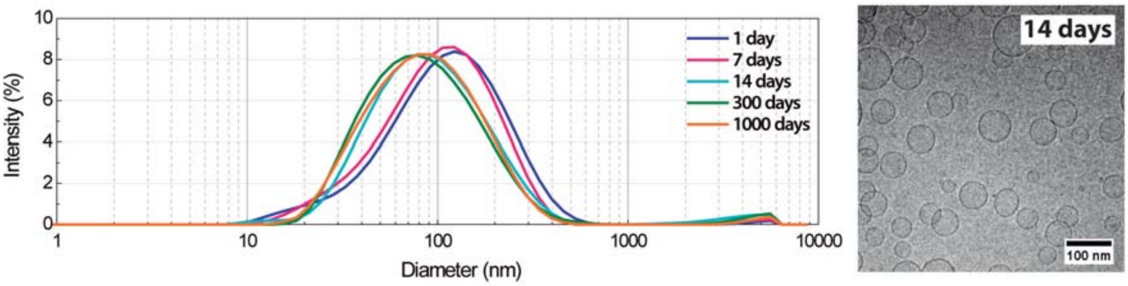

Figure 2.40.: Size evolution (left) of Chol-CTAB (W10Et-DELOS) quatsomes measured with time. Cryo-TEM image (right) of Chol-CTAB (W10Et-DELOS) quatsomes taken 14 days after sample prepared. Samples were stored at 277 K.

As previously mentioned, liposomes made with phospholipids are thermodynamically unstable colloidal system and they tend to aggregate over time [64]. Besides, liposomes suffer chemical and physical alterations, which shorten their self-life and limit, as a consequence, drug stability and conditions of storage [67].

With the objective of comparing the stability 1,000 days after sample preparation of Chol-CTAB (W10Et-DELOS) quatsome and a liposomal system, Chol:DPPC (dipalmitoylphosphatidylcholine) (1:1 mol:mol) liposomes having the same cholesterol molar content were prepared by the same methodology, the DELOS-SUSP method (see Section 6.5.1.1 of the Experimental Part for liposome preparation). This new vesicle system, called Chol-DPPC (W5Et-DELOS) liposomes (Table 6.4 of the Experimental Part), was studied after 14 and 1,000 days of aging with the sample stored at 277 K.

Table 2.9 and Figure 2.41 show the size distributions, the Z-potential values and the cryo-TEM images of Chol-CTAB (W10Et-DELOS) quatsomes and Chol-DPPC (W5Et-DELOS) liposomes analyzed 14 days after sample preparation. As shown, at this time both obtained vesicles were nanoscopic and homogeneous in size.

Table 2.9.: Physicochemical characteristics of Chol-DPPC (W5Et-DELOS) liposomes and Chol-CTAB (W10Et-DELOS) quatsomes measured 14 days after sample preparation.

Vesicle[a]	**Size**		**Stability**
sample	**Mean(nm)**[b]	**PdI**[c]	**Z-pot.(mV)**
Chol-DPPC (W5Et-DELOS) liposomes	118.8 ± 0.60	0.205 ± 0.007	-0.179 ±0.129
Chol-CTAB (W10Et-DELOS) quatsomes	73.47 ± 0.94	0.262±0.006	110 ± 6

[a] Samples were stored at 277 K.

[b] Intensity weighted mean hydrodynamic size of the collection of vesicles measured by dynamic light scattering.

[c] Polidispersity index showing the width of the particle size distribution.

Figure 2.41a shows that after 1,000 days of aging, the macroscopic appearance of the quatsome suspension presents a homogeneous translucent aqueous system, and cryo-TEM images of such quatsomes demonstrate that their morphology was retained after this period of time. In contrast, Chol-DPPC (W5Et-DELOS) liposomes (Figure 2.41b) undergo macroscopic phase separation as evidenced by the black colloidal precipitate deposited at the bottom of the vessel, which correspond to the oxidation of the lipidic component. Due to this obvious degradation, further characterizations were not carried out of this liposomal sample.

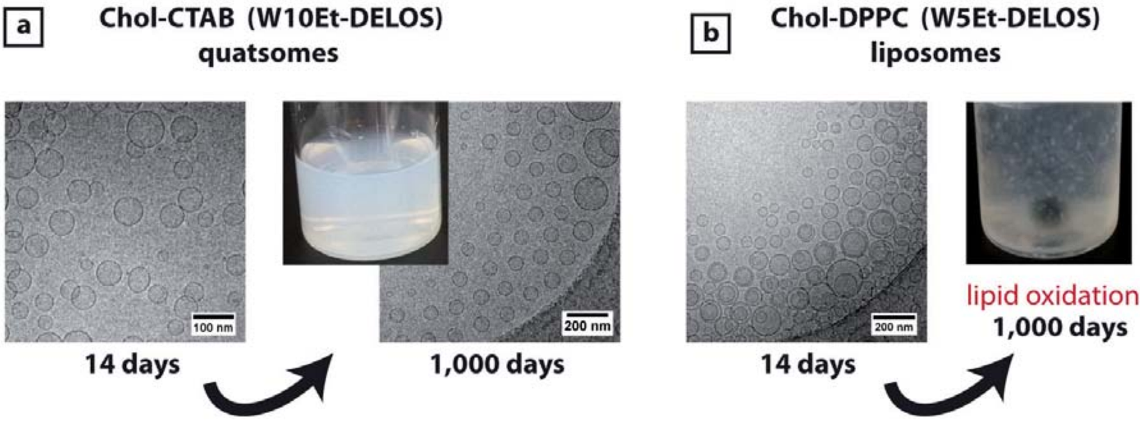

Figure 2.41.: (a) Cryo-TEM images of Chol-CTAB (W10Et-DELOS) quatsomes recorded after 14 days and 1,000 days of aging. Additionally, a picture of the suspension 1,000 days after sample preparation is shown. (b) Cryo-TEM image of Chol-DPPC (W5Et-DELOS) liposomes recorded 14 days after sample preparation and a picture of the suspension after 1,000 days of aging. Both samples were stored at 277 K.

As a result, that study highlights that Chol-CTAB (W10Et-DELOS) quatsomes have extremely long term stability of at least 1,000 days with the sample stored at 277 K.

2.3.2.2. Evolution of Chol-CTAB (W10Et-DELOS) quatsome structure with temperature

The thermal stability of Chol-CTAB (W10Et-DELOS) quatsomes was evaluated by DLS. The evolution of particle size was followed by heating the suspension from 298 K to 343 K inside the DLS equipment. The particle size was measured at 298, 303, 310, 313, 318, 323 and 343 K (Table 2.10 and Figure 2.42a). The obtained results indicated that as the temperature increases, the particle size distribution becomes slightly smaller. To get further insights on any structural changes that may take place during this experiment, we directly visualized the structure of the quatsomes by cryo-TEM, and as shown in Figure 2.42b, the quatsome morphology was maintained after heating the sample to 343 K.

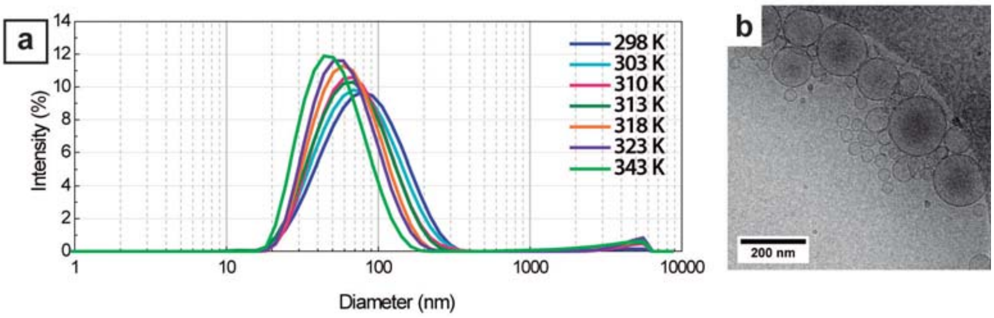

Figure 2.42.: (a) Particle size distributions of Chol-CTAB (W10Et-DELOS) quatsomes measured by DLS at 298, 303, 310, 313, 318, 323 and 343 K. (b) Representative cryo-TEM image of Chol-CTAB quatsomes taken after heating the sample to 343 K.

Table 2.10.: Size evolution of Chol-CTAB (W10Et-DELOS) quatsomes with temperature.

Temperature	**Size**	
(K)	**Mean (nm)** [a]	**PdI** [b]
298	69.35 ± 0.45	0.237±0.002
303	65.95 ± 0.20	0.240±0.006
310	62.14 ± 0.19	0.225±0.004
313	60.72 ± 0.11	0.231±0.006
318	58.15 ± 0.21	0.217±0.003
323	56.09 ± 0.22	0.220±0.008
343	48.55 ± 0.15	0.217±0.003

[a] Intensity weighted mean hydrodynamic size of the collection of vesicles measured by dynamic light scattering.

[b] Polidispersity index showing the width of the particle size distribution.

Therefore, the preparation of Chol-CTAB quatsomes in water with 10% of EtOH in volume by DELOS-SUSP yields homogeneous small unilamellar vesicles with an extremely long term stability of at least 1,000 days with samples stored at 277 K. Moreover, these vesicular assemblies do not change shape upon heating between 298 and 343 K. Due to this high degree of structural homogeneity and this great stability with time and temperature, the Chol-CTAB (W10Et-DELOS) quatsomes can be also considered thermodynamically stable vesicles.

2.3.3. Viscoelastic properties of Chol-CTAB quatsomes

The mechanical properties of membranes have gained more attention as vesicles are more widely used as drug delivery systems (DDS) where the membrane is not only a compartment for cargo, but can actively influence the overall outcome of a treatment [183, 184]. Membranes used in drug delivery systems are relatively simple, compared with cell membranes, that are dynamic and contain many specific regions with various properties [185, 186]. Their role is however quite different – instead of adjusting to dynamic environment, membranes used in drug delivery systems should be stable over prolonged periods of time (shelf-life) with unchanged properties.

In this Section, the viscoelastic properties of Chol-CTAB quatsomes compared with Chol-DOPC (1,2-Dioleoyl-sn-glycero-3-phosphocholine) liposomes at 1:4 cholesterol:DOPC molar ratio were studied. Both systems were prepared by DELOS-SUSP method (see Section 6.2.1 of the Experimental Part). A phosphate buffered solution (PBS, 100 mM, pH = 7.4) was used as the aqueous medium in both preparations in order to test vesicles properties in a context resembling physiological conditions as much as it was possible. It has to be noted that the possibility to prepare both vesicle systems by DELOS-SUSP in the phosphate buffered solution was studied before by Dr. Elisa Elizondo from the *Nanomol* group (ICMAB-CSIC) in her PhD work [187]. These vesicle samples have been called Chol-CTAB (PBS10Et-DELOS) quatsomes and Chol-DOPC (PBS10Et-DELOS) liposomes (see Table 6.3 and Table 6.4 of the Experimental Part).

In order to prepare the Chol-CTAB (PBS10Et-DELOS) quatsomes, 76 mg of cholesterol in 2.88 ml of ethanol were pressurized with CO_2 at $X_{CO_2} = 0.6$ and depressurized over 24 ml of a phosphate buffered solution (PBS, 100 mM, pH = 7.4) containing 72 mg of CTAB. The membrane components concentration was 5.4 mg/ml (7.3 mM cholesterol and 7.3 mM CTAB) in 100 mM PBS containing 10% ethanol (vol. %). To prepare the Chol-DOPC (PBS10Et-DELOS) liposomes, 4.28 mg of cholesterol and 35.61 mg of DOPC in 1.9 ml of ethanol were pressurized with CO_2 at $X_{CO_2} = 0.84$ and depressurized over 17 ml of an aqueous solution of PBS buffer (PBS, 100 mM, pH = 7.4). The membrane components concentration was 2.1 mg/ml (0.6 mM cholesterol and 2.4 mM DOPC) in 100 mM PBS containing 10% ethanol (vol. %). Both vesicle samples were stored at 277 K and were further characterized 14 days after sample preparation.

The mean and polydispersity index (PdI) of the particle size distributions measured by DLS for the obtained vesicles are presented in Table 2.11. DLS measurements and cryo-TEM images (Figure 2.43) revealed that both systems, Chol-CTAB quatsomes and Chol-

DOPC liposomes, were nanoscopic unilamellar vesicles.

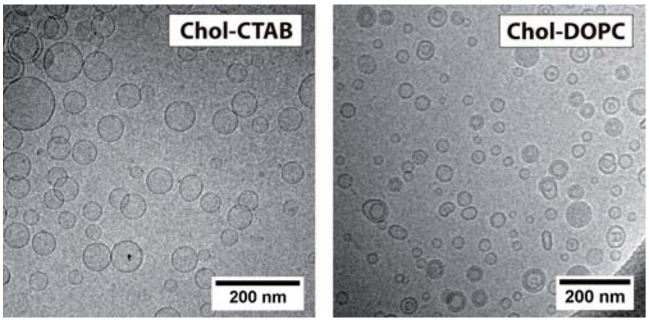

Figure 2.43.: Cryo-TEM images of Chol-CTAB (PBS10Et-DELOS) quatsomes and Chol-DOPC (PBS10Et-DELOS) liposomes prepared by DELOS-SUSP in PBS buffer with 10% of EtOH (vol. %).

Table 2.11.: Physicochemical characteristics of Chol-CTAB (PBS10Et-DELOS) quatsomes and Chol-DOPC (PBS10Et-DELOS) liposomes obtained by DELOS-SUSP method.

Vesicle[a] **sample**	**Size**		**Morphology**[d]
	Mean (nm)[b]	**PdI**[c]	
Chol-CTAB quatsomes	118.7 ± 1.6	0.134 ± 0.011	SUVs
Chol-DOPC liposomes	94.77 ± 0.51	0.262 ± 0.006	SUVs

[a] Samples were stored at 277 K.

[b] Intensity weighted mean hydrodynamic size of the collection of vesicles measured by dynamic light scattering.

[c] Polidispersity index showing the width of the particle size distribution.

[d] Morphology of the vesicles observed by cryo-TEM. SUVs: Small unilamellar vesicles.

After the preparation and the physicochemical characterization of these vesicle systems, their viscoelastic properties were studied by Dr. Witold Tatkiewicz from the *Nanomol* group (ICMAB-CSIC) in his PhD work [188]. In these studies, the viscoelastic characteristics of these vesicles were studied after the deposition and absorption of these systems over gold surfaces forming vesicular layers, analyzing these layers using the Quartz Crystal Microbalance with Dissipation (QCM-D) and the Surface Plasmon Resonance (SPR) techniques (Figure 2.44) (in Section A.5 of the Appendix these techniques are explained in detail). Combining QCM-D with SPR data by an iterative protocol developed by Dr. Witold Tatkiewicz (ICMAB), the thickness of material deposited over the gold surfaces and the viscosity values of the deposited vesicles were possible to be investigated.

It is noteworthy that both techniques allow to perform label-free and real time measurements. Besides, since one technique is designed to measure acoustic and the other optical properties, coupling them offers the possibility of getting complementary data.

Although with the iterative process it is possible to get reliable data on the thickness, from QCM-D it is also possible to use a model-independent analysis in order to calculate this value for an adsorbed vesicular layer, known as *Sauerbrey heighte* [189].

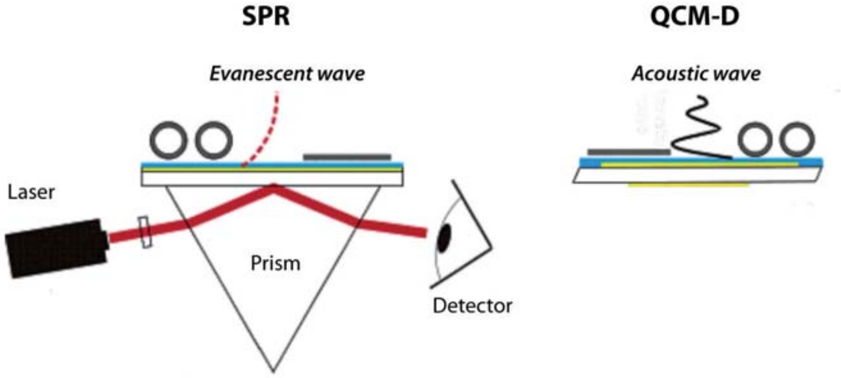

Figure 2.44.: Schematic illustration of the measurements configuration. Coupling both techniques enables to obtain optical (SPR) and sonic (QCM-D) sensors/properties. Image adapted from [190].

A brief summary of the most significant results is explained below.

The comparison of layer thicknesses of vesicles deposited over the gold surfaces for Chol-CTAB (PBS10Et-DELOS) quatsomes and Chol-DOPC (PBS10Et-DELOS) liposomes are shown in Figure 2.45. $d_{effecive}$ is the vesicle layer thickness calculated by the iterative protocol combining SPR and QCM-D data, *Sauerbrey height* is the vesicle layer thickness calculated using only QCM-D data and DLS (mean) is the mean size of vesicles reported by DLS measurements (see Table 2.11). Different concentrations of vesicles were used.

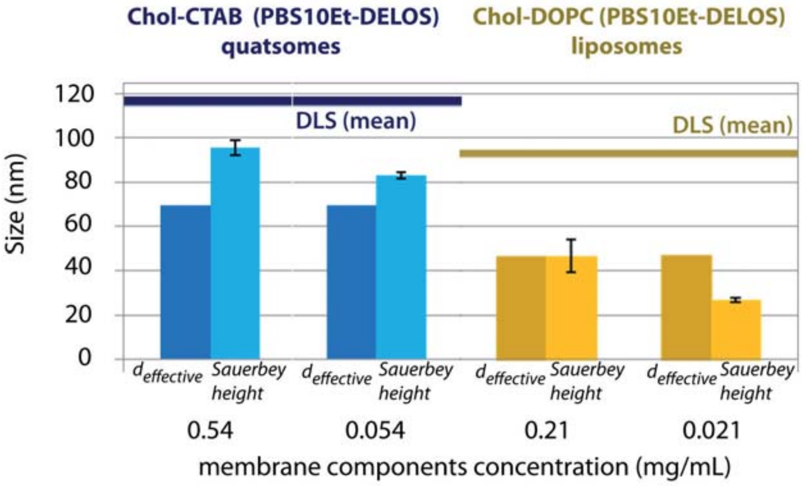

Figure 2.45.: Comparison of vesicular layer thicknesses: $d_{effecive}$ is the vesicle thickness calculated by the iterative protocol combining SPR and QCM-D data, *Sauerbrey height* is the vesicle thickness calculated using only QCM-D data and DLS (mean) is the mean size of vesicles reported by DLS measurements (see Table 2.11). Results for Chol-CTAB (PBS10Et-DELOS) quatsomes and Chol-DOPC (PBS10Et-DELOS) liposomes at high and low concentrations.

As expected, vesicles are soft molecular materials and undergo deformation upon adsorption on a substrate giving place to a final vesicle layer thickness much smaller than the mean size of the vesicles measured with DLS in suspension. In fact, the thickness of Chol-CTAB vesicle layer is ca. 58% of the initial vesicle mean diameter in suspension. In case of Chol-DOPC liposomes, the final vesicular layer thickness is only ca. 50% of the initial vesicle mean diameter size.

The thickness of vesicle layer calculated combining SPR and QCM-D data is in the range of 70-90 nm and 40-50 nm for Chol-CTAB quatsomes and Chol-DOPC liposomes, respectively. The total layer density obtained from iterative calculations for all cases is close to the density of the buffer ~ 1000 kg/m^3 as presented in Table 2.12. Based on the DLS data (Table 2.11) regarding the mean size of the vesicles in bulk (suspension) we can state that Chol-CTAB quatsomes are much more rigid than Chol-DOPC liposomes because vesicles undergo smaller deformation upon adsorption (see Figure 2.46).

Table 2.12.: Viscoelastic properties of Chol-CTAB (PBS10Et-DELOS) quatsome and Chol-DOPC (PBS10Et-DELOS) liposome layers calculated via iterative fitting of SPR and QCM-D data.

Vesicle sample	**Chol-CTAB quatsomes**		**Chol-DOPC liposomes**	
Membrane components concentration (mg/ml)	0.54	0.054	0.21	0.021
Total layer density (ρ) **(kg/m^3)**	998	972	1018	1019
Viscosity (η) **(kg/m·s×10^{-3})**	3.95	3.97	2.23	1.84

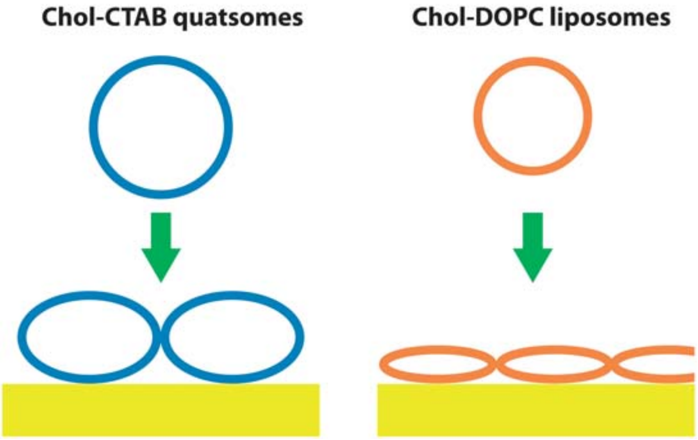

Figure 2.46.: Comparison of deformation of vesicles upon deposition on gold. Chol-CTAB quatsomes behave as much more rigid objects than Chol-DOPC liposomes. Sizes of vesicles before and after deposition are scaled according to the obtained data.

The higher rigidity of the Chol-CTAB vesicles is confirmed with the viscosity values (Table 2.12) calculated with the iterative protocol developed by Dr. Witold Tatkiewicz (ICMAB). The Chol-DOPC liposome layer present a lower value of viscosity than the Chol-CTAB quatsome layer, thus Chol-DOPC liposomes deform more upon adsorption than Chol-CTAB quatsomes. This observation is a clear evidence of the influence of the internal supramolecular structure of the bilayer on the mechanical properties of vesicles.

The higher rigidity of Chol-CTAB quatsomes can be attributed to the unique properties of cholesterol and CTAB molecules that form the stable bilayer when mixed in equimolar proportions.

2.3.4. Recovery of structure after lyophilization

It is well known that lyophilization or freeze-drying is a promising approach to ensure the long-term stability of vesicles because it allows to convert colloidal systems into solids providing products with better properties for distribution and storage. This process consists of removing water from a frozen sample by sublimation and desorption under vacuum. A typical freeze-drying process consists of three stages; that is, freezing, primary drying, and secondary drying. Freezing is an efficient dessication step where most of the solvent, typically water, is separated from the solutes to form ice. Primary drying, or ice sublimation, begins whenever the chamber pressure is reduced and the shelf temperature is raised to supply the heat removed by ice sublimation. During primary drying, the chamber pressure is well below the vapor pressure of ice, and ice is transferred from the product to the condenser by sublimation and crystallization onto the cold coils/plates in the condenser. Secondary drying is the stage where water is desorbed from the freeze concentrate, usually at elevated temperature and low pressure. Some secondary drying occurs even at the very beginning of primary drying as ice is removed from a region, but the bulk of secondary drying occurs after primary drying is over and the product temperature has increased [191]. This technique has been largely discussed in many articles devoted to liposomal formulations and it has been reported that it is recommendable the addition of cryogenic protectors to preserve the vesicle membrane. These cryogenic protectors prevent fusion of vesicles, prevent the rupture of bilayers by ice crystals and maintain the integrity of the bilayers in the absence of water [192, 193].

Taking into account all these requirements, we carried out the lyophilization of a Chol-CTAB (W10Et-DELOS) quatsome sample (see Table 6.3 of the Experimental Part) using trehalose as a cryogenic protector. An aliquot of 250 µl of quatsomes was diluted into 250 µl of Milli-Q water with trehalose (6 % w/v). The resulting sample was lyophilized following the experimental protocol described in Section 6.2.4 of the Experimental Part and following the experimental parameters of Table 2.13. The lyophilized sample was resuspended in 500 µl of water to keep the same concentration of quatsomes in solvent as in the original suspension before lyophilized, and the size distribution and morphology of the final vesicles were analyzed. As shown in Figure 2.47, quatsomes keep their structure after lyophilization. Indeed, dynamic light scattering (DLS) measurements and cryo-TEM images revealed that the nanovesicles obtained after lyophilization and further hydration were homogeneous, spherically-shaped and unilamellar. Furthermore, the resulting cake obtained after lyophilization of the suspension was well formed (Figure 2.47). Thus, it was demonstrated that lyophilization process did not influence the physicochemical characteristics and the morphology of the cholesterol-CTAB quatsomes prepared by DELOS-SUSP.

Table 2.13.: Parameters followed in quatsome lyophilization.

Freezing		Primary drying			Secondary drying		
T (°C)	**Rate (°C/min)**	**P (mbar)**	**T (°C)**	**time (h)**	**P (mbar)**	**T (°C)**	**time (h)**
-55	1	0.060	-35	24	0.01	25	9

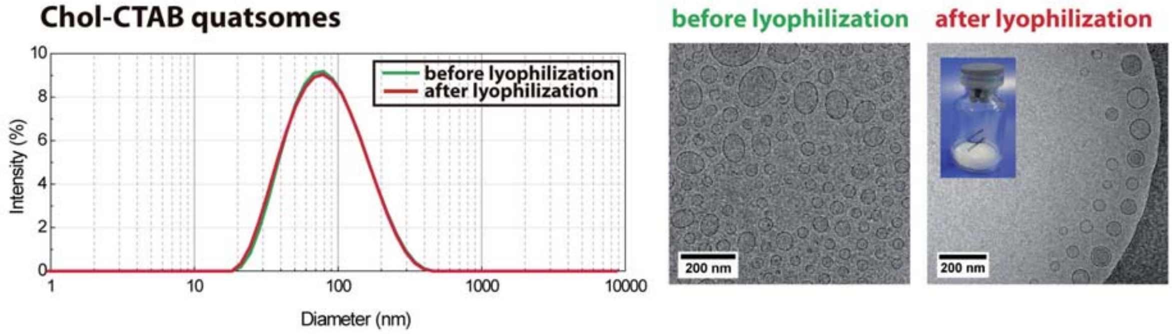

Figure 2.47.: On the left is shown the DLS measurements of the Chol-CTAB (W10Et-DELOS) quatsomes before lyophilization and after lyophilization and hydration. On the right is a representative cryo-TEM picture for both situations and a picture of the cake after lyophilization before hydration.

The extremely good recovery of the Chol-CTAB quatsome shape and size, shows the reversibility of these vesicles upon change of an external factor.

2.3.5. Summary

- The large bending constant *(k_c)*, the high degree of structural homogeneity observed by cryo-TEM and SAXS and the formation of two-bilayer vesicles adding $NaHCO_3$ electrolyte suggest that Chol-CTAB (W-US) quatsomes are stabilized by the energy costs of deviations from the spontaneous curvature (elastically stabilized). Therefore, cholesterol-CTAB (W-US) quatsomes in water are thermodynamically stable vesicular structures.

- The preparation of Chol-CTAB quatsomes in water with 10% of EtOH in volume by DELOS-SUSP yields homogeneous small unilamellar vesicles with an extremely long term stability of at least 1,000 days with samples stored at 277 K. Moreover, these vesicular assemblies do not change shape upon heating between 298 and 343 K. Due to this high degree of structural homogeneity and this great stability with time and temperature, the Chol-CTAB (W10Et-DELOS) quatsomes can be also considered thermodynamically stable vesicles.

- QCM-D and SPR techniques have demonstrated that Chol-CTAB (PBS10Et-DELOS) quatsomes were more rigid and more viscous than Chol-DOPC (PBS10Et-DELOS) liposomes.
- Lyophilization process did not influence the physicochemical characteristics and the morphology of Chol-CTAB (W10Et-DELOS) quatsomes.

2.4. Preparation of stable Chol-CTAB (W10Et) quatsomes by several routes

The properties of any material are determined by their structure at nanoscopic and supramolecular level. It is well known that in crystalline or condensed matter, a solid organic compound having the same chemical composition can be organized forming non-crystalline (amorphous) forms and crystalline forms with different polymorphs. These changes in the internal organization can exhibit different physical and functional properties. For instance, many drugs which are fundamentally organic compounds, receive regulatory approval for only a polymorph. One high profile case of polymorphism in pharmaceutical compounds was ritonavir, a peptidomimetic drug used to treat HIV-1 infection and introduced in 1996. In 1998, a lower energy, more stable polymorph (form II) appeared, causing slowed dissolution of the marketed dosage form and compromising the oral bioavailability of the drug. This event forced the removal of the oral capsule formulation from the market [194, 195].

A vesicular system, with a specific chemical composition, can also exhibit different structures at nanoscopic and supramolecular level. In the case of non-stable vesicular systems, these structures tend to change over time and it is difficult to obtain the same vesicle supramolecular organization preparing these systems by different synthetic routes.

According to Marques [78], the formation and properties of the thermodynamically stable vesicles, like Chol-CTAB quatsomes explained in the previous Section, have to be independent of the method of preparation. In this regard, the purpose of this Section was to explore whether stable and homogeneous Chol-CTAB (W10Et) quatsomes could be prepared by several routes of preparation.

2.4.1. Preparation of Chol-CTAB (W10Et) vesicular systems

The preparation of stable Chol-CTAB (W10Et) quatsomes was attempted by several preparation routes schematized in Figure 2.48. DELOS-SUSP and sonication methods maintain the membrane components in solution during vesicle preparation, however the TFH method involves an intermediate stage where the solvent is removed (solvent-free state) and a film of cholesterol and CTAB is formed.

In all preparations, the final concentration of membrane components was 5.4 mg/ml (7.3 mM cholesterol and 7.3 mM CTAB) and the same amount of alcohol, 10% in volume, was added to the hydration water. All the samples were stored at 277 K and were characterized at least 14 days after sample preparation.

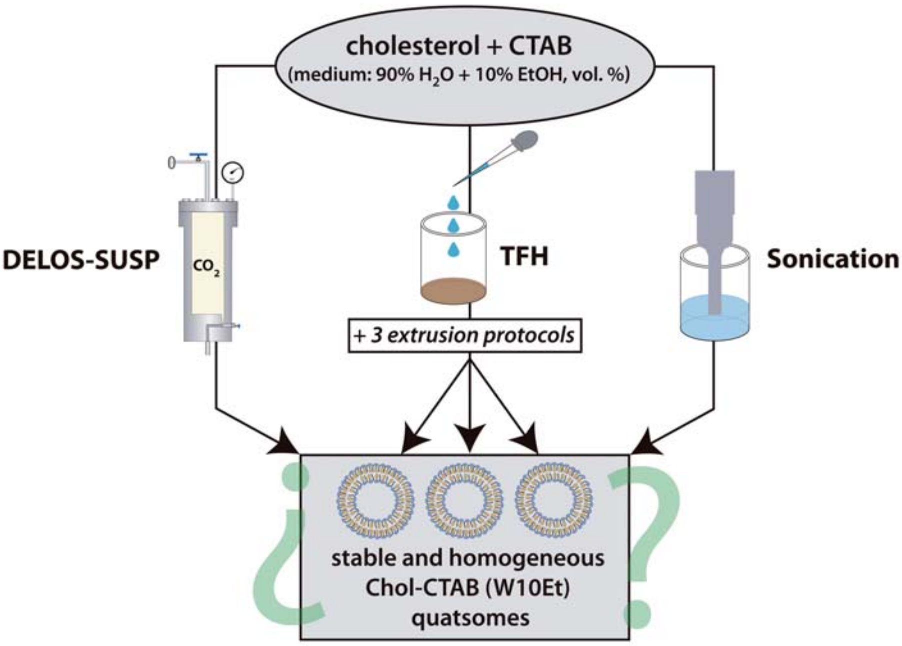

Figure 2.48.: Scheme of the different explored routes for the preparation of cholesterol-CTAB quatsomes in water with 10% of EtOH (v/v), Chol-CTAB (W10Et) quatsomes.

2.4.1.1. Preparation of Chol-CTAB (W10Et) quatsomes by DELOS-SUSP

The preparation of Chol-CTAB (W10Et) quatsomes by DELOS-SUSP was already studied in the previous Section (see Section 2.3.2). Briefly, in order to prepare Chol-CTAB (W10Et-DELOS) quatsomes, 76 mg of cholesterol in 2.88 ml of ethanol was pressurized with CO_2 at X_{CO_2} = 0.6 and depressurized over 24 ml of Milli-Q water containing 72 mg of CTAB.

2.4.1.2. Preparation of Chol-CTAB (W10Et) quatsomes by Thin Film Hydration methodology followed by extrusion

The preparation of stable and homogeneous Chol-CTAB (W10Et) quatsomes was also attempted by the conventional Thin Film Hydration method (TFH) [178]. Vesicles were prepared following the multi-step procedure schematized in Figure 2.49. The detailed information about vesicles formation by the TFH method is included in Section 6.2.2 of the Experimental Part.

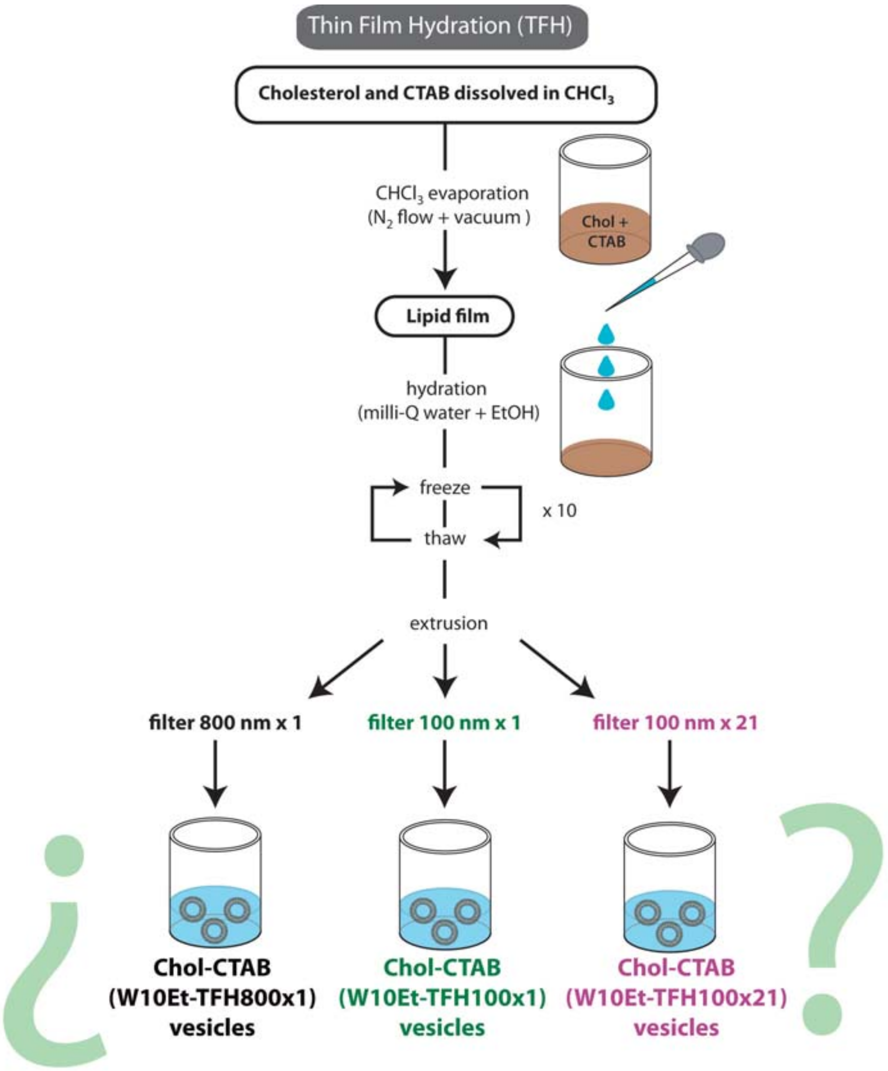

Figure 2.49.: Schematic diagram showing the preparation of Chol-CTAB (W10Et) vesicles by the TFH method.

2.78 mg of cholesterol and 2.62 mg of CTAB were dissolved in chloroform and mixed in a 2 ml glass vial for a total lipid mass of 5.4 mg. The solvent was slowly evaporated under N_2 flow to create a thin lipid film and the glass vial were placed in vacuum for at least 3 hours in order to remove any remaining solvent. The lipid film was then hydrated overnight using 1 ml of Milli-Q water with 10% of ethanol (vol. %), at room temperature. Next, the sample was taken through 10 rounds of freeze/thaw cycles by transferring it between liquid nitrogen and a water bath (313 K) and finally, the sample was extruded reducing the size of the quatsomes by mechanical energy. In this extrusion-step, the suspension is forced through a polycarbonate membrane filter with a defined pore size to yield particles having a diameter near the pore size of the filter used. A commercially available manual extruder (Avanti® Mini-Extruder, Avanti Polar Lipids, Alabaster, AL, USA), was used for that purpose (Figure 6.6 of the Experimental Part). Three different extrusion protocols were conducted in order to investigate the effect in the final nanostructure of both, the pore size of the polycarbonate membrane filter used and the number of extrusions performed. The first one was to use a membrane filter with a pore size of 800 nm and the sample was passed through the extruder one time. The second protocol was to reduce the pore size of the membrane filter from 800 nm to 100 nm, keeping constant the number of the extrusions (one time). And the third protocol was to use a membrane filter with 100 nm pore size and the sample was passed through the extruder twenty-one times. Consequently, three different Chol-CTAB samples were obtained by TFH. The vesicular products obtained by these three different preparation protocols have been called Chol-CTAB (W10Et-TFH800x1), Chol-CTAB (W10Et-TFH100x1) and Chol-CTAB (W10Et-TFH100x21) (see Table 6.3 of the Experimental Part).

Usually in two steps of this Thin Film Hydration method, the hydration-step and the extrusion-step, the working temperature should be above the thermotropic phase transition (T_m) of membrane components, in order to hydrate and extrude in their fluid phase. This transition temperature was studied for preformed Chol-CTAB (W10Et-DELOS) quatsomes (Section 2.4.1.1). The measurements were conducted using a VP-DSC microcalorimeter equipment and are presented in Section 6.6 of the Experimental Part. As explained, the Chol-CTAB quatsome bilayer adopted a liquid-ordered (L_o) phase and did not exhibit a thermotropic phase transition (T_m), therefore all the steps of this vesicle preparation can be conducted at room temperature.

2.4.1.3. Preparation of Chol-CTAB (W10Et) quatsomes by sonication

The last route tested for the preparation of stable and homogeneous Chol-CTAB (W10Et) quatsomes was sonication (see Section 6.2.3 of the Experimental Part). 26.2 mg of CTAB and 27.8 mg of cholesterol were added directly to 10 ml of Milli-Q water with 10 % ethanol (vol. %). The resulting dispersion was sonicated at 298 K for 4 min until a homogeneous dispersion was achieved (Figure 2.50). From now on these vesicles have been called Chol-CTAB (W10Et-US) (Table 6.3 of the Experimental Part).

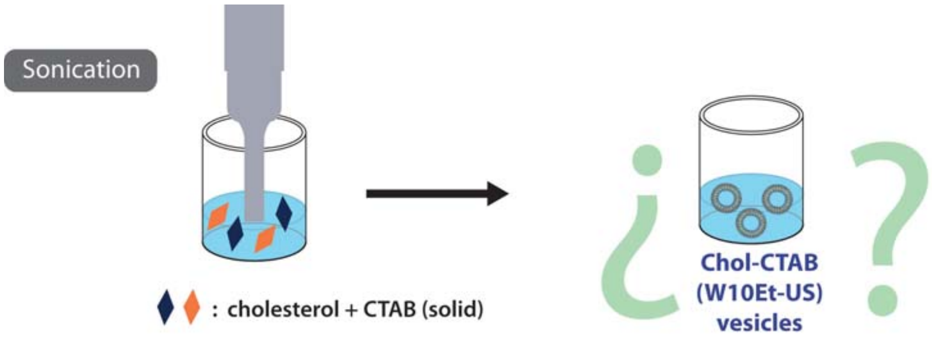

Figure 2.50.: Scheme of sonication method for the preparation of Chol-CTAB (W10Et) vesicles.

2.4.2. Qualitative and quantitative characterization of the vesicular systems

All the above described Chol-CTAB vesicular systems prepared by different routes (DELOS-SUSP, sonication and TFH + extrusion) were fully characterized to determine if they were formed or not as stable and homogeneous Chol-CTAB (W10Et) quatsomes. The characterizations were conducted by DLS (Section 6.3.3 of the Experimental Part), to study the vesicle size distribution, polydispersity and Z-potential (surface charge), by cryo-TEM microscopy (Section 6.3.1 of the Experimental Part), to gain information on the morphology of the obtained vesicles, and by SAXS (Section 6.3.11 of the Experimental Part), to investigate the shape, lamellarity and homogeneity of such vesicles.

All the SAXS measurements were performed in the beamline NCD of synchrotron ALBA (Cerdanyola del Vallés, Spain). The SAXS data were analyzed by Dr. Evelyn Moreno from *Nanomo*l group (ICMAB-CSIC). In Section A.4 of the Appendix, is detailed the description of the theoretical model that we have used to interpret the scattering data of vesicles.

In Table 2.14 is gathered all the physicochemical characteristics of the obtained Chol-CTAB vesicular systems studied by DLS. Additionally, the morphology of such vesicles observed by cryo-TEM is also indicated (Figure 2.51).

Table 2.14.: Physicochemical characteristics of Chol-CTAB (W10Et) vesicles prepared by DELOS-SUSP, sonication and TFH + extrusion methods.

Chol-CTAB sample[a]	**Size**		**Stability**	**Morphology**[d]
	Mean(nm)[b]	**PdI**[c]	**Z-pot.(mV)**	
W10Et-TFH800x1	236.6± 4.7	0.325 ± 0.057	97.2 ±6.7	SUVs, LUVs, MVVs
W10Et-TFH100x1	154.8± 1.4	0.191 ± 0.013	83.1 ±2.9	SUVs, LUVs, MVVs
W10Et-TFH100x21	118.8± 1.9	0.085 ± 0.021	78.1 ±4.6	SUVs
W10Et-DELOS	73.47 ± 0.94	0.262 ± 0.006	110 ±6	SUVs
W10Et-US	76.71 ± 0.05	0.241 ± 0.009	100 ±4	SUVs

[a] Samples were stored at 277 K.

[b] Intensity weighted mean hydrodynamic size of the collection of vesicles measured by dynamic light scattering.

[c] Polidispersity index showing the width of the particle size distribution.

[d] Morphology of the vesicles observed by cryo-TEM. SUVs: Small unilamellar vesicles. LUVs: Large unilamellar vesicles. MVVs: Multivesicular vesicles.

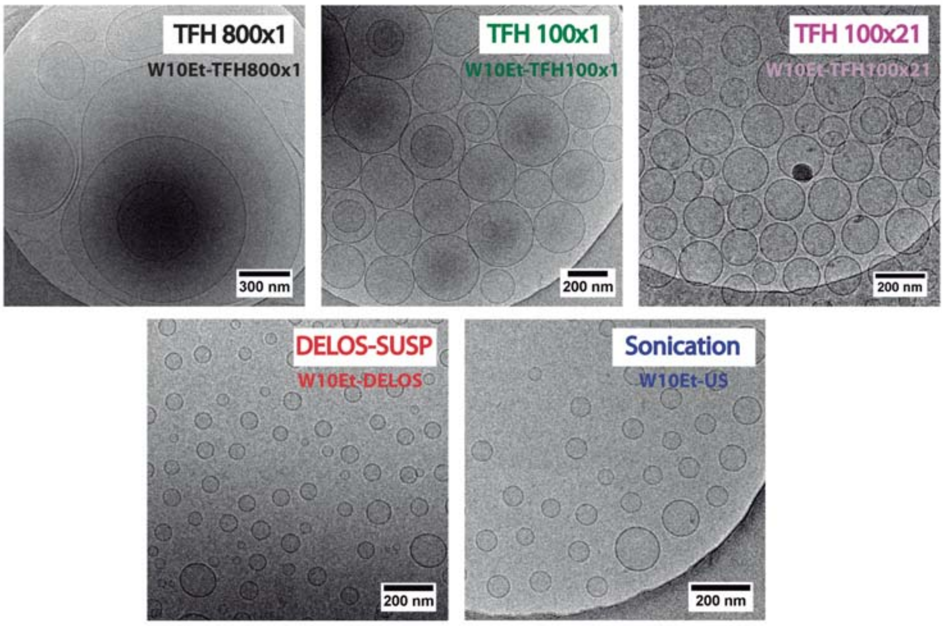

Figure 2.51.: Cryo-TEM images of Chol-CTAB (W10Et-TFH800x1), Chol-CTAB (W10Et-TFH100x1), Chol-CTAB (W10Et-TFH100x21), Chol-CTAB (W10Et-DELOS) and Chol-CTAB (W10Et-US) vesicles. Samples were stored at 277 K prior to vitrify them with liquid ethane.

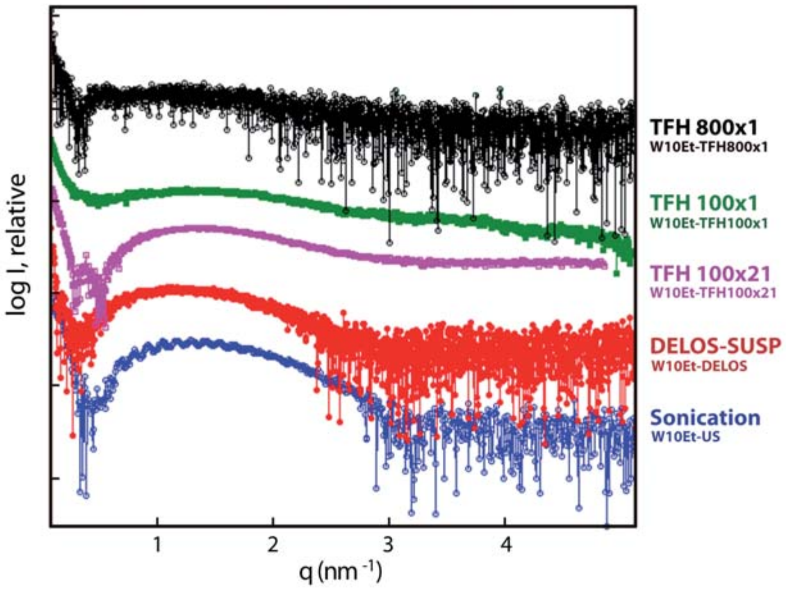

Figure 2.52.: SAXS curves of Chol-CTAB (W10Et-TFH800x1), Chol-CTAB (W10Et-TFH100x1), Chol-CTAB (W10Et-TFH100x21), Chol-CTAB (W10Et-DELOS) and Chol-CTAB (W10Et-US) vesicles. Data collected in the beamline NCD of the ALBA at 298 K.

SAXS data presented in Figure 2.52 and measured at 298 K for Chol-CTAB vesicles prepared by DELOS-susp, sonication and TFH 100x21 methodologies display only broad and diffuse peaks centred between 1.34 and 1.42 nm^{-1} (q_{max}), which indicates that the samples consist of unilamellar vesicles with a repeated distance between 4.42 and 4.69 nm ($d = 2\pi/q_{max}$). As mentioned in a previous Section, in the case of unilamellar vesicles this repeated distance includes the bilayer membrane and the ordered layer of hydration water (see Figure 2.31) [176]. DLS measurements (Table 2.14) and cryo-TEM images (Figure 2.51) also revealed that the obtained vesicles using these three preparation routes were homogeneous in size, spherically-shaped and unilamellar. Thus by DELOS-SUSP, sonication and TFH 100x21 routes, Chol-CTAB quatsomes in water with 10% of EtOH (v/v) with a high level of structural homogeneity can be prepared. Besides, it is important to note that the scattering curve of Chol-CTAB (W10Et-US) quatsomes prepared by sonication shows the well-defined high frequency oscillations studied in the previous Section 2.3.1.4 and attributed to an extremely narrow size distribution. Thus this finding suggests that sonication method allows vesicles with a higher level of homogeneity with regard to particle size.

In contrast to the scattering curves of the above mentioned quatsomes, the SAXS data of Chol-CTAB vesicles prepared by TFH 100x1 and TFH 800x1 methods (Figure 2.52) show completely smeared curves. This fact might be due to the high polydispersity in thickness membrane and size of the obtained systems. DLS measurements (Table 2.14) revealed larger particle size for the vesicles of those Chol-CTAB systems, and cryo-TEM images (Figure 2.51) show the presence of a mixture of small unilamellar vesicles (SUVs), large unilamellar vesicles (LUVs) and multivesicular vesicles (MVVs). Additionally, using the TFH 800x1 route, nonspherical vesicles were also observed.

The differences between the final nanostructures of vesicles prepared by the TFH method with different extrusion protocols, TFH 800x1, TFH 100x1 and TFH 100x21, can be explained due to the phase separation that cholesterol and CTAB suffer during film formation, a solvent-free state. As reported by Buboltz *et al.* [101], those preparation methods involving a solvent-free state, such as a lipid film, may favor demixing of membrane components and therefore an heterogeneous formation of the individual vesicles in an ensemble.

This cholesterol and CTAB phase separation was already observed by Dr. Elisa Elizondo from *Nanomol* group (ICMAB-CSIC) in her PhD work [187] and in [196]. These previous studies, using a confocal fluorescence microscopy-based assay, revealed that by the TFH 800x1 route, Chol-CTAB vesicles with a low level of structural homogeneity were achieved due to the lipid demixing of cholesterol and CTAB and the formation of cholesterol-rich domains during film formation (Figure 2.53).

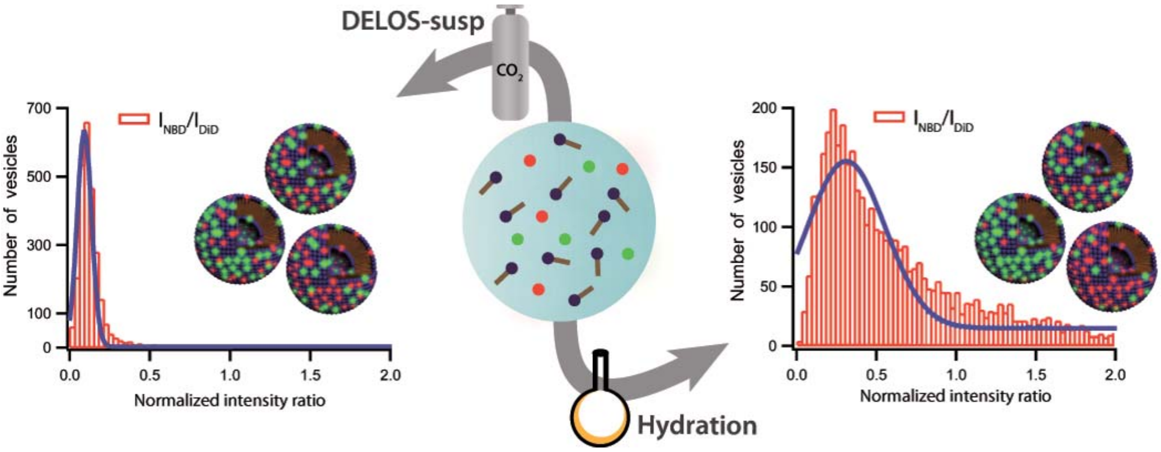

Figure 2.53.: Histograms of vesicular samples prepared by DELOS-SUSP (left) and the hydration method (right). In each histogram the distribution of the ratio of the two integrated intensities, I_{NBD}/I_{DiD}, of two dyes is represented. Each integrated intensity belongs to the NBD and DiD dyes that are located in the vesicle membrane and mimic their components. The I_{NBD}/I_{DiD} ratio should be constant if all the individual vesicles had the same membrane composition and identical supramolecular organization; so the narrower the distribution is, the higher the homogeneity in the supramolecular arrangement of lipids in the membranes. Adapted from [196].

In the present Thesis, it was thought to investigate the effect of reducing the pore size of the membrane filter of the extrusion step from 800 to 100 nm. This pore size reduction might break the cholesterol-rich domains formed during film formation and might help to form Chol-CTAB vesicles with higher level of structural homogeneity. As explained above, this pore size reduction was not enough to improve the structural homogeneity of the Chol-CTAB (W10Et) vesicles (TFH 100x1), and better results were obtained when the sample was passed through the extruder twenty-one times (TFH 100x21). Figure 2.54 shows a scheme of these obtained results and an example of the Chol-CTAB phase separation in the solvent-free state compared with a typical lipid thin film of a liposomal system, like Chol-DPPC.

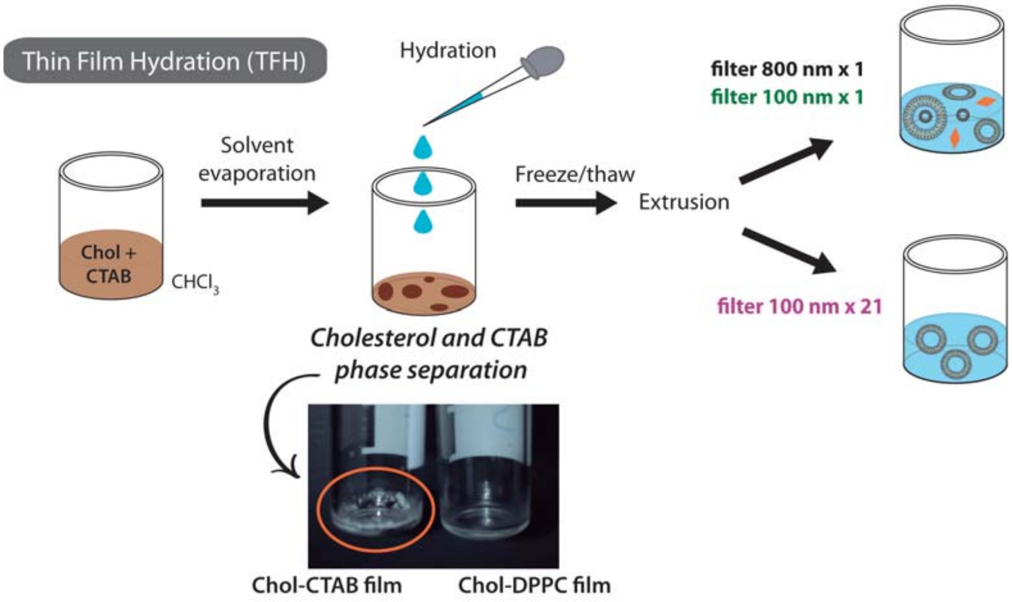

Figure 2.54.: Scheme of the Chol-CTAB (W10Et) vesicle preparation by Thin Film Hydration (TFH) using different extrusion protocols. Picture (bottom) showing an example the cholesterol and CTAB phase separation in the thin film formation compared with a typical Chol-DPPC lipid thin film of a liposomal system.

Therefore, it is clear that the preparation route of soft systems like Chol-CTAB (W10Et) quatsomes could be very critical regarding the final nanostructure due to the cholesterol hydrophobicity. Unilamellar and homogeneous Chol-CTAB (W10Et) quatsomes can be obtained using routes that maintain the membrane components in solution during vesicle preparation, such as DELOS-susp and sonication. In the case that the quatsome preparation method involves an intermediate solvent-free state, such as the TFH route where cholesterol and CTAB suffer a phase separation, vesicles with a low level of structural homogeneity are achieved (TFH 800x1 and TFH 100x1). In order to obtain homogeneous Chol-CTAB (W10Et) quatsomes by this route, a high mechanical energy has to be applied to break the formed cholesterol-rich domains extruding the sample twenty-one times (TFH 100x21).

We next explored the behavior of the obtained Chol-CTAB (W10Et) vesicular systems as function of temperature by SAXS. We studied the thermal stability of two opposite cases, vesicles with a high degree of homogeneity prepared by the DELOS-SUSP method, and vesicles with a low degree of homogeneity prepared by the TFH 800x1 route.

2.4.2.1. Thermal stability of Chol-CTAB (W10Et) vesicular systems prepared by different routes

The small-angle X-ray scattering (SAXS) technique was also used to check the vesicle thermal stability. Specifically, SAXS measurements of Chol-CTAB (W10Et) vesicles prepared by DELOS-SUSP and TFH 800x1 methods (Figure 2.48) were conducted at different temperatures.

The SAXS measurements of Chol-CTAB (W10Et-DELOS) quatsomes (Figure 2.55) were performed at the X33 beamline of the European Molecular Biology laboratory (EMBL, Hamburg, Germany) and were carried out at 298, 303, 308 and 313 K. As shown in Figure 2.55, the shape of the curves is retained in all the measurements. Therefore, it can be assumed that Chol-CTAB (W10Et) quatsomes prepared by DELOS-SUSP do not lose their spherical morphology with temperature at least up to 313 K.

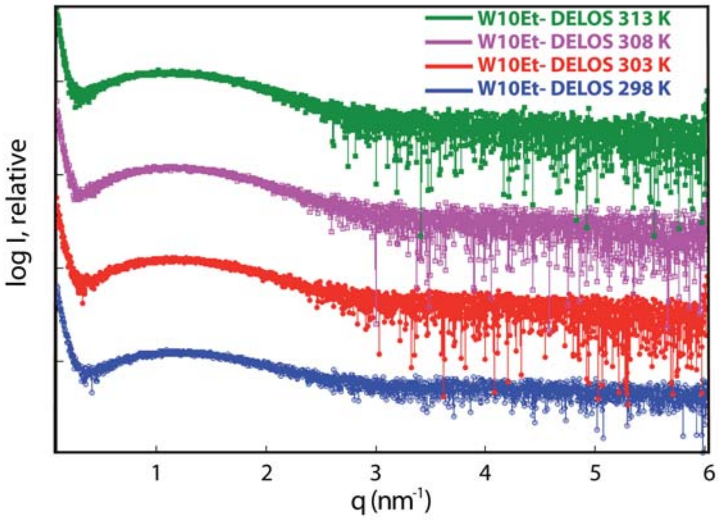

Figure 2.55.: SAXS curves of Chol-CTAB (W10Et-DELOS) quatsomes measured at 298, 303, 308 and 313 K. Data collected at X33 beamline at the EMBL.

The SAXS measurements as function of temperature of Chol-CTAB (W10Et-TFH800x1) vesicles were performed in the BM16 beamline of the European Synchrotron Radiation Facility (ESRF, Grenoble, France). These measurements were conducted at 298 and 313 K. As displayed in Figure 2.56, the high stability of Chol-CTAB quatsomes studied before is not maintained when this vesicle system is prepared by TFH 800x1 route. Bragg peaks at 0.58 and 1.26 nm^{-1} with a periodicity typical of planar lamellar phases *($q_1 = q_2/2$)* appeared at 313 K. This can be caused by a transition from mainly unilamellar vesicular structures at 298 K to large ordered membrane stacks in multilamellar vesicles at 313 K. Alternatively, it is also possible that the mainly unilamellar vesicular structures obtained at 298 K undergoes a phase transition into a planar lamellar phase at 313 K. In any case, this is an indication of the presence of unstable vesicular phases obtained by TFH 800x1 method.

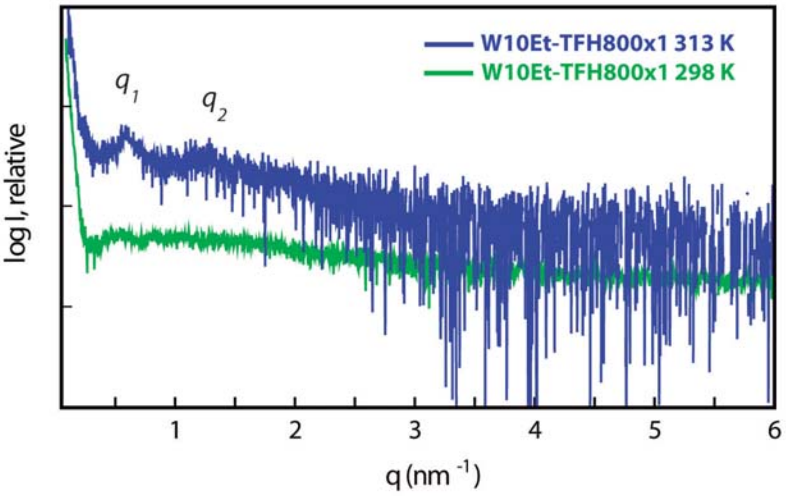

Figure 2.56.: SAXS curves of Chol-CTAB (W10Et-TFH800x1) vesicles measured at 298 and 313 K. Data collected at BM16 beamline at the ESRF.

The results evidenced that if the Chol-CTAB (W10Et) vesicles are homogeneous in size, spherically-shaped and unilamellar (SUVs), such the quatsomes obtained by DELOS-SUSP route (Figure 2.51), there is no variation in the vesicle membrane as function of temperature at least up to 313 K. However, if the vesicles present a low degree of structural homogeneity, as Chol-CTAB (W10Et) vesicles prepared by TFH 800x1 route, changes in the membrane are observed when heating the sample.

On the other hand, we have shown with this work that SAXS is a powerful tool for the characterization of vesicular systems able to give quantitative information of the relevant parameters that define the nanostructure of vesicular assemblies. These parameters would normally be inaccessible with microscopic experiments which provide only local information which cannot be quantitatively analyzed.

In summary, the findings of this work demonstrated that stable and homogeneous Chol-CTAB (W10Et) quatsomes can be prepared by several routes, such as DELOS-susp, sonication and TFH 100x21. Furthermore, it has been exposed that such homogeneous quatsomes present an outstanding stability against temperature, in contrast to systems with a low degree of structural homogeneity.

2.4.3. Summary

- It has been demonstrated that stable and homogeneous Chol-CTAB (W10Et) quatsomes can be prepared by several routes, such as DELOS-susp, sonication and TFH 100x21 (Figure 2.57).

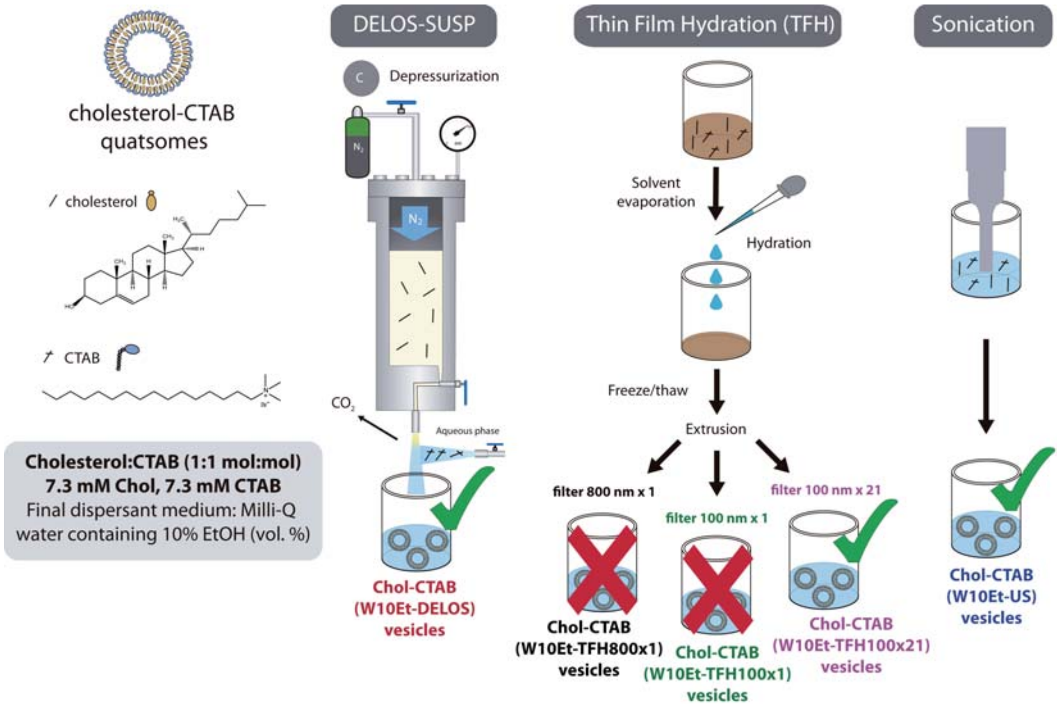

Figure 2.57.: Preparation routes to obtain stable and homogeneous Chol-CTAB (W10Et) quatsomes.

- Preparation routes, which go trough solvent-free states where solid cholesterol is formed, do not yield stable homogeneous quatsomes, unless a high mechanical energy is applied.

2.5. Preparation of quatsome-like vesicles using components alternative to Chol-CTAB

It is well known that free CTAB has a certain degree of toxicity since this cationic surfactant molecule can kill cells. Recent studies state that CTAB acts by two active mechanisms: i) direct interaction with the phospholipid bilayer that destabilizes the cell membrane, leading to cell death; and ii) catalytic action of CTAB's dissociation products, which might cause the quenching of the enzyme ATP synthase and thus lead to energy deprivation and cellular death [197]. Although CTAB could be toxic, it is important to recall that this toxicity depends on the assembling of this molecule, i.e. CTAB in monomers (free), micelles and vesicles could have different degrees of toxicity. For that reason, at present studies comparing these values are being performed by other members of *Nanomol* group.

In this Thesis, we studied the formation of quatsome-like structures using single-chain amphiphile molecules alternative to CTAB and other sterols than cholesterol by DELOS-susp (see Section 6.2.1 of the Experimental Part). Molecules approved by the U.S. Food and Drug Administration (FDA) and with current use in medical applications [198] were attempted to use.

2.5.1. Single-chain amphiphile molecules other than CTAB

The molecular dynamics simulations of the Chol-CTAB synthon described in Section 2.2.3 have shown that the size and the shape of the CTAB molecule are important parameters in order to build the specific synthon with cholesterol to form bilayers. Then, in this Section the formation of vesicles with mixtures of cholesterol and single-chain amphiphile molecules with similar structure to CTAB was investigated.

In Table 2.15, the candidate molecules studied to replace the CTAB in the formation of vesicles are given. In this study neutral molecules, anionic molecules and cationic molecules were used. Moreover Table 2.15 gives the possible routes of administration of such compounds based in previously FDA registered formulations using these molecules [198], and their structuration in water. In Figure 2.59 are depicted all the candidate molecules.

In order to form these new vesicle formulations, DELOS-SUSP method (Figure 2.58 and see Section 6.2.1 of the Experimental Part) was employed obtaining vesicles in water with 10% of EtOH (vol. %). Unless explicitly indicated, the method consisted in the loading of the 7.5 ml high-pressure autoclave with a solution containing 76 mg of cholesterol in 2.88 ml of ethanol. The solution was then pressurized with compressed CO_2 at a molar fraction of X_{CO_2}= 0.6 until reaching a working pressure of 10 MPa, which produced a volumetric expanded organic solution of cholesterol. Finally, the expanded organic phase was depressurized over an aqueous solution (24 ml) containing one of the new single-chain amphiphile molecules (Figure 2.59 and Table 2.15) at a concentration over its critical micellar concentration (cmc). For Chol-CTAB (W10Et-DELOS) quatsomes, vesicles are formed after depressurization, consequently the characterization of the new formulation systems was carried out in this stage. If the single-chain amphiphile molecule used was insoluble in water, it was added in the organic solution of the high-pressure autoclave. If possible experimentally, equimolar ratios between surfactant and sterol were used for the preparation of quatsome-like systems with a final concentration of 7.3 mM. All the obtained samples were stored at 277 K.

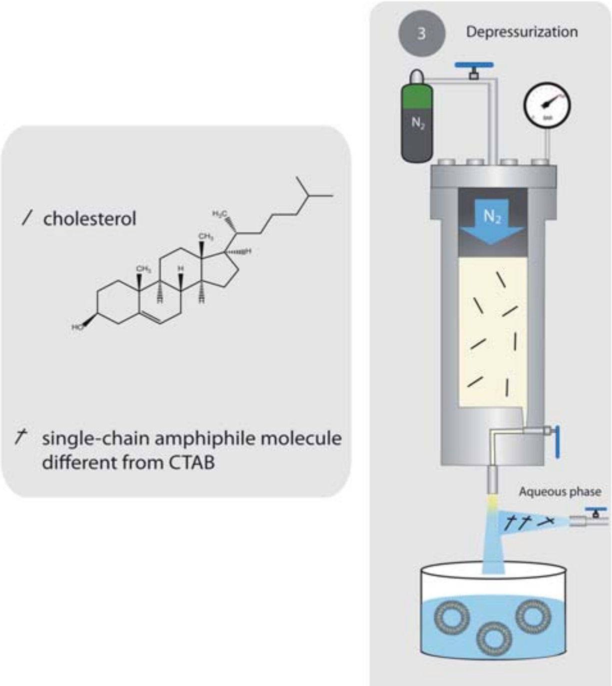

Figure 2.58.: Schematic representation of the DELOS-SUSP method to obtain new quatsome-like systems using cholesterol and single-chain amphiphile molecules other than CTAB presented in Table 2.15. If the single-chain amphiphile molecule used was insoluble in water, the compound was added in the organic solution together with cholesterol.

The mean and polydispersity index (PdI) of the particle size distributions measured by DLS for every measurable sample are presented in Table 2.16, including information regarding the morphology of the vesicular formulations analyzed by cryo-TEM. The stability of each vesicular system is described through the Z-potential values (see

Table 2.15.: Candidate molecules alternative to CTAB for the formation of quatsome-like vesicles [198–202].

Molecule	Chemical formula	Route of [a] administration	Phase in water
Neutral single-chain amphiphile molecules			
Myristic acid	$NaC_{12}H_{25}SO_4$	Oral	Water-insoluble
N-(2-(2-(vinylsulfonyl) ethoxy)ethyl) dodecanamide (VS-1)	$C_{18}H_{35}NO_4S$	Not studied, lauric acid derivative	Water-insoluble
N-(2-(2-(vinylsulfonyl) ethoxy)ethyl) oleamide (VS-2)	$C_{24}H_{45}NO_4S$	Not studied, oleic acid derivative	Water-insoluble
1-(vinylsulfonyl) octadecane (VS-3)	$C_{20}H_{40}O_2S$	Not studied	Water-insoluble
Anionic single-chain amphiphile molecules			
Sodium dodecyl sulfate (SDS)	$C_{14}H_{28}O_{12}$	Buccal/sublingual, dental,oral, topical, vaginal	Micelles
Cationic single-chain amphiphile molecules			
Myristalkonium chloride (MKC)	$C_{23}H_{42}ClN$	Intravenous, intramuscular, nasal, oral, topical	Micelles
Cetylpyridinium chloride (CPC)	$C_{21}H_{38}ClN$	Oral, inhalation, topical	Micelles

[a] Possible routes of administration of such compounds based in previously FDA registered formulations using these molecules.

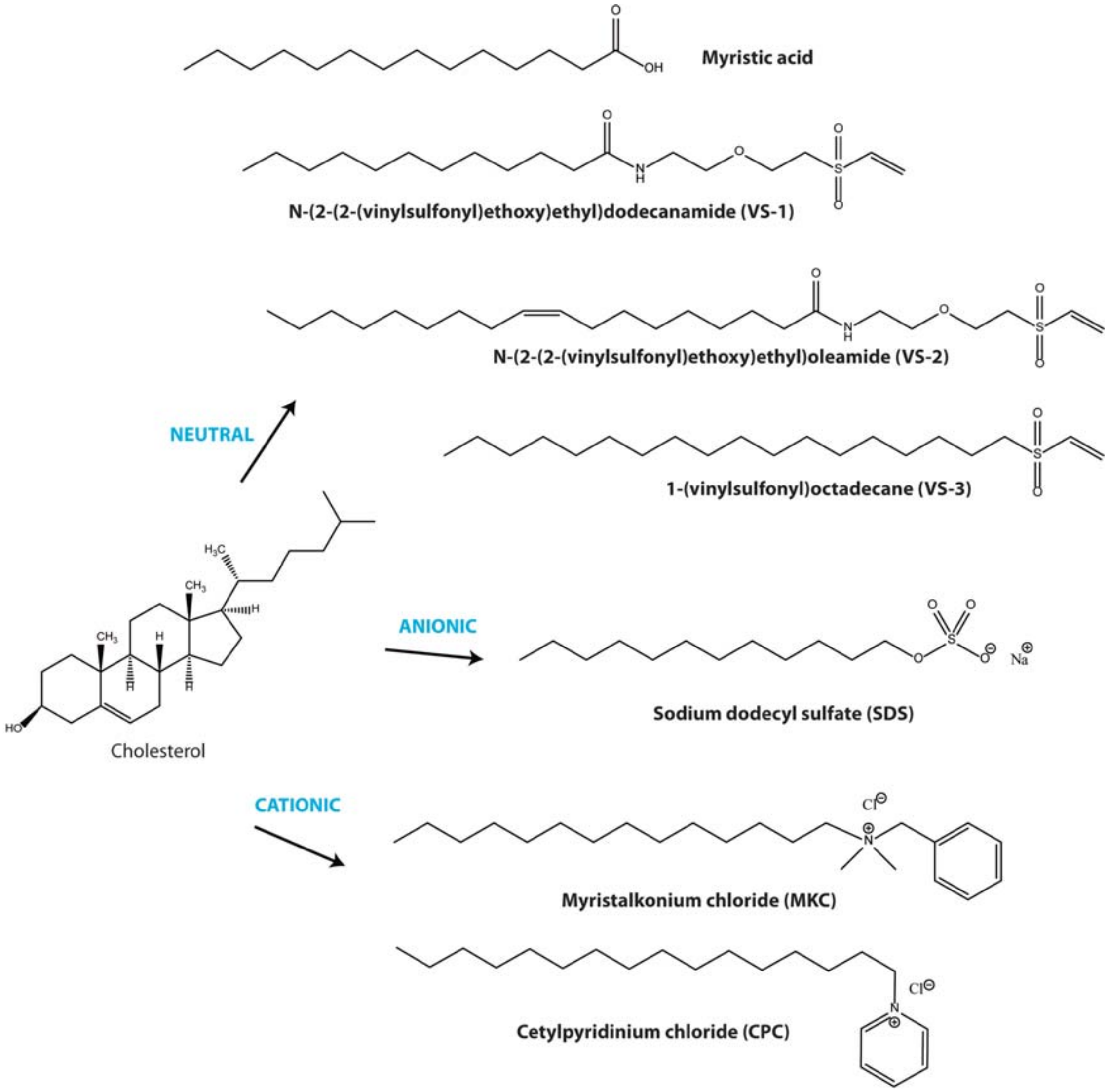

Figure 2.59.: Molecular structure of the single-chain amphiphile molecules used for the formation of quatsome-like structures with cholesterol.

Table 2.16.: Physicochemical characteristics of the different quatsome-like vesicular structures prepared by DELOS-SUSP method.

Quatsome-like[a] structure	Molar ratio	Size Mean(nm)[b]	Size PdI[c]	Stability Z-pot.(mV)	Morpho.[d]
Chol:CTAB:VS-1	(5:4:1)	61.26 ± 0.36	0.133 ± 0.017	151 ±5	SUVs
Chol:CTAB:VS-2	(5:4:1)	72.87± 0.38	0.102 ± 0.008	142 ±3	SUVs
Chol:SDS	(1:2)	146.1 ± 3.5	0.307 ± 0.004	-139 ± 5	SUVs
Chol:MKC	(1:1)	114.3 ± 5.6	0.507 ± 0.076	104 ± 5	distorted vesicles
Chol:MKC	(1:2)	52.77 ± 0.56	0.171 ± 0.004	109 ± 3	SUVs
Chol:CPC	(1:1)	137.1 ± 9.8	0.389 ± 0.070	129 ± 2	distorted vesicles
Chol:CPC	(1:2)	62.67 ± 0.50	0.152 ± 0.004	121 ± 4	SUVs

[a] Samples were stored at 277 K.

[b] Intensity weighted mean hydrodynamic size of the collection of vesicles measured by dynamic light scattering.

[c] Polidispersity index showing the width of the particle size distribution.

[d] Morphology of the vesicles observed by cryo-TEM. SUVs: Small unilamellar vesicles.

Table 2.16).

2.5.1.1. Use of neutral molecules

The production of quatsome-like structures was attempted using myristic acid (Table 2.15 and Figure 2.59) and cholesterol. Myristic acid has a low solubility in water (20 mg/L at 293 K), and consequently this compound does not form micelles in aqueous environments. Due to this low water solubility, the preparation of vesicles using DELOS-SUSP method was carried out dissolving both membrane components at equimolar ratio (76 mg cholesterol and 45 mg myristic acid) in ethanol and adding this organic solution inside the reactor (see Figure 2.58). The depressurization of the expanded solution over an aqueous phase gave a colloidal suspension like the one shown in Figure 2.60a. The macroscopic appearance did not show the typical translucent aqueous system obtained for vesicular colloidal systems. Instead, a white opalescent suspension was obtained with a large amount of aggregate solid.

The optical microscopy images (Section 6.3.7 of the Experimental Part) reveal solid aggregates of several microns in size. The presence of these structures indicates that the formation of vesicles is unlikely, therefore the formation of vesicles by DELOS-SUSP using myristic acid was discarded.

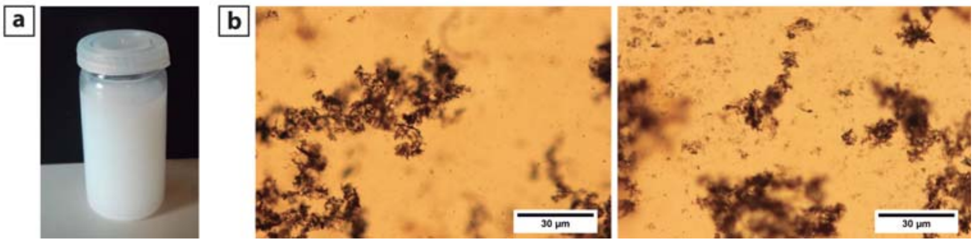

Figure 2.60.: (a) Photograph showing the macroscopic aspect of the sample performed at 1:1 Chol:Myristic acid molar ratio prepared by DELOS-SUSP. (b) Optical microscopy images of such sample.

In a second approach, we used neutral fatty acids derivatives to produce quatsome-like vesicular structures by DELOS-SUSP. The fatty acids derivatives molecules were synthesized by the group of Prof. Francisco Santoyo from the University of Granada [202] and are presented in Table 2.15 and Figure 2.59 (see Section 6.9 of the Experimental Part for synthesis and characterization of such compounds). All these molecules comprise a molecule of lipid nature and a vinyl sulphone group. Since these neutral molecules were insoluble in water, they were solubilized in the ethanolic phase together with cholesterol, instead of being dissolved in the aqueous phase (see Figure 2.58).

First of all, we tried to produce vesicles using an equimolar ratio between cholesterol and the lauric acid derivative (VS-1) (76 mg cholesterol, 71 mg lauric acid derivative), but a suspension with a large amount of aggregate solid was obtained (Figure 2.61a). In order to incorporate some lauric acid derivative molecules (VS-1) in the quatsome membrane, a new strategy was carried out by using a combination of CTAB and VS-1 at 4:1 CTAB:VS-1 molar ratio, to self-assemble with cholesterol and form the bilayer. This new experiment was performed at 5:4:1 cholesterol:CTAB:VS-1 molar ratio and yielded a translucent stable aqueous system (Figure 2.61b). The resulting vesicles presented sizes with values around 61 nm when measured by DLS (Figure 2.61b and Table 2.16), and homogeneous vesicle population as indicated by its small polydispersity index. Furthermore, the obtained Z-potential value around 151 mV indicate that these vesicles have an excellent stability along time. The morphology of the sample, studied through the cryo-TEM images (Figure 2.61b), demonstrated homogeneous, spherically-shaped and unilamellar nanovesicles. These results suggest that part of CTAB can be replaced by

VS-1 for the formation of homogeneous quatsome-like vesicular structures with cholesterol.

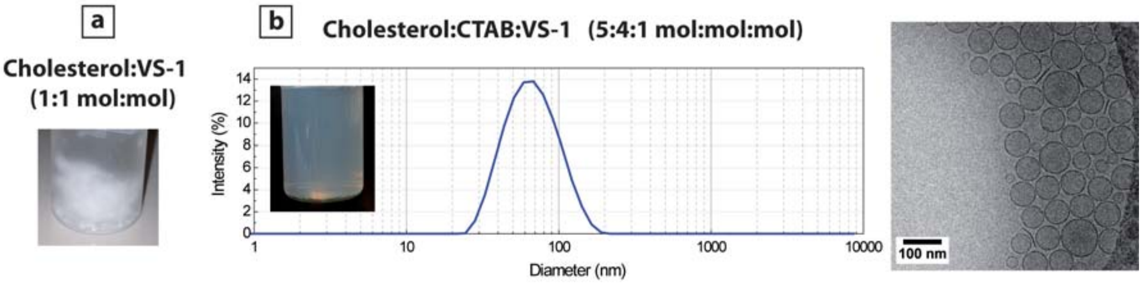

Figure 2.61.: (a) Photograph showing the macroscopic aspect of the suspension at 1:1 cholesterol:lauric acid derivative (VS-1) molar ratio. (b) Particle size distribution (left) and cryo-TEM image (right) corresponding to vesicles obtained at 5:4:1 cholesterol:CTAB:lauric acid derivative (VS-1) molar ratio by DELOS-SUSP. Insert: Photograph showing the macroscopic aspect of the suspension.

Taking into account this excellent result, the same strategy for the other two fatty acids derivatives molecules, the oleic acid derivative (VS-2) and the 1-(vinylsulfonyl)octadecane (VS-3), was carried out. The new experiments were performed at 5:4:1 cholesterol:CTAB:VS-2 molar ratio and at 5:4:1 cholesterol:CTAB:VS-3 molar ratio. As shown in Figure 2.62, DLS measurements and cryo-TEM revealed that vesicles obtained using VS-2 were homogeneous, spherically-shaped and unilamellar, so part of CTAB can also be replaced by VS-2 for the formation of homogeneous quatsome-like vesicular structures with cholesterol. By contrast, the suspension obtained using VS-3 was heterogeneous and size measurements did not meet DLS quality criteria because of high polydispersity and presence of large aggregates. Cryo-TEM pictures (Figure 2.63) revealed these large aggregates, consequently VS-3 could not be incorporated into quatsome membrane and it tended to precipitate.

It has to be noted that these results using neutral fatty acids derivatives should be considered a preliminary step, further studies using other molar proportions will be conducted soon.

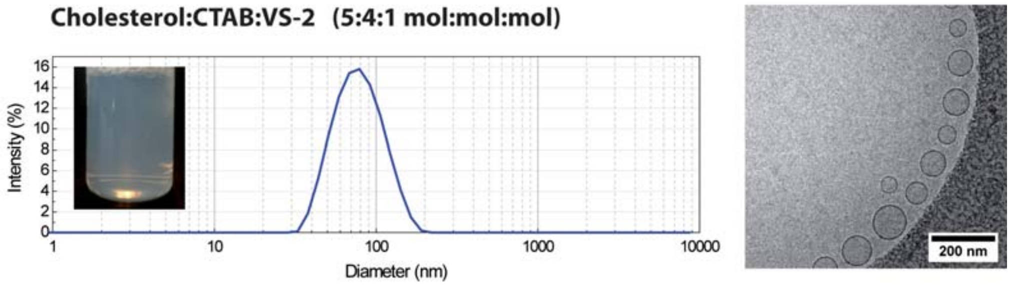

Figure 2.62.: Particle size distribution (left) and cryo-TEM image (right) corresponding to vesicles obtained at 5:4:1 cholesterol:CTAB:oleic acid derivative (VS-2) molar ratio by DELOS-SUSP. Insert: Photograph showing the macroscopic aspect of the suspension.

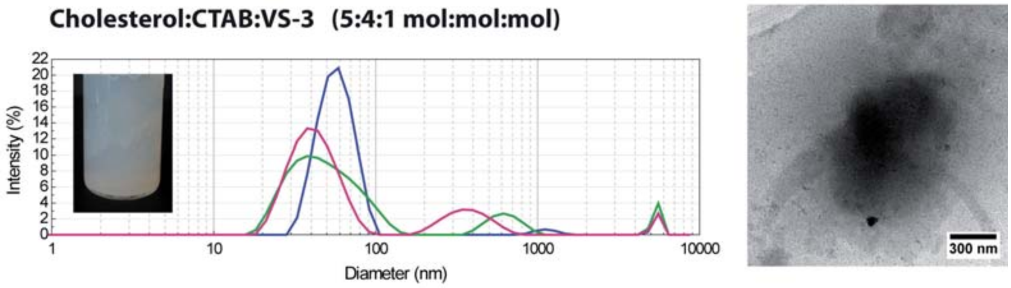

Figure 2.63.: Particle size distribution (left) and cryo-TEM image (right) corresponding to systems obtained at 5:4:1 cholesterol:CTAB:VS-3 molar ratio by DELOS-SUSP. DLS measurements did not meet quality criteria because of high polydispersity and presence of large aggregates. Insert: Photograph showing the macroscopic aspect of the suspension.

2.5.1.2. Use of anionic molecules

Surface charge of vesicles is related to biological behaviors of these systems, such as tissue diffusing, biodistribution, cell uptake, cytotoxicity, and protein binding [203]. Electrostatic interaction between vesicles and cells is very important in applications such as gene delivery, cell uptake enhancing, and endosome escaping [204]. Although cationic vesicles with positive charge appears to improve the efficacy of imaging, gene transfer, and drug delivery [205, 206], a general disadvantage of these vesicles is that they can cause cytotoxicity both *in vitro* and *in vivo* [204, 207, 208]. Due to this fact, anionic vesicles with negative charge can be an alternative to cationic vesicles [209].

In this context, we tried to produce quatsome-like vesicles using an anionic molecule, such as sodium dodecyl sulfate (SDS) (Table 2.15 and Figure 2.59).

The critical micelle concentration of SDS at 298 K is 8 mM (8 times higher than the cmc of CTAB). Keeping constant the amount of cholesterol in the reactor (76 mg), it cannot be used an equimolar proportion of cholesterol and SDS since the final SDS concentration is below the cmc and micelles cannot be formed. In order to dispose of

SDS micelles in the aqueous phase, the experiment was performed at 1:2 cholesterol:SDS molar ratio (113 mg SDS, 14.6 mM). As shown in the insert of Figure 2.64, this experiment yielded a translucent stable aqueous system. The cryo-TEM images (Figure 2.64) demonstrated that the obtained aqueous system was constituted by nanoscopic unilamellar vesicles with two different sizes. These two population of vesicles are also observed in DLS measurements (Figure 2.64 and Table 2.16), where is presented a bimodal size distribution centred in an average size of 60 nm and 120 nm. The Z-potential value (Table 2.16) high and negative is an indicative of a good stability along time. Although further phase behavior analysis of Chol-SDS system is required, these results show the potential of the DELOS-SUSP process for the one-step production of quatsomes using anionic single-chain amphiphile molecules and cholesterol. Furthermore, it is worth mentioning that SDS is used in FDA approved buccal/sublingual, dental, oral, topical and vaginal pharmaceutical formulations, so Chol-SDS (W10Et-DELOS) quatsomes (Table 6.3 of the Experimental Part) can be obtained by DELOS-SUSP if quatsomes with negative charge are required for biomedical applications.

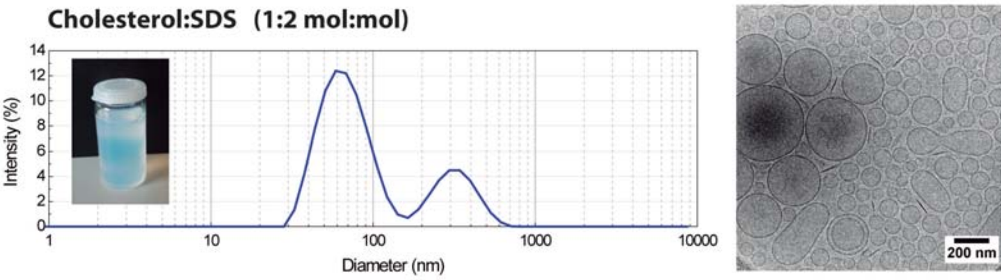

Figure 2.64.: Particle size distribution (left) and cryo-TEM image (right) corresponding to vesicles obtained at 1:2 cholesterol:SDS molar ratio by DELOS-SUSP. Insert: Photograph showing the macroscopic aspect of the suspension.

It is worthy to remark that the formation of cholesterol-SDS quatsomes using our sonication methodology published in [177] was also studied by Ghosh *et al.* [210]. They reported the formation of unilamellar vesicles using equimolar proportions of cholesterol and SDS (20 mM) in aqueous solutions.

2.5.1.3. Use of cationic molecules

Cationic liposomes are being used as gene vectors to successfully transfect a variety of mammalian cell types *in vitro* and *in vivo*; the ability to form desirable electrostatic interactions with DNA [211] makes them effective gene transfer vehicles [205, 206].

Besides, cationic liposomes have emerged as a novel adjuvant and antigen delivery system to enhance vaccine efficacy [212].

Within this framework, the formation of quatsome-like vesicles using cationic molecules was investigated. Specifically, quaternary ammonium surfactant molecules such as myristalkonium chloride (MKC) and cetylpyridinium chloride (CPC) (Table 2.15 and Figure 2.59) were used. Regarding medical applications, it is worth highlighting that MKC is used in FDA approved intravenous, intramuscular, nasal, oral and topical pharmaceutical formulations, and CPC in oral, inhaled and topical pharmaceutical formulations, therefore these new molecules can extend the use of quatsomes for the development of a large variety of nanomedicines.

Keeping constant the amount of cholesterol in the reactor (76 mg), and taking into account that surfactant micelles should be formed in the aqueous phase (cmc below 7.3 mM), DELOS-SUSP experiments working at equimolar proportion between cholesterol and these cationic surfactants were possible to perform (the cmc at 298 K is 2.16 mM for MKC and 0.98 mM for CPC [200]). Thus, we investigated the preparation of cholesterol:MKC (72 mg MKC, 7.3 mM) (Figure 2.65) and cholesterol:CPC (70 mg CPC, 7.3 mM) (Figure 2.66) vesicles by DELOS-SUSP in the same way used to form Chol-CTAB (W10Et-DELOS) quatsomes.

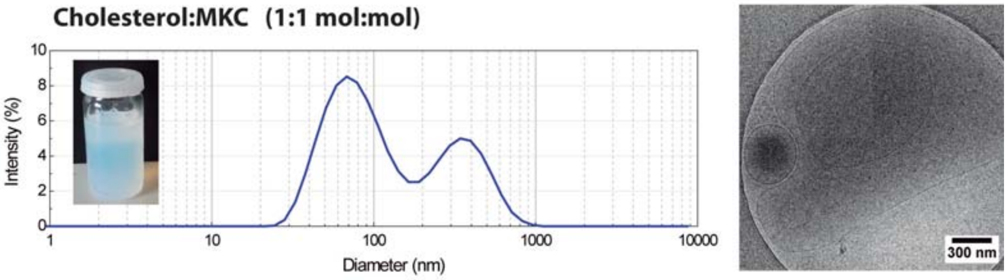

Figure 2.65.: Particle size distribution (left) and cryo-TEM image (right) corresponding to vesicles obtained at 1:1 cholesterol:MKC molar ratio by DELOS-SUSP. Insert: Photograph showing the macroscopic aspect of the suspension.

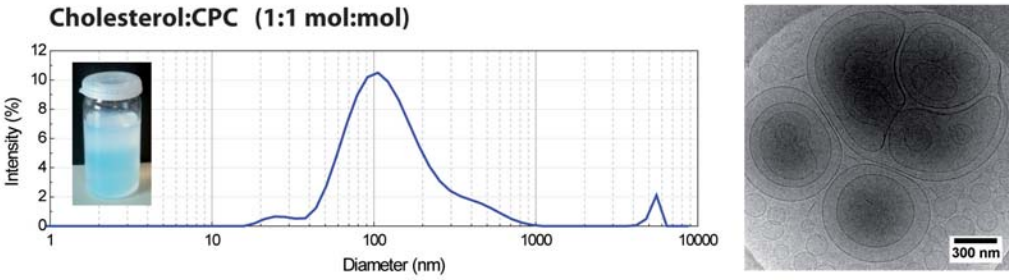

Figure 2.66.: Particle size distribution (left) and cryo-TEM image (right) corresponding to vesicles obtained at 1:1 cholesterol:CPC molar ratio by DELOS-SUSP. Insert: Photograph showing the macroscopic aspect of the suspension.

In both cases, the DELOS-SUSP experiment yielded a translucent stable aqueous system (Figure 2.65 and Figure 2.66). Although the high Z-potential value (Table 2.16) is an indicative of a good stability along time for both systems, dynamic light scattering (DLS) measurements and cryo-TEM showed the formation of non-homogeneous vesicles (Figure 2.65, Figure 2.66 and Table 2.16).

Taking into account that MKC and CPC are quaternary ammonium surfactant molecules like CTAB, and considering the previous Chol-CTAB sonication study performed at the beginning of this Chapter (Figure 2.6) where non-homogeneous vesicles were obtained with an excess of cholesterol in the system, DELOS-SUSP experiments were conducted decreasing the amount of cholesterol. Specifically, the production of small unilamellar vesicles was studied at 1:2 cholesterol:surfactant molar ratio. In both experiments, the amount of cholesterol was reduced to the half of its initial value (38 mg) and the concentration of the cationic surfactants was kept at 7.3 mM.

The characterization of the obtained sample at 1:2 Chol:MKC molar ratio is shown in Figure 2.67. As can be observed, the formation of vesicles was achieved. Indeed, dynamic light scattering (DLS) measurements and cryo-TEM images revealed that these nanovesicles were homogeneous, spherically-shaped and unilamellar (Figure 2.67 and Table 2.16). Furthermore, the Z-potential value given in Table 2.16 indicated that these quatsomes have an excellent stability along time.

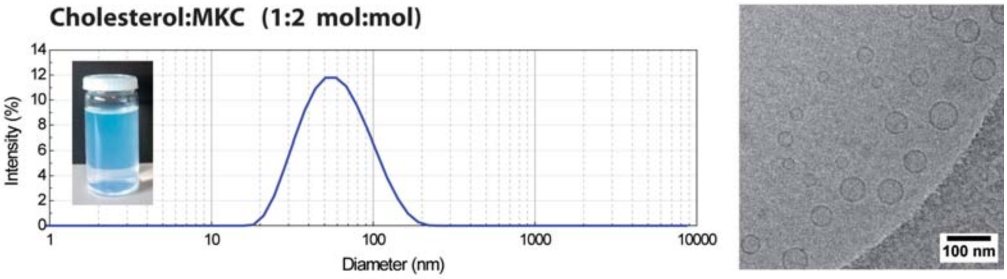

Figure 2.67.: Particle size distribution (left) and cryo-TEM image (right) corresponding to quatsomes obtained at 1:2 cholesterol:MKC molar ratio by DELOS-SUSP. Insert: Photograph showing the macroscopic aspect of the suspension.

On the other hand, the characterization of the obtained sample at 1:2 Chol:CPC molar ratio is shown in Figure 2.68. Cryo-TEM images demonstrated that the obtained aqueous system was constituted by spherically-shaped and unilamellar nanoscopic vesicles. DLS measurements (Figure 2.68 and Table 2.16) showed that these nanoscopic vesicles presented an unimodal size distribution centred in an average size of 63 nm and the Z-potential value (Table 2.16) high and positive is an indicative of a good stability along time.

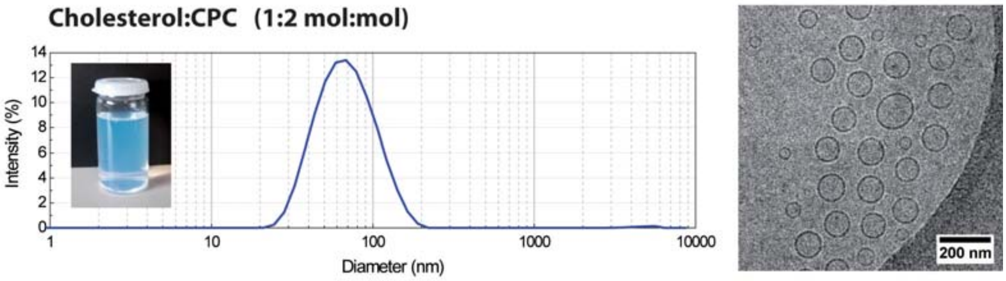

Figure 2.68.: Particle size distribution (left) and cryo-TEM image (right) corresponding to quatsomes obtained at 1:2 cholesterol:CPC molar ratio by DELOS-SUSP. Insert: Photograph showing the macroscopic aspect of the suspension.

Therefore, quatsomes with positive charge different from Chol-CTAB can be obtained using mixtures of cholesterol and MKC and cholesterol and CPC. These new cationic vesicles have been called Chol-MKC and Chol-CPC (W10Et-DELOS) quatsomes (see Table 6.3 of the Experimental Part). It is worth mentioning that these new formulations produced homogeneous vesicles in size and morphology and widely accepted. Additionally, these systems are synthesized by a method that allows the encapsulation of drugs in an easy way.

On the other hand, it is worth highlighting that the formation of cationic quatsomes using our sonication methodology published in [177] was also studied by other investigation groups. Specifically, it has been published the formation of cationic quatsomes using mixtures of benzyldimethylhexadecylammonium chloride (BHDC) and cholesterol [213]; 1-hexadecyl-3-methylimidazolium chloride ([C_{16}mim]Cl) and cholesterol [213]; tetradecyltrimethylammonium bromide (TTAB) and cholesterol [214] and CPC and cholesterol [215].

2.5.2. Sterol other than cholesterol

In this Section, we investigated the formation of quatsome-like structures using the plant sterol β-sitosterol instead of cholesterol by DELOS-SUSP (Figure 2.69). In this experiment, an equimolar ratio between β-sitosterol and CTAB was used with a final concentration of 7.3 mM.

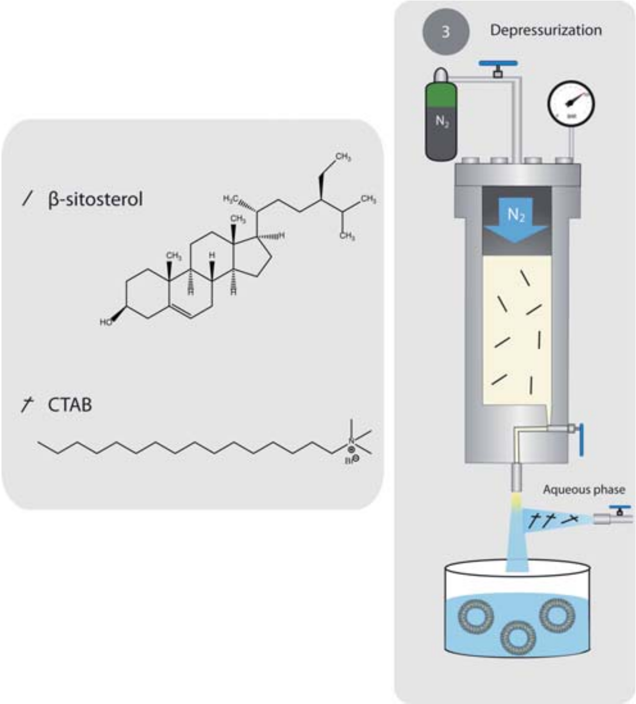

Figure 2.69.: DELOS-SUSP method to obtain new quatsome-like structures using β-sitosterol and CTAB.

Briefly, using the equipment and the procedure described in Section 6.2.1 of the Experimental Part, the method consisted in the loading of the 7.5 ml high-pressure autoclave with a solution containing 82 mg of β-sitosterol in 2.88 ml of ethanol. The solution was then pressurized with CO_2 at a molar fraction of $X_{CO_2}= 0.6$ until reaching a working pressure of 10 MPa, which produced a volumetric expanded organic solution of β-sitosterol. Finally, the expanded organic phase was depressurized over 24 ml of an aqueous solution containing 72 mg of CTAB at a concentration over its critical micellar concentration (cmc). After this stage, the resulting sample was characterized. Its size distribution, polydispersity index and Z-potential were determined using the dynamic light scattering (DLS) equipment and these values are given in Figure 2.70.

The DLS measurements of these vesicles revealed a mean size of 152.5 ± 2.4 nm (PdI 0.277 ± 0.016). Besides, the obtained Z-potential value larger than + 30 mV indicate that these quatsomes have an excellent stability along time. The morphology of this sample, studied through the cryo-TEM images, showed homogeneous, spherically-shaped and unilamellar nanovesicles (Figure 2.70). Thus, β-sitosterol-CTAB (W10Et-DELOS) quatsomes (Table 6.3 of the Experimental Part) can be prepared using DELOS-SUSP.

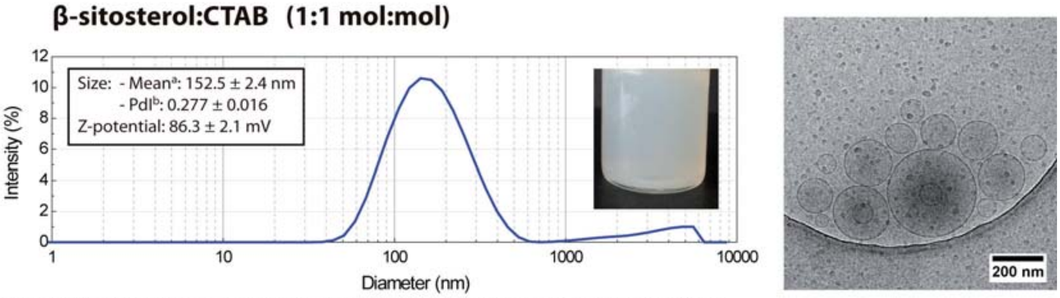

[a] Intensity weighted mean hydrodynamic size of the collection of vesicles measured by dynamic light scattering.
[b] Polidispersity index showing the width of the particle size distribution.

Figure 2.70.: Physicochemical characteristics (left) and cryo-TEM image (right) of β-sitosterol:CTAB quatsomes at equimolar ratio prepared by the DELOS-SUSP method. Sample was stored at 277 K.

Therefore, all these excellent results show the potential of the DELOS-SUSP process for the one-step production of quatsome-like structures alternative to cholesterol-CTAB, allowing to extend the use of quatsomes in nanomedicine.

2.5.3. Summary

- The same synergy observed for cholesterol and CTAB to form vesicular structures has been observed for other mixtures of sterols and ionic surfactants. Specifically, it has been shown that quatsome-like structures might be formed using mixtures of cholesterol with SDS, an anionic surfactant, and with MKC and CPC, cationic surfactants. Furthermore, quatsomes using an equimolar ratio between β-sitosterol and CTAB were achieved. These new formulations can extend the use of quatsomes to many applications in nanomedicine.

- Part of CTAB in Chol-CTAB (W10Et-DELOS) quatsomes can be replaced by neutral fatty acids derivatives for the formation of homogeneous quatsome-like vesicular structures.

2.6. Scaling-up production of Chol-CTAB quatsomes using DELOS-SUSP

While the use of vesicles as models of biomembranes is confined to the research laboratory, their successful application in the entrapment and delivery of bioactive agents will depend not only on a demonstration of the superiority of the vesicle carrier for the intended purpose, but also upon technical and economic feasibility of the vesicular formulation [216]. Despite all the existing methodologies for vesicle manufacturing at labscale, only a very few liposomal products have reached the pharmaceutical market. Among the reasons that prevent a wider use of these systems for human benefit, the low reproducibility, the inefficient drug entrapment and the high cost and difficulty of upscaling the production, are perhaps the more important ones. An ideal methodology for producing vesicles at industrial scale would be one that allows obtaining vesicle formulations with suitable and batch-to-batch reproducible characteristics, involving a minimum number of steps and equipment, and also meeting the requirements of the pharmaceutical industry and the good manufacturing practices (GMP). Reproducibility under scaling-up has been checked to evaluate the potentiality of the DELOS-SUSP as a platform for the production of nanovesicles that provides sufficient quantities for clinical studies of potential nanomedicines. The production of Chol-CTAB (W10Et-DELOS) quatsomes was repeated under the same experimental conditions explained in Section 6.2.1 of the Experimental Part but in a 40-fold larger high pressure reactor (from 7.5 ml to 315 ml) using the same equipment configuration with minor modifications in the automation procedure. For the scale-up experiments the cholesterol was dissolved in ethanol and introduced in the reactor already warmed at 308 K. After 15 min of thermal equilibration, CO_2 was introduced to achieve the desired working pressure and molar ratio of CO_2 (X_{CO_2}= 0.6). After 45 min, the CO_2-expanded solution was depressurized through a one-way automatic valve into a T mixer, to an aqueous solution containing CTAB, pumped at 900 ml/min. Details of the experimental procedure and the equipment configuration are given in Section 6.2.1.2 of the Experimental Part. With this scale-up the batch volume of the resulting vesicle suspension was increased from milliliter up to liter scale, which could allow the production of vesicle batches to be used in pre-clinical and even clinical studies when the process is performed under GMPs. The influence of DELOS-SUSP scale-up on the physicochemical characteristics of the quatsomes was analyzed in terms of size and morphology. The results are reported in Table 2.17 and Figure 2.71 together with the results obtained in the small scale reactor for comparison.

Table 2.17.: Physicochemical characteristics of Chol-CTAB (W10Et-DELOS) quatsomes obtained with different reactors.

Quatsome[a]	**Size**		**Stability**	**Morphology[d]**
sample	**Mean(nm)[b]**	**PdI[c]**	**Z-pot.(mV)**	
Small scale reactor	73.47 ± 0.94	0.262 ± 0.006	110 ±6	SUVs
Large scale reactor	72.19 ± 0.76	0.292 ± 0.008	88.9 ±3.6	SUVs

[a] Quatsomes analyzed 14 days after sample preparation. Samples were stored at 277 K.

[b] Intensity weighted mean hydrodynamic size of the collection of vesicles measured by dynamic light scattering.

[c] Polidispersity index showing the width of the particle size distribution.

[d] Morphology of the vesicles observed by cryo-TEM. SUVs: Small unilamellar vesicles.

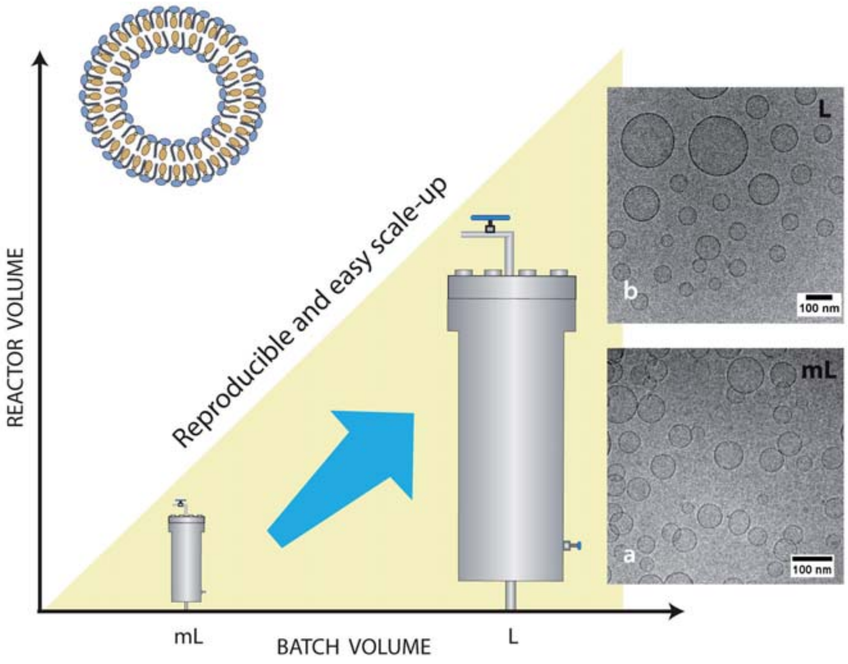

Figure 2.71.: Scale-up of DELOS-SUSP method for the production of Chol-CTAB (W10Et-DELOS) quatsomes in water using both a small (7.5 ml) and a large (315 ml) high pressure reactors. Cryo-TEM images of quatsomes obtained with (a) the small scale and (b) the large scale.

As observed in Table 2.17, both reactors (7.5 ml and 315 ml) produced vesicles with similar physicochemical characteristics. Besides, in the case of the large reactor, the manual depressurization valve was substituted for an automatic depressurization valve that allows a better operational control and hence a higher vesicle homogeneity and batch-to-batch reproducibility (Experimental Section 6.2.1.3). Cryo-TEM images of quatsomes produced using the large scale reactor show unilamellar and spherical nanovesicles confirming the great degree of homogeneity achieved (Figure 2.71). Moreover it is important to highlight here that DELOS-SUSP operates under sterile conditions due to the use of compressed CO_2, which is another important issue in the manufacturing of vesicles for human and animal use. The good reproducibility in terms of physicochemical characteristics between batches produced with the two reactors, demonstrate the feasibility of scaling-up the DELOS-SUSP method for the production of quatsome based vesicular systems.

2.6.1. Summary

- The possibility of scaling-up the method for the preparation of quatsome-like structures was demonstrated by the good reproducibility in terms of physicochemical characteristics between batches of Chol-CTAB (W10Et-DELOS) quatsomes with both, a mL scale reactor and a L scale reactor.

2.7. Quatsomes as potential drug nanocarriers

Development of drug delivery systems to improve disease-specific targeting, to control drug release rates and/or to produce a pharmaceutical formulation suitable for clinical use is desirable. One of the strategies has been encapsulation of the active substance(s) in the aqueous phase of a vesicle, or incorporation or binding to the membrane components [217]. The precise definition of relevant physicochemical properties of a vesicle-based delivery systems is critical to ensure its quality, and the pharmacological properties strongly depend on the structural characteristics of the conjugates. The European Medicines Agency described in [217] the general parameters that should be defined for the approval of a vesicular pharmaceutical formulation.

The evidence presented in this Chapter suggests that quatsomes constitute an attractive alternative to conventional liposomes. Using Chol-CTAB quatsomes as a quatsome model, we have observed that such new vesicular structures show an outstanding stability along time, since they can be stored for more than three years without any change in their physicochemical properties. Furthermore these colloidal objects remain stable with temperature changes and upon dilution, contrary to surfactant micelles whose structures are strongly affected by these two parameters [218]. In addition, Chol-CTAB quatsomes have full recovery after lyophilisation. Moreover the unilamellarity of quatsome-like structures and their homogeneous morphology makes these systems ideal for the precise functionalization of their membranes, which is very important for a robust and efficient drug targeting [44, 219, 220]. Another important characteristic of quatsomes is that their membrane components are not expensive and are available at a pharmaceutical grade. For instance, the surfactants forming the quatsome membrane are widely used as disinfectants, algaecides, preservatives, detergents and antistatic components [221]. Finally different kind of molecules can be integrated in quatsomes, either by a covalent attachment to the sterol-like molecules or by electrostatic interaction with the ionic heads of the surfactant units (Figure 2.72). Alternatively, molecules can also be integrated by hydrophobic interactions with the bilayer or by encapsulation into the inner aqueous lumen of these vesicles.

On the other hand, the DELOS-SUSP route to produce quatsomes is a green, robust and easy scalable productive process that can work under GMP regulations. In addition, this method allows an efficient integration of actives in such quatsomes. Moreover the presence of a high ethanol percentage in the dispersant medium (10%, v/v) using this route makes quatsomes promising carriers for attaining good skin penetrability [222]. For all these reasons, quatsomes could be considered as potential drug nanocarriers, especially for topical delivery.

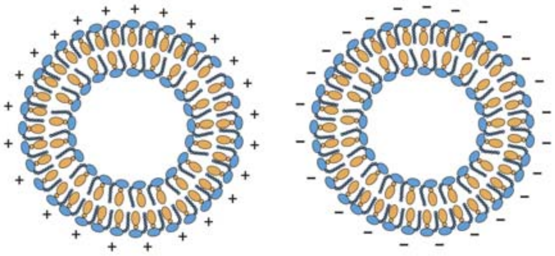

Figure 2.72.: Ionic molecules can be integrated in quatsomes by electrostatic interaction with the ionic heads of the surfactant units, both positive and negative.

The goodness of DELOS-SUSP for the encapsulation of an active compound was tested for the first time by Dr. Elisa Elizondo in her PhD thesis work [187]. Gentamicin sulfate (GS) was used as a model hydrophilic drug which was dissolved in the aqueous phase for its entrapment in cholesterol-CTAB quatsomes. Afterwards, a variety of quatsome-based conjugates using DELOS-SUSP were investigated by Dr. Ingrid Cabrera in her PhD thesis work [182]. In these studies, very stable loaded quatsome conjugates with nanometric sizes, great degree of unilamellarity and with high entrapment efficiencies were successfully prepared using the bovine serum albumin (BSA) protein and an epidermal growth factor polypeptide (rhEGF) [122, 223]. Especially, it was found that if this epidermal growth factor (protein used in regenerative medicine) is integrated into quatsomes obtained by DELOS-SUSP method, a drastic increase in epidermal regeneration activity of this protein is observed. This effect was successfully demonstrated on the treatment of diabetic foot ulcers (DFU) (Figure 2.73) avoiding the amputation of the limb. This new nanomedicine, based on rhEGF loaded quatsomes, has been tested in animal models and in compassionate treatment in humans, obtaining a complete ulcer scarring within just 8 weeks. Besides, the new nanoformulation has also the advantage of allowing a topical administration of the drug, which is much less painful than the conventional infiltration method currently used with the therapies already on the market. Due to these remarkable results, the rhEGF loaded quatsomes can be considered as a future potential nanomedicine for the topical treatment of diabetic foot ulcer (DFU) and in general for complex wounds, and for that reason this nanoconjugte has been protected under patent [124] application number WO2014/019555.

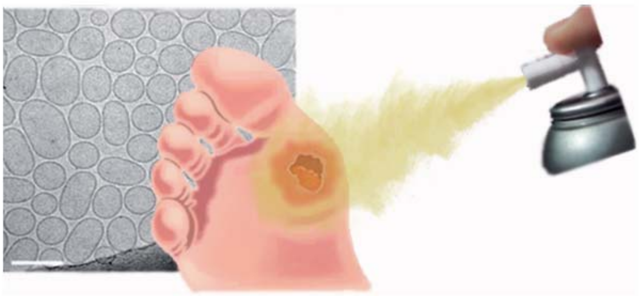

Figure 2.73.: rhEGF loaded quatsomes can be considered as a future potential nanomedicine for the topical treatment of diabetic foot ulcer (DFU).

It is worth highlighting that other functionalities of quatsome-like structures have been studied by other investigation groups, where quatsomes were prepared using our sonication methodology published in [177]. For instance, Ghosh *et al.* [214] studied the protection of ESIPT (Excited-State Intramolecular Proton Transfer) fluorophores in aqueous media using quatsomes, where they obtained remarkable results. Ghosh and co-workers [210] also studied the strong electrostatic interaction between the surface charge of quatsomes and the rhodamine 6G perchlorate (R6G ClO_4). And Thomas *et al.* [215] studied the use of quatsomes for the treatment of Staphylococcus aureus biofilm, where quatsomes showed a dose-dependent anti-biofilm effect.

2.7.1. Summary

- Quatsomes fulfill the structural and physicochemical requirements to be a potential encapsulation platform for time and site specific delivery of therapeutic and diagnostic actives. These non-liposomal vesicles formed by sterols and ionic surfactants have outstanding thermodynamic stability and a high vesicle to vesicle homogeneity regarding size and lamellarity. They are therefore promising nanocarriers in the development of new nanomedicines.

3

From quatsomes to nanoribbons

3.1. Introduction

As stated in the Introduction of this Thesis, the actual form assumed by a colloidal aggregate depends on the molecular structure, the geometry of the constituent amphiphiles and the preparation route. This means that the component parts spontaneously aggregate into a well-defined object based purely on the chemical structure and geometry of the subunits and do not require external guidance to yield the desired product [224]. Thus, depending on the balance between the hydrophilic/hydrophobic parts of amphiphilic molecules, self-organization in the solutions can be observed through various morphological structures.

For cholesterol and CTAB molecules in aqueous solution, Molecular Dynamic (MD) simulations with atomistic detail have revealed in Chapter 2, that Chol-CTAB pair works as a unique supramolecular architecture for the formation of more complex vesicular colloidal phases. It is known that CTAB surfactant would form micelles, whereas cholesterol would form rigid crystals when putting them in water. The key of the success is that, when putting together in water the hydrophilic head of the cholesterol molecule gets hide into CTAB structure, forming spontaneously vesicles. As can be observed, the size and the shape of both CTAB and cholesterol molecules, and their noncovalent inteaction are crucial in order to build complex structures. Within this framework, the objective of this Chapter is to study the impact on self-assembling of the progressive substitution of the cholesterol molecule, in an equimolar mixture Chol:CTAB, by novel cholesterol molecules bearing vinyl sulphone and ferrocene groups, which were synthesized for the development of functionalized quatsomes (Figure 3.1). These new moieties modify the cholesterol polarity and this change in the composition of the system can lead to a different colloidal self-assembly behavior. Therefore, other supramolecular organizations different from vesicles can be formed.

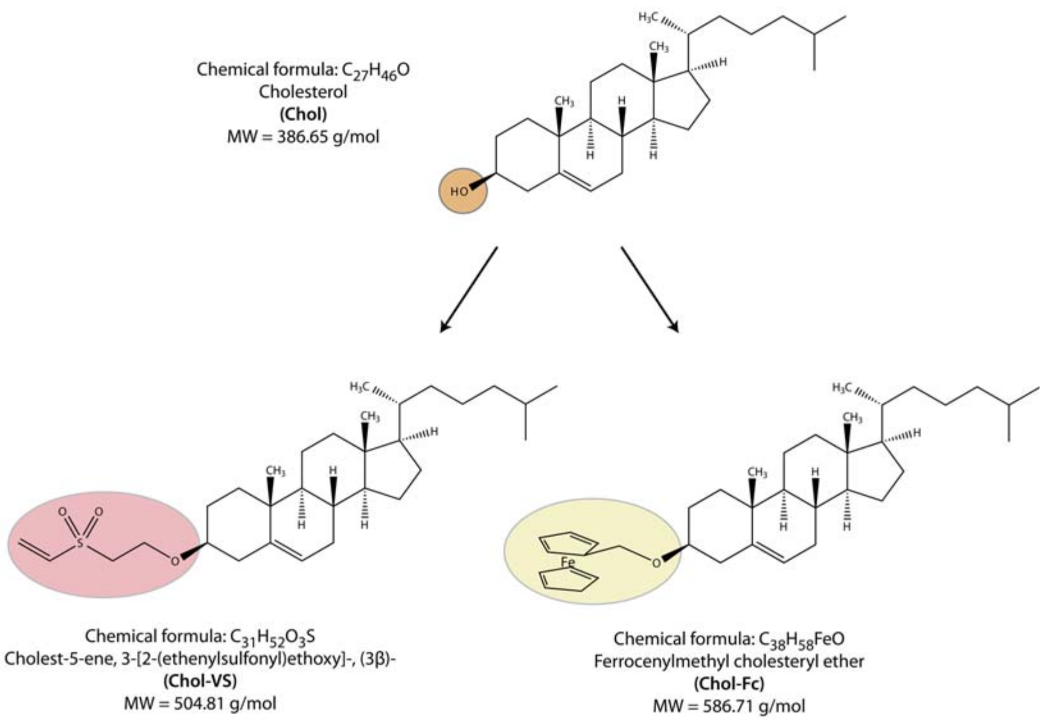

Figure 3.1.: Molecular structures of the studied functionalized cholesterol derivatives. Cholest-5-ene, 3-[2-(ethenylsulfonyl)ethoxy]-, (3β)- (referred as Chol-VS) and ferrocenylmethyl cholesteryl ether (referred as Chol-Fc).

On the one hand, we have studied the substitution of cholesterol by functionalized cholesterol with a vinyl sulphone (VS) group, the Cholest-5-ene, 3-[2-(ethenylsulfonyl) ethoxy]-, (3β)- molecule, from now on called Chol-VS. The election of Chol-VS was motivated to perform thiol-Michael click reactions over this targeting molecule on the surface of the quatsomes [225]. The Michael-type reaction, which commonly refers to the conjugation reaction between activated electrophilic olefin and nucleophiles, has been extensively applied in biomedical fields because it occurs rapidly without side products under mild reaction conditions [226]. In addition, the VS group is quite stable in aqueous solution [227]. Therefore, obtaining quatsomes functionalized with VS group extend their applications in several fields such as nanomedicine (targeting quatsomes).

On the other hand, we have studied the same substitution but using functionalized cholesterol with a ferrocene (Fc) group, the ferrocenylmethyl cholesteryl ether molecule, hereinafter referred as Chol-Fc. The election of this functionalized cholesterol was motivated to form redox-active quatsomes containing ferrocene moieties [228, 229].

Both functionalized cholesterol molecules, Chol-VS and Chol-Fc, were synthesized by the group of Prof. Francisco Santoyo from the University of Granada (see Section 6.9 of the Experimental Part for synthesis and characterization of such compounds).

3.2. Self-assembling of cholesterol, Chol-VS and CTAB in aqueous medium

In this Section it is described the molecular self-assembling of Chol, Chol-VS and CTAB molecules in an aqueous medium, and the impact of Chol and Chol-VS content on it. A new parameter called *VS* ratio has been defined as the moles of Chol-VS over the total moles of cholesterol-like molecules (Chol + Chol-VS). Indeed, as it depicted schematically in Figure 3.2, starting from equimolar mixtures of cholesterol and CTAB (*VS* ratio = 0), which self-assemble as vesicles (see Chapter 2), we have progressively substituted cholesterol by Chol-VS, increasing the *VS* ratio, and analyzed the impact of this compositional change on the self-assembling of the system.

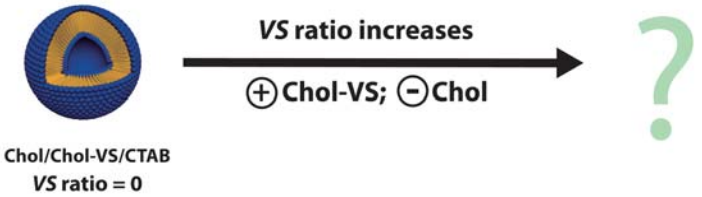

Figure 3.2.: Schematic representation of the increase of *VS* ratio in the preparation of Chol/Chol-VS/CTAB aqueous mixtures. *VS* ratio is defined as the moles of Chol-VS over the total moles of cholesterol-like molecules (Chol and Chol-VS). Chol_{total}:CTAB 1:1 (molar ratio).

3.2.1. Preparation of Chol/Chol-VS/CTAB aqueous mixtures

Different aqueous mixtures increasing the *VS* ratio with a substitution of Chol by Chol-VS (Figure 3.1) were prepared by DELOS-SUSP method (see Figure 3.3). In all experiments, the molar ratio between CTAB and total moles of cholesterol-like molecules was maintained constant, where in both cases the concentration was 6.4 mM. All the prepared aqueous mixtures are detailed in Table 3.1.

Since the solubility behavior of Chol-VS in ethanol and CO_2 was not known, a gas filter (*FG*) was used in the reactor configuration in order to collect any solid that cannot be solubilized inside the reactor during the addition of CO_2 (see Section 6.2.1.1 of the Experimental Part).

Table 3.1.: Chol:Chol-VS molar ratios and *VS* ratios of the different mixtures prepared and further characterized.

Chol:Chol-VS molar ratio	***VS* ratio**^{a,b} **(moles Chol-VS/moles Chol**$_{total}$**)**
1:0	0
1:0.13	0.11
1:0.23	0.19
1:0.33	0.25
1:0.48	0.32
1:0.96	0.49
1:1.9	0.66
1:2.8	0.74
0:1	1

[a] The aqueous phase in all mixtures was composed by Milli-Q with 20% of EtOH (v/v).

[b] Moles Chol$_{total}$ = moles Chol + moles Chol-VS; moles Chol$_{total}$ = moles CTAB. [CTAB] = 6.4 mM.

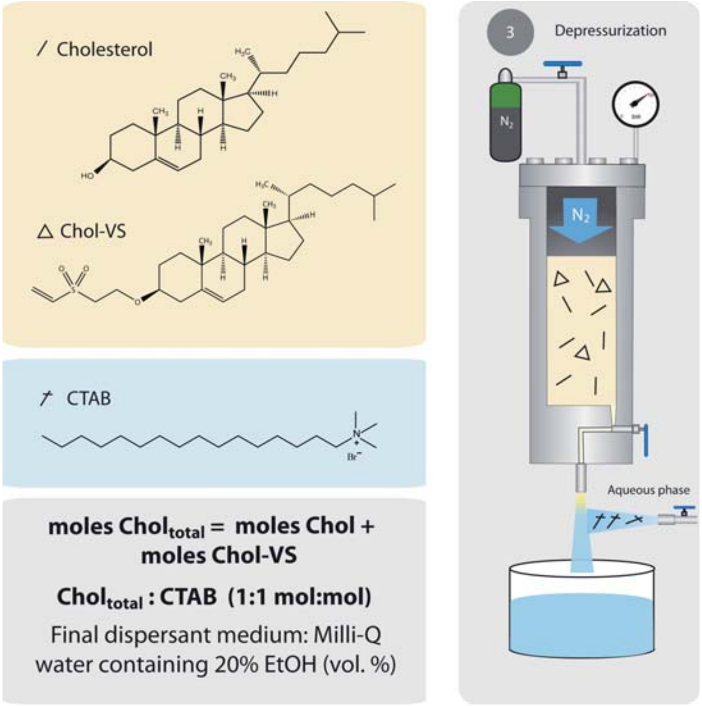

Figure 3.3.: Schematic representation of the DELOS-SUSP methodology used for the preparation of the different Chol/Chol-VS/CTAB aqueous mixtures at different *VS* ratios (see Table 3.1).

The preparation method illustrated in Figure 3.3 consisted in the loading of a 7.5 ml high-pressure autoclave (Section 6.2.1 of the Experimental Part) with a solution containing cholesterol and Chol-VS (7.24 x 10^{-5} total moles of cholesterol-like molecules) in 2.26 ml of ethanol. The solution was then pressurized with compressed CO_2 at a molar fraction of X_{CO_2}= 0.8 until reaching a working pressure of 10 MPa, which produced a volumetric expanded organic solution. Finally, the expanded organic phase was depressurized over 9 ml of an aqueous solution containing 26.4 mg of CTAB. The concentration of total cholesterol-like molecules and CTAB was in both cases 6.4 mM in water with 20% of EtOH (vol. %). It has to be noted that in order to use smaller quantities of the synthesized Chol-VS compound in these systems, the total cholesterol-like concentration and the CTAB concentration were smaller than in Chol-CTAB (W10Et-DELOS) quatsomes (Table 6.3 of the Experimental Part). All the prepared aqueous mixtures were stored at 277 K and were characterized at least 14 days after sample preparation. It is worth mentioning that all the prepared colloidal mixtures, summarized in Table 3.1, were translucent aqueous systems with a slight tendency towards white opalescent solutions upon increasing the *VS* ratio. Besides, negligible amounts of Chol-VS were found in the filter gas (*FG*) used in the reactor configuration (Section 6.2.1.1 of the Experimental Part), thus the Chol-VS compound was easily solubilized inside the reactor.

3.2.2. Supramolecular characterization of Chol/Chol-VS/CTAB aqueous mixtures

The mean and polydispersity index (PdI) of the particle size distributions, corresponding to the supramolecular structures present in the colloidal mixtures of Table 3.1, were measured by dynamic light scattering (DLS). The obtained physicochemical characterizations are summarized in Table 3.2. Additionally, the stability of each system analyzed by Z-potential was also included.

It has to be noted that at high values of *VS* ratio, the size measurements of these samples did not meet DLS quality criteria because of presence of large structures. Thus, the volumetric particle size distribution of these aqueous mixtures was studied by light scattering, which covers the full size range from 0.01 to 3500 μm (Table 3.3, see Section 6.3.5 of the Experimental Part).

Table 3.2.: Physicochemical characteristics of the aqueous mixtures obtained at different *VS* ratios. *Note: The aqueous mixtures were prepared by DELOS-SUSP and were characterized 14 days after sample preparation. Samples were stored at 277 K.*

VS[a]	**Size**		**Stability**
ratio	**Mean(nm)**[b]	**PdI**[c]	**Z-pot.(mV)**
0	61.96± 0.72	0.160 ± 0.004	143 ±3
0.11	70.22± 0.93	0.168 ± 0.028	138 ±3
0.19	70.70± 0.09	0.104 ± 0.002	127 ±3
0.25	76.18 ± 0.25	0.086 ± 0.017	120 ±4
0.32	73.84 ± 0.53	0.150 ± 0.005	115 ±2
0.49	Size > 10 μm[d]	n/a	114 ±8
0.66	Size > 10 μm[d]	n/a	92.9 ±2.8
0.74	Size > 10 μm[d]	n/a	86.3 ±3.1
1	Size > 10 μm[d]	n/a	80.5 ±2.0

[a] *VS* ratio = moles Chol-VS/moles $Chol_{total}$; moles $Chol_{total}$ = moles Chol + moles Chol-VS; $Chol_{total}$:CTAB 1:1 (molar ratio).

[b] Intensity weighted mean hydrodynamic size of the systems measured by dynamic light scattering.

[c] Polidispersity index showing the width of the particle size distribution.

[d] Sample size exceeds the measuring range.

Table 3.3.: Volumetric particle size distribution measured with light scattering of Chol/Chol-VS/CTAB aqueous mixtures with high *VS* ratios. *Note: Size distributions expressed in percentiles of 10, 50 and 90% of accumulated volume, corresponding respectively to D10, D50 and D90 values. D50 value corresponds to the median volumetric particle size distribution. VS ratio comprises the moles of Chol-VS over the total moles of cholesterol-like molecules (Chol and Chol-VS).* $Chol_{total}$*:CTAB 1:1 (molar ratio).*

VS	**Light Scattering (μm)**		
ratio	**D10**	**D50**	**D90**
0.49	28	80.3	194
0.66	30.9	87.5	254
0.74	30.1	87.2	248
1	22.2	58.9	133

Chol/Chol-VS/CTAB aqueous mixtures at *VS* ratios from 0 to 0.25

The particle size distributions and cryo-TEM images of the Chol/Chol-VS/CTAB aqueous mixtures with 0, 0.11, 0.19 and 0.25 *VS* ratios are displayed in Figure 3.4.

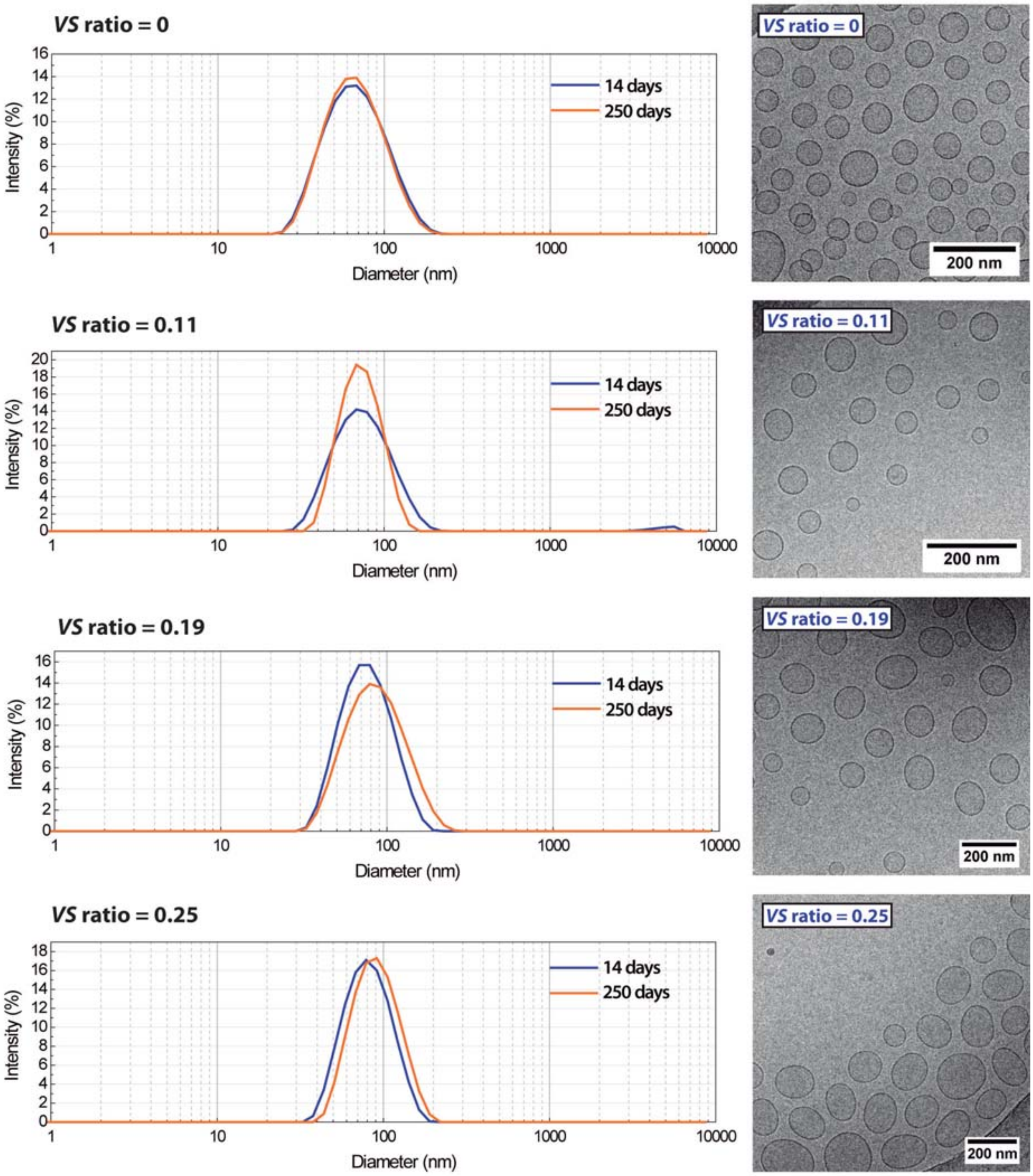

Figure 3.4.: DLS measurements and cryo-TEM images of Chol/Chol-VS/CTAB aqueous mixtures with 0, 0.11, 0.19 and 0.25 *VS* ratios. Particle size distributions (left) measured 14 and 250 days after sample preparation. Cryo-TEM images (right) of aqueous mixtures taken 14 days after sample preparation. Chol_{total}:CTAB 1:1 (molar ratio).

At 0 *VS* ratio, plain Chol-CTAB quatsomes were prepared, in this case called Chol-CTAB (W20Et-DELOS) (Table 6.3 of the Experimental Part). Furthermore, as can be inferred from Figure 3.4 and Table 3.2, despite the partial substitution of cholesterol molecules by Chol-VS, in all mixtures with *VS* ratios between 0 and 0.25, homogeneous, spherically-shaped and unilamellar nanovesicles were obtained 14 days after sample preparation. By comparing the mean size of these systems (Table 3.2), we can observe a moderate increase in the vesicle size as *VS* ratio increases, which might be due to the presence of Chol-VS in the vesicle membrane. Besides, a slight tendency towards lower Z-potential values might be appreciated upon augmenting *VS* ratio.

Additionally, in order to check the stability of these vesicles with time, their particle size distributions were also measured 250 days after sample preparation. As shown in Figure 3.4, minor variations in the size distributions were found for all mixtures, indicating a good stability with time.

Therefore, if the *VS* ratio is lower or equal to 0.25, substitution of cholesterol by Chol-VS molecules in the vesicle-like assemblies present in the aqueous mixtures was achieved (Figure 3.5).

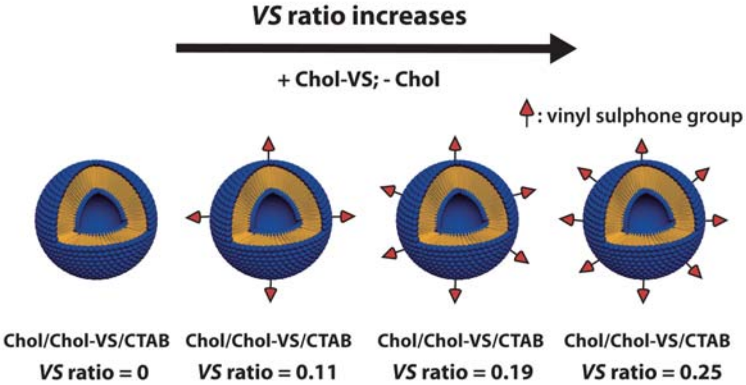

Figure 3.5.: Vesicles with different densities of vinyl sulphone moieties on their bilayer surface can be achieved by fine-tuning the *VS* ratio.

These are remarkable results because using Chol-VS, vesicles with a high degree of structural homogeneity were obtained, and consequently a tuning of the density of vinyl sulphone moieties on the surface of the vesicles can be easily performed. The possibility to produce Michael reactions over these vinyl sulphone groups [226] extend the use of these vesicles as platforms to prepare functional materials.

Chol/Chol-VS/CTAB aqueous mixture at *VS* ratio of 0.32

The particle size distributions of the Chol/Chol-VS/CTAB aqueous mixture obtained at 0.32 *VS* ratio 14, 30 and 45 days after sample preparation are displayed in Figure 3.6.

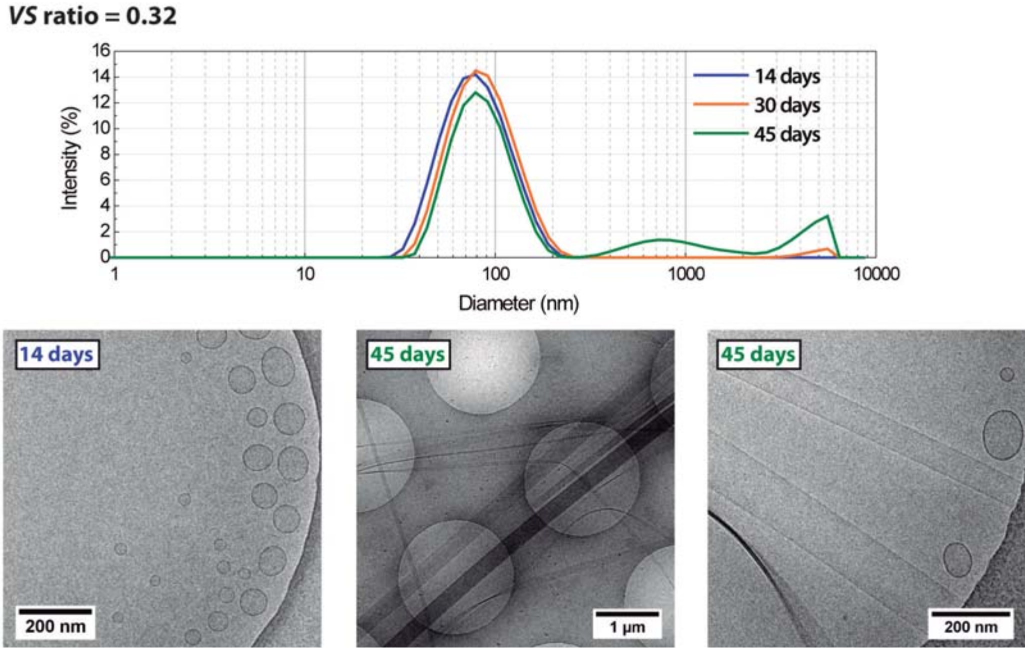

Figure 3.6.: DLS measurements and cryo-TEM images of Chol/Chol-VS/CTAB aqueous mixture at 0.32 *VS* ratio. Particle size distributions (top) measured 14, 30 and 45 days after sample preparation. Cryo-TEM images (bottom) of aqueous mixture taken 14 and 40 days after preparation. Chol_{total}:CTAB 1:1 (molar ratio).

After 14 days of aging (Table 3.2 and Figure 3.6), DLS measurements showed an unimodal size distribution centred in an average size around 74 nm. Cryo-TEM images (Figure 3.6) revealed the presence of spherically-shaped and unilamellar nanovesicles. 30 days after sample preparation (Figure 3.6), the same size distribution around 74 nm was found, however after 45 days (Figure 3.6), larger peaks in size were observed. Due to this unexpected change, this aqueous mixture was studied again under cryo-TEM, and at this time we discovered the presence of one-dimensional (1-D) supramolecular structures known as flat nanoribbons (Figure 3.6) [224, 230–232]. These systems were many micrometers in length, and widths varying from 20 – 300 nm. Additionally, as shown in Figure 3.7, these ribbon-like structures presented different grey levels in the cryo-TEM images, which indicates that they had different thicknesses.

Therefore, the experimental data obtained at 0.32 *VS* ratio revealed a coexistence between vesicles and micrometer-long ribbons 45 days after sample preparation. It is noteworthy that the formation of these nanoribbons at this *VS* ratio needs several weeks to be formed.

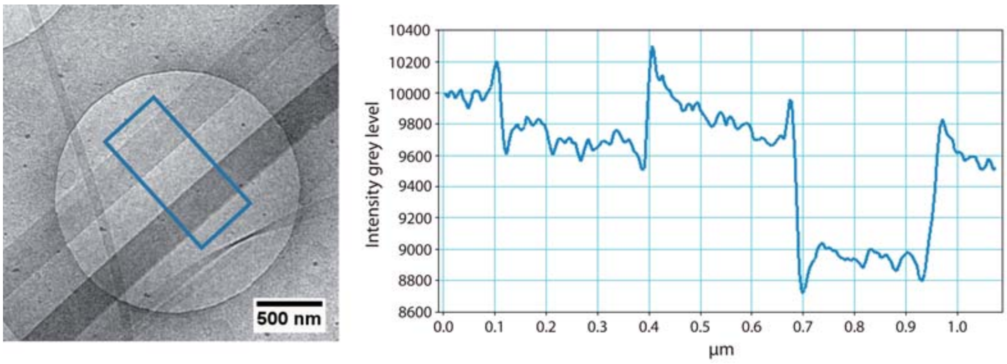

Figure 3.7.: Detail extracted from a original cryo-TEM image of Chol/Chol-VS/CTAB aqueous mixture at 0.32 *VS* ratio. A square is drawn through the desired section of the image and a plot of the grey level vs. distance according to the square of the resulting 2D image is shown.

Chol/Chol-VS/CTAB aqueous mixtures at *VS* ratios from 0.49 to 0.74

DLS measurements of these Chol/Chol-VS/CTAB aqueous mixtures from 0.49 to 0.74 *VS* ratios did not meet quality criteria because of presence of large structures. For that reason, the volumetric particle size distributions of these aqueous mixtures were studied by light scattering, which covers the full size range from 0.01 to 3500 µm (Table 3.3, see Section 6.3.5 of the Experimental Part).

Figure 3.8 shows the volumetric particle size distribution and cryo-TEM images of the colloidal aggregates present in these aqueous mixtures analyzed 14 days after sample preparation. As shown, light scattering measurements revealed for all aqueous mixtures the presence of systems around 100 µm. Besides, all cryo-TEM images exhibited the coexistence of unilamellar spherical nanovesicles with thin micrometer-long ribbons. At these *VS* ratios, these nanoribbons presented narrower thickness than the sample studied before, varying from 5 – 80 nm. Moreover, it is worthy to remark that there were no observed changes in size or shape of these supramolecular assemblies with time.

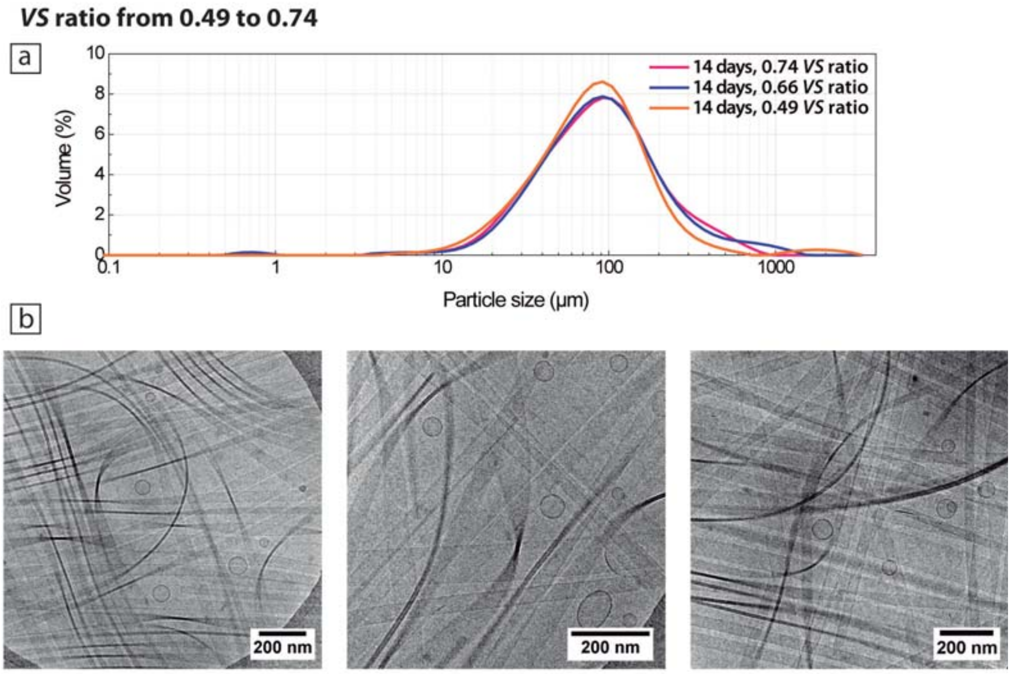

***VS* ratio = 0.49** ***VS* ratio = 0.66** ***VS* ratio = 0.74**

Figure 3.8.: (a) Light scattering measurements and (b) cryo-TEM images of Chol/Chol-VS/CTAB aqueous mixtures from 0.49 to 0.74 *VS* ratios analyzed 14 days after sample preparation. Chol_{total}:CTAB 1:1 (molar ratio).

Due to the high presence of nanoribbons in these colloidal mixtures, a further characterization of the Chol/Chol-VS/CTAB aqueous mixture at 0.49 *VS* ratio was carried out by an alternate electron microscopy technique, the negatively stained TEM (NS-TEM) using chemical fixation (Figure 3.9, see Section 6.3.13 of the Experimental Part).

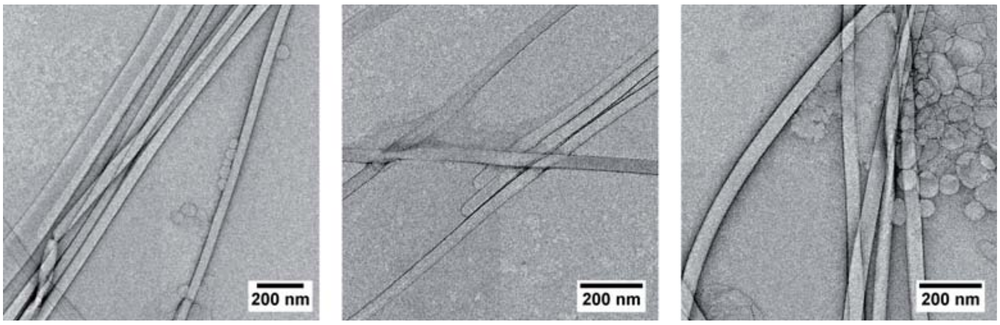

Figure 3.9.: NS-TEM images showing the thin micrometer-long ribbons obtained at 0.49 *VS* ratio recorded 14 days after sample preparation.

This negatively stained TEM (NS-TEM) provides high contrast, is easy to perform and is inexpensive [129]. Briefly, a sample drop was adsorbed onto a carbon-supported film, excess solution was removed by blotting with filter paper, and the sample was fixed by adding uranyl acetate. Finally, the sample was air-dried and examined in the TEM at room temperature. As shown in Figure 3.9, the nanoribbons can be clearly identified with similar thickness as the observed before by cryo-TEM (Figure 3.8), the fact that these structures could be observed by TEM demonstrated that these ribbon-like assemblies were highly stable systems.

On the other hand, after characterizing these ribbon assemblies by microscopy techniques, we then studied these systems by small-angle X-ray scattering (SAXS) (Figure 3.10). SAXS analysis were performed of Chol/Chol-VS/CTAB aqueous mixtures from 0 to 0.25 *VS* ratios, where only vesicles were formed, and at 0.49 *VS* ratio, where a coexistence of vesicles and nanoribbons was observed 14 days after sample preparation. Measurements were conducted at the SAXS beamline of the Elettra (Trieste, Italy) 1 month after sample preparation. The experimental procedures are detailed in Section 6.3.11 of the Experimental Part. Data were analyzed by Dr. Evelyn Moreno from the *Nanomol* group (ICMAB-CSIC).

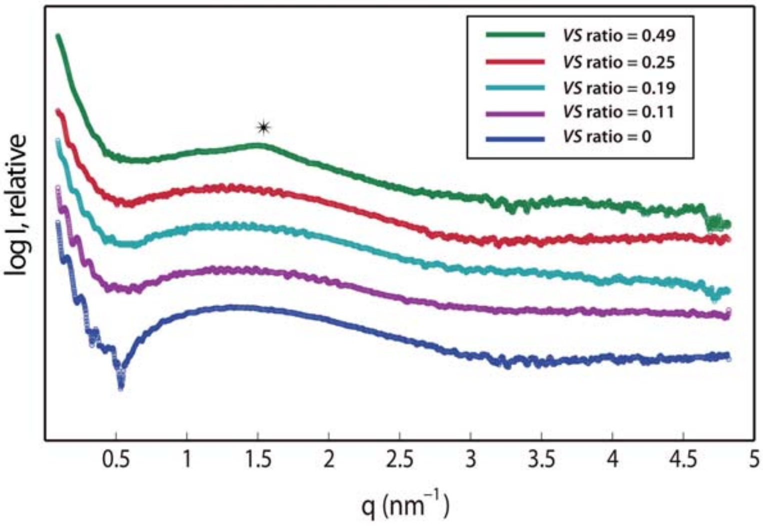

Figure 3.10.: SAXS curves of Chol/Chol-VS/CTAB aqueous mixtures at different *VS* ratios. Data collected at SAXS beamline of the Elettra at 298 K 1 month after sample preparation. Bragg peak at 0.49 *VS* ratio is marked by ✳.

As shown in Figure 3.10, the scattering curves corresponding to the aqueous mixtures from 0 to 0.25 *VS* ratios display only broad and diffuse peaks centred around 1.30 nm^{-1} (q_{max}), which indicates that these samples consist of unilamellar vesicles with a repeated distance of 4.83 nm $(d = 2\pi/q_{max})$ (this repeated distance includes the bilayer membrane and the ordered layer of hydration water). The obtained scattering curves of the aqueous mixture at 0.49 *VS* ratio, presented both contributions, the broad peak associated to unilamellar vesicles and one Bragg peak at $q \approx 1.51$ nm^{-1} marked by ✳.

From the q-value of this peak we can obtain the repeated distance by using the equation $d = 2\pi/q$. Accordingly, the obtained d value is around 4.16 nm. Therefore, SAXS scattering curves indicated a change in the nature of the self-assembled structures at 0.49 *VS* ratio compared with the SAXS data obtained at lower *VS* ratios. This is in good agreement with the cryo-TEM images (Figure 3.8), where a coexistence of vesicles and nanoribbons was observed at this *VS* ratio.

Chol/Chol-VS/CTAB aqueous mixture at *VS* ratio of 1

Finally at 1 *VS* ratio, the complete substitution of cholesterol by Chol-VS was done, so this aqueous mixture was formed only by CTAB and Chol-VS (Figure 3.11).

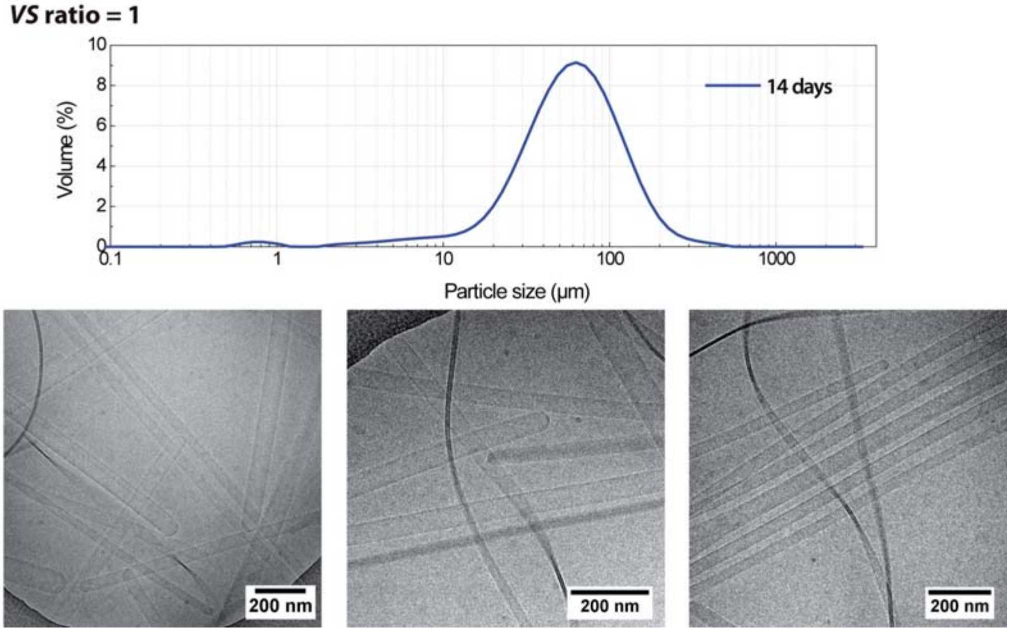

Figure 3.11.: Light scattering measurements (top) and cryo-TEM images (bottom) of Chol/Chol-VS/CTAB aqueous mixture at 1 *VS* ratio analyzed 14 days after sample preparation. Chol_{total}:CTAB 1:1 (molar ratio).

Cryo-TEM images (Figure 3.11) displayed the presence of micrometer-long ribbons with widths varying from 30 – 80 nm, however they did not show the presence of vesicles. Accordingly, vesicle-like assemblies were not formed using only mixtures of CTAB and Chol-VS. Unlike previous samples, these ribbons assemblies were thicker and shorter since their ends were easy to found. Additionally, light scattering measurements (Figure 3.11) also revealed systems with smaller sizes, around 65 μm, compared with the 100 μm systems measured before (Figure 3.8). In addition, it is worth highlighting that such ends were rounded, giving some tubular aspect to these ribbon structures.

Moreover, it is worthy to remark that there were no observed changes in size or shape of these supramolecular assemblies with time.

The stability of these nanoribbons was studied upon sonication and dilution to get further insight into the nature of these systems. The sample was sonicated 30 minutes in a bath sonication and then it was analyzed under cryo-TEM. As shown in Figure 3.12a, nanoribbons keep their structure upon sonication process. Moreover the sample was 10-fold diluted in Milli-Q water and immediately it was analyzed by both, cryo-TEM and negatively stained TEM (NS-TEM) (see Section 6.3.13 of the Experimental Part). The dilution process implied a final concentration of CTAB around 0.64 mM, which was below the cmc of CTAB in water, approximately 1 mM [233]. The cryo-TEM and NS-TEM images are displayed in Figure 3.12b,c. As can be checked by both microscope techniques, the ribbon-like assemblies retained their structure after the dilution process, even below the CTAB cmc, and again the possibility to observe these structures by NS-TEM indicates that they were highly stable.

Therefore, it has been demonstrated that the nanoribbons obtained at 1 *VS* ratio, when only CTAB and Chol-VS were used, presented an outstanding stability, since they did not change shape upon sonication and dilution.

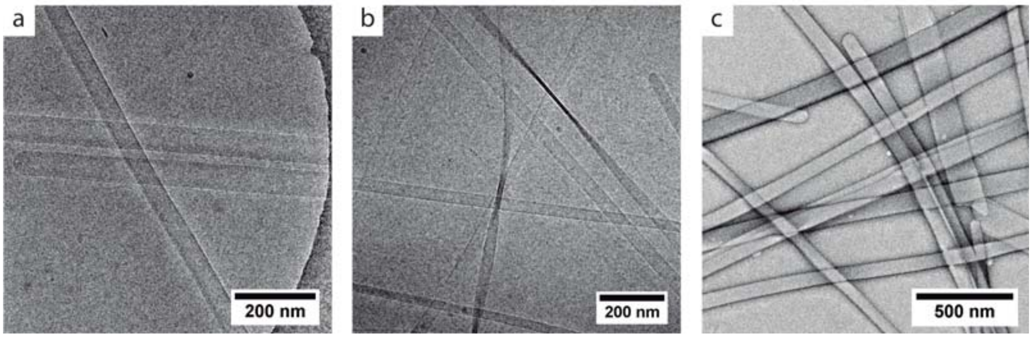

Figure 3.12.: Images of Chol/Chol-VS/CTAB aqueous mixture at 1 *VS* ratio. (a) Cryo-TEM image taken after 30 minutes of bath sonication. (b) Cryo-TEM and (c) NS-TEM images taken after diluting the sample with Milli-Q water (10-fold).

Pure Chol-VS free of CTAB

An additional DELOS-SUSP experiment was performed to investigate the role of the CTAB in the formation of the ribbon-like structures studied before. This new experiment was carried out using only Chol-VS, thus neither CTAB nor cholesterol were employed. Briefly, a solution containing 7.24 x 10^{-5} moles of Chol-VS in 2.26 ml of ethanol was loaded into the 7.5 ml high-pressure autoclave (Section 6.2.1 of the Experimental Part). The solution was then pressurized with compressed CO_2 at a molar fraction of X_{CO_2}= 0.8

until reaching a working pressure of 10 MPa, which produced a volumetric expanded organic solution. Finally, the expanded organic phase was depressurized over 9 ml of Milli-Q water. After this stage, the macroscopic appearance did not show the typical translucent aqueous system obtained before with the Chol/Chol-VS/CTAB aqueous mixtures, instead the presence of suspended solid with large sizes was observed. This sample was also studied by cryo-TEM, however, almost nothing could be detected. Particles bigger than 1 micron are difficult to observe by this technique, since, either they are removed during the drying step of the sample preparation procedure, or if present, they cannot be observed due to the too thick layer of ice necessary to hold such objects, which prevents the electrons to pass through. Since cryo-TEM was not useful for the correct characterization of this sample, the manual microscope facility of the Morphologi G3 was employed (see Section 6.3.8 of the Experimental Part). As shown in Figure 3.13, if only Chol-VS is used in the DELOS-SUSP experiment, heterogeneous Chol-VS solid particles regarding size and shape were obtained.

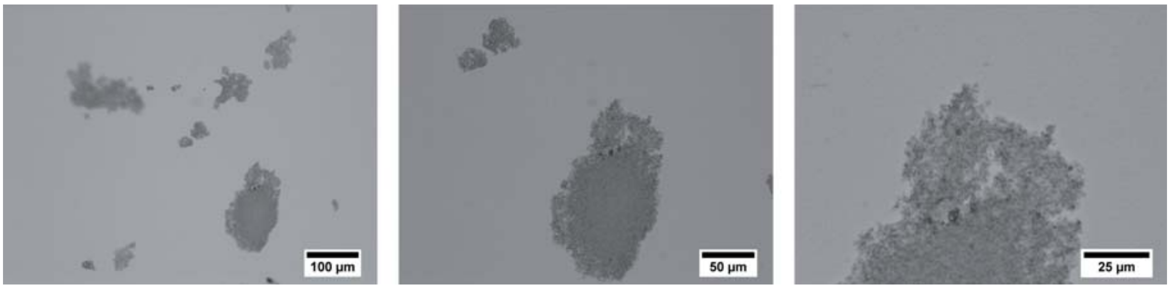

Figure 3.13.: Image of Chol-VS in water with 20% of EtOH (vol. %) captured using the manual microscope facility of the Morphologi G3.

3.2.2.1. Viscosity (η) of Chol/Chol-VS/CTAB aqueous mixtures

The impact of the different nature of self-assemblies over the bulk viscosities of systems was studied.

The bulk viscosities of the aqueous mixtures at different *VS* ratios were measured using a rheometer from Thermo Electron Corporation at 298 K (see Section 6.3.15 of the Experimental Part). The viscosity measurements were conducted 50 days after sample preparation and 1 ml of each solution was used for the determination of bulk viscosity of the obtained systems.

The variation of bulk viscosity of the medium is shown in Figure 3.14. From 0 to 0.25 *VS* ratios, when only vesicles were detected with a moderate increase in the vesicle size as *VS* ratio increases, a slight tendency towards lower bulk viscosity values was observed upon increasing such ratio. It is well know that there is clear effect of vesicle size on the relative viscosity of vesicle suspensions. A smaller vesicle size and greater number of vesicles mean an increase in the specific surface area of the disperse phase, hence a higher viscosity due to the increase in particle-solvent and particle-particle interaction [234]. Thus at 0 *VS* ratio, the aqueous mixture present a higher bulk viscosity due to the smaller size of vesicles. From 0.32 to 0.74 *VS* ratios, when vesicles and nanoribbons were detected, a clear tendency towards higher bulk viscosity values was discovered upon rising the *VS* ratio, with a maximum at 0.74 *VS* ratio. Thus, the increase of the long ribbon-like structures in the samples induces a higher bulk viscosity. At last, at 1 *VS* ratio, when only CTAB and Chol-VS were employed, a decrease in the bulk viscosity value was observed, probably due to the presence of shorter ribbon-like structures.

Therefore, a clear change in the bulk viscosity was observed when the *VS* ratio increases. It is worthy to remark that the maximum in bulk viscosity was achieved at 0.74 *VS* ratio, where a large presence of long nanoribbons was detected.

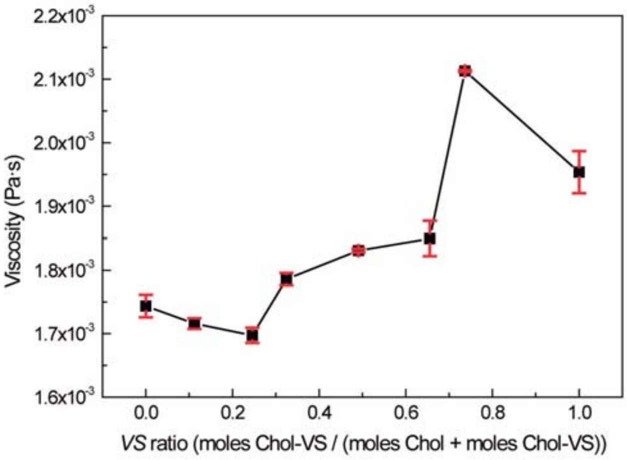

Figure 3.14.: Variation of bulk viscosity of Chol/Chol-VS/CTAB aqueous mixtures at different *VS* ratios.

3.2.3. Experimental summary

The molecular self-assembling of Chol/Chol-VS/CTAB aqueous mixtures with a progressive substitution of cholesterol by Chol-VS, increasing the *VS* ratio, is studied (see Figure 3.15). *VS* ratio has been defined as the moles of Chol-VS over the total moles of cholesterol-like molecules (cholesterol and Chol-VS).

At *VS* ratio of 0, when only cholesterol and CTAB were used, plain Chol-CTAB (W20Et-DELOS) quatsomes were obtained. Increasing the *VS* ratio, from 0 to 0.25, substitution of cholesterol by Chol-VS molecules in the vesicle-like assemblies present in the aqueous

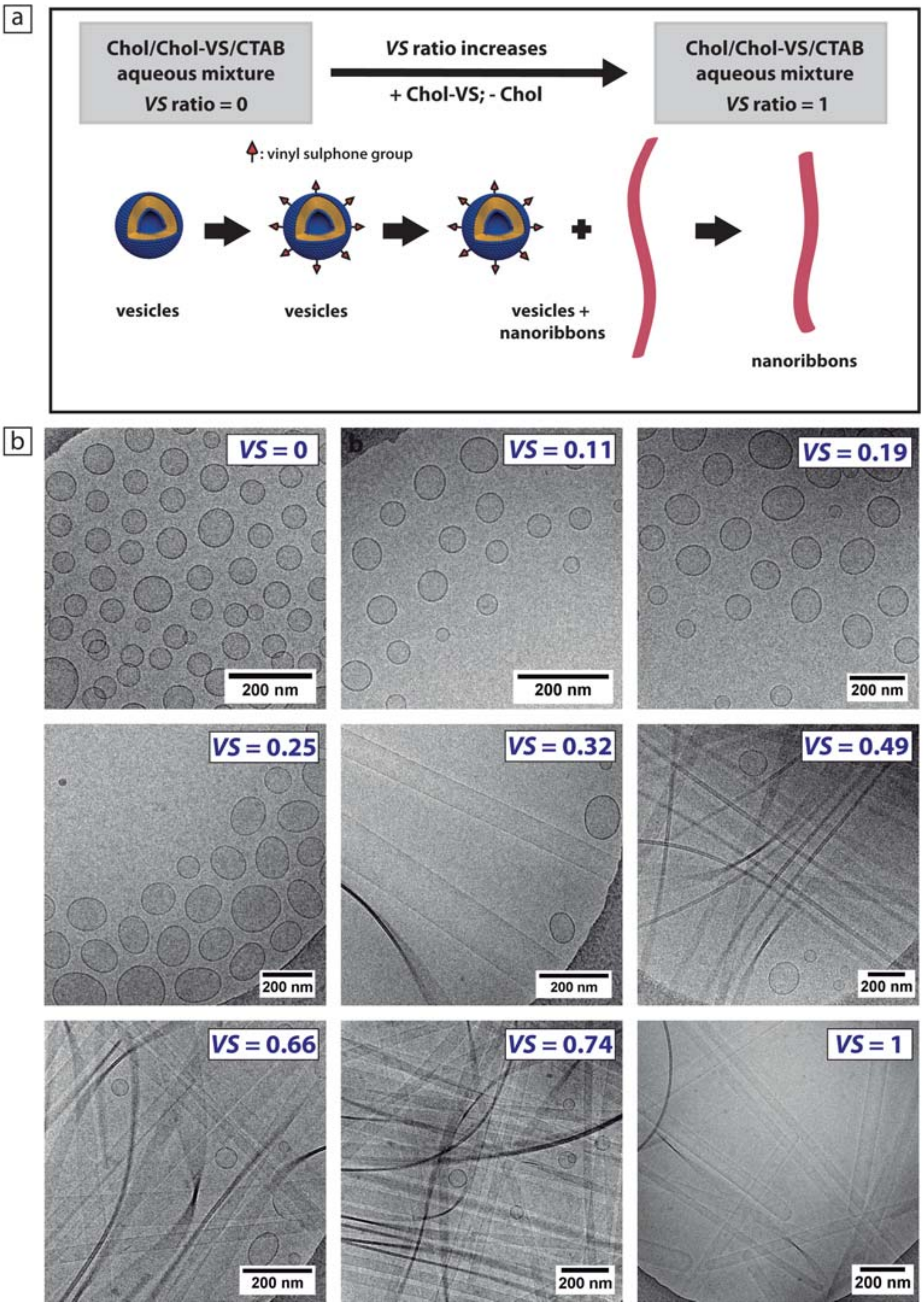

Figure 3.15.: (a) Schematic illustration and (b) cryo-TEM images of the different self-assembled colloidal structures discovered in the studied Chol/Chol-VS/CTAB aqueous mixtures. *VS* ratio comprises the moles of Chol-VS over the total moles of cholesterol-like molecules (cholesterol and Chol-VS). Chol_{total}:CTAB 1:1 (molar ratio).

mixtures was achieved. Thus, vinyl sulphone (VS)-functionalized vesicles were formed. From 0.32 to 0.74 *VS* ratios, a coexistence of vesicles and flat nanoribbons was discovered. And at *VS* ratio of 1, when only CTAB and Chol-VS compounds were used, shorter flat nanoribbons were detected.

Therefore, this study has demonstrated the formation of several supramolecular structures as the *VS* ratio increases. We can state both, that at *VS* ratio of 0, CTAB and cholesterol spontaneously aggregate into vesicles, and at *VS* ratio of 1, CTAB and Chol-VS spontaneously aggregate into nanoribbons. However, when the systems are prepared using Chol, Chol-VS and CTAB, mixtures of the three compounds could be involved in the formation of the vesicle-like and ribbon-like assemblies.

3.2.4. Molecular Dynamics (MD) simulations of Chol-VS

To have a molecular picture of the interaction between Chol-VS and CTAB, and to understand why in this case these two molecules form nanoribbons instead of vesicle-like structures, Molecular Dynamics (MD) simulations were performed. These simulations were conducted by Silvia Illa, in her Master's Thesis [235], under the supervision of Dr. Jordi Faraudo, both from the Institut de Ciència de Materials de Barcelona (ICMAB-CSIC).

It is noteworthy that the functionalized molecule Chol-VS has never been studied before by MD, thus first of all, the development of a model based on CHARMM force field of cholesterol molecule functionalized with a vinyl sulphone group was performed. After that, using Molecular Dynamics simulations with this model, it was predicted the amphiphilic behavior of the Chol-VS molecule, determined its optimal surface area *(*a_0*)* and studied its interactions with CTAB in bulk water.

In Figure 3.16 is depicted the molecular structure of Chol-VS used in the MD simulations.

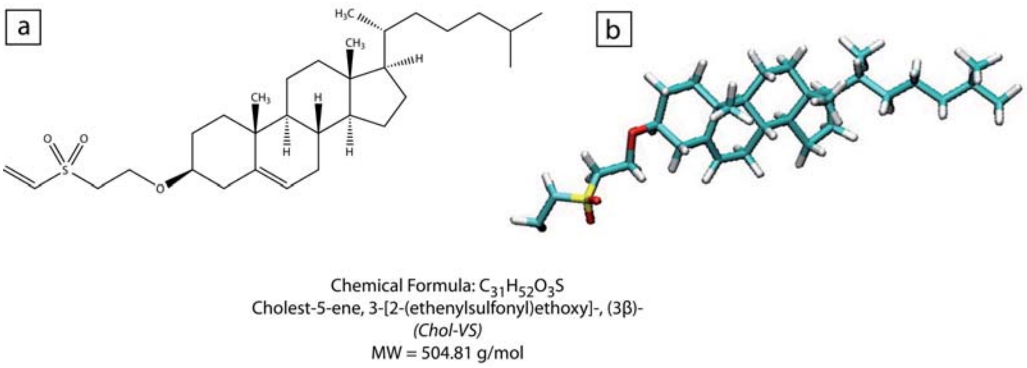

Figure 3.16.: (a) Molecular structure and (b) atomistic structure with bonds-only format of Chol-VS molecule.

Extensive simulations of Chol-VS molecule in different situations were performed in Silvia Illa Master's Thesis [235]. It was simulated: one molecule of Chol-VS at water-chloroform interface, a monolayer of Chol-VS at water-chloroform interface and one molecule of Chol-VS with one molecule of CTAB in bulk water. The main obtained conclusions were the following:

- Chol-VS molecule is an amphiphilic molecule due to the hydrogen bond interactions that this molecule can made with water. These interactions, with a distance of 1.85 Å (exact tabulated value of hydrogen bond interactions [236]), were observed between oxygen atoms of Chol-VS and hydrogen atoms of water (Figure 3.17).

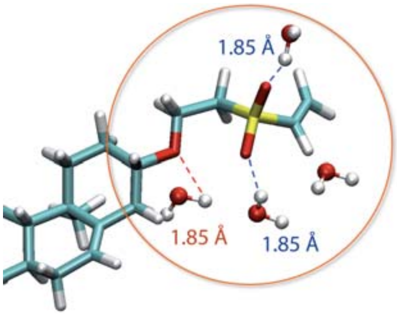

Figure 3.17.: Hydrogen bond interactions between oxygen atoms of Chol-VS molecule and hydrogen atoms contained in water.

- The approximately average value for the optimal surface area *(a_0)* of Chol-VS was 37.28 Å^2 [235]. This value is necessary to calculate the packing parameter *(p)* [17,18] of such molecule.
- Simulations of one Chol-VS molecule with one CTAB molecule in bulk water showed that exists a clear tendency of the polar heads of such molecules to be

close as the average distance is about 5-6 Å. Figure 3.18 shows the distance between the sulphur atom of the vinyl sulphone cholesterol (Chol-VS) molecule with the nitrogen atom of the cetrimonium bromide (CTAB) with time. As shown, almost all time both molecules were together in parallel with a head-head conformation, that means, the hydrophilic part of both molecules were side-by-side and the same with the chains, but they did not associate.

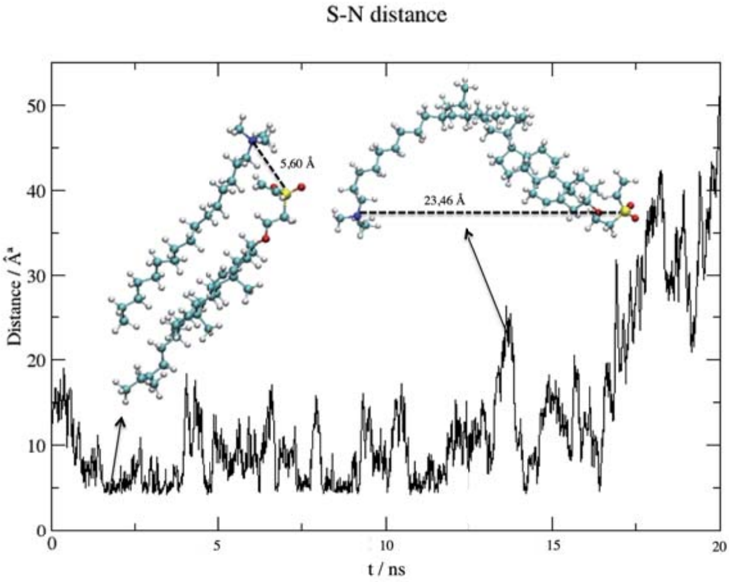

Figure 3.18.: Distance between the polar heads of the CTAB/Chol-VS molecules vs. time in ns. Distance calculated between the sulphur atom of the vinyl sulphone cholesterol (Chol-VS) molecule with the nitrogen atom of the cetrimonium bromide (CTAB). Besides, screenshots of the different conformations are also shown.

At this point, it was possible to make predictions by focusing on the packing parameter *(p)* concept [17, 18] for the Chol-VS/CTAB system. In the same way that the packing parameter of the Chol/CTAB bimolecular synthon was calculated in Section 2.2.3 of the Chapter 2, obtaining a value around 0.85 typical for the formation of vesicles, the packing parameter of the Chol-VS/CTAB synthon was also investigated.

The packing parameter links geometrical molecular characteristics with the shape (curvature) of complexes that form by spontaneous self-assembly in solution. As stated in the introduction of this Thesis, the packing parameter is defined as the ratio of hydrophobic-to-hydrophilic cross-sectional areas, $p = v/a_0 l_c$, where v is the volume of the hydrocarbon chains of the molecule, l_c is the length of the hydrocarbon chain, and a_0 is the optimal cross-sectional area per headgroup at the polar hydrocarbon/water interface of the assembly. Thus, the packing parameter for amphiphilic molecules determines the preferred curvature of the aggregates formed: $p < 1/3$ spherical micelles; $1/3 < p < 1/2$, cylindrical micelles; $1/2 < p < 1$, vesicles; $p = 1$, planar bilayers; $p > 1$, reverse phases.

The packing parameters of cholesterol, CTAB and Chol-VS molecules are gathered in Table 3.4. Furthermore, as mentioned before, the Chol-VS is amphiphilic, which means that the hydrophobic part corresponds to the cholesterol chain and the hydrophilic part to the functionalized part of the Chol-VS molecule. So as the hydrophobic part of cholesterol and Chol-VS molecules are the same, the v and the l_c values can be considered equal.

In order to calculate the packing parameter of the Chol-VS/CTAB synthon and taking into account the screenshot of the conformation of both molecules when having 5.6 Å distance (see Figure 3.18), the length of the hydrocarbon tail of this Chol-VS/CTAB supramolecular synthon *(l_c)* was taken as that of the Chol-VS molecule (1.73 nm) and its volume *(v)* as the sum of both ($0.54 + 0.40 = 0.94$ nm^3). The value of a_0 for the synthon can be also taken as the sum of both ($64 + 37.28 = 101.28$ Å^2) (see again the snapshot of Figure 3.18). Using these values, the obtained packing parameter *(p)* for the Chol-VS/CTAB supramolecular synthon is 0.54, and this value corresponds to the frontier between cylindrical micelles and vesicles. Thus, this information is very relevant in order to understand the formation of the nanoribbons observed in the experimental part of this study.

Table 3.4.: Packing parameter values of cholesterol, CTAB and Chol-VS. *Note: l_c is the length of the hydrocarbon chain, v is the volume of the hydrocarbon chain and a_0 is the optimal cross-sectional area per headgroup at the polar hydrocarbon/water interface of the assembly. The packing parameter is calculated by $p = v/a_0 l_c$.*

Molecule	**v (nm^3)**	**l_c (nm)**	**a_0 (Å^2)**	**$p = v/a_0 \cdot l_c$**
Cholesterol	0.40	1.73	19.00	1.22
CTAB	0.54	1.93	64	0.42
Chol-VS	0.40	1.73	37.28	0.62
Chol/CTAB synthon	0.94	1.73	64	0.85
Chol-VS/CTAB synthon	0.94	1.73	101.28	0.54

Finally, a new simulation was performed (simulation S1-VS, Section A.2 of the Appendix) to study the interaction between 64 molecules of CTAB and 64 molecules of Chol-VS in water. Figure 3.19 shows a snapshot of this simulation on it is clearly visible that mixed systems of CTAB and Chol-VS in water cause the formation of tubular structures, where the hydrophobic parts of both molecules are orientated inside these tubular assemblies, and the hydrophilic heads of Chol-VS and CTAB are in contact with water.

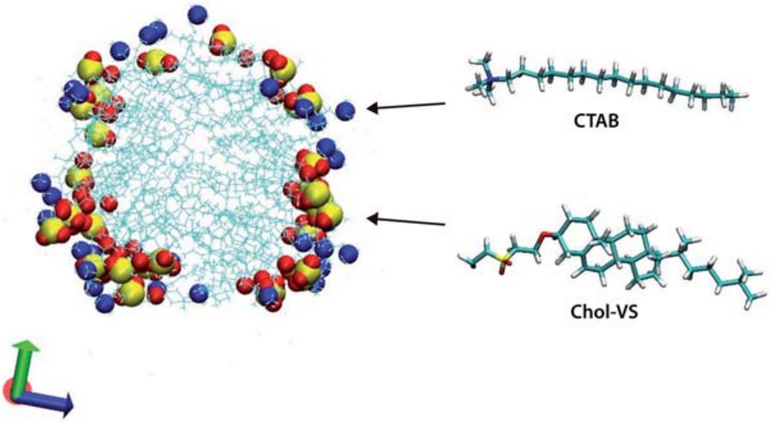

Figure 3.19.: Snapshot corresponding to the interaction between 64 molecules of CTAB and 64 molecules of Chol-VS in water (simulation S1-VS, Table A.2 of the Appendix). For the sake of clarity, the hydrophobic parts of Chol-VS and CTAB are shown with bonds-only format, whereas the hydrophilic parts are shown using the van der Waals atomic radius. The color code employed is the standard crystallographic convention (i.e., red corresponds to oxygen, blue to nitrogen, cyan to carbon, white to hydrogen and yellow to sulphur). Water molecules are not shown.

The formation of these tubular structures using Chol-VS and CTAB agrees with the ribbon-like structures observed experimentally (Section 3.2.2). This association between Chol-VS/CTAB is very different from that observed in the case of Chol/CTAB in Section 2.2.3 of the Chapter 2. In the case of Chol/CTAB system, the cholesterol molecule is wrapped with the CTAB surfactant, which behaves as a second hydrophobic tail for CTAB. On the contrary, in the Chol-VS/CTAB case, the two molecules are together in parallel, head to head in most of the time. This change in the interaction cause a decrease in the packing parameter and consequently, the formed assemble tend to be tubular structures (Figure 3.19).

Therefore, it was demonstrated experimentally and theoretically by MD simulations, that cholesterol molecule bearing a vinyl sulphone group changes the way in which this functionalized molecule assemble with CTAB. Experimental and theoretical studies revealed the formation of long structures in one direction. According to the studied packing parameter for the Chol-VS/CTAB system, mixtures of Chol-VS and CTAB molecules in water induces to sphere-to-cylindrical transition of CTAB micelles; and these cylindrical micelles probably direct the growth of the nanoribbons observed experimentally (Figure 3.20).

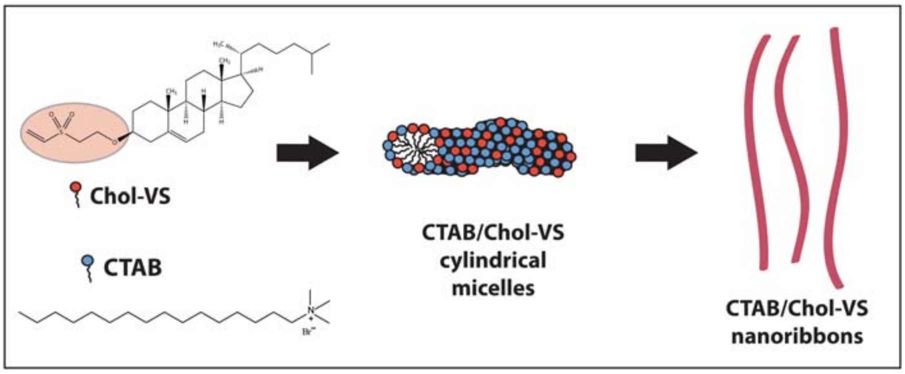

Figure 3.20.: Schematic illustration of the proposed mechanism for the formation of nanoribbons observed experimentally.

3.2.5. Thiol-Michael click reactions over VS-functionalized vesicles

As stated in the introduction of this Chapter, the aim to incorporate Chol-VS molecules into vesicles was motivated to perform thiol-Michael click reactions over these targeting molecules on the surface of quatsomes (Figure 3.21).

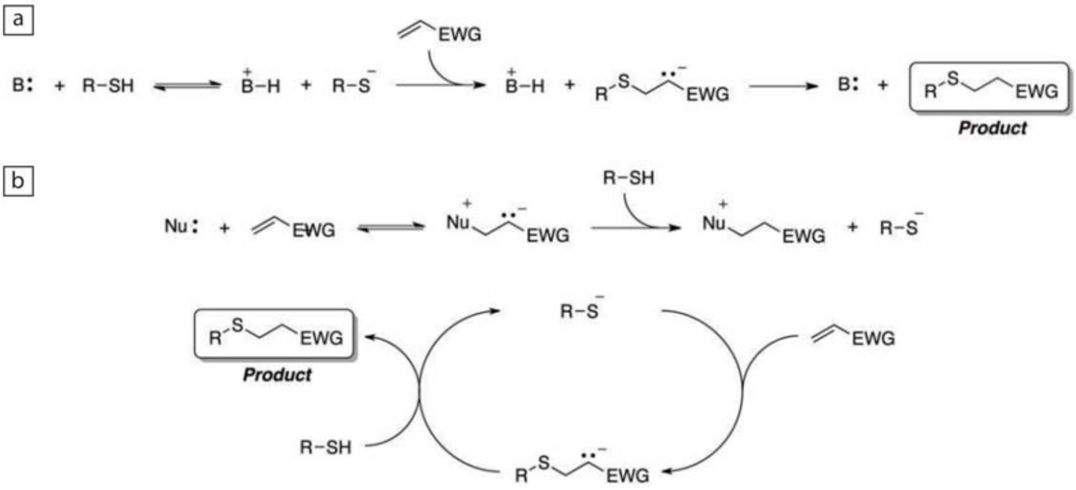

Figure 3.21.: Proposed mechanisms for (a) base-catalyzed and (b) nucleophile-catalyzed thiol–Michael addition reactions. EWG is defined as an electron withdrawing group. Obtained from [237].

The thiol-Michael addition reaction or the conjugate addition of thiols or thiolate anions, to electron-deficient C=C bonds has garnered significant attention, primarily due to its facile, powerful nature. Furthermore, even in very dilute systems, both the nucleophile- and base-catalyzed thiol-Michael addition mechanisms do not lead to the formation of significant side products. This ability to proceed to quantitative conversion without side product formation even under dilute conditions renders the thiol-Michael addition the reaction of choice for many materials chemistry applications [225, 226].

As explained in Section 3.2.2, vesicles with different densities of vinyl sulphone moieties on their bilayer surface were prepared trough Chol/Chol-VS/CTAB aqueous mixtures by fine-tuning the *VS* ratio from 0 to 0.25 (Table 3.1). Vinyl sulphone is a good electrophile group and an excellent Michael acceptor since this functional group has a highly electron deficient vinyl. Additionally, the thiol-Michael addition product of vinyl sulfone forms a very stable thioether sulfone bond [237]. Thus, preliminary Michael reactions were conducted over VS moieties on the surface of vesicles. Specifically, vesicles obtained in the Chol/Chol-VS/CTAB aqueous mixture at 0.25 *VS* ratio were employed (Table 3.1). As a nucleophile group we used the 2-mercaptobenzothiazole compound (MBT) (Figure 3.22), with a thiol group. We performed a base-catalyzed thiol–Michael addition reaction (Figure 3.21a), thus in order to deprotonate the thiol group of the MBT compound to form the thiolate anion, 25 mM $NaHCO_3$buffer at pH 8 was used as medium of this reaction. As explained in Section 2.3.1.3 of the Chapter 2, the addition of $NaHCO_3$ buffer to quatsomes leads to the formation of two-bilayer vesicles, thus all these Michael reactions were conducted over two-bilayer quatsomes.

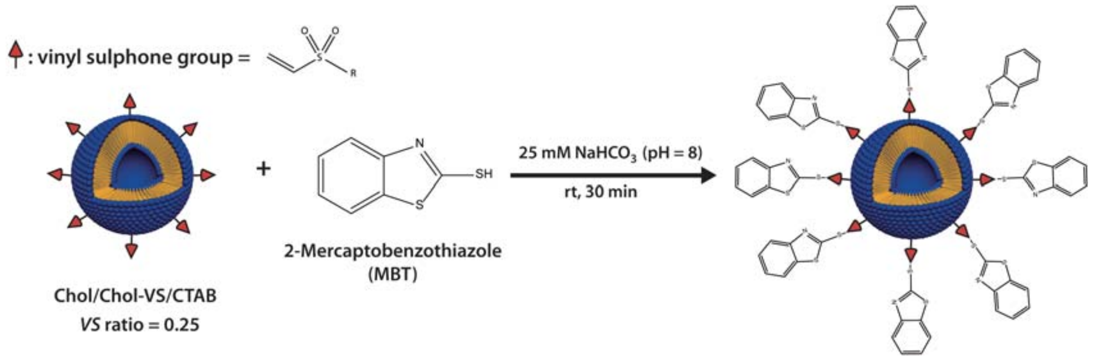

Figure 3.22.: Schematic representation of the thiol–Michael addition of 2-mercaptobenzothiazole (MBT) compound over functionalized vesicles with VS moieties.

The reaction was performed in neat conditions with a stoichiometry of thiol to vinyl of 1 to 1. 100 µl of VS-functionalized Chol-CTAB quatsomes (0.25 *VS* ratio, see Table 3.1, $2.11x10^{-7}$moles Chol-VS) were diluted into 2900 µl of 25 mM $NaHCO_3$ buffer (pH = 8) containing $2.11x10^{-7}$moles of MBT compound. The reaction was left at room temperature for 30 minutes. After the conjugation step, the free thiol was separated from the total sample by centrifugation using centrifugal filter devices (Centricon, Merck Millipore) with 30 KDa Nominal Molecular Weight Limit (NMWL). Finally, the amount of MBT remaining in the sample was determined using UV-Vis spectroscopy (Section 6.3.14).

It is worthy to remark that the MBT compound can be also integrated in vesicle-like systems by hydrophobic interactions. Additionally, since Chol-CTAB quatsomes present a positive charged surface, the thiolate anion of the MBT can be also interact with vesicles by electrostatic interactions. With the objective of determining the real amount of thiol involved in the Michael reaction, the same reaction performed over VS-functionalized Chol-CTAB quatsomes was also conducted over plain Chol-CTAB quatsomes (0 *VS* ratio, see Table 3.1). Thus, we will be able to estimate the amount of MBT interacting with the VS moieties using the reaction over plain Chol-CTAB quatsomes as a blank (Figure 3.23). The two reactions were carried out at the same time.

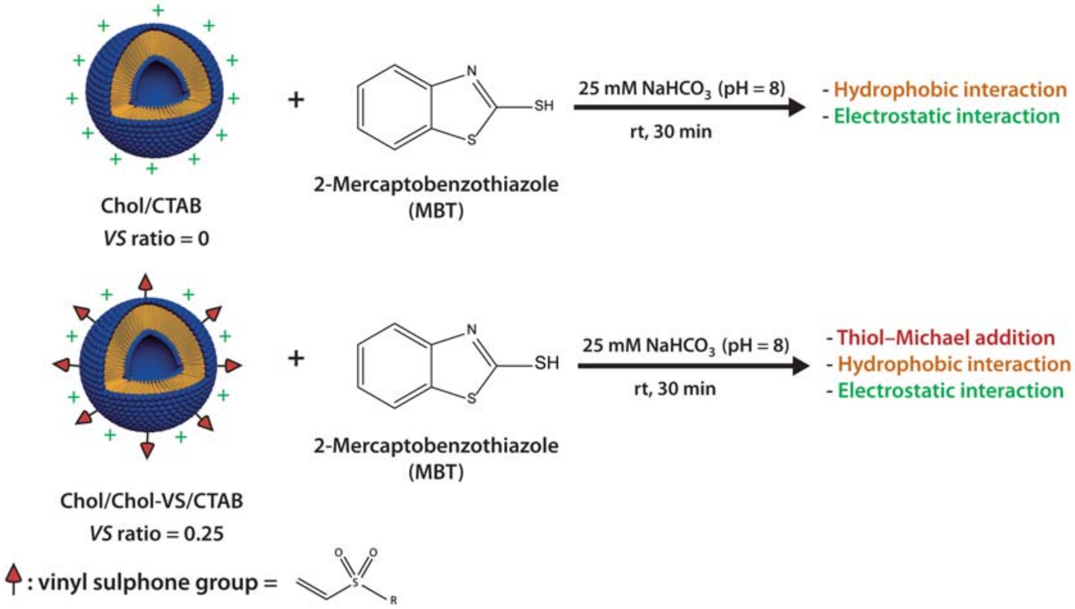

Figure 3.23.: Schematic representation of the interaction between 2-mercaptobenzothiazole (MBT) with plain and VS-functionalized Chol-CTAB quatsomes.

For the separation of the free MBT, the centricons were equilibrated three times with the 25 mM $NaHCO_3$ buffer before their use. In all cases, 1,500 µl of reaction mixture was loaded into the centricon and centrifugated at 6,500 rpm until the concentrated volume was 500 µl. In order to eliminate all the free MBT, the centrifugation process was repeated again adding 1,000 µl of 25 mM $NaHCO_3$ buffer to the 500 µl of sample. Finally, the 500 µl of the concentrated final sample (vesicles containing MBT compound) was diluted into 1,000 µl of 25 mM $NaHCO_3$ buffer and was collected from the filter device sample reservoir using a pipette. Then, the final amount of MBT present in the plain and VS-functionalized vesicles was quantified by UV-Vis spectroscopy. It has to be noted that MBT has an absorption band around λ_{max}= 315 nm in alkaline medium [238]. Figure 3.24a shows the obtained UV-Vis abosrbance spectra for both reactions mixtures. Besides, cryo-TEM images of the obtained systems are also presented in Figure 3.24b,c.

As shown, a higher absorbance of MBT compound was discovered for the reaction with VS-functionalized vesicles. In order to quantify the final amount of MBT presents in both samples, two standard calibration curves at the same measuring conditions used for the studied samples were conducted, one for the the plain Chol-CTAB vesicles (0 *VS* ratio, see Table 3.1) and another one for the VS-functionalized Chol-CTAB vesicles (0.25 *VS* ratio, see Table 3.1). See Section 6.7 of the Experimental Part for the prepared standard calibration curves. The quantified MBT in the final reaction mixtures was 1.70x10^{-8} and 3.32x10^{-8} moles for the plain and VS-functionalized Chol-CTAB vesicles, respectively. As explained before, we can approximate that the difference between these two values are the moles of MBT involved in the thiol-Michael addition. Thus, 1.62x10^{-8} moles of MBT might be involved in the thiol-Michael addition over the VS moieties of the VS-functionalized Chol-CTAB vesicles. Besides, it is noteworthy that there is a shift in the maximum wavelength of MBT in the presence of plain and VS-functionalized Chol-CTAB quatsomes, which indicates a change in the polarity media surrounding the MBT compound.

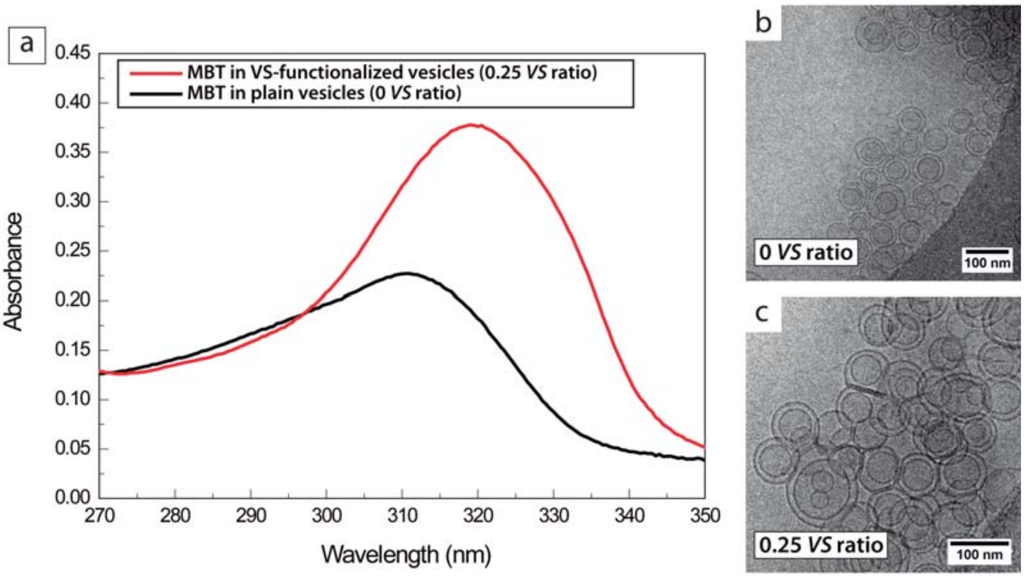

Figure 3.24.: (a) UV-Vis absorbance spectra of the final reaction mixtures containing MBT (plain Chol-CTAB vesicles (λ_{max} = 312 nm), VS-functionalized Chol-CTAB vesicles (λ_{max} = 319 nm)). Cryo-TEM images of the final reactions mixtures of MBT with (b) plain and (c) VS-functionalized Chol-CTAB quatsomes.

Therefore, though more experiments may be required to fully elucidate the mechanistic of this thiol-Michael addition, our findings generally support that a higher concentration of thiol compound (MBT) was found in the vesicles containing VS moieties. This fact suggests that a thiol-Michael addition was accomplished over the

VS-functionalized Chol-CTAB vesicles.

3.2.6. Summary

- The molecular self-assembling of Chol/Chol-VS/CTAB aqueous mixtures with a progressive substitution of cholesterol by Chol-VS, leads to the formation of several supramolecular structures. Experimental and theoretical studies revealed the formation of long structures different from the vesicular structures observed by mixtures of CTAB and cholesterol. According to the studied packing parameter for the Chol-VS/CTAB system, mixtures of Chol-VS and CTAB molecules in water induces to sphere-to-cylindrical transition of CTAB micelles; and these cylindrical micelles, composed by CTAB and Chol-VS, probably direct the growth of the nanoribbons observed experimentally. On the other hand, when Chol/Chol-VS/CTAB aqueous mixtures were performed with small quantities of Chol-VS, VS-functionalized Chol-CTAB vesicles were obtained. In that case, a thiol-Michael click reaction over these targeting molecules was accomplished, which opens a nice strategy for the preparation of functionalized stable nanovesicles with huge applications in drug delivery and material science.

3.3. Self-assembling of cholesterol, Chol-Fc and CTAB in aqueous medium

In this Section it is described the molecular self-assembling of Chol, Chol-Fc and CTAB molecules in an aqueous medium, and the impact of Chol and Chol-Fc content on it. The followed strategy was the same use in the previous Section with Chol-VS. A new parameter called *FC* ratio has been defined as the moles of Chol-Fc over the total moles of cholesterol-like molecules (Chol + Chol-Fc). As it depicted schematically in Figure 3.25, starting from equimolar mixtures of cholesterol and CTAB (*FC* ratio = 0), which self-assemble as vesicles, we have progressively substituted cholesterol by Chol-Fc, increasing the *FC* ratio, and analyzed the impact of this compositional change on the self-assembling of the system.

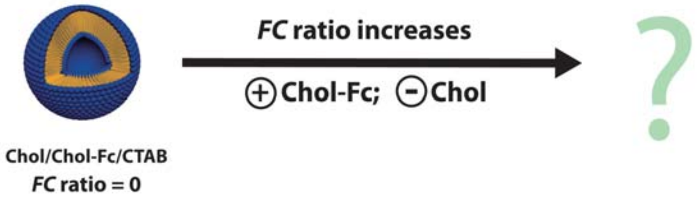

Figure 3.25.: Schematic representation of the increase of *FC* ratio in the preparation of Chol/Chol-Fc/CTAB aqueous mixtures. *FC* ratio is defined as the moles of Chol-Fc over the total moles of cholesterol-like molecules (Chol and Chol-Fc). Chol_{total}:CTAB 1:1 (molar ratio).

3.3.1. Preparation of Chol/Chol-Fc/CTAB aqueous mixtures

Different aqueous mixtures increasing the *FC* ratio with a substitution of Chol by Chol-Fc (Figure 3.1) were prepared by DELOS-SUSP (see Figure 3.26). In all experiments, the molar ratio between CTAB and total moles of cholesterol-like molecules was maintained constant, where in both cases the concentration was 6.4 mM. All the prepared aqueous mixtures are detailed in Table 3.5.

Again, since the solubility behavior of Chol-Fc in ethanol and CO_2 was not known, a gas filter (*FG*) was used in the reactor configuration in order to collect any solid that cannot be solubilized inside the reactor during the addition of CO_2 (see Section 6.2.1.1 of the Experimental Part).

Table 3.5.: Chol:Chol-Fc molar ratios and *FC* ratios of the different mixtures prepared and further characterized.

Chol:Chol-Fc molar ratio	***FC* ratio**[a,b] **(moles Chol-Fc/moles Chol$_{total}$)**
1:0	0
1:0.13	0.11
1:0.24	0.19
1:0.37	0.27

[a] The aqueous phase in all mixtures was composed by Milli-Q with 20% of EtOH (v/v).

[b] Moles Chol$_{total}$ = moles Chol + moles Chol-Fc; moles Chol$_{total}$ = moles CTAB. [CTAB] = 6.4 mM.

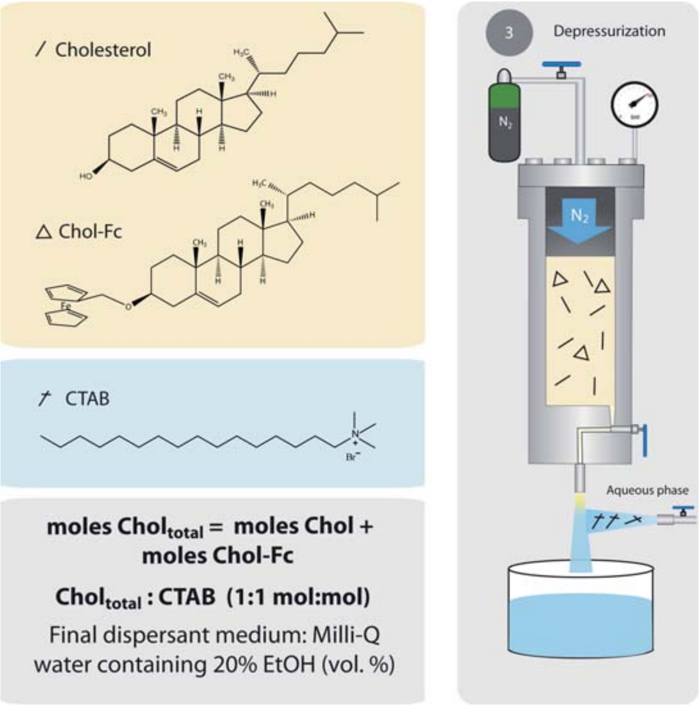

Figure 3.26.: Schematic representation of the DELOS-SUSP methodology used for the preparation of the different Chol/Chol-Fc/CTAB aqueous mixtures at different *FC* ratios (see Table 3.5).

The preparation method illustrated in Figure 3.26 consisted in the loading of the 7.5 ml high-pressure autoclave (Section 6.2.1 of the Experimental Part) with a solution containing cholesterol and Chol-Fc (7.24 x 10^{-5} total moles of cholesterol-like molecules) in 2.26 ml of ethanol. The solution was then pressurized with compressed CO_2 at a molar fraction of X_{CO_2} = 0.8 until reaching a working pressure of 10 MPa, which produced a volumetric expanded organic solution. Finally, the expanded organic phase was depressurized over 9 ml of an aqueous solution containing 26.4 mg of CTAB. The final concentration of total cholesterol-like molecules and CTAB was 6.4 mM in water with 20% of EtOH (vol. %). All the prepared aqueous mixtures were stored at 277 K and were characterized at least 14 days after sample preparation. It is worth mentioning that all the prepared colloidal mixtures, summarized in Table 3.5, were translucent aqueous systems with a slight tendency towards yellow solutions upon increasing the *FC* ratio. Furthermore, negligible amounts of Chol-Fc were found in the filter gas *(FG)* used in the reactor configuration (Section 6.2.1.1 of the Experimental Part), thus the Chol-Fc compound was easily solubilized inside the reactor.

3.3.2. Supramolecular characterization of Chol/Chol-Fc/CTAB aqueous mixtures

The mean and polydispersity index (PdI) of the particle size distributions, corresponding to the supramolecular structures present in the colloidal mixtures of Table 3.5, were measured by dynamic light scattering (DLS). The obtained physicochemical characterizations are summarized in Table 3.6. Besides, the stability of each system analyzed by Z-potential was also included.

In these studies, the final concentration of Chol-Fc in each Chol/Chol-Fc/CTAB aqueous mixture was controlled by the inductively coupled plasma optical emission spectrometry (ICP-OES) technique (see Section 6.3.4 of the Experimental Part). Using this analytical technique, the detection of trace metals [239] is possible to investigate. Since Fe is only present in the Chol-Fc molecule, with an equimolar relation between Fe and Chol-Fc, the final concentration of Chol-Fc in each aqueous mixture can be easily controlled if one knows the final concentration of Fe.

Table 3.7 shows the theoretical and the quantified concentration values of Fe in each Chol/Chol-Fc/CTAB aqueous mixture obtained at different *FC* ratios (see Table 3.5). As can be ascertained, a clear tendency towards higher Fe concentrations can be appreciated upon augmenting the theoretical *FC* ratio. Additionally, it is noteworthy that the the theoretical and quantified Fe (mg/l) concentration values were analogous in all cases.

Table 3.6.: Physicochemical characteristics of the aqueous mixtures obtained at different *FC* ratios. *Note: The aqueous mixtures were prepared by DELOS-SUSP and were characterized 14 days after sample preparation. Samples were stored at 277 K.*

FC[a]	**Size**		**Stability**
ratio	**Mean(nm)**[b]	**PdI**[c]	**Z-pot.(mV)**
0	61.96± 0.72	0.160 ± 0.004	143 ±3
0.11	48.93± 0.25	0.154 ± 0.017	102 ±0
0.19	62.28± 0.15	0.217 ± 0.013	122 ±2
0.27	67.46 ± 0.13	0.172 ± 0.019	111 ±6

[a] *FC* ratio = moles Chol-Fc/moles Chol$_{total}$; moles Chol$_{total}$ = moles Chol + moles Chol-Fc; Chol$_{total}$:CTAB 1:1 (molar ratio).

[b] Intensity weighted mean hydrodynamic size of the systems measured by dynamic light scattering.

[c] Polidispersity index showing the width of the particle size distribution.

Table 3.7.: Theoretical and quantified Fe (mg/l) concentration values by ICP-OES of Chol/Chol-Fc/CTAB aqueous mixtures.

***FC* ratio**[a]	**Theorical Fe (mg/l)**	**Quantified Fe (mg/l)**[b]
0	0	<0.8
0.11	43	28
0.19	67	52
0.27	81	60

[a] *FC* ratio = moles Chol-Fc/moles Chol$_{total}$; moles Chol$_{total}$ = moles Chol + moles Chol-Fc; Chol$_{total}$:CTAB 1:1 (molar ratio).

[b] Concentration of Fe (mg/l) quantified by ICP-OES.

Chol/Chol-Fc/CTAB aqueous mixtures at *FC* ratios from 0 to 0.11

Since no Chol-Fc was employed at 0 *FC* ratio, this aqueous mixture is the same system explained before where plain Chol-CTAB (W20Et-DELOS) quatsomes were prepared (Section 3.2.2). As previously mentioned, homogeneous, spherically-shaped and unilamellar nanovesicles were obtained 14 and 250 days after sample preparation.

The particle size distribution and cryo-TEM images of the Chol/Chol-Fc/CTAB aqueous mixture at *FC* ratio of 0.11 are presented in Figure 3.27 and Table 3.6. As can be inferred from Figure 3.27, despite the partial substitution of cholesterol molecules by Chol-Fc, vesicles with a high degree of structural homogeneity were obtained 14 and 250 days after sample preparation.

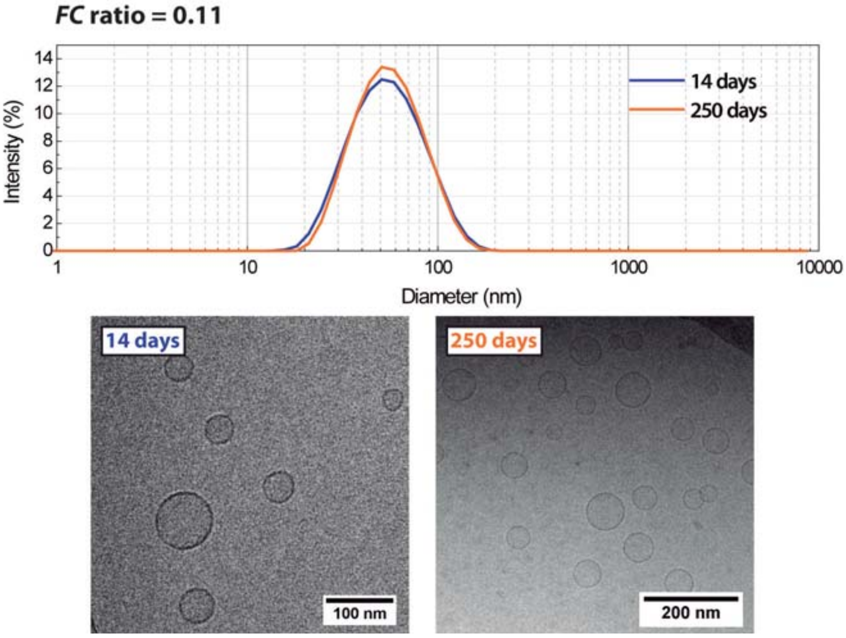

Figure 3.27.: DLS measurements and cryo-TEM images of Chol/Chol-Fc/CTAB aqueous mixture at 0.11 *FC* ratio. Particle size distributions (top) and cryo-TEM images (bottom) analyzed 14 and 250 days after sample preparation. Chol_{total}:CTAB 1:1 (molar ratio).

Since there were no observed other structures in this aqueous mixture, substitution of cholesterol by Chol-Fc molecules in the vesicle-like assemblies was achieved. These are interesting results because redox-active vesicles containing ferrocene moieties can be prepared [228, 229, 240] (Figure 3.28).

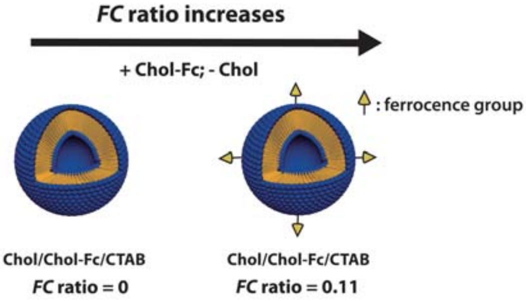

Figure 3.28.: Vesicles with different densities of ferrocene moieties on their bilayer surface can be achieved by fine-tuning the *FC* ratio.

Chol/Chol-Fc/CTAB aqueous mixture at *FC* ratio of 0.19

The particle size distributions and the cryo-TEM images of the Chol/Chol-Fc/CTAB aqueous mixture obtained at 0.19 *FC* ratio 14 and 250 days after sample preparation are presented in Figure 3.29 and Table 3.6.

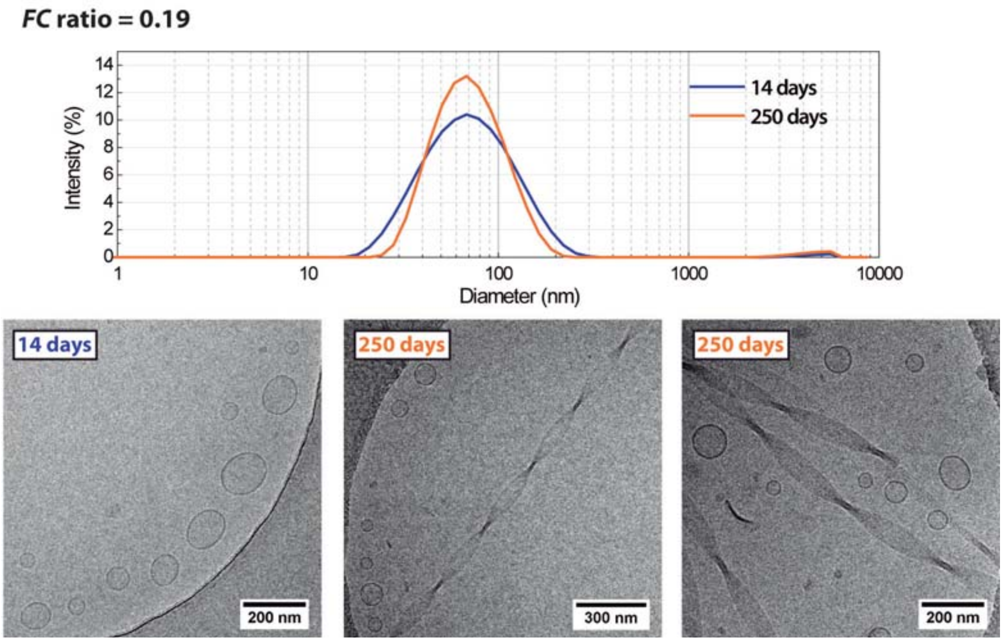

Figure 3.29.: DLS measurements and cryo-TEM images of Chol/Chol-Fc/CTAB aqueous mixture at 0.19 *FC* ratio. Particle size distributions (top) and cryo-TEM images (bottom) analyzed 14 and 250 days after sample preparation. Chol$_{total}$:CTAB 1:1 (molar ratio).

DLS measurements showed an unimodal size distribution centred in an average size around 62 nm after 14 days and 250 days of aging. However, cryo-TEM images (Figure 3.29) revealed the presence of different self-assembled structures at these aging times. 14 days after preparation, spherically-shaped and unilamellar nanovesicles were obtained, however after 250 days, the presence of twisted nanoribbons with a Gaussian or saddle-like curvature was discovered [230, 231, 241]. Cryo-TEM images (Figure 3.29) showed that these systems were many micrometers in length and the pitch length was totally uniform along all the observed ribbons. According to the literature, these twisted structures are normally formed by certain chiral amphiphilic molecules, thus the Chol/Chol-Fc/CTAB aqueous mixture at this *FC* ratio is forming a specific synthon which self-assembles with a certain degree of chirality [242–244]. Further studies to understand the composition of this chiral synthon and the formation of these twisted nanoribbons will be performed soon by MD simulations. Besides, the handedness of these chiral nanoribbons and their pitch characteristics will be also studied in the near future.

On the other hand, the stability of these twisted nanoribbons was studied upon dilution. The sample was 10-fold diluted in Milli-Q water and immediately it was analyzed by cryo-TEM. This dilution process implied a final concentration of CTAB around 0.64 mM, which was below the cmc of CTAB in water, approximately 1 mM [233]. The cryo-TEM images are displayed in Figure 3.30. As can be checked by this technique, the twisted nanoribbons retain their structure after this dilution process, even below the CTAB cmc, therefore these nanoribbons were highly stable self-assembled structures.

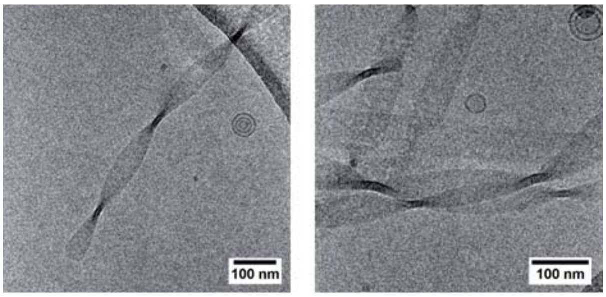

Figure 3.30.: Cryo-TEM images taken after diluting the Chol/Chol-Fc/CTAB aqueous mixture at 0.19 *FC* ratio with Milli-Q water (10- fold).

Chol/Chol-Fc/CTAB aqueous mixture at *FC* ratio of 0.27

Figure 3.31 and Table 3.6 present the particle size distributions of Chol/Chol-Fc/CTAB aqueous mixture at 0.27 *FC* ratio 14 and 250 days after sample preparation.

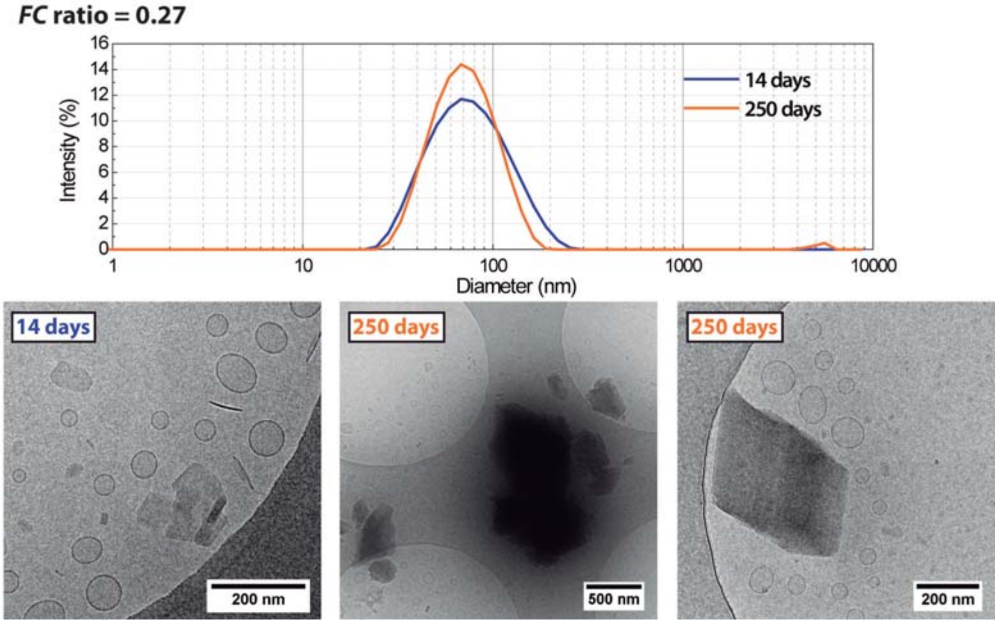

Figure 3.31.: DLS measurements and cryo-TEM images of Chol/Chol-Fc/CTAB aqueous mixture at 0.27 *FC* ratio. Particle size distributions (top) and cryo-TEM images (bottom) analyzed 14 and 250 days after sample preparation. Chol$_{total}$:CTAB 1:1 (molar ratio).

As shown, at both aging times, DLS measurements revealed an unimodal size distribution centred in an average size around 67 nm. At this *FC* ratio cryo-TEM images, also displayed in Figure 3.31, show the coexistence of vesicles and a large amount of particles with a plate-like morphology after 14 days of aging. Further, as the images taken after 250 days shown, these particles became larger with time. Due to an increased degree of cholesterol substitution by Chol-Fc molecules in this aqueous mixture, these plate-like particles might be precipitated hydrophobic nanocrystals of Chol-Fc compound. It is noteworthy that at this *FC* ratio, there were no observed twisted nanoribbons at any studied time, thus in this aqueous mixture, the Chol-Fc compound tend to precipitate and no interaction with the other components, CTAB and Chol, was achieved.

Unlike the preparation of aqueous mixtures using Chol-VS, where experiments were performed until equimolarity of Chol-VS and CTAB (*VS* ratio = 1), further experiments increasing the *FC* ratio were not performed due to the detection of this large amount of Chol-Fc hydrophobic nanocrystals.

3.3.3. Experimental summary

The molecular self-assembling of Chol/Chol-Fc/CTAB aqueous mixtures with a progressive substitution of cholesterol by Chol-Fc (increasing the *FC* ratio) is studied. In Figure 3.32 are schematically represented the different types of self-assembled structures which are progressively formed. In all the prepared aqueous mixtures, the molar ratio between CTAB and the total moles of cholesterol-like molecules (cholesterol and Chol-Fc) was maintained constant at equimolar ratio.

At 0 *FC* ratio, when only cholesterol and CTAB were used, plain Chol-CTAB (W20Et-DELOS) quatsomes were obtained. Increasing the *FC* ratio, from 0 to 0.11, substitution of cholesterol by Chol-Fc molecules in the vesicle-like assemblies present in the aqueous mixtures was achieved. Thus, ferrocene (Fc)-functionalized vesicles were formed. At 0.19 *FC* ratio, a coexistence of vesicles and twisted nanoribbons with a Gaussian or saddle-like curvature was discovered. And finally, at 0.27 *FC* ratio, the presence of vesicles and plate-like nanocrystals was observed.

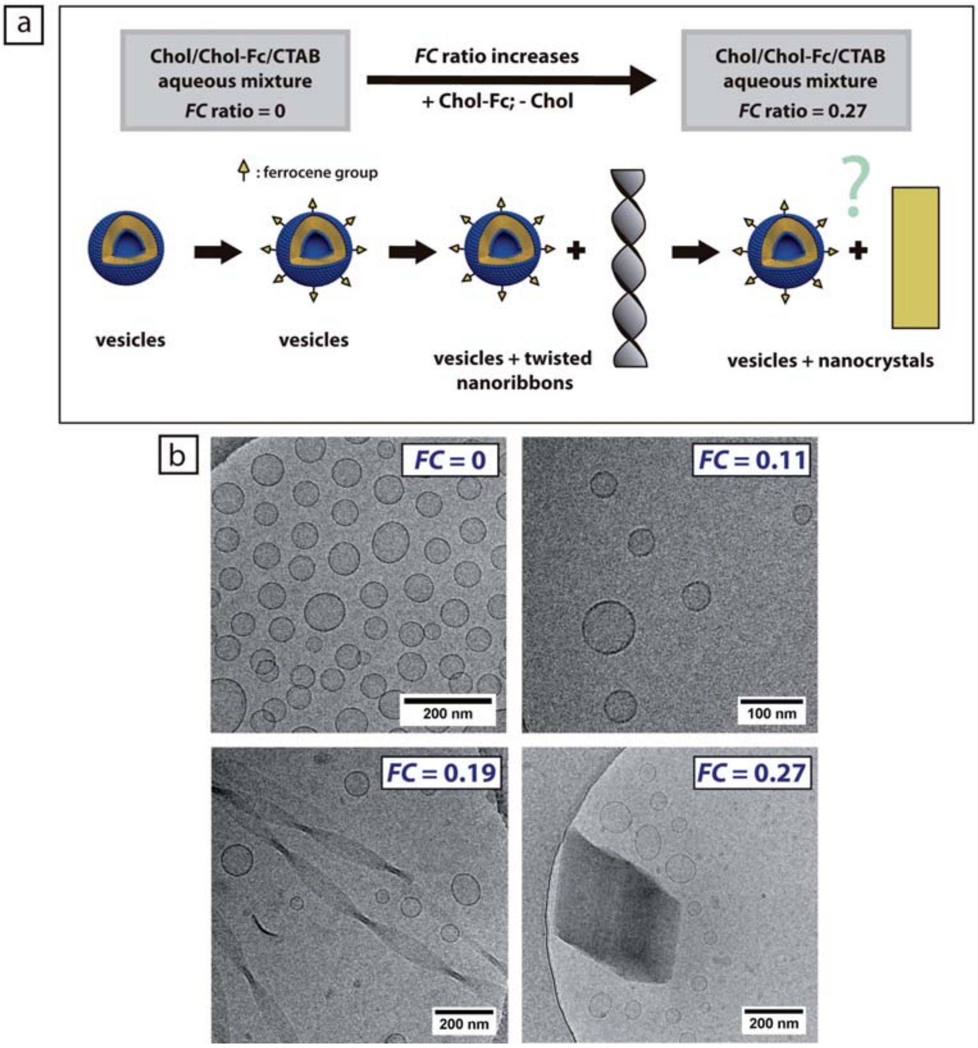

Figure 3.32.: (a) Schematic illustration and (b) cryo-TEM images of the different self-assembled colloidal structures discovered in the studied Chol/Chol-Fc/CTAB aqueous mixtures. *FC* ratio comprises the moles of Chol-Fc over the total moles of cholesterol-like molecules (cholesterol and Chol-Fc). Chol$_{total}$:CTAB 1:1 (molar ratio).

Therefore, this study has demonstrated that the substitution of cholesterol by Chol-Fc in Chol/Chol-Fc/CTAB aqueous mixtures leads to the formation of several supramolecular assemblies as the *FC* ratio increases. Among these structures, it is worth highlighting the formation of the interesting twisted nanoribbons at 0.19 *FC* ratio.

3.3.4. Preparation of Chol/Chol-Fc/CTAB aqueous mixture at 0.19 *FC* ratio by other routes

Since twisted nanoribbons were obtained in Chol/Chol-Fc/CTAB aqueous mixture at 0.19 *FC* ratio by DELOS-SUSP (Table 3.5), the formation of these supramolecular structures was also studied by other routes of preparation. Specifically, experiments with the TFH route [178] with different extrusion protocols were conducted (see Figure 3.33).

In order to prepare the Chol/Chol-Fc/CTAB aqueous mixture at 0.19 *FC* ratio by TFH, the same final concentration of compounds used before by DELOS-SUSP were employed (Section 3.3.1). The followed procedure is explained in Section 6.2.2 of the Experimental Part.

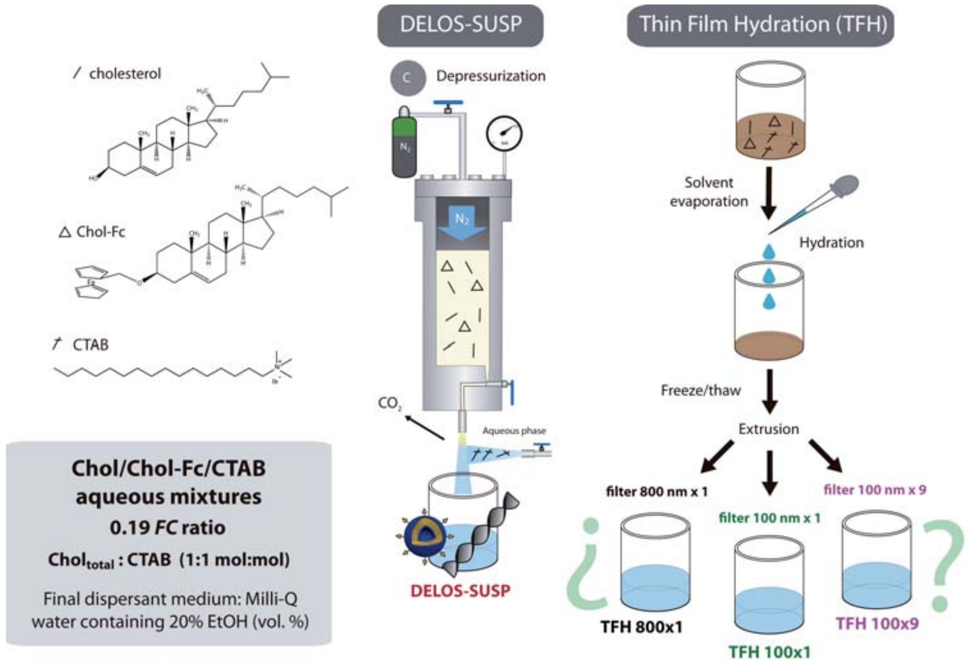

Figure 3.33.: Scheme of the different explored routes for the preparation of twisted nanoribbons at 0.19 *FC* ratio (Table 3.5).

After the hydration step with Milli-Q water containing 20% of EtOH (vol. %) (Figure 3.33), the precipitation of a yellow solid was evident as shown in Figure 3.34a. Despite this fact, the sample preparation was followed by extrusion using three different protocols. The first one was to use a membrane filter with a pore size of 800 nm and the sample was passed through the extruder one time. The second protocol was to reduce the pore size of the membrane filter from 800 nm to 100 nm, keeping constant the number of the extrusions (one time). And the third protocol was to use a membrane filter with 100 nm pore size and the sample was passed through the extruder nine times (more extrusiones were impossible as solid would simply obstruct the filter pores). As shown in Figure 3.34b,c, a large proportion of the yellow solid observed before was retained in the membrane filters used in the extrusion process.

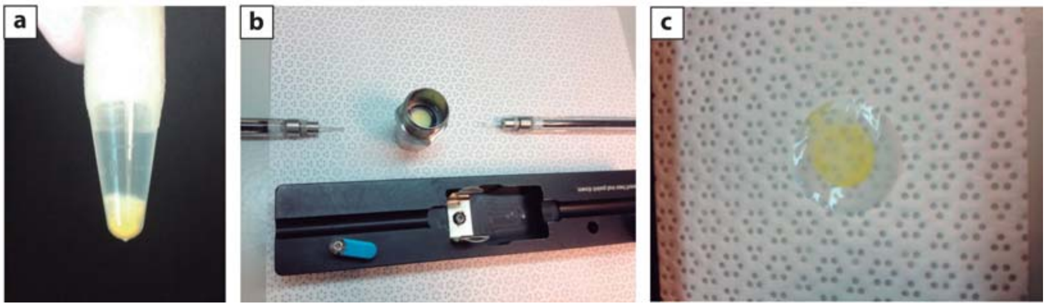

Figure 3.34.: Formation of Chol/Chol-Fc/CTAB aqueous mixture at 0.19 *FC* ratio by TFH followed by different extrusion protocols. (a) Picture of the sample after the hydration step showing the precipitation of a yellow solid. (b-c) Pictures showing the yellow solid retained in the membrane filters after extrusion process.

First of all, the final concentration of Fe in each Chol/Chol-Fc/CTAB aqueous mixture prepared by TFH was quantified by ICP-OES technique after sample preparation (see Section 6.3.4 of the Experimental Part) (Table 3.8).

Table 3.8.: Theoretical and quantified Fe (mg/l) concentration values by ICP-OES of Chol/Chol-Fc/CTAB aqueous mixtures at 0.19 *FC* ratio prepared by different routes.

Methodology	*FC* ratio[a]	Theoretical Fe (mg/l)	Quantified Fe (mg/l)[b]
DELOS-SUSP	0.19	67	52
TFH 800x1	0.19	67	6.5
TFH 100X1	0.19	67	4.7
TFH 100x9	0.19	67	4.6

[a] *FC* ratio = moles Chol-Fc/moles Chol_{total}; moles Chol_{total} = moles Chol + moles Chol-Fc; Chol_{total}:CTAB 1:1 (molar ratio).

[b] Concentration of Fe (mg/l) quantified by ICP-OES.

As shown in Table 3.8, as the pore size of the membrane filter used in the extrusion step decreases and higher number of extrusions have been carried out, the present amount of Fe in the aqueous mixtures decreases. In addition, comparing the concentration value of Fe in the DELOS-SUSP and TFH aqueous mixtures, there is a reduction of at least 8 times using the TFH method. Moreover, Figure 3.35 displays a picture showing the macroscopic appearances of the DELOS-SUSP and TFH (800x1) aqueous mixtures. As illustrated, the DELOS-SUSP sample was yellower than the one prepared by TFH due to the high presence of Chol-Fc. Thus, all these evidences demonstrated that by TFH method there is a loss of Chol-Fc compound in the final aqueous mixtures. Accordingly we can state that the yellow solid observed before in the sample preparation (Figure 3.34) was solid Chol-Fc, which was precipitated in the hydration step likely due to its hydrophobicity.

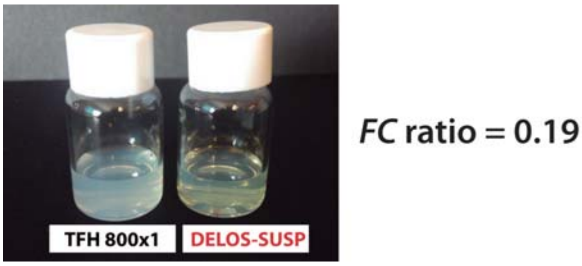

Figure 3.35.: Picture showing the macroscopic appearances of Chol/Chol-Fc/CTAB aqueous mixtures at 0.19 *FC* ratio prepared by DELOS-SUSP and TFH (800x1) methods.

ICP-OES technique has shown that a small incorporation degree of the Chol-Fc compound in Chol/Chol-Fc/CTAB aqueous mixtures was achieved when the TFH methodology was used. However, the three Chol/Chol-Fc/CTAB aqueous mixtures prepared by TFH method using different extrusion protocols were characterized by DLS and cryo-TEM 250 days after sample preparation, where the twisted nanoribbons were observed before with the DELOS-SUSP method. The mean and polydispersity index (PdI) of the particle size distributions and the cryo-TEM images of the aqueous mixtures are displayed in Table 3.9 and Figure 3.36, respectively.

Table 3.9.: Physicochemical characteristics of Chol/Chol-Fc/CTAB aqueous mixtures at 0.19 *FC* ratio prepared by TFH with different extrusion protocols. *Note: Characterizations were carried out 250 days after sample preparation. Samples were stored at 277 K.*

Methodology	***FC***[a] **ratio**	**Size**	
		Mean(nm)[b]	**PdI**[c]
TFH 800x1	0.19	124.6± 2.1	0.288 ± 0.021
TFH 100x1	0.19	93.69± 1.45	0.154 ± 0.006
TFH 100x9	0.19	74.08 ± 0.80	0.100 ± 0.009

[a] *FC* ratio = moles Chol-Fc/moles $Chol_{total}$; moles $Chol_{total}$ = moles Chol + moles Chol-Fc; $Chol_{total}$:CTAB 1:1 (molar ratio).

[b] Intensity weighted mean hydrodynamic size of the systems measured by dynamic light scattering.

[c] Polidispersity index showing the width of the particle size distribution.

As can be ascertained from Figure 3.36, only vesicular systems were observed in all the prepared TFH aqueous mixtures. Besides, vesicles with higher degree of structural homogeneity were achieved reducing the pore size of the filter membrane and increasing the number of extrusions. Thus, owing to the small degree of incorporation of Chol-Fc compound in the TFH aqueous mixtures at 0.19 *FC* ratio, twisted nanoribbons were not discovered in any preparation.

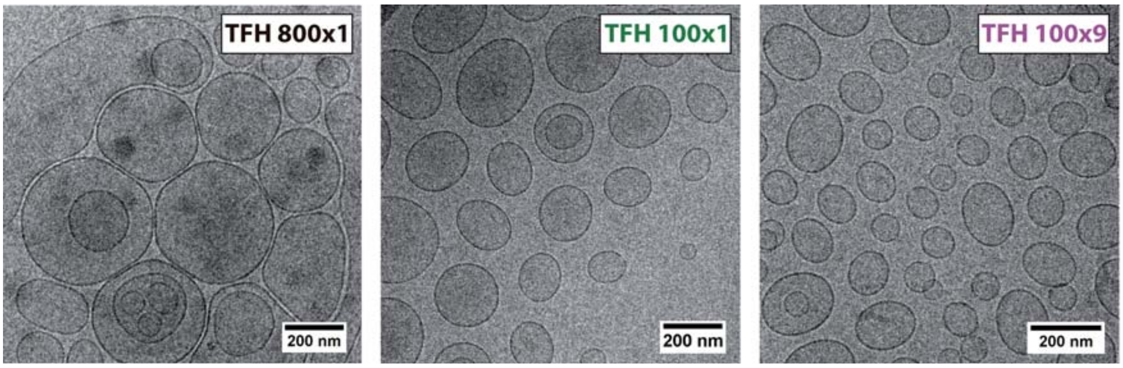

Figure 3.36.: Cryo-TEM images of Chol/Chol-Fc/CTAB aqueous mixtures at 0.19 *FC* ratio prepared by TFH followed by extrusion: (a) 800 nm x 1 time, (b) 100 nm x 1 time and (c) 100 nm x 9 times.

Therefore, ICP-OES technique has shown that a higher incorporation degree of the Chol-Fc compound in Chol/Chol-Fc/CTAB aqueous mixtures was achieved when the DELOS-SUSP methodology was used, consequently twisted nanoribbons were only formed when using this method. For that reason we can state that the DELOS-SUSP process is the best option among the ones studied here if hydrophobic molecules, like Chol-Fc, have to be integrated in aqueous mixtures.

3.3.5. Redox-active Fc-functionalized vesicles

The Chol/Chol-Fc/CTAB aqueous mixture at 0.19 *FC* ratio prepared by DELOS-SUSP (Table 3.5) revealed in Section 3.3.2 the formation of only vesicles after sample preparation (14 days). Due to the presence of Chol-Fc in the system, these vesicles should contain ferrocene moieties and should be redox-active systems, thus they were studied by cyclic voltammetry (CV) technique (Figure 3.37). Furthermore, Chol-CTAB quatsomes prepared also by DELOS-SUSP at 0 *FC* ratio (Table 3.5) were characterized by CV in order to study the plain (non-redox active) quatsomes.

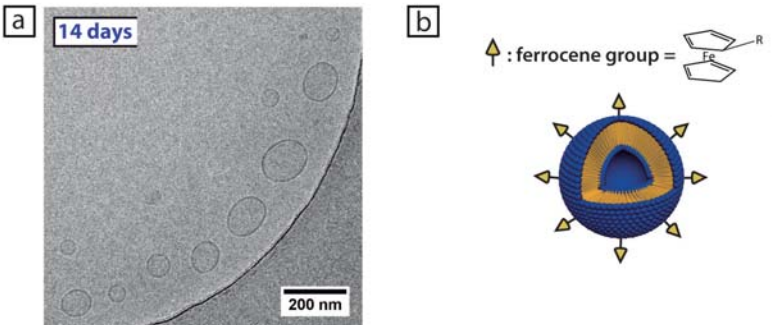

Figure 3.37.: (a) Cryo-TEM image of Fc-functionalized Chol-CTAB vesicles (0.19 *FC* ratio prepared by DELOS-SUSP (Table 3.5)) 14 days after sample preparation. (b) Schematic representation of the Fc-functionalized Chol-CTAB vesicles containing ferrocene moieties.

The CV measurements were conducted by Dr. Núria Crivillers from *Nanomol* group (ICMAB-CSIC) after sample preparation (see Section 6.3.2 of the Experimental Part). The Fc^0 of the Chol-Fc molecule can be easily oxidized to Fc^+(ferricenium, Figure 3.38) which can be reversibly reduced back to the neutral form [240, 245]. In this technique the sample is subject to cyclic potential sweeps at the same time that its electrochemical activity is recorded with an increase of current. Usually an ionic medium is necessary to carry out a cyclic voltammetry experiment but, taking into account the presence of the CTA^+ and the counterion Br^- in the solution, the sample was measured without the addition of an electrolyte. Platinum wires were used as working and counter electrodes and a Ag wire was used as reference electrode. The samples were subjected to 2 potential cycles sweeping the voltage between 0.0 V and + 0.6 V at scan rate of 0.4 V/s.

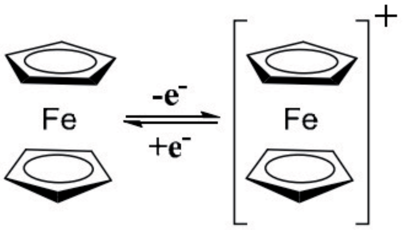

Figure 3.38.: Reversible mono electronic oxidation of ferrocene.

Figure 3.39 displays the cyclic voltammograms of plain and Fc-functionalized Chol-CTAB vesicles (0 and 0.19 *FC* ratio). As shown, the plain quatsomes did not reveal any redox peak, however the Fc-functionalized Chol-CTAB vesicles exhibited one reversible redox wave due to the redox system Fc^0/ Fc^+ at $E^{1/2}$ = 0.28 V (*vs.* Ag (wire)) with a peak to peak separation *(ΔE_{pp})* of 0.120 V. A fast, reversible, one electron transfer would ideally have a ΔE_{pp} = 0.059 V at 298 K. The discrepancy from this ideal value is attributed to slow electron transfers and solution resistance.

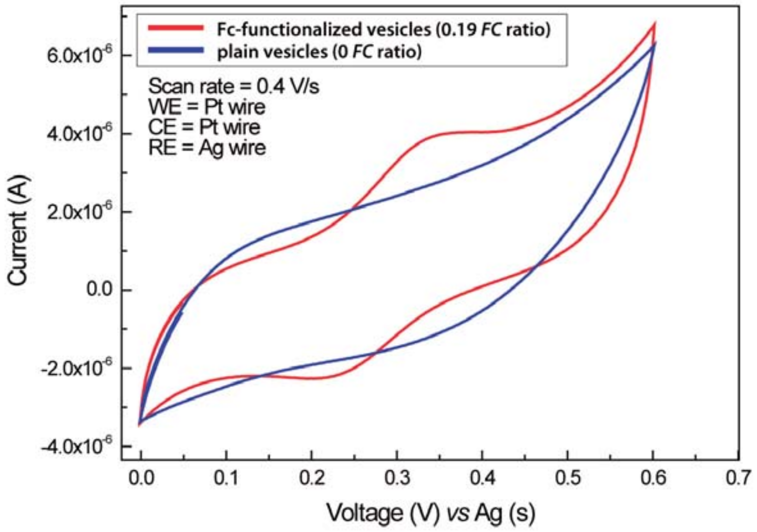

Figure 3.39.: Cyclic voltammograms of plain and Fc-functionalized Chol-CTAB vesicles (0 and 0.19 *FC* ratio).

By CV technique, we have demonstrated successful incorporation of redox-active Chol-Fc molecules into vesicles in an aqueous solution. Therefore, redox-active systems can be prepared by DELOS-SUSP using Chol/Chol-Fc/CTAB aqueous mixtures.

3.3.6. Summary

- This study has demonstrated that the substitution of cholesterol by Chol-Fc in Chol/Chol-Fc/CTAB aqueous mixtures leads to the formation of both, redox-active vesicles and novel self-assembled twisted nanoribbons. By TFH methodology, the incorporation of hydrophobic molecules, like Chol-Fc, is much harder than by DELOS-SUSP, as a result twisted nanoribbons were not obtained by this method. Therefore, DELOS-SUSP method is the the best option among the ones studied here if hydrophobic molecules have to be integrated in aqueous mixtures.

3.4. One-dimensional (1D) self-assembled nanostructures

One-dimensional (1D) nanostructures, especially ribbons and nanotubes with a single dimension that is much longer than the others [224], are still regarded as exotic structures that fall outside the well-accepted paradigms of the field of self-assembly, as opposed to the self-assembly of amphiphilic molecules into conventional aggregates/phases such as micelles, vesicles, and lyotropic liquid crystals, which is a mature and well-understood subject [230].

Upon the studies described in this Chapter, we can state that working with CTAB and cholesterol in Milli-Q water with 20% of EtOH (vol. %), the substitution of cholesterol by cholesterol derivatives functionalized with new moieties changes the packing parameter of the aqueous mixtures and several self-assembled colloidal nanostructures can be observed. Specifically, using the both studied cholesterol derivatives, Chol-VS and Chol-Fc, and working with the DELOS-SUSP method, one-dimensional (1D) nanoribbons were formed by hydrophobic interactions, which are the driving force for the self-organization [230] (Figure 3.40). Besides, other weak interactions like hydrogen bonding or aromatic $\pi - \pi$ stacking can also assisted the formation of these nanoribbons [224].

Self-assembly of small molecules into one-dimensional (1-D) nanostructures offers many potential applications in electronically and biologically active materials. The potential of 1-D nanostructure is great given their inherent ability to serve as conduits of charge and to align elements in their surroundings such as molecules, macromolecules, and even cells. Additionally, 1-D objects are ubiquitous in biology and serve critical functions such as the fibrils in the structural and signaling machinery of extracellular matrices, the cellular cytoskeleton, axons, dendrites, and many others. Moreover, 1-D nanostructures, readily form three-dimensional networks giving rise to gel matter from solutions. Gel-like matter with high content of one-dimensional soft nanostructures is the substrate to create functionality in mammalian biology (organs, tissues), and there must be an equivalent phase space of synthetic structures that could be accessed and designed for novel functions [224, 232].

In nanotechnology, 1-D assemblies were further used as scaffolds for creating nanowires [246] and nanowires complexes carrying electric signals, for creating layered nanoparticles [247], as well as for mineralization. In addition, helical nanostructures, like twisted nanoribbons, are important targets for use in biomaterials, nonlinear optics, and stereoselective catalysis [232].

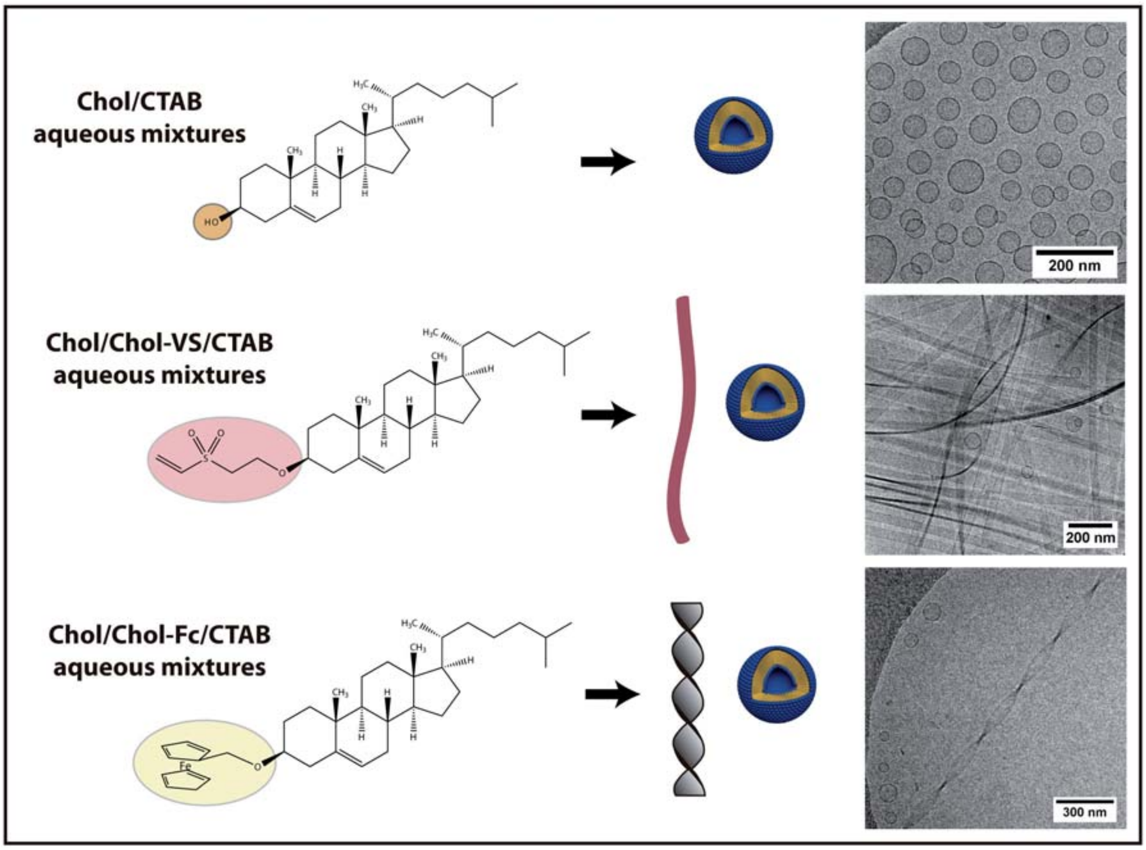

Figure 3.40.: Nanoribbons revealed in the Chol/Chol-VS/CTAB aqueous mixtures and Chol/Chol-Fc/CTAB aqueous mixtures studied in this Chapter.

Therefore, the obtained flat and twisted nanoribbons described in this Chapter have a lot of potential applications in many different fields.

4

Highly fluorescent silicon nanocrystals stabilized in water using quatsomes

4.1. Introduction

One of the fundamental goals in biology is to understand the complex spatio-temporal interplay of biomolecules from the cellular to the integrative level [248]. To study these interactions, researchers commonly use fluorescent labelling for both *in vivo* cellular imaging and *in vitro* assay detection [249]. However, the intrinsic photo-physical properties of organic and genetically encoded fluorophores, which generally have broad absorption/emission profiles [249] and low photobleaching thresholds, have limited their effectiveness in long-term imaging and 'multiplexing' (simultaneous detection of multiple signals) without complex instrumentation and processing [248, 250]. Against this background, quantum dots, nanocrystals of a semiconducting material with diameters in the range of 2-10 nanometers, have the potential to overcome these difficulties [251–254].

The luminescence characteristics of molecular dyes and quantum dot nanocrystals are a consequence of their electronic structure. Whilst molecules have a discrete energy level spectrum and solids have continuous bands of energy levels, nanoparticles are intermediate and can be viewed either as large molecules or small pieces of the solid. The color of luminescence from these systems depends on the energy gap between the highest occupied molecular orbital and the lowest unoccupied molecular orbital. Nanoparticles in the size range where the electronic properties are changing between solid-like and molecular have luminescence characteristics strongly dependent on their size. These particles are commonly known as quantum dot nanocrystals because the size-dependent changes in electronic structure are related to the constraint imposed on the electron wavefunctions by the surface as the particle radius decreases – an effect known as quantum confinement [251, 255].

Quantum dot nanocrystals possess several distinct advantages over their organic counterparts. Firstly, a narrow emission spectrum reduces spectral overlap. This increases the feasibility of distinguishing multiple fluorophores simultaneously. Secondly, the broad excitation spectrum of quantum dots facilitates the use of a single excitation wavelength to excite quantum dots of different colors. Thirdly, the large separation between the excitation and emission wavelength of quantum dots (the Stokes' shift) enables the whole emission spectra to be collected, resulting in improved sensitivity of detection. Quantum dot nanocrystals are often brighter than conventional dyes due to the compounded effects of extinction coefficients that are an order of magnitude larger than those of most dyes, comparable quantum yield, and similar emission saturation levels [248, 252]. They are also not prone to variations in luminescence efficiency due to self-quenching. However, their main advantage resides in their resistance to bleaching over long periods of time (minutes to hours): this allows the acquisition of images that are both crisp and have high contrast. This increased photostability is particularly useful for three-dimensional (3D) optical sectioning, where bleaching of the fluorophores during acquisition of successive z-sections is a major issue [252]. Some applications of quantum dot nanocrystals as multimodal contrast agents in bioimaging are summarized in Figure 4.1 [251, 252].

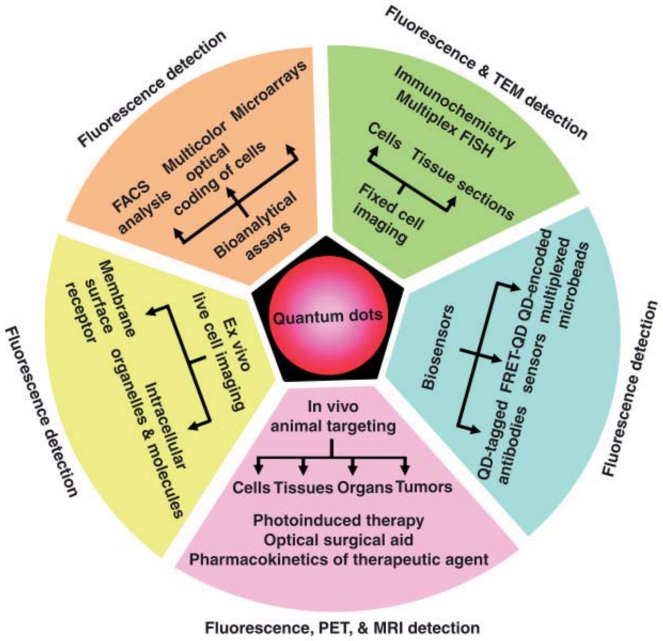

Figure 4.1.: Applications of quantum dot nanocrystals as multimodal contrast agents in bioimaging. Obtained from [252].

Although quantum dot nanocrystals have been studied extensively for biomedical imaging applications due to their fluorescence properties as well as photostability, many systems utilize heavy metals such as cadmium that have shown to be toxic [252, 253]. In this context, silicon nanocrystals (SiNCs) offer a biocompatible alternative to toxic quantum dots that exhibit emission in the visible to near-infrared region (NIR) [251, 256–258]. Although silicon is an indirect band gap material, at the nanoscale the emission spectrum can be tuned according to the nanocrystal size, with 2.8 nm SiNCs emitting orange [251, 259, 260]. These nanocrystals can be stably dispersed in organic solvents following the covalent attachment of capping ligands which result in hydrophobic SiNCs, but as far as we are concern, these hydrophobic SiNCs have never been stably dispersed in water [251, 256, 258, 261, 262].

Silicon nanocrystals for use in medical applications must be dispersible in water and one common approach to achieve this for hydrophobic particles is to use colloidal nanoparticles, such as micelles, vesicles and polymer nanoparticles, as vehicles for their stabilization in aqueous media [258, 262–270].

In this context, the purpose of this Chapter was to explore whether fluorescent SiNCs could be integrated into Chol-CTAB quatsomes, with the intention of providing a system that has long term stability for delivering the nanocrystals into aqueous environments. As mentioned in Chapter 2, the morphology of Chol-CTAB quatsomes is unaffected upon increasing the temperature or by dilution, making them ideal candidates for use *in vivo*. Besides, these Chol-CTAB quatsomes are an interesting option to stabilize SiNCs, since they are highly stable aqueous colloidal structures, they have antibacterial and anti-biofilm properties [215], and they were already used successfully for the preparation of stable vesicle-biomolecule conjugates [122, 124, 223] and for the protection of ESIPT fluorophores in aqueous media [214]. These results make them promising nanocarriers in the development of new nanovesicle-nanocrystal hybrids.

Within this framework, during this Thesis a short research stay was conducted during four months at the University of Texas at Austin, under the supervision of Prof. Brian A. Korgel. There I worked together with the PhD student Dorothy Silbaugh. In this research stay I became familiar with the nanoparticle preparation and manipulation and we studied the possibility to create quatsome-nanocrystal hybrids.

4.2. Incorporation of silicon nanocrystals into Chol-CTAB quatsomes

4.2.1. Preparation of SiNCs

The silicon nanocrystals (SiNCs) were synthesized according to previously reported methods [256]. The preparation of these nanocrystals is explained in the Section 6.8.1 of the Experimental Part. These SiNCs were prepared using 1-octene (MW = 112.24 g/mol) as a ligand (Figure 4.2).

Figure 4.2.: Molecular structure of the ligand use in the silicon nanocrystal preparation.

The obtained SiNCs were imaged using transmission electron microscopy (TEM) (see Section 6.3.13 of the Experimental Part) and they are shown in Figure 4.3a-c. Results from measuring 150 SiNCs from TEM images determined that the average size was 2.80 nm with a standard deviation of 0.60 nm (Figure 4.3d).

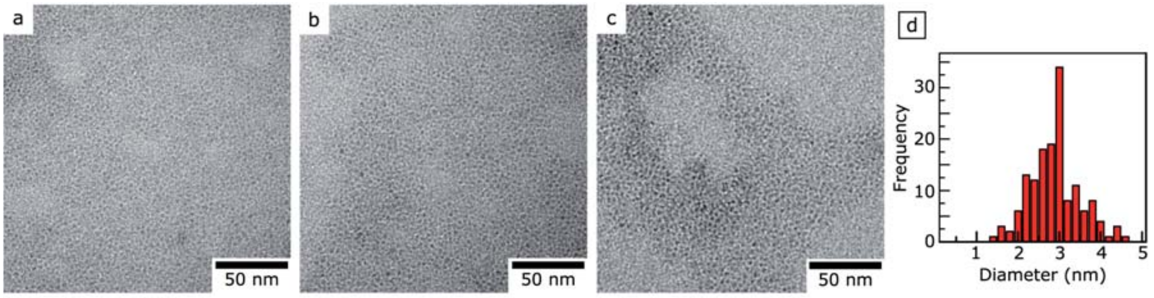

Figure 4.3.: TEM images (a-c) of octene-coated SiNCs prepared. A sample of 150 nanocrystals (25 each from 6 images) were measured from the TEM images and the histogram is shown in (d), with the average size found to be 2.80 nm with a standard deviation of 0.60 nm.

To calculate the final concentration of these SiNCs in chloroform, a known volume of sample was dried and weighed to determine the mass of the nanocrystals in this volume. The obtained concentration was approximately 6.75 mg/ml in chloroform. Besides, the relative amount of Si and organic capping ligand in the nanocrystal sample was determined using thermal gravity analysis (TGA) (Figure 4.4). During TGA, organic ligands are removed, leaving inorganic Si core oxidized to SiO_2. The relative mass of Si and organic ligand in the sample was determined from the remaining mass of SiO_2 and the total weight loss was due to the removal of the organic ligands. It was determined that the prepared SiNCs had an estimated mass fraction of ligand of 63% and silicon core of 37%.

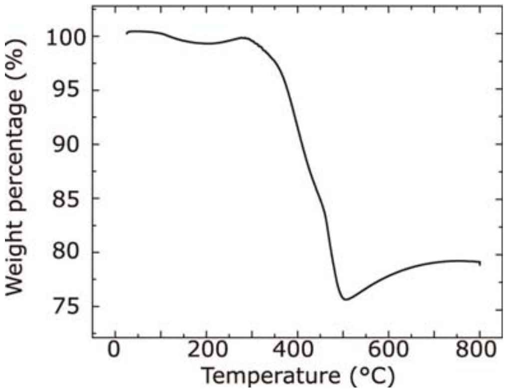

Figure 4.4.: Results of thermogravimetric analysis of silicon nanocrystals coated with octene ligand.

TGA data can be used to calculate the average number of ligand per nanocrystal by assuming spherical nanocrystal with density of bulk material (2.329 x 10^{-21}g/nm^3) [271].

$$N_{ligand/nanocrystal} = \frac{4}{3}\pi r^3 \rho_{Si} x \frac{(1 - Si_{wt}\%)}{Si_{wt}\%} x \frac{6.02x10^{23}}{MW_{ligand}} \tag{4.1}$$

In Equation 4.1, r is average radius of Si nanocrystal determined by TEM, ρ_{si} is the bulk density of Si, $Si_{wt}\%$ is weight percentage of Si in the Si nanocrystal determined by TGA, and MW_{ligand} is molecular weight of 1-octene. The ligand packing density can be calculated dividing the average number of ligand per NC by the surface area of the NC ($4\pi r^2$). For a 2.8 nm diameter nanocrystal, the calculated average number of ligand per NC was 244.67, and the ligand density on the surface of the NC was approximately 9.93 ligands/nm^2.

The molar mass of these nanocrystals (M_{NC}, in units of grams per mole of nanocrystals) was calculated using the following expression:

$$M_{NC} = \frac{4}{3}\pi r^3 \rho_{Si} x \frac{1}{Si_{wt}\%} x \frac{6.02x10^{23} NC}{mole} = 43,554.9\, g/mole \tag{4.2}$$

A schematic representation of the synthesized silicon nanocrystals (SiNCs) is shown in Figure 4.5.

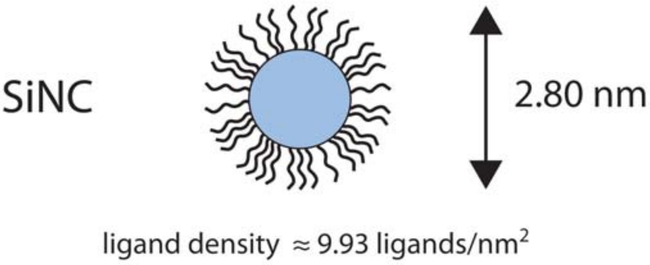

Figure 4.5.: Schematic representation of the synthesized SiNCs.

Finally, Figure 4.6 displays the prepared octene-coated SiNCs under ambient light and 365 nm UV light. As shown, the SiNC exhibit bright photoluminescence (PL) upon excitation by UV light.

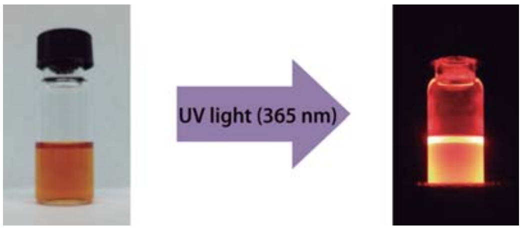

Figure 4.6.: Photographs of prepared SiNCs dispersed in chloroform under ambient light and 365 nm UV light to show the nanocrystal fluorescence.

4.2.2. Chol-CTAB quatsome preparation

Chol-CTAB (W10Et-DELOS) quatsomes (Table 6.3 of the Experimental Part) were synthesized using the DELOS-SUSP procedure (see Section 6.2.1 of the Experimental Part). Briefly, 76 mg of cholesterol in 2.88 ml of ethanol was pressurized with CO_2 at X_{CO_2} = 0.6 and depressurized over 24 ml of Milli-Q water containing 72 mg of CTAB. The final concentration of quatsomes in this vesicular phase, 7.3 mM Chol-CTAB quatsomes, included 7.3 mM cholesterol and 7.3 mM CTAB in high purity water containing 10% ethanol (vol. %).

The dynamic light scattering (DLS) measurements of these quatsomes revealed a mean size of 78.36 ± 0.69 nm (PdI 0.345 ± 0.004). As displayed in Figure 4.7a, unilamellar and spherical nanovesicles were obtained.

Besides, these vesicles were observed under 365 nm UV light, and as shown in Figure 4.7b, these plain vesicles did not fluoresce.

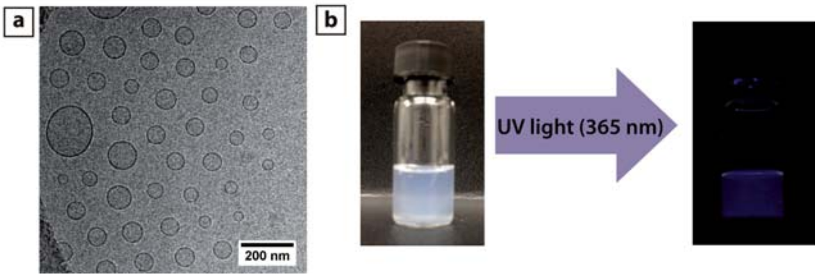

Figure 4.7.: (a) Cryo-TEM image of obtained Chol-CTAB (W10Et-DELOS) quatsomes in water with 10% EtOH (vol. %). (b) Photographs of such quatsomes under ambient light and 365 nm UV light showing that these plain vesicles did not fluoresce.

4.2.3. Incorporation methodology and operational parameters

In order to incorporate the obtained SiNC (Section 4.2.1) into Chol-CTAB quatsomes, different approaches were studied. First of all, attempts were made to add SiNCs directly into the DELOS-SUSP process to form quatsomes, but the result was a non-fluorescent dispersion (data not shown). Most likely, the SiNCs degraded during the process due to the pressure and temperature used in the DELOS-SUSP procedure, or perhaps the nanocrystals were not incorporated into quatsomes and instead became stuck in the DELOS-SUSP setup. Afterwards, other attempts were carried out assembling the SiNCs with pre-made Chol-CTAB (W10Et-DELOS) quatsomes (Section 4.2.2). Specifically, vortexing and bath sonication were used at room temperature to provide energy to the system. As shown in Figure 4.8, attempts to use 5 minutes of vortexing to incorporate 20 µl SiNCs in chloroform (6.75 mg/ml) to 750 µl of Chol-CTAB quatsomes (7.3 mM) resulted in very limited fluorescence in solution. However, as presented in the same Figure, 5 minutes of bath sonication using the same amount of components provided a fluorescent sample.

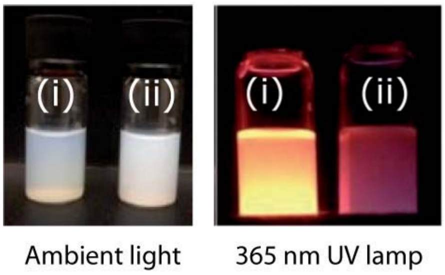

Figure 4.8.: Comparison of (i) 5 minute bath sonication to (ii) 5 minute vortex to incorporate 20 µl SiNCs in chloroform (6.75 mg/ml) into 750 µl of Chol-CTAB quatsomes (7.3 mM), under ambient light and 365 nm UV light. Vortexed vial appeared cloudy and did not fluoresce.

Due to this remarkable finding using 5 minutes of bath sonication (Misonix 1510R-

MT or Bransonic M1800 bath sonicator, 40 kHz), further experiments were explored to disperse the SiNCs in Chol-CTAB (W10Et-DELOS) quatsomes (Figure 4.9).

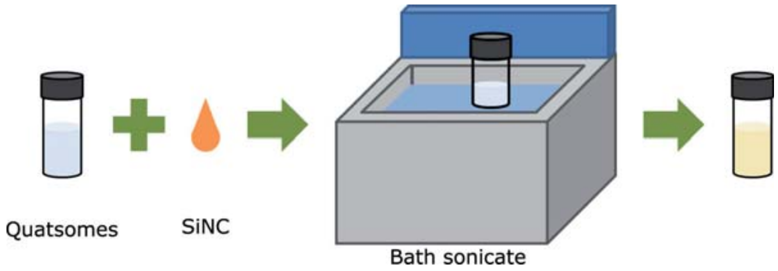

Figure 4.9.: Schematic representation of the studied process for incorporating SiNCs into quatsomes through bath sonication.

First of all, the volumes and concentrations of SiNCs added to quatsomes were examined to maximize incorporation of nanocrystals while not disrupting the quatsome structures (see Figure 4.10). To each of 5 vials, 750 µl Chol-CTAB (W10Et-DELOS) quatsomes (7.3 mM Chol-CTAB) was added. Then, 135 µg of SiNCs was added to each vial, though at different concentrations and thus in different volumes of chloroform, and the samples were sonicated 5 minutes at room temperature. The ratio between quatsomes and SiNC was maintained constant. The amounts added were: (i) 10 µl of 13.5 mg/ml SiNC in chloroform, (ii) 20 µl of 6.75 mg/ml SiNC in chloroform, (iii) 40 µl of 3.375 mg/ml SiNC in chloroform, (iv) 80 µl of 1.6875 mg/ml SiNC in chloroform, (v) 200 µl of 0.675 mg/ml SiNC in chloroform. Images of the vials taken over several days after preparation indicate that while all exhibited fluorescence from SiNC incorporation, only the vial prepared with 20 µl of 6.75 mg/ml SiNC in chloroform did not have any precipitate (Figure 4.10). In vial (i) an orange-brown precipitate was observed after one day, likely containing SiNCs that were not incorporated into the quatsomes. In vials (iii), (iv), and (v) the solutions became cloudy white and the bottoms of the vials had white precipitate. Water and chloroform are immiscible solvents, thus the high volume fraction of chloroform added with the SiNCs had a destabilizing effect on the quatsomes and caused the structures to break apart.

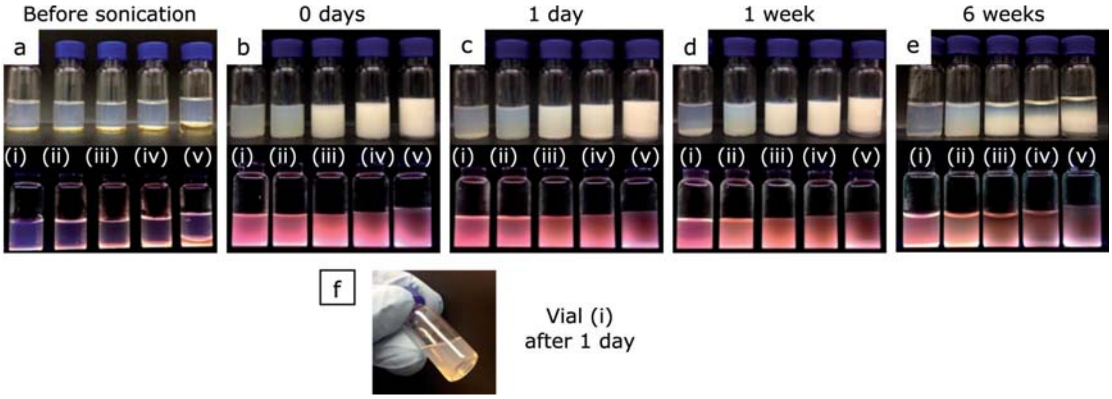

Figure 4.10.: Results of adding different volume ratios of SiNCs (in chloroform) : quatsomes (in water with 10% EtOH), under ambient light (top row) and on a 254 nm UV lamp (bottom row). In each sample 135 µg of SiNCs was added, though in different concentrations, and thus volumes over 750 µl of Chol-CTAB (W10Et-DELOS) quatsomes. Samples from left to right are: (i) 10 µl of 13.5 mg/ml SiNC in chloroform, (ii) 20 µl of 6.75 mg/ml SiNC in chloroform, (iii) 40 µl of 3.375 mg/ml SiNC in chloroform, (iv) 80 µl of 1.6875 mg/ml SiNC in chloroform, (v) 200 µl of 0.675 mg/ml SiNC in chloroform. Within one day after preparation (f), vial (i) had orange-brown precipitate consistent with SiNCs, while vials (iii), (iv), and (v) had white precipitate and remained very cloudy.

Therefore, experiments to determine how the chloroform may interact with the quatsomes found that the volume ratio of quatsomes to SiNCs in chloroform influenced the assemblies stability. A small amount of chloroform is known to enhance the incorporation of dodecanethiol-capped Au nanocrystals into liposomes [264], and a similar interaction may be occurring with quatsomes, resulting in successful incorporation without destroying the quatsomes when 20 µl of chloroform is added.

Therefore, the best results were obtained adding 20 µl of 6.75 mg/ml SiNC in chloroform into 750 µl of Chol-CTAB (W10Et-DELOS) quatsomes, consequently this ratio was used in the following experiments.

4.2.4. Stability of dispersions of silicon nanocrystals in Chol-CTAB quatsomes

Once the preparation operational parameters were properly defined, samples of SiNCs dispersed with Chol-CTAB (W10Et-DELOS) quatsomes in water with 10% ethanol were prepared through 5 minutes of bath sonication, along with control samples prepared with only CTAB, no quatsomes, or no SiNCs, as outlined in Table 4.1 and Figure 4.11a-e. Besides, 10-fold diluted Chol-CTAB (W10Et-DELOS) quatsomes in water with 10% ethanol, with a final concentration of 0.73 mM Chol-CTAB, were also used to disperse the SiNCs in order to investigate the influence of the SiNC/quatsome ratio. Thus, Chol-CTAB quatsomes with CTAB concentration above (7.3 mM) and below (0.73 mM) the critical micelle concentration (cmc) of CTAB, where used as dispersants (samples (1) and (2)). It has to be noted that the cmc of CTAB in water with 10% EtOH is 1.5 mM [233].

Besides, taking into account that molar mass of the SiNCs used was 43,554.9 g/mole (calculated in Section 4.2.1), the molar ratio of components in each sample was calculated and is given in Table 4.1.

Table 4.1.: Description of samples (1-5) monitored in stability testing.

Sample	**SiNCs**	**Dispersant**	**Molar ratio of components**
(1)	20 μl of 6.75 mg/ml SiNCs in chloroform	750 μl of 7.3 mM quatsomes (7.3 mM CTAB, 7.3 mM Chol) in water (10% EtOH)	1 SiNC: 1695 CTAB: 1695 Chol
(2)	20 μl of 6.75 mg/ml SiNCs in chloroform	750 μl of 0.73 mM quatsomes (0.73 mM CTAB, 0.73 mM Chol) in water (10% EtOH)	1 SiNC: 170 CTAB: 170 Chol
(3)	20 μl of 6.75 mg/ml SiNCs in chloroform	750 μl of 7.3 mM CTAB in water (10% EtOH)	1 SiNC: 1695 CTAB
(4)	20 μl of 6.75 mg/ml SiNCs in chloroform	750 μl of water (10% EtOH)	-
(5)	20 μl of chloroform	750 μl of 7.3 mM quatsomes (7.3 mM CTAB, 7.3 mM Chol) in water (10% EtOH)	-

The fluorescence stability, the absorbance spectroscopy (see Section 6.3.14 of the Experimental Part) and the photoluminescence spectroscopy (PL) (see Section 6.3.9 of the Experimental Part) of all these samples were monitored for 12 weeks (Figure 4.11). Immediately following bath sonication the solutions containing Chol-CTAB quatsomes and CTAB micelles (samples (1), (2), (3)) appeared cloudy, however after one day the turbidity dissipated. The initial turbidity likely occurred as a result of the high energy applied causing changes in the supramolecular structures. In the case where SiNCs were directly added to water, the nanoparticles precipitated to the bottom of the vial after 5 minutes of bath sonication, which was anticipated for hydrophobic nanocrystals added to an aqueous solution.

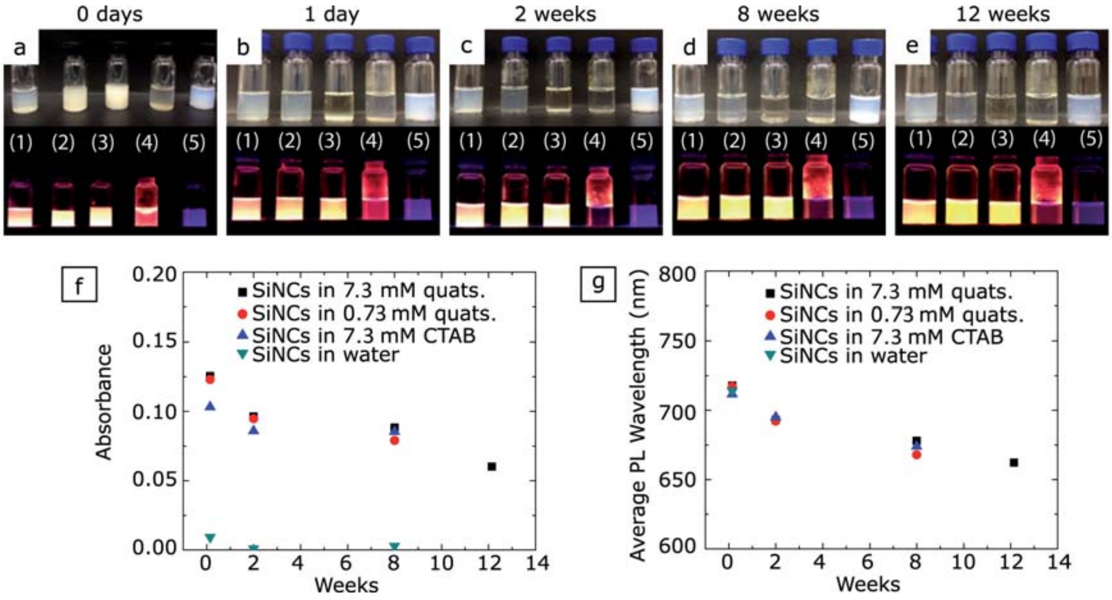

Figure 4.11.: Fluorescence stability tracking of SiNCs incorporated into quatsomes and control solutions, over time. All the dispersant media were water with 10% ethanol. The five samples monitored were (1) SiNCs in 7.3 mM Chol-CTAB quatsomes (with CTAB concentration above cmc), (2) SiNCs in 0.73 mM Chol-CTAB quatsomes (with CTAB concentration below cmc), (3) SiNCs in 7.3 mM CTAB micelles, (4) SiNCs in water with 10% EtOH, and (5) chloroform in 7.3 mM Chol-CTAB quatsomes. Vials were prepared by adding 20 µl SiNC (in chloroform, 6.75 mg/ml) to 0.75 ml of solution, and then bath sonicated for 5 minutes. Photographs of vials under ambient light (top) and on a 365 nm UV lamp (bottom) taken (a) immediately, (b) one day, (c) 2 weeks, (d) 8 weeks, and (e) 12 weeks after preparation. Absorbance (f) measured at 320 nm for samples with SiNCs and average PL wavelength (g) for samples with SiNCs (excited at 320 nm) demonstrate the stability of the nanoparticle fluorescence in quatsomes.

As can be ascertained from Figure 4.11, samples prepared with Chol-CTAB quatsomes above (7.3 mM) and below (0.73 mM) the 1.5 mM CTAB cmc, sample (1) and sample (2), respectively, [233] were both observed to maintain similar absorbance and PL over time (Figure 4.11f,g). The lack of a significant blue shift (only 56 nm over twelve weeks) in the PL spectra indicates that the nanoparticles are protected from oxidation or degradation that would normally occur if the nanocrystals were directly dispersed into aqueous solutions, as seen in sample (4). Besides, as shown in Figure 4.11, SiNCs could also be dispersed with 7.3 mM CTAB micelles with good dispersion and fluorescence stability. To get further insights into the structures formed in samples (1), (2), and (3), they were also studied under cryo-TEM.

It is noteworthy that in sample (5), where 20 µl of chloroform without SiNCs was added to quatsomes and bath sonication was performed, no precipitation of material was observed, suggesting that the amount of chloroform could not destabilize the quatsome structure.

4.2.4.1. Sample (1): SiNCs dispersed in Chol-CTAB quatsomes (molar ratio SiNC:CTAB:Chol 1:1695:1695)

Sample (1), where 20 µl of SiNCs (6.75 mg/ml) were dispersed in 750 µl of 7.3 mM Chol-CTAB quatsomes, was monitored for twelve weeks by cryo-TEM (Figure 4.13).

As can be inferred from Figure 4.13, although many of the quatsomes are free of nanocrystals, there was still a significant amount of association between the SiNCs and the quatsomes. The nanocrystals formed aggregates that were either on one side of one or multiple quatsomes or that appeared to form spherical structures with similar sizes as the quatsomes without NC aggregates. Besides, there were no observed changes in size or shape during this time period.

Figure 4.12 illustrates such structures, where examples are shown for spherical structures of SiNCs with similar sizes as plain quatsomes (red arrows), quatsomes with SiNCs on one side (green arrows), and quatsomes connected by SiNC aggregates (blue arrows).

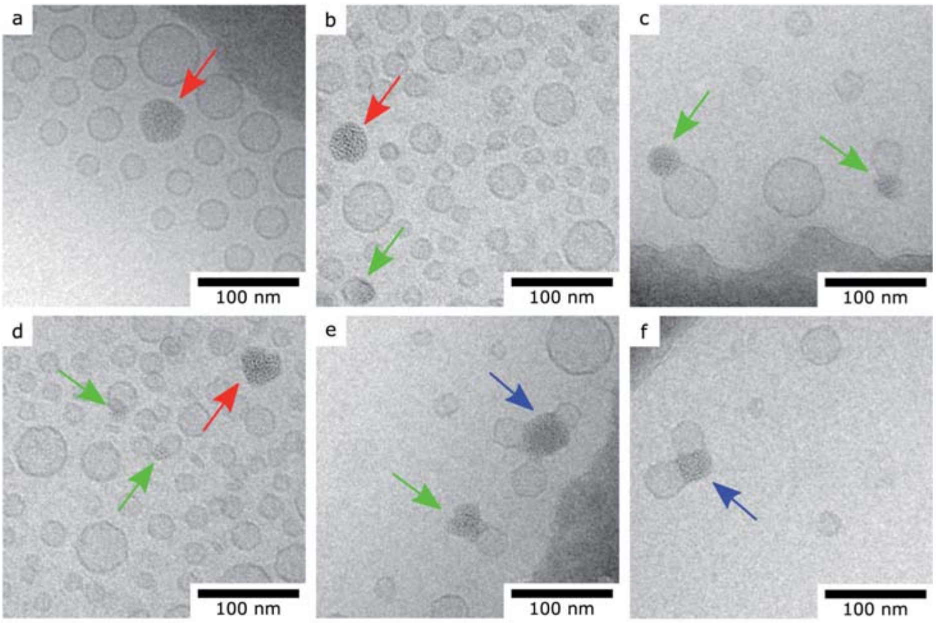

Figure 4.12.: Cryo-TEM images of fluorescent dispersions of quatsomes and SiNCs. Examples are shown for spherical structures of SiNCs with similar sizes as plain quatsomes (red arrows), quatsomes with SiNCs on one side (green arrows), and quatsomes connected by SiNC aggregates (blue arrows). Empty quatsomes with no SiNCs incorporated are also present in each image.

In order to compare the fluoresence properties of SiNCs dispersed in chloroform and the same SiNCs dispersed in Chol-CTAB quatsomes, the absorbance (Section 6.3.14 of the Experimental Part), photoluminescence (PL) and photoluminescence excitation (PLE) (Section 6.3.9 of the Experimental Part) of both systems were measured and

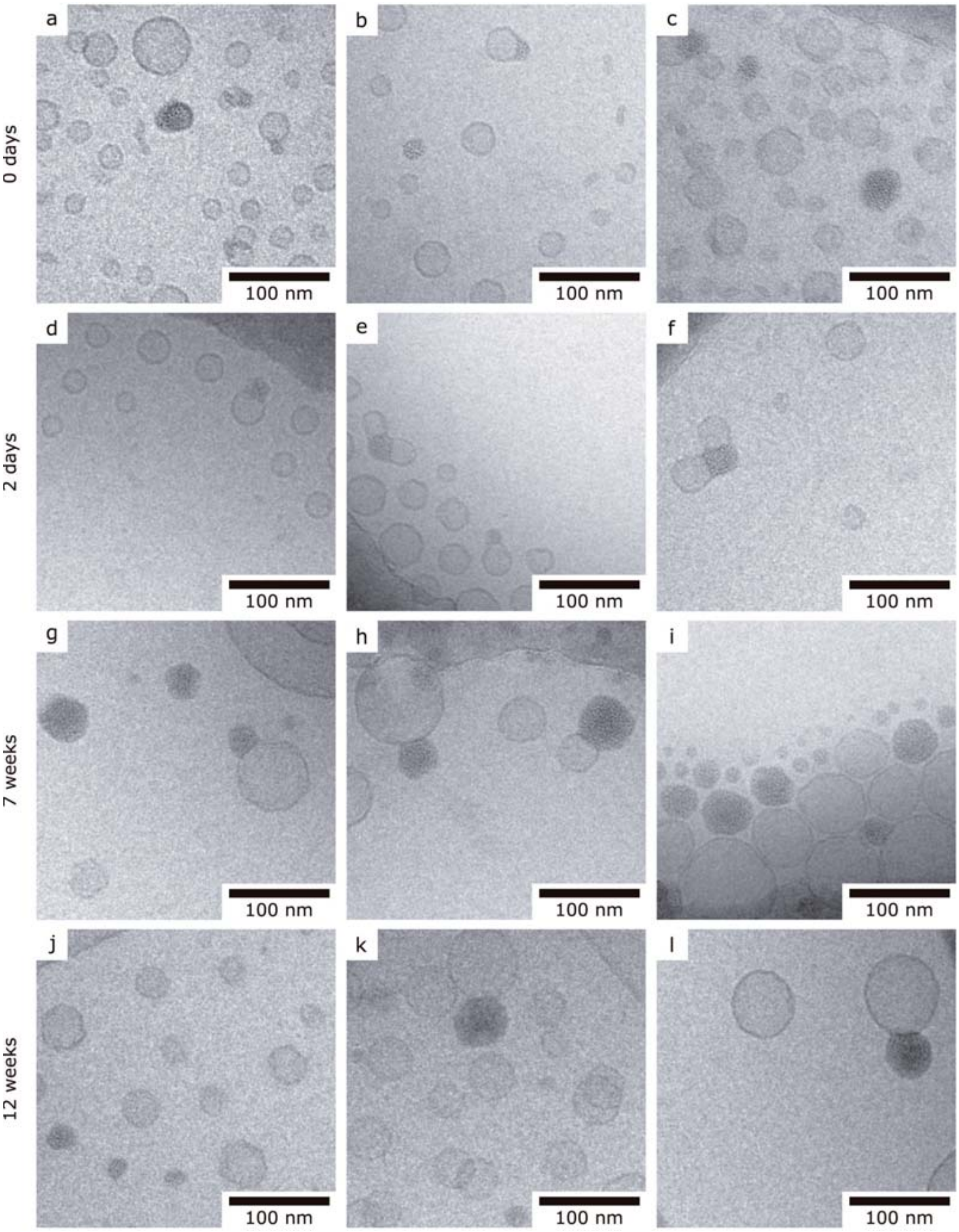

Figure 4.13.: Cryo-TEM images of the structures observed after incorporation of SiNCs into quatsomes (7.3 mM Chol-CTAB) through 5 minutes of bath sonication (sample (1)). Sample prepared at 1:1695:1695 SiNC:CTAB:Chol molar ratio. Images were taken (a-c) on day sample prepared, (d-f) 2 days after sample prepared, (g-i) 7 weeks after sample prepared, (j-l) 12 weeks after sample prepared.

plotted together (Figure 4.14).

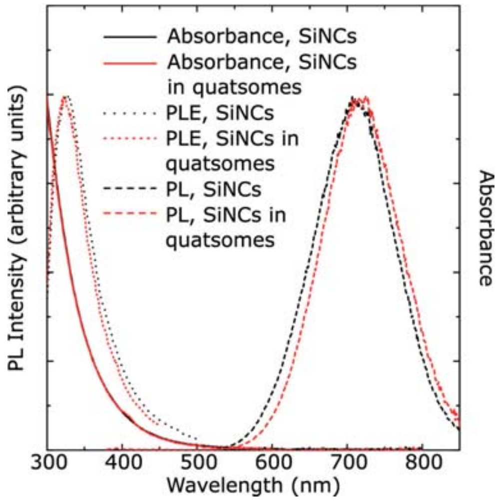

Figure 4.14.: Normalized absorbance (solid lines), PL (320 nm excitation) (dashed lines), and PLE (660 nm emission for SiNC in chloroform, 670 nm emission for SiNC in quatsomes) (dotted lines) spectra for octene coated SiNCs dispersed in chloroform (black) or incorporated into quatsomes (red) in an aqueous media.

As shown in Figure 4.14, the spectra of each sample are similar, indicating that the incorporation of the nanocrystals into the quatsomes, in an aqueous media, did not change the fluorescence properties of the nanocrystals when dispersed in chloroform.

This type of optical properties of SiNC in an aqueous medium have not been observed previously, as far as we know, and demonstrate the goodness of quatsomes for the stabilization of SiNC in aqueous media.

4.2.4.2. Sample (2): SiNCs dispersed in Chol-CTAB quatsomes (molar ratio SiNC:CTAB:Chol 1:170:170)

Sample (2), where a higher SiNC/quatsome molar ratio was used compared with sample (1), was also investigated under cryo-TEM. As outlined in Table 4.1, 750 µl of 0.73 mM Chol-CTAB quatsomes was combined with 20 µl of 6.75 mg/ml SiNCs in chloroform The images obtained (Figure 4.15) indicate that the structures formed are similar to those when 7.3 mM Chol-CTAB quatsomes was used, including one sided and full quatsome aggregates. The fact that the Chol-CTAB quatsomes at 7.3 mM and 0.73 mM have similar stability suggests that these systems have a high ability to stabilize nanocrystals even when working with very different SiNC/quatsome molar ratios.

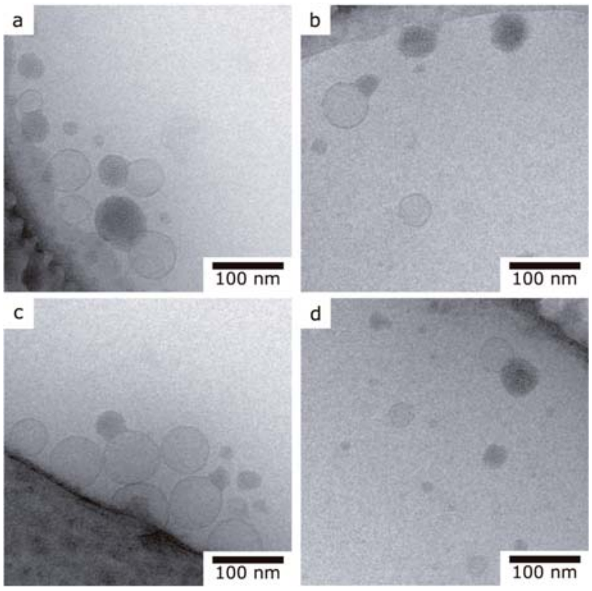

Figure 4.15.: Cryo-TEM images of sample (2), SiNCs in low concentration of quatsomes (below CTAB cmc). 750 µl of 0.73 mM Chol-CTAB quatsomes was combined with 20 µl of 6.75 mg/ml SiNCs in chloroform, and the mixture was bath sonicated for 5 minutes. Sample prepared at 1:170:170 SiNC:CTAB:Chol molar ratio.

4.2.4.3. Sample (3): SiNCs dispersed in CTAB micelles (molar ratio SiNC:CTAB 1:1695)

Unlike samples (1) and (2), where vesicles were used to stabilize the SiNCs, CTAB micelles were used for the same purpose in sample (3). As stated in Figure 4.11, SiNCs could also be dispersed with 7.3 mM CTAB micelles with good dispersion and fluorescence stability. For that reason, sample (3) was also studied under cryo-TEM. The obtained images (Figure 4.16) showed that the CTAB-stabilized nanocrystals were irregularly shaped aggregates that were both very small and very large, thus the shape of the nanocrystal aggregates were quite different than those stabilized by the quatsomes. For medical applications consistent size and concentration of load delivery is important, and thus the wide size distribution observed with CTAB micelles would not be ideal for those applications.

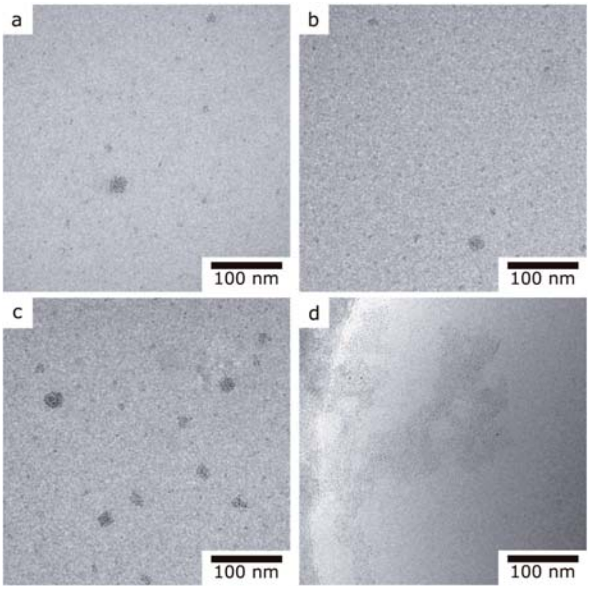

Figure 4.16.: Cryo-TEM images of sample (3), CTAB stabilized SiNCs. 750 µl of 7.3 mM CTAB micelles in water was combined with 20 µl of 6.75 mg/ml SiNCs (in chloroform), and the mixture was bath sonicated for 5 minutes. Sample prepared at 1:1695 SiNC:CTAB molar ratio.

4.2.5. Stability of SiNCs dispersed in Chol-CTAB quatsomes and in CTAB micelles upon dilution

Medical diagnostic or theranostic applications where fluorescent NCs dispersions are used as contrast agents, usually involve the dilution of the fluorescent formulations. Therefore, it is very important for this kind of formulations to demonstrate that they keep they physicochemical and fluorescent properties upon dilution.

The stability of SiNCs dispersed with Chol-CTAB quatsomes and CTAB micelles at equal CTAB concentrations was assessed by dialysis into water, as shown in Figure 4.17. Sample (1) (SiNCs dispersed with Chol-CTAB quatsomes) and sample (3) (SiNCs dispersed with CTAB micelles) of Table 4.1 were used for this investigation. The molar ratio between SiNC:CTAB was 1:1695 in both samples.

One day after bath sonication of SiNCs with either 7.3 mM Chol-CTAB quatsomes (sample (1)) or 7.3 mM CTAB micelles (sample (3)) in 10% ethanol, the samples were each added to dialysis tubing (SnakeSkin Dialysis Tubing, 22 mm 10 K molecular weight cutoff, Life Technologies) and sealed at both ends with locking closures. The dialysis bags were then immersed in 1 L of DI water under magnetic stirring. After 24 hours the water was changed, and this process was repeat for a total of six water changes. Following completion of the dialysis the remaining solutions inside the dialysis tubing were transferred to glass vials.

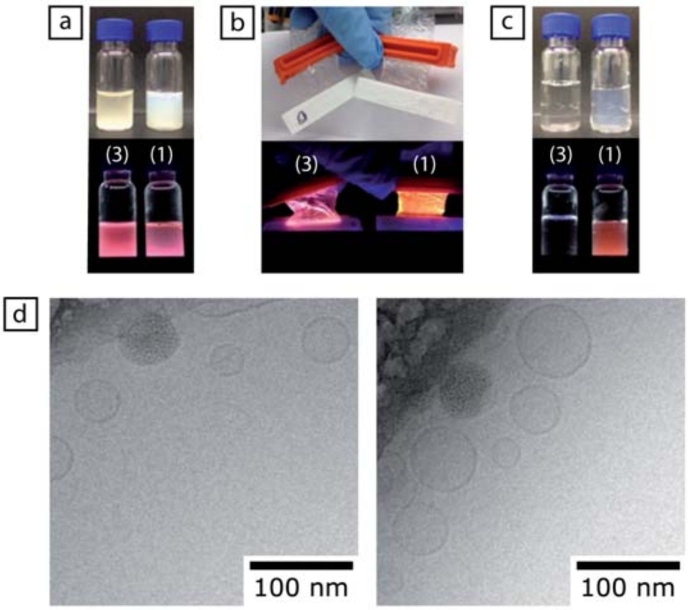

Figure 4.17.: Dilution by dialysis of SiNCs dispersed in 7.3 mM CTAB micelles (sample (3), left in each photograph) or 7.3 mM Chol-CTAB quatsomes (sample (1), right in each photograph). (a) Photographs of vials containing both samples one day after preparation with 5 minutes of bath sonication, prior to addition into dialysis tubing, under ambient light (top) and on 254 nm UV lamp (bottom). (b) Photograph of dialysis tubing with solutions after 6 rounds of dialysis, under ambient light (top) and on a 254 nm UV lamp (bottom). (c) Photograph of solutions removed from dialysis tubing after 6 rounds of dialysis, under ambient light (top) and on 254 nm UV lamp (bottom). (d) Cryo-TEM images of sample (1) with Chol-CTAB quatsomes and SiNCs following 6 rounds of dialysis.

Both dispersions were initially fluorescent, but as shown in Figure 4.17c, only the quatsome dispersion remained fluorescent after dialysis. This suggests that the CTAB surfactant is only weakly associated with the SiNCs in the micelles, and that with repeated dilutions the structures disassemble. In contrast, quatsome-SiNC assemblies imaged by cryo-TEM after six rounds of dialysis still show structures similar to the freshly prepared materials, which indicates that even after multiple dilutions these assemblies are stable (Figure 4.17d). This finding shows the benefit of the Chol-CTAB quatsome assemblies as compared to the CTAB micelles: while both maintain fluorescence for 12 weeks (Figure 4.11), only the quatsome-SiNC hybrids keep their structure upon dilution, which makes them more adequate for fluorescence labeling for *in vivo* imaging applications.

4.2.6. Comparison to liposomal structures

Stabilization of SiNC with charge-neutral DOPC and anionic DOPG liposomal systems was attempted, for comparison purposes with SiNC stabilized with Chol-CTAB (W10Et-

DELOS) quatsomes.

DOPC liposomes were prepared by DELOS-SUSP (see Section 6.5.2 of the Experimental Part). The final concentration of DOPC in the liposomal system was 3.6 mM in high purity water containing 17% ethanol, thus these systems were called DOPC (W17Et-DELOS) liposomes (see Table 6.4 of the Experimental Part).

The DOPG liposomes were formed by TFH method with extrusion with a 100 nm membrane pore size, extruding the sample 21 times (see Section 6.5.3 of the Experimental Part). The final concentration of DOPG in the liposomal system was 7 mM in 10 mM HEPES buffer with 10 mM NaCl, thus these systems were called DOPG (HEPES-TFH100x21) liposomes (see Table 6.4 of the Experimental Part).

DLS measurements (Table 4.2) and cryo-TEM images of DOPC and DOPG liposomes (Figure 4.18b,f) revealed that in both systems, unilamellar and spherical nanovesicles were obtained.

Once the DOPC and DOPG liposomes were prepared and characterized, SiNCs were incorporated into them the same manner as the quatsomes: 20 µl of 6.75 mg/ml SiNCs (0.135 mg) was added to 750 µl of either 3.6 mM DOPC or 7 mM DOPG liposomes and then bath sonicated for 5 minutes.

Table 4.2.: Physicochemical characteristics of DOPC (W17Et-DELOS) liposomes and DOPG (HEPES-TFH100x21) liposomes measured after preparation.

Liposomal[a] system	**Size**		**Morphology[d]**
	Mean(nm)[b]	**PdI[c]**	
DOPC liposomes	58.05 ± 1.73	0.230 ± 0.008	SUVs
DOPG liposomes	71.19 ± 0.86	0.298 ± 0.008	SUVs

[a] Samples were stored at 277 K.
[b] Intensity weighted mean hydrodynamic size of the collection of vesicles measured by dynamic light scattering.
[c] Polidispersity index showing the width of the particle size distribution.
[d] Morphology of the vesicles observed by cryo-TEM. SUVs: Small unilamellar vesicles.

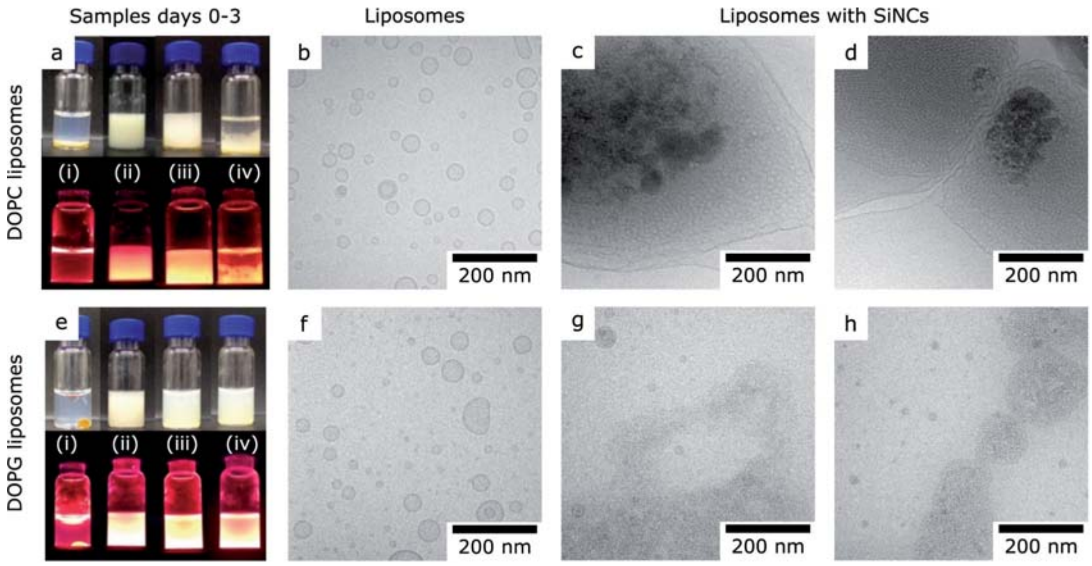

Figure 4.18.: Results from preparing DOPC (neutral) and DOPG (anionic) liposomes separately and then adding 20 µl SiNCs in chloroform (6.75 mg/ml) and bath sonicating for 5 minutes. Photographs of vials of (a) DOPC and (e) DOPG were taken under ambient light and on a 365 nm UV lamp (i) before bath sonication, (ii) immediately after sonication, (iii) after 1 day, and (iv) after 3 days, showing that DOPC precipitated out of solution while the DOPG solution remained turbid. Cryo-TEM images of the liposomes before adding nanocrystals showed that the (b) DOPC and (f) DOPG liposomes formed small unilamellar vesicles (SUVs). Cryo-TEM images (c-d) of the DOPC liposomes after bath sonication, in the presence of SiNC, showed that NCs incorporated with the lipid, forming large complexes. Cryo-TEM images (g-h) of the DOPG liposomes after bath sonication, in the presence of SiNC, showed that the NCs aggregated outside of empty liposomes, and no incorporation with the liposomes was observed.

As the cryo-TEM images shown in Figure 4.18c,d, the charge-neutral DOPC liposomes become multilamellar and large SiNC aggregates are observed. Besides, the fluorescence stability tracking of the vial containing the DOPC liposomes and SiNCs (Figure 4.18a) revealed after 3 days, a white precipitate at the bottom vial that was likely large lipid structures.

Figure 4.18e-h indicates that the anionic DOPG liposomes retained their initial size, but no SiNCs were observed to associate with the liposomes. The dispersion, however, was fluorescent and separate lipid-stabilized aggregates of SiNCs were observed. These dispersions loose their fluorescence after the third day.

These results indicate that SiNCs do not incorporate into size-monodisperse DOPC or DOPG liposomes through the bath sonication process that has been demonstrated as an efficient process for the formation of quatsome-SiNC hybrids.

4.2.7. SiNCs incorporation into Chol-CTAB quatsomes free of ethanol

To assess the impact of the presence of ethanol in the quatsome-SiNC suspension, Chol-CTAB (W-US) quatsomes were prepared with no ethanol using the sonication methodology previously described in Chapter 2 (Section 2.3.1.2) (see Table 6.3 of the Experimental Part). Briefly, 38.6 mg of cholesterol and 36.4 mg of CTAB were weighed into a glass bottle and suspended in 10 ml of Milli-Q water. The dispersion was then sonicated at 298 K for 4 minutes to form a homogeneous dispersion.

After allowing the mixture to stabilize for one week at 298 K, silicon nanocrystals were incorporated using the standard incorporation process (20 µl SiNCs 6.75 mg/ml in chloroform added to 750 µl quatsomes, then bath sonicated for 5 minutes). The samples appeared consistent with quatsome-SiNC assemblies studied before using quatsomes with 10% of EtOH prepared by DELOS-SUSP method. Cryo-TEM images of the samples show the nanocrystals incorporated into some of the quatsomes. This data shows that the presence of ethanol is not a requirement for the formation of quatsome-SiNC structures.

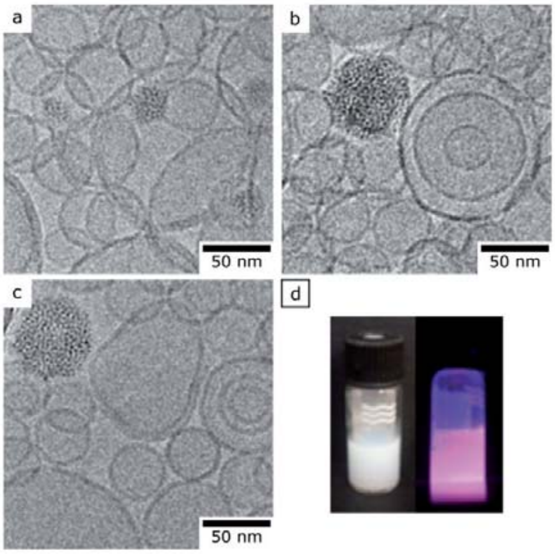

Figure 4.19.: Results of incorporating SiNCs into Chol-CTAB (W-US) quatsomes formed with only water (no ethanol). (a-c) Cryo-TEM images showing assembly of SiNCs into quatsomes. (d) Photographs of vials containing the quatsomes under ambient light (left) and on a 365 nm ultraviolet lamp (right), showing the characteristic fluorescence from the silicon nanocrystals.

4.2.8. Effects of bath sonication on quatsome structure

To explore the effects of bath sonication on the quatsome structures, 1 minute, 5 minutes, 15 minutes, and 30 minutes of bath sonication were used following addition of 20 µl SiNCs in chloroform (6.75 mg/ml) to 750 µl of 7.3 mM Chol-CTAB (W10Et-DELOS) quatsomes.

As can be ascertained from Figure 4.20, both cryo-TEM images and DLS data indicated that bath sonication affect the size of the quatsomes in solution. While the quatsomes maintained similar size distributions after bath sonication for 1 or 5 minutes, a high decrease of the quatsome sizes was observed with sonication times of 15 or 30 minutes. Therefore, this study revealed that the bath sonication process can decrease quatsome sizes due to a redistribution of quatsome membrane molecules. A similar peak narrowing phenomena was observed in vesicle assemblies formed by cholesterol and zwitterionic surfactants [272].

Furthermore, it is worth highlighting that in all samples studied with different bath sonication times (Figure 4.20), association between the SiNCs and the quatsomes was observed.

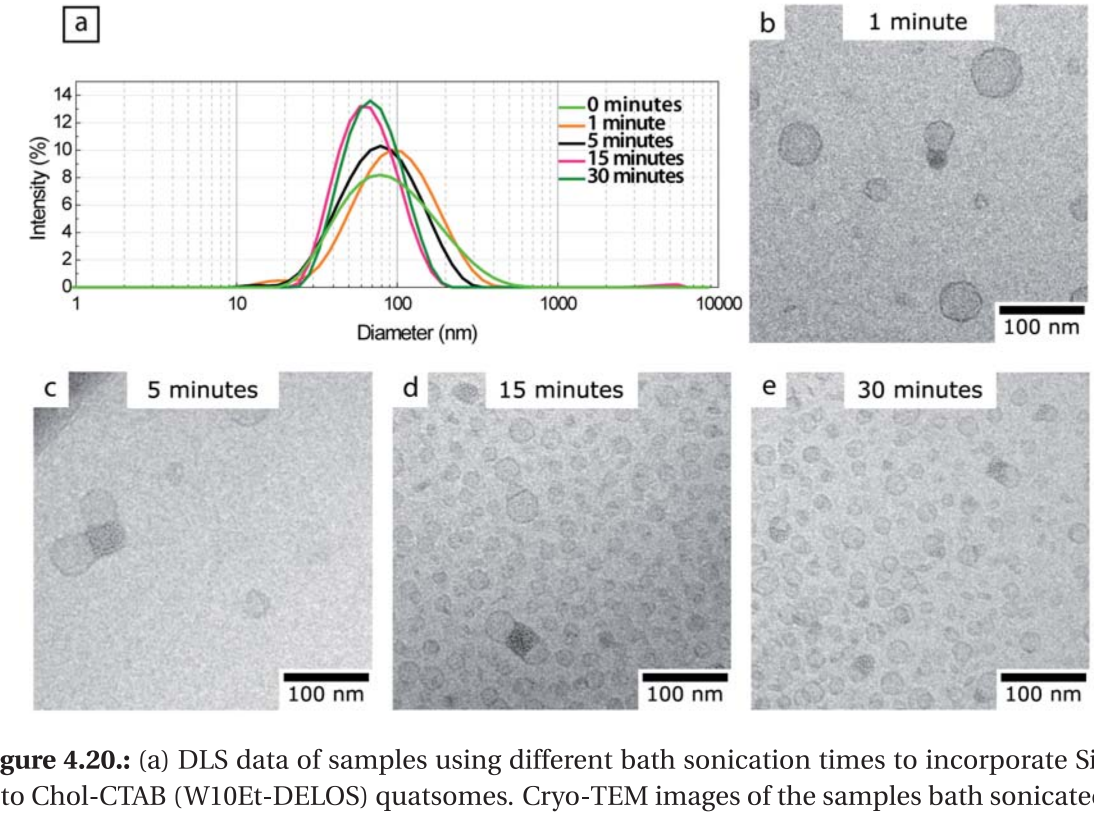

Figure 4.20.: (a) DLS data of samples using different bath sonication times to incorporate SiNCs into Chol-CTAB (W10Et-DELOS) quatsomes. Cryo-TEM images of the samples bath sonicated for (b) 1 minute, (c) 5 minutes, (d) 15 minutes, and (e) 30 minutes revealed that at the longer time points of 15 and 30 minutes, quatsomes appear smaller in size.

4.3. Incorporation of gold nanocrystals into Chol-CTAB quatsomes

In order to explore the capability of quatsomes for the water stabilization of other NC, in this Thesis was attempted the formation of quatsome-gold nanocrystal (AuNC) hybrids.

4.3.1. Preparation of AuNCs

Gold nanocrystals were synthesized using previously reported methods [263]. The preparation of these nanocrystals is explained in the Section 6.8.2 of the Experimental Part. The AuNCs were prepared using 1-dodecanethiol (MW = 202.40 g/mol) as a ligand (Figure 4.21).

Figure 4.21.: Molecular structure of the ligand use in the gold nanocrystal preparation.

Gold nanocrystals prepared were imaged under transmission electron microscopy (TEM) (see Section 6.3.13 of the Experimental Part) to confirm size and shape characteristics (Figure 4.22a,b). Results from measuring 150 AuNCs from TEM images determined that the average size was 1.77 nm with a standard deviation of 0.41 nm (Figure 4.22c).

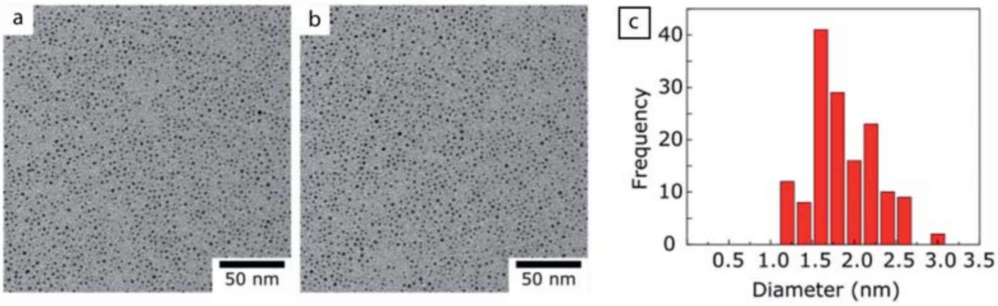

Figure 4.22.: (a-b) TEM images of the obtained gold nanocrystals. A sample of 150 nanocrystals were measured from the TEM images and the histogram is shown in (c), with the average size found to be 1.77 nm with a standard deviation of 0.41 nm.

To calculate the final concentration of these AuNCs in chloroform, a known volume of sample was dried and weighed to determine the mass of the nanocrystals in this volume. The obtained concentration was approximately 3 mg/ml in chloroform.

AuNCs, as prepared per the methods described in the Experimental Part, have an estimated mass fraction of ligand of 27% and Au core of 73% [264]. These data can be used to calculate the average number of ligand per nanocrystal by assuming spherical nanocrystal with density of bulk material (19.3 x 10^{-21}g/nm^3) [271].

$$N_{ligand/nanocrystal} = \frac{4}{3}\pi r^3 \rho_{Au} x \frac{(1 - Au_{wt}\%)}{Au_{wt}\%} x \frac{6.02x10^{23}}{MW_{ligand}} \tag{4.3}$$

In Equation 4.3, r is average radius of Au nanocrystal, ρ_{Au} is the bulk density of Au, $Au_{wt}\%$ is weight percentage of Au in the Au nanocrystal (0.73), and MW_{ligand} is molecular weight of 1-dodecanethiol. The ligand packing density can be calculated dividing the average number of ligand per NC by the surface area of the NC *($4\pi r^2$)*. For a 1.8 nm diameter nanocrystal [264], the calculated average number of ligand per NC was 64.83, and the ligand density on the surface of the NC was approximately 6.37 ligands/nm^2. It is worth highlighting that this is less dense than the coverage for silicon nanocrystals, which was estimated approximately 9.93 ligands/nm^2.

A schematic representation of the synthesized gold nanocrystals (AuNCs) is shown in Figure 4.23.

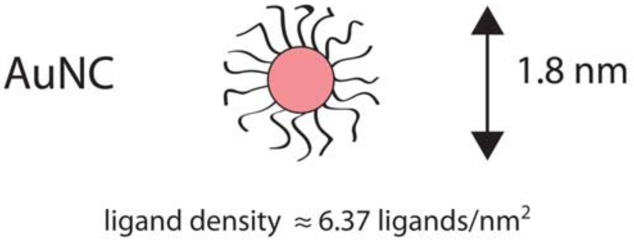

Figure 4.23.: Schematic representation of the synthesized AuNCs.

4.3.2. Stability of dispersions of AuNCs in Chol-CTAB quatsomes

We attempted to disperse the 1.8 nm diameter dodecanethiol-capped gold nanocrystals (AuNCs) with quatsomes. 20 µl of 3 mg/ml AuNCs, which initially appeared brown-black in chloroform, was added to 750 µl 7.3 mM Chol-CTAB (W10Et-DELOS) quatsomes (Section 4.2.2) and the mixture was bath sonicated for 5 minutes. Immediately after sonication, the solution appeared cloudy and had a grey hue, indicating that the nanocrystals were dispersed throughout the solution with no visible precipitate (Figure 4.24a). The group of Prof. Brian A. Korgel has previously demonstrated that AuNCs incorporate into the lipid bilayer of phosphatidylcholine liposomes [263, 264], however the dispersions of AuNCs with Chol-CTAB quatsomes were not stable and changed from a grey to purple color after just a few days. A plasmon peak at around 520 nm emerged in the absorbance spectra, indicating that nanocrystals had aggregated or coalesced, since 1.8 nm gold nanocrystals that are well dispersed do not exhibit a plasmon peak, while aggregates or particles of larger sizes result in plasmonic resonance in the range of 500-600 nm, depending on the particle size, shape, and surrounding conditions [264].

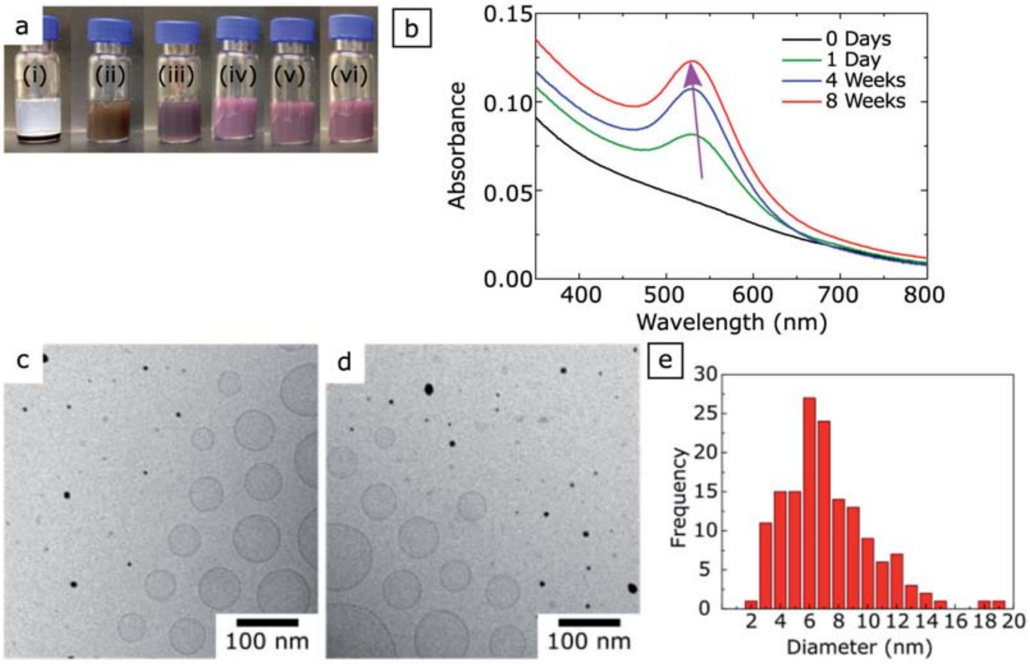

Figure 4.24.: Results of incorporating 1.8 nm dodecanethiol capped AuNCs into quatsomes through 5 minutes of bath sonication (750 µl of 7.3 mM Chol-CTAB quatsomes with 20 µl of AuNC 3 mg/ml in chloroform). (a) Photographs of vial with AuNC and quatsomes over 8 weeks showed a gradual change in color from brown-grey to purple. From left to right: (i) before sonication, (ii) immediately after sonication, (iii) after 1 day, (iv) after 2 weeks, (v) after 4 weeks, and (vi) after 8 weeks. UV-Vis data for samples over time (b) showed increase in plasmon peak intensity (samples diluted 1/20 for measurements). Cryo-TEM images (c,d) of purple AuNC-quatsome dispersion, showing coalesced gold nanoparticles separate from empty quatsomes. (e) Measurements of nanocrystal size indicating that while the gold nanocrystals in chloroform had an average size of 1.77 nm with a standard deviation of 0.41 nm, after the dispersion turned purple the AuNC average size was 6.72 nm with a standard deviation of 3.00 nm.

Indeed, cryo-TEM of the purple solution (Figure 4.24c,d) found that the nanocrystals had coalesced into larger particles separate from the empty quatsomes. Results from measuring 150 Au coalesced particles from cryo-TEM images determined that the average size was 6.72 nm with a standard deviation of 3.00 nm (see Figure 4.24e).

4.4. Proposed interaction mechanism between NC and quatsome structure

4.4.1. Molecular Dynamics (MD) simulations of SiNCs and AuNCs

In order to better understand at molecular level, why SiNC can be stabilized in aqueous media in the presence of Chol-CTAB quatsomes and why AuNC cannot, all-atomic Molecular Dynamics (MD) simulations of the two types of NCs were performed by Dr. Jordi Faraudo from the Institut de Ciència de Materials de Barcelona (ICMAB-CSIC).

Molecular Dynamics (MD) simulations were used to numerically solve the Newtonian equations of motion for the atoms of a model of both Si and Au nanoparticles with their respective capping molecules at the given thermodynamic conditions. All simulations were done using the NAMD 2.9 (CUDA version) software [141]. Simulations were performed for both Si and Au nanoparticles with their respective capping molecules in two different solvents (water and chloroform) at a temperature of 298 K and pressure of 1 atm. According to experimental data, a Si particle was made of a core of 342 Si atoms (in order to obtain a NC diameter of 2.8 nm as in experiments) and 242 capping molecules (1-octene). An Au particle was made of 281 Au atoms (in order to obtain a NC diameter of 1.8 nm as in experiments) and 65 capping molecules (1-dodecanethiol). This corresponds to a coverage of 9.8 molecules/nm^2 for SiNCs and 6.4 molecules/nm^2 for AuNCs. Typical simulation systems, which included passivated particles and solvent, contained several tens of thousands of atoms. The interactions between atoms were modeled employing the standard CHARMM force field for Si, Au and water and the CGenFF version of the CHARMM force field [273] for chloroform, 1-octene and 1-dodecanethiol. More details on the preparation of systems, system details and simulation protocols can be found in the Section A.3 of the Appendix.

In Figure 4.25, images of snapshots from the MD simulations are shown corresponding to the two kinds of particles considered in this work (SiNC and AuNC with their organic capping ligands) in the two different solvents involved in the experiments (water and chloroform). As seen in Figure 4.25, the structure of the capping layer of the two NCs is very different. Silicon nanocrystals have a very compact, solid-like layer of octane molecules, which form ordered patterns that are clearly visible both in water and chloroform. In both cases, octane molecules covering SiNCs are found in an extended configuration, which corresponds to a fully extended chain. In contrast, gold nanocrystals have a disordered, fluid-like, hairy layer of 1-dodecanethiol capping molecules, which is more disordered in chloroform than in water. The simulations indicated that 1-dodecanethiol molecules covering AuNCs do not follow well defined orientations, in contrast with the case of 1-octene molecules capping SiNC (see Section A.3 of the Appendix).

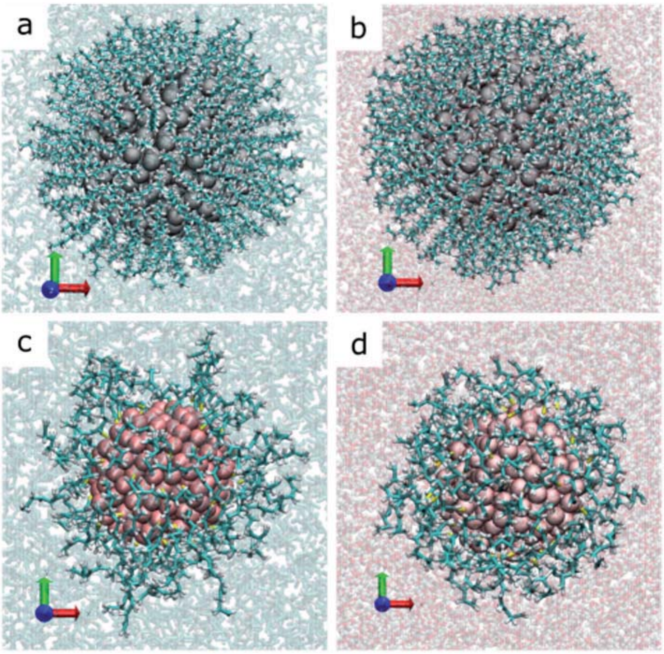

Figure 4.25.: Snapshots from MD simulations using the Visual Molecular Dynamics (VMD) program [142]. A SiNC capped with 1-octene molecules in (a) chloroform and (b) water. An Au NC capped with 1-dodecanethiol in (c) chloroform and (d) water. Si and Au atoms are shown with their Van der Waals radius. Capping molecules are shown in bond representation. Solvent molecules are drawn translucent. The results show that SiNCs have denser packed ligand layers than the AuNCs, and that in chloroform the ligands are more extended.

The simulations also computed the thickness of the coating organic layer, which takes into account ligand lengths and their orientation (angle) with the surface (see Section A.3 of the Appendix for a description of the procedure). The obtained thickness of the organic layer was 1.14 nm for SiNCs (for both solvents), which results in a particle with a total diameter of 5.1 nm. For the thickness of the layer of 1-dodecanethiol of AuNCs we obtain 0.89 nm and 1.14 nm in water and chloroform respectively, which gives total particle diameters of 3.7 nm and 4.2 nm, respectively. Therefore, according to the simulations, the two particles have similar sizes but with very different organic coating layer structures, a compact layer on SiNCs versus a hairy layer on AuNCs. The origin of this different structure of the coating layer can be attributed to a nanoscale effect due to the higher curvature of the AuNCs as compared with SiNCs (higher curvature corresponds to smaller radius). Indeed, additional simulations performed over a flat surface (infinite radius, zero curvature) with the same capping ligand density as in the case of AuNCs and SiNCs give a compact, solid-like organic layer in both cases (see Section A.3.3 of the Appendix).

4.4.2. Proposed mechanism for the formation of quatsome-SiNC assemblies

As it is depicted in Figure 4.25 and discussed in the paragraphs below, the different interaction of SiNC and AuNC with quatsomes, can be attributed to the different structure of the coating layer of both nanocrystals (Figure 4.26a).

The proposed mechanism is summarized schematically in Figure 4.26b,c. Both kinds of particles (based on Au and Si) have a hydrophobic coating, so they tend to aggregate when dispersed in water due to the strong attractive hydrophobic interaction. As the aggregates or clusters of particles form, they interact with other clusters of particles and with the hydrophilic surfaces of quatsomes.

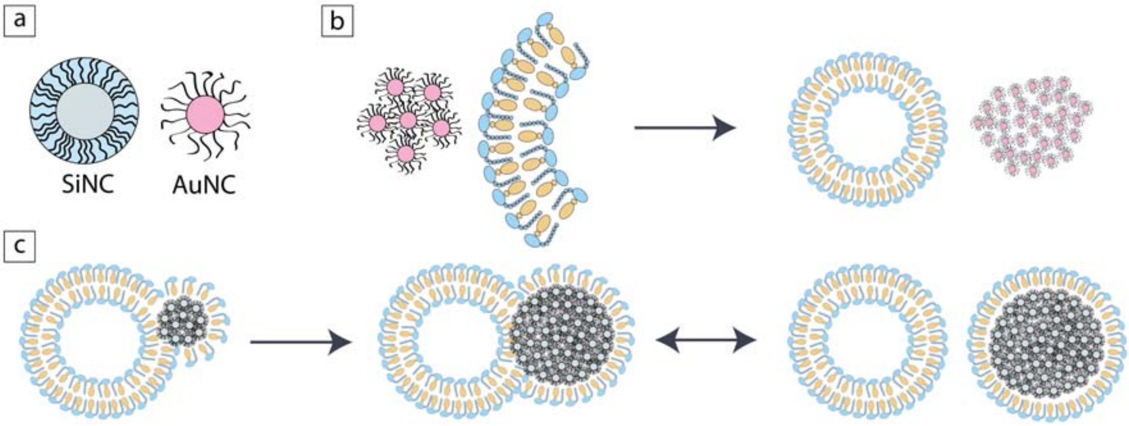

Figure 4.26.: Proposed mechanism for the formation of quatsome-SiNC assemblies. In the diagram, CTAB is the blue headed structure, cholesterol is the yellow structure, AuNC are shown as red spheres and SiNC are shown as grey spheres. The ligands are shown schematically. (a) Scheme of the different structure of the organic layer covering SiNC and AuNC (compact versus hairy layer). (b) Scheme of the interactions of Au particles and quatsomes. (c) Scheme of the interactions of Si particles and quatsomes, and the formation of the stable SiNC covered with a monolayer of quatsomes.

Let us consider first the case of Au particles (Figure 4.26b). The clusters of Au particles experience a repulsive interaction with the quatsome vesicles due to the hairy organic layer of the Au particles. This is due to the fact that the molecules of the hairy layer have less possible configurations near a surface (in this case, the surface of the quatsomes) than far from the surface, inducing a repulsion of entropic origin. This kind of repulsive interaction, known as “brush repulsion” plays a substantial role in self-assembly processes of nanoparticles [274]. As a result, the Au particles aggregate into large clusters, without incorporation to the quatsomes.

In the case of Si particles (Figure 4.26c), the brush repulsion interaction is absent because the capping layer is compact in this case. Instead, we think that the interaction of a quatsome vesicle with a cluster of Si particles is more similar to the interaction of a vesicle with a hydrophobic solid surface. In this case, the layers of the quatsome vesicles were spread onto the surface of the clusters of Si particles. This spreading process requires first the breaking of vesicles and the input of energy. Vesicles are dynamic structures that can be reformed or reduced in size with the addition of sonication energy [275, 276]. We found that when Chol-CTAB quatsomes with SiNCs were sonicated for 15 or 30 min, they were smaller than those sonicated for 1 minute or 5 minutes (Section 4.2.8). Thus, it can be hypothesized that when quatsomes are sonicated they are broken down through a redistribution of membrane molecules. When the sonication is performed in the presence of hydrophobic SiNCs with a “compact organic layer” coverage, this redistribution would allow small aggregates of SiNCs to become stabilized by the hydrophobic part of Chol-CTAB monolayers (Figure 4.26c). The resulting self-assembled structure (clusters of Si particles covered by a quatsome monolayer) is now stable in water and acquires the radius corresponding to the spontaneous curvature of the quatsome building blocks (the bimolecular entities made by the association between CTAB and cholesterol explained in Section 2.3.1 of the Chapter 2). The result of this process is the coexistence between quatsome vesicles and these self-assembled clusters of Si covered by CTAB and cholesterol with a diameter similar to that of quatsome vesicles.

Although the nanoparticles are aggregated in quatsomes, it is still apparent that the synergy between cholesterol and CTAB, found before in plain quatsomes (Chapter 2), leads to the stable interaction between quatsomes and SiNCs. When CTAB micelles were sonicated with SiNCs, the SiNCs appeared as either very small or very large, irregularly shaped clusters (Figure 4.16).

Additionally, cryo-TEM images of SiNCs incorporated into Chol-CTAB quatsomes in Figure 4.12 show that the SiNC aggregations are approximately the same size as quatsomes without any SiNCs. Since the size of quatsomes is influenced by the interaction between cholesterol and CTAB, the size of SiNCs aggregated suggests that they are associated with the same Chol-CTAB units. Further, as shown in the dilution experiment in Figure 4.17, only SiNC dispersed in quatsomes remain stable after several rounds of dilution, while SiNC dispersed in CTAB micelles result in precipitation of the SiNCs after multiple dilutions. Thus, it is specifically the quatsomes where cholesterol and CTAB interact as bimolecular building blocks that contribute to stabilizing the SiNCs.

4.4.3. Summary

Silicon nanocrystals with core diameters of approximately 2.8 nm and octene capping ligands were incorporated into pre-formed Chol-CTAB quatsomes using a 5 minute bath sonication procedure, as outlined in Figure 4.27a. The quatsome dispersion, initially cloudy blue/grey, became light yellow following addition of the SiNCs and bath sonication, with no visible precipitate or phase separation (Figure 4.27b). Under 365 nm ultraviolet lamp illumination the colloidal dispersion exhibited orange fluorescence characteristic of the silicon nanoparticles, which keeps stable at least up 12 weeks.

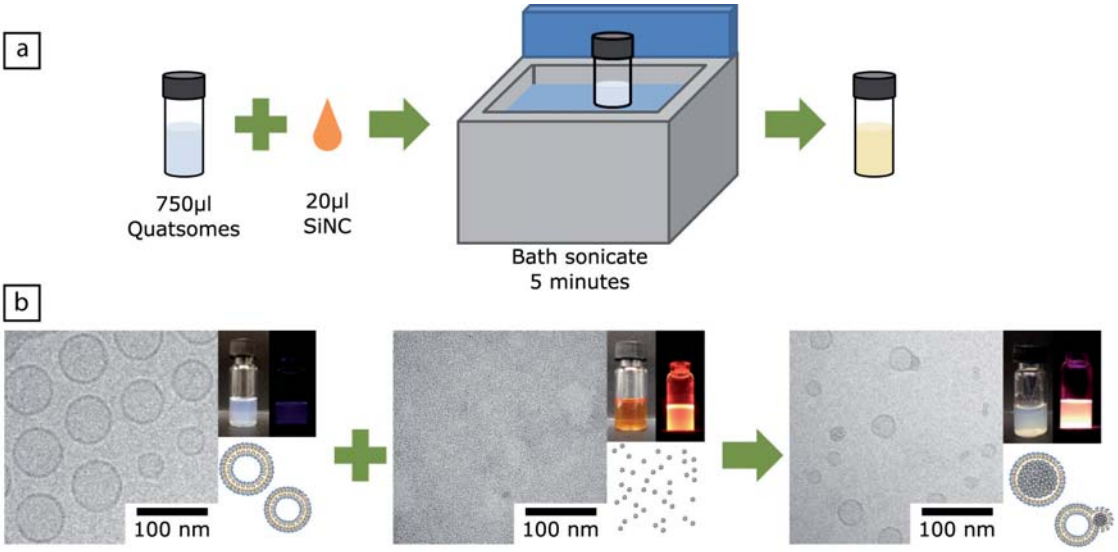

Figure 4.27.: (a) Schematic representation of the process for incorporating SiNCs into quatsomes through bath sonication. (b) Cryo-TEM and TEM images of quatsomes, SiNCs, and assemblies, respectively, as well as photographs of vials under ambient light (left) and on a 365 nm ultraviolet lamp (right) and diagrams of structures.

Therefore, a method to disperse fluorescent SiNCs in aqueous media with long-term stability was developed, utilizing Chol-CTAB quatsomes, which are non-liposomal vesicular structures. The stable SiNC aqueous dispersions can be made with five minutes of bath sonication. The NCs remain dispersed in water for several weeks and maintain the fluorescence properties of the SiNCs for several weeks and after dilution with the addition of water. The experimental data show that the association of SiNCs with Chol-CTAB quatsomes is unique to the nanocrystal type (as compared to AuNCs) as well as the method of preparation.

Quatsomes, which have been shown to have extremely long term stability of at least three years in aqueous solutions (see Section 2.3.2.1 of the Chapter 2), provide a vehicle for the dispersion of hydrophobic SiNCs into *in vitro* or *in vivo* environments, even under dilute conditions.

The biocompatibility of quatsomes and near infrared emitting SiNCs make these structures excellent candidates for biomedical imaging applications. Furthermore, quatsomes have been shown to enhance protein activity and to protect proteins against premature degradation in topical pharmaceutical formulations, as well as to treat biofilms [124, 215]. Therefore, the incorporation of both biomolecules and SiNCs into quatsome structures offers the possibility of exploring the behavior of these systems in biological environments and their use for theranostics.

5

Conclusions

From the work accomplished in this PhD Thesis on the preparation of stable self-assembled colloidal nanostructures using cholesterol as molecular building block, we conclude the following:

- Stable unilamellar nanovesicles, named quatsomes, are formed with aqueous mixtures of cholesterol and ionic surfactants, which form crystals and micelles, respectively, when they are alone in aqueous media. These nanovesicular structures have a huge range of applications from drug nanocarriers, in nanomedicine development, to nanoscopic templates, in material preparation.

- Cholesterol and CTAB form a bimolecular synthon, which self-assembles forming thermodynamically stable quatsomes with spontaneous curvature. Chol-CTAB quatsomes have a high vesicle to vesicle homogeneity regarding size, lamellarity and bilayer structure, in comparison to other vesicular systems, such as liposomes.

- Aqueous mixtures of cholesterol derivatives with ionic surfactants, self-assemble as quatsome-like structures or other colloidal structures, such as one-dimensional (1D) nanoribbons, depending on the chemical nature of the molecular components and its proportion.

- Fine decoration of quatsomes surface with functional groups (i.e. reactive and electroactive groups) has been achieved by partial substitution of cholesterol molecules, forming quatsomes structures, with cholesterol-functionalized molecular units. This finding adds a large versatility to these stable nanovesicles for the preparation of colloidal systems with controlled and well-defined structure at nanoscopic level.

- It has been demonstrated that DELOS-SUSP method, based on the use of compressed CO_2, is a mild methodology for the one-step preparation of cholesterol-rich colloidal nanostructures, without the need of further downstream processing.

- Hydrophobic SiNCs have been stabilized for the first time in aqueous media through their interaction with Chol-CTAB quatsomes. This finding opens the possibility to use these high fluorescent NCs as labels for fluorescent *in vitro* and *in vivo* techniques.

This Thesis therefore contributes to improve the knowledge about cholesterol-based supramolecular assemblies and demonstrates the enormous potential of CF-based methodologies for the production of stable self-assembled colloidal nanostructures with high content of cholesterol.

6

Experimental Part

6.1. Materials

5-Cholesten-3β-ol (Chol, purity 95%) and sodium bicarbonate ($NaHCO_3$, purity 99%) were obtained from Panreac (Barcelona, Spain). Cetyltrimethylammonium bromide (CTAB, ultra for molecular biology) was purchased from Fluka-Aldrich. Myristalkonium chloride (MKC, purity ≥ 98%), cetylpyridinium chloride (CPC, purity ≥ 99,5%), myristic acid (purity ≥ 99,5%), sodium dodecyl sulfate (SDS, purity ≥ 98,5%) and 2-mercaptobenzothiazole (MBT, purity ≥ 97%) were obtained from Sigma-Aldrich (Tres Cantos, Madrid). β-Sitosterol was obtained from Arboris (Savannah, Georgia). 1,2-Dipalmitoyl-sn-glycero-3- phosphocholine (DPPC) and 1,2-dioleoyl-sn-glycero-3-phosphocholine (DOPC) were supplied by Avanti Polar Lipids (Alabaster, AL, USA).

Ethanol and chloroform, HPLC grade, were obtained from Teknokroma (Sant Cugat del Vallès, Spain) and carbon dioxide (purity 99.9%) was supplied by Carburos Metálicos S.A. (Barcelona, Spain). The water used was pretreated with the Milli-Q Advantage A10 water purification system (Millipore Ibérica, Madrid, Spain). PBS buffer (pH = 7.4) with a 100 mM concentration of salts (0.094 M in NaCl, 0.0031 M in Na_2HPO_4, 0.0009 M in NaH_2PO_4) was used for vesicle preparation.

Studies of quatsome-nanocrystal hybrids: Hydrogen silsesquioxane (HSQ) was purchased from Dow Corning. Hydrofluoric acid (HF, 48%) was purchased from Macron Fine Chemicals. Ethanol was purchased from Pharmco-Aaper. Cetyl trimethyl ammonium bromide (CTAB, high purity grade) was purchased from Amresco. Cholesterol was purchased from Anatrace. 1-Dodecanethiol (98%) was purchased from Acros Organics. 1-octene (98%), gold(III) chloride trihydrate (≥ 99.9%), tetraoctylammonium bromide (TOAB, 98%), and sodium borohydride (≥ 98.0%) were purchased from Sigma-Aldrich. Hydrochloric Acid (HCl), hexanes (≥ 98.5%), chloroform (≥ 99.8%), and toluene (≥ 99.5%) were purchased from Fisher. 1,2-dioleoyl-sn-glycero-3-phosophocholine (DOPC) and

1,2-dioleoyl-sn-glycero-3-(1'-rac-glycerol) (DOPG) in chloroform were purchased from Avanti Polar Lipids. Water used in all experiments was high purity water (18.2 $M\Omega/cm$) and was obtained from a Millipore Synergy Ultrapure water system.

All chemicals were used without further purification.

6.2. Preparation and processes of cholesterol-rich colloidal self-assemblies

6.2.1. Preparation by DELOS-SUSP

6.2.1.1. Equipment and procedure for preparation at lab-scale

Equipment The equipment used for the preparation of cholesterol-rich colloidal self-assemblies by DELOS-SUSP using a 7.5 ml reactor is schematized in Figure 6.1. The configuration comprises a 7.5 ml reactor *(RX)*, whose temperature is controlled by an external heating jacket; a thermostated syringe pump (model 260D, ISCO Inc., Lincoln, US) *(P)* to introduce CO_2 inside *RX* through valve *V-4*; a depressurization valve *(V-7)*, from which the expanded liquid solution is depressurized into the aqueous phase placed in a collector *(C)* located after *V-7*. N_2 can be introduced through *V-6* directly from a pressurized reservoir. A one-way valve is located after *V-6* to prevent contamination of CO_2 in the N_2 line. *V-2*, *V-3* and *V-5* are divinding the CO_2 and N_2 pipelines with other equipment. There is also a pressure indicator *(PI)* and other one-way valve before the reactor.

The gas filter *(FG)* is an optional filter and is located before *V-7*. It has to be in consideration that the use of the gas filter implies an increase of the reactor volume to 11 ml *(RX+FG)*.

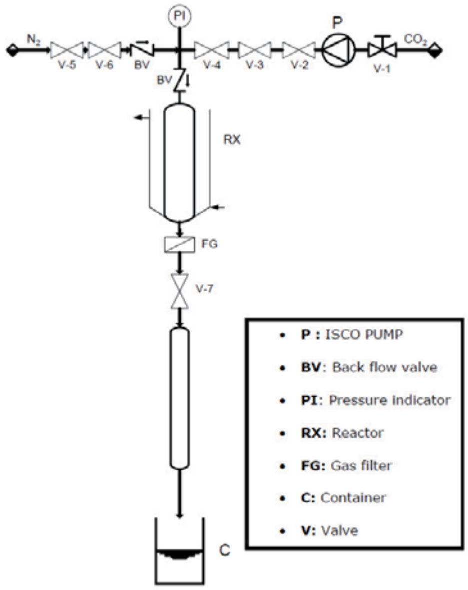

Figure 6.1.: Scheme of the lab-scale set-up used for the DELOS-SUSP experiments.

Experimental procedure The preparation of cholesterol-rich colloidal self-assemblies by DELOS-SUSP was performed according to the following procedure. A volume *V* of a solution of the components (except ionic surfactants) in EtOH is introduced into the reactor, which has been previously driven to the working temperature (T_w = 308 K). After 30 minutes, once the solution has achieved T_w, the autoclave is pressurized with compressed CO_2 through valve *V-4*, producing a volumetric expanded liquid solution with the desired molar fraction of CO_2, X_w, at the working pressure *(P_w)*. The "solute/EtOH/CO_2" system is left to equilibrate during at least one hour, keeping CO_2 pump on and *V-4* opened in order to maintain a constant P_w inside the reactor. The CO_2-expanded solution is then depressurized from P_w to atmospheric pressure through the valve *V-7* over an aqueous solution (with the ionic surfactants). A current of N_2 at P_w is used as embolus to push down the expanded solution in order to maintain constant pressure in the reactor during depressurization. The average time per experiment was around 2 hours.

6.2.1.2. Equipment and procedure for preparation at pilot plant scale

Equipment To scale-up the production of nanovesicles by DELOS-SUSP we used the system schematized in Figure 6.2. In this configuration, CO_2 is pumped through a high pressure pump, *B-1*, which head is cooled by a cooling unit. Before entering into the 315 ml reactor, *R*, CO_2 is heated to the working temperature, T_w, using a heat exchanger, *HCO_2*. The amount of CO_2 added to the reactor through valve *V-1* is measured by a mass flowmeter, *FCO_2*. Inside *R* a variable speed stirrer *(VF)* warrants the homogeneity of the mixture in the volumetrically expanded phase. The vessel temperature is controlled using an external fluid heating jacket. *R* is connected through *V-6* to a filter, *F1*, which has been previously pressurized with N_2 at the working pressure *(P_w)* through *V-7* in order to separate the solid that could precipitate due to the antisolvent effect of CO_2 before the depressurization step. *F1* is connected to a T-mixer *(VM-2)*, where the depressurized solution is mixed with the aqueous phase after opening the depressurization valve *V-8*. *V-8* is remotely controlled. During the depressurization step, the aqueous phase is pumped at a constant flow using *B-3*. Vesicles are collected in *T* after their formation. The system is also equipped with pressure, *PI1*, *PI2*, *PIC*, and temperature, *TI*, *TI1*, indicators, as well as with safety devices like rupture disks, *DR1* and *DR2*.

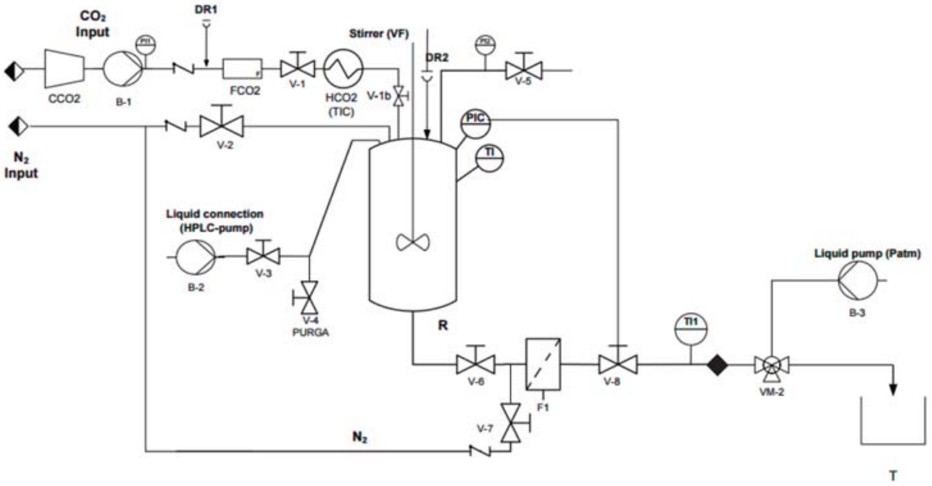

Figure 6.2.: Scheme of the 315 ml set-up used for the DELOS-SUSP experiments.

Experimental procedure For the scale-up preparation of Chol-CTAB (W10Et-DELOS) quatsomes (Table 6.3), 3.8 g of cholesterol were dissolved in 144 ml of EtOH and introduced in a 315 ml reactor already warmed at 308 K. After 15 min of thermal equilibration, CO_2 was introduced to achieve the desired P_w (10 MPa) and X_{CO_2}(0.6). After at least 45 min, the CO_2-expanded solution was depressurized through a one-way automatic valve into a T mixer, to which 1,200 ml of an aqueous solution containing 3.4 g of CTAB were pumped at 900 ml/min, to form the vesicles. Average time per experiment was 2 hours and the quatsomes prepared were stored at 277 K until characterization.

6.2.1.3. Differences between the equipment configurations for the small and large scale reactors

Apart from the capacity of the high pressure vessels (7.5 ml vs 315 ml), there are other differences between both equipment configurations (Figure 6.3).

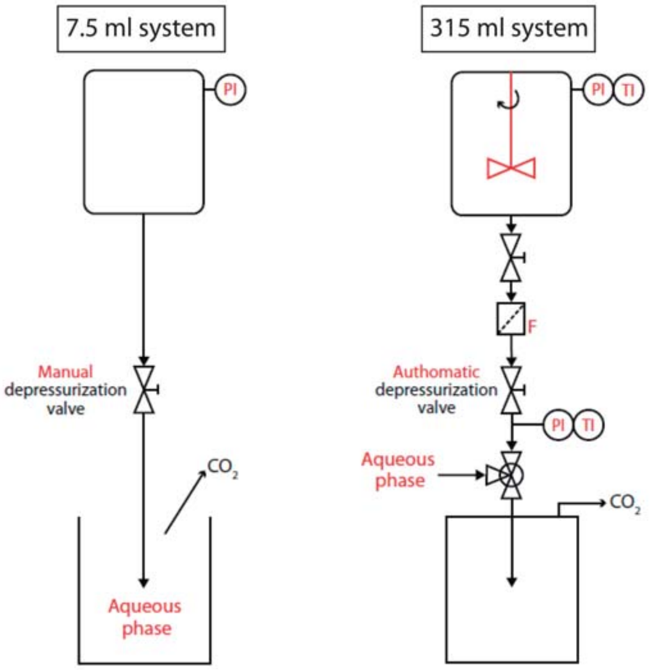

Figure 6.3.: Differences between the small scale and the large scale equipment configurations.

One of the variations is in regard to the mixing of the alcoholic solution with CO_2 in the high pressure container. While unnecessary at small scale, a mechanical stirrer is used for a quicker achievement of the thermodynamic equilibrium of the CO_2-expanded solution in the 315 ml system. The depressurization configuration also changed at larger scale, where the manual depressurizing valve used in the 7.5 ml system is substituted by an automatic one, whose flow rate can be better controlled. Another important divergence concerns the way in which the CO_2-expanded solution and the aqueous phase are mixed. Whereas the depressurization of the 7.5 ml container is performed directly over a vessel containing the aqueous phase, good mixing between the two solutions at larger scale is ensured by depressurizing the expanded solution into a T mixer to which the aqueous phase is simultaneously pumped.

6.2.1.4. Solubility behavior of cholesterol in CO_2-expanded ethanol

In order to prepare any vesicular system using DELOS-SUSP is necessary that the lipids forming the membrane are completely soluble in the CO_2-expanded organic solvent, presenting one phase at the working conditions of pressure, P_w, temperature, T_w and CO_2 molar fraction, X_i. Therefore for the preparation of cholesterol-rich vesicles by DELOS-SUSP method is always necessary to analyze the solubility behavior of the used sterol in CO_2-expanded solvents, by means of a detailed phase diagram study. Figure 6.4 shows the solubility curve of cholesterol in CO_2-expanded ethanol. A co-solvent behavior of CO_2 is observed until $X_i = 0.76$, which means that below this molar fraction one single phase is obtained when the CO_2 is added over a saturated solution of cholesterol in pure ethanol.

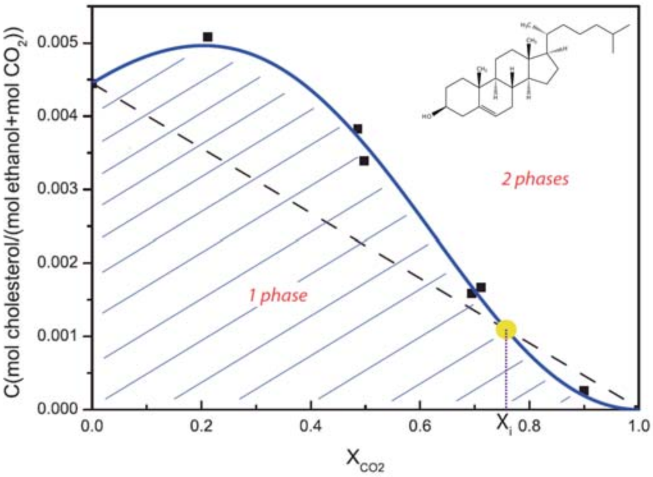

Figure 6.4.: Solubility curve (solid line) of cholesterol in ethanol/CO_2 at 10 MPa and 308 K (blue curve). The dashed line represents the solubility variation of a three component system, in which no interaction among the components exist, in an ideal process. X_i is the intersection point between the ideal solution line and the real solubility curve. Adapted from [187].

6.2.2. Preparation by Thin Film Hydration (TFH)

The preparation of nanovesicles by hydration methodology was performed according to the following procedure. The appropriate quantities of the membrane components dissolved in chloroform are mixed in a glass vial and the solvent is slowly evaporated under a N_2 flow to create a lipid thin film. The glass vial is then placed in vacuum for at least 4 hours for removing the possible entrapped solvent. Once dried, the lipid film is hydrated overnight using the appropriate aqueous medium. Next, the sample is taken through 10 rounds of freeze/thaw cycles by transferring it between liquid nitrogen (77 K–1 min) and water bath (313 K – 5 min) for finally being extruded through a polycarbonate filter with a specific pore size. The filters used in our experiments had pore size of 800 nm and 100 nm and were purchased from Avanti Polar Lipids. A commercially available manual extruder (Avanti® Mini-Extruder, Avanti Polar Lipids, Alabaster, AL, USA), was used for that purpose (Figure 6.6). The obtained vesicles were stored at 277 K until characterization.

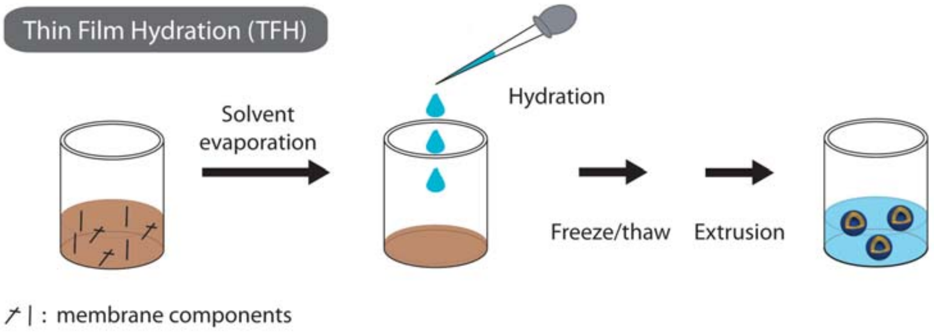

Figure 6.5.: Scheme of the vesicle preparation by Thin Film Hydration (TFH) method.

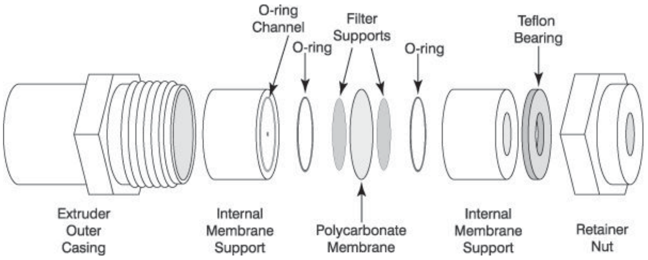

Figure 6.6.: Schematic illustration of the parts comprising the manual mini-extruder.

6.2.3. Preparation by sonication

The preparation of nanovesicles by sonication methodology was performed according to the following procedure. The dry membrane components were added directly to 10 ml of an aqueous solution. The resulting dispersion was sonicated at 298 K, using a Vibracell Sonifier titanium probe working at 20 kHz (Sonic and Materials Corporation) for 4 min until a homogeneous dispersion was achieved (Figure 6.7).

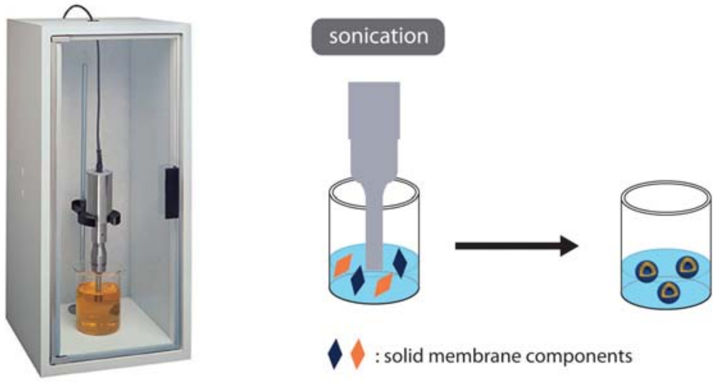

Figure 6.7.: Photograph of the Vibracell Sonicator used in the experiments (left) and scheme of sonication method for the preparation of vesicles (right).

6.2.4. Lyophilization of Chol-CTAB (W10Et-DELOS) quatsomes

Lyophilization or freeze drying is a process in which water is removed from a product after it is frozen and placed under a vacuum, allowing the ice to change directly from solid to vapor without passing through a liquid phase. Lyophilization or freeze-drying has been done in collaboration with Telstar Company (Terrasa, Spain). The lyophlization equipment consists of a heating plate and a condenser connect to a vacuum pump. The process consists of three separate, unique, and interdependent processes:

- Freezing: proper freezing will ensure a good cake. The objective is to produce a frozen matrix with sufficient crystal structure to allow the sublimating material to escape. The freezing was conducted at -55 °C with a 1 °C/min rate.

- Primary drying: the pressure is reduced to a value lower its critical temperature and as a consequence there is a phase transitions from solid to gas: sublimation. Sublimation drives the unbound moisture out the product. This is usually the longest process. It was performed at -35 °C and 0.06 mbar for 24 hours.

- Secondary drying: it is also called, desorption. In this process, the ionically bound water goes out of the material and this occurs by heating the product. It was carried out at 25 °C and 0.01 mbar for 9 hours. The resulting cake obtained after lyophilization of the suspensions was well formed.

6.3. Instruments, techniques and procedures used for the characterization of the colloidal systems

6.3.1. Cryogenic transmission electron microscopy (cryo-TEM)

The morphology of the self-assembled colloidal nanostructures was studied by cryogenic transmission electron microscopy (cryo-TEM). Cryo-TEM images were obtained using a JEOL JEM-2011 transmission electron microscope (JEOL LTD., Tokio, Japan) operating at 120 kV. A small drop of sample was placed on a copper grid coated with a perforated polymer film. Excess solution was thereafter removed by blotting with filter paper. Immediately after film preparation, the grid was plunged into liquid ethane held at a temperature just above its freezing point (94 K). The vitrified sample was then transferred to the microscope for analysis. To prevent sample perturbation and the formation of ice crystals, the specimens were kept cool (77 K) during both the transfer and viewing procedures.

In cryo-TEM images, unilamellar vesicles appear as uniformly dark circular rings; contrast in the image is generated by the variation of the projection of the electron beam, which is normal to the image in these figures, through the vesicle membrane. Where the vesicle bilayer is oriented parallel to the electron beam (edges of the vesicle), the projection through the bilayer is greater than where the bilayer is perpendicular to the electron beam (center of the vesicle).

In quatsome-nanocrystal hybrid studies (Chapter 4), cryogenic transmission electron microscopy (cryo-TEM) images were taken using an FEI Tecnai Biotwin TEM operated at 80 kV accelerating voltage, and acquired digitally. Cryo-TEM samples were prepared using a Leica EM GP by dropping 3 μl of sample onto Quantifoil R1.2/1.3 holey carbon on 300 mesh copper grids (Electron Microscopy Science) inside the environmental control chamber set to 25 °C and 90% humidity. After a blotting time of 3.5 seconds, the grid was plunged into liquid ethane to vitrify the sample. The grid was then transferred to a Gatan 626 Cryo-Transfer Holder under liquid nitrogen. FEI low dose software was used to obtain images of cryo-TEM samples.

6.3.2. Cyclic voltammetry (CV)

600 μl of samples were recorded using a VersaSTAT 3 potenciostat (Princetown Applied Research, USA). Samples were measured without the addition of an electrolyte. Platinum wires were used as working and counter electrodes and a Ag wire was used as reference

electrode. The samples were subjected to 2 potential cycles sweeping the voltage between 0.0 V and + 0.6 V at scan rate of 0.4 V/s.

6.3.3. Dynamic light scattering (DLS) and zeta potential (Z-potential)

Particle size and zeta potential (Z-potential) were measured using a dynamic light scattering analyzer combined with non-invasive backscatter technology (NIBS) (Malvern Zetasizer Nanoseries, Malvern Instruments, U.K.). This DLS instrument employs a 4 mW He-Ne laser (λ = 633 nm) and is equipped with a thermostatic sample chamber, besides the detector angle is fixed at 173°.

Samples (1 ml) were analyzed without any modification or dilution. The reported size and Z-potential values are the average result of 3 consecutive measurements on the same sample. In this work, sizes and particle size distributions have been presented in terms of scattering intensity. They provide information about the % of light scattered by particles, of each size in a sample. These are the most recommendable data when using dynamic light scattering, since they are the original data provided by the analyzer and no assumptions are involved for calculating particle size.

DLS measures the time-dependent fluctuations of light scattered from particles experiencing Brownian motion, which results from collisions between suspended particles and solvent molecules. Since the Brownian motion depends on the size of the particles, the rate at which the intensity fluctuations occur also depends on this parameter. Thus, small particles, which are "kicked" further by the solvent molecules and have faster Brownian motions, cause the intensity to fluctuate more rapidly than the large ones [19, 277]. Analysis of these intensity fluctuations enables the determination of the diffusion coefficients *(D)* of the particles which are converted into a size distribution through the Stokes–Einstein equation:

$$d(H) = \frac{kT}{3\pi\eta D} \tag{6.1}$$

where *d(H)* is the hydrodynamic radius of the particles under study, k is the Boltzmann constant, T is the temperature, and η is the solvent viscosity.

The hydrodynamic radius (Stokes radius) of the particle is defined as the apparent size of the hydrated sphere and is calculated from the radius of a sphere that diffuses at the same rate, that is, that has the same translational diffusion coefficient as the particle being measured. The translational diffusion coefficient will depend not only on the size of the particle “core” but also on any surface structure, as well as the concentration and type of ions in the medium [19].

In the present Thesis, the polydispersity index (PdI) of the analyzed samples is also reported. If one were to assume a single size population following a Gaussian distribution, then the polydispersity index would be related to the standard deviation (σ) of the hypothetical Gaussian distribution in the fashion shown below:

$$PdI = \frac{\sigma^2}{Z_D^2} \tag{6.2}$$

From a theoretical point of view Z-potential is the potential difference between the dispersion medium and the stationary layer of fluid attached to the dispersed particle, and is indicative of the degree of repulsion between adjacent particles in such dispersion. When the potential is low, attraction exceeds repulsion and the dispersion will break and flocculate. So, colloids with high zeta potential (negative or positive) are electrically stabilized while colloids with low zeta potentials tend to coagulate or flocculate as outlined in Table 6.1. From a practical point of view, when the zeta potential value of a suspension is higher, in absolute value, than 30 mV it is possible to say that this suspension is stable over time as the electrical charges present on the particle surface make them repel each other. On the contrary, if the zeta potential does not exceed this value, the particles will tend to aggregate and finally flocculate with time.

Table 6.1.: Table showing an indicative relationship between the stability of nanoparticle (or vesicle) suspensions and their Z-potential values.

Z-potential (mV)	Stability behaviour of the suspensions
0 - ±5	Rapid coagulation or flocculation
±10 - ±30	Incipient instability
±30 - ±40	Moderate stability
±40 - ±60	Good stability
≥ ±60	Excellent stability

Zeta potential is measured by applying a voltage across a pair of electrodes at either end of a cell containing the particle dispersion. Particles will migrate toward the oppositely charged electrode with a velocity proportional to the magnitude of their zeta potential. This velocity is measured and expressed as particle velocity in a unit electric field (electrophoretic mobility). This mobility *(U_E)* is converted to the zeta potential *(ζ)* using the Henry equation (see Equation 6.3) by inputting the dielectric constant *(ε)* and viscosity (η) of the dispersant and Henry's function *($F(\kappa a)$)*, which according to the Smoluchowski approximation is 1.5 for aqueous media.

$$U_E = \frac{2\varepsilon\zeta F(\kappa a)}{3\eta} \tag{6.3}$$

6.3.4. Inductively coupled plasma optical emission spectrometry (ICP-OES)

The ICP-OES measurements were performed using an inductively coupled plasma optical emission spectrometer (Optima 4300DV, Perkin Elmer), at Servei d'Anàlisi Química (SAQ) of the Universitat Autònoma de Barcelona (UAB).

Inductively coupled plasma-optical emission spectrometry (ICP-OES) is a powerful tool for the determination of metals in a variety of different sample matrices [239]. With this technique, liquid samples are injected into a radiofrequency (RF)-induced argon plasma where the kinetic energy of ions Ar^+can generate high temperatures (8000 °C). The argon plasma serves to atomize, ionize, and excite the elements in the sample. The emitted radiation is sorted by wavelength in a spectrometer and the intensity is measured at each wavelength.

It is important to note that in the method development to quantify the concentration of Fe in the studied Chol/Chol-Fc/CTAB aqueous mixtures, a repeatability study was conducted where small errors (%RSD 1.1 - 2) were identified.

6.3.5. Light scattering (LS)

The volumetric particle size distribution was investigated by light scattering (LS) using a particle size analyzer (Mastersizer 2000, Malvern Instruments, UK). Mastersizer 2000 uses the technique of laser diffraction to measure the size of particles. It does this by measuring the intensity of light scattered as a laser beam passes through a dispersed particulate sample. This data is then analyzed to calculate the size of the particles that created the scattering pattern. Laser diffraction measures particle size distributions by measuring the angular variation in intensity of light scattered as a laser beam passes through a dispersed particulate sample. The angular scattering intensity data is then analyzed to calculate the size of the particles responsible for creating the scattering pattern, using the Mie theory of light scattering. The Mie theory was developed to predict the way light is scattered by spherical particles and deals with the way light passes through, or is adsorbed by, the particle. Therefore, the more isotropic is the particle, the best accuracy will be obtained.

Milli-Q water was used as dispersant medium in all the experiments. The experimental procedure for particle size distribution analysis by LS comprises cleaning the measuring system with pure dispersant medium, laser alienation, measuring the pure dispersant medium particle size as background and finally analysing the sample under study.

In this case, size is presented in terms of volume. It provides information about the % of the volume of the total sample that is occupied by particles of each size present in such sample. Volumetric particle size distributions are expressed in percentiles of 10, 50 and 90% of accumulated volume (D10, D50 and D90). D50 value corresponds to the median volumetric particle size distribution.

6.3.6. Optical density measurements

Optical density (OD) is the absorbance per unit length, i.e., the absorbance divided by the thickness of the sample. Optical density is given as:

$$OD_\lambda = \frac{A_\lambda}{l} \tag{6.4}$$

where *(l)* is the distance that light travels through the sample (the sample thickness), measured in cm, and *(A_λ)* the absorbance at wavelength *(λ)*. The wavelength selected to measure the optical density should be one in which the system does not absorb. A measurement of optical density is like a measurement of the turbidity of the system, i.e., it is a measure of light diffracted by the sample. Through optical density measurements, it is possible to detect phase changes in liquid systems to micro- and nanoscopic level [137, 138].

The optical density values for a given sample are closely linked to the concentration and size of its constituent phases. Thus, a solution of a compound with a homogeneous liquid single phase will have a optical density value equal to 0, whereas a heterogeneous system that is not optically transparent, such as an emulsion, a vesicular system, or a suspension of particles present optical density values other than zero. However, those formed by an optically transparent single phase but with some structuration at nanoscopic level, as micelles, have optical density values different from zero and lower than those formed by heterogeneous systems with several phases.

The optical density has been used to study changes in the supramolecular organization of different mixtures of cholesterol and CTAB. The variation of optical density induced by the addition of cholesterol in the system was studied by analyzing their ultraviolet-visible absorption spectra recorded on a Perkin-Elmer Lambda 2 UV/Vis spectrophotometer (Perkin-Elmer, USA), using a pair of cuvettes with 1 cm optical path and thermostated at 298 K. The wavelength selected to measure the optical density of the Chol/CTAB systems was $\lambda = 500$ nm, at which neither cholesterol nor CTAB absorb.

6.3.7. Optical microscopy

Optical microscope images were performed using an Olympus Bx51 microscope equipped with a CCD camera Olympus DP20.

6.3.8. Morphologi G3 particle characterization system

Particles were characterized using the manual microscope facility of the Morphologi G3 (Malvern Instruments, UK).

6.3.9. Photoluminescence (PL) and photoluminescence excitation (PLE)

Photoluminescence (PL) and photoluminescence excitation (PLE) spectra were acquired on a Varian Cary Eclipse fluorescence spectrophotometer (Agilent Technologies). Spectra were measured at room temperature by diluting the SiNC aqueous colloidal dispersions by a factor of 20 with water in glass cuvettes, and the average PL emission wavelength was calculated from the PL curve.

6.3.10. Powder X-ray diffraction (PXRD)

Diffraction patterns of samples were recorded on a Siemens D5000 powder diffractometer (Bragg-Brentano geometry) using Cu Kα radiation ($\lambda = 1.5406$ Å), at a voltage of 40 kV and an intensity of 35 mA. Samples were mounted on a flat glass sample holder and were scanned in reflection mode from 2.0° to 60° of 2θ, at a scan rate of 0.02° 2θ s^{-1}.

6.3.11. SWAXS measurements

The X-ray scattering experiments devoted to study the vesicular nanostructures were performed at the X33 beamline of the European Molecular Biology Laboratory (EMBL, Hamburg, Germany), the SAXS beamline of the Elettra (Trieste, Italy), the BM16 beamline of the the European Synchrotron Radiation Facility (ESRF, Grenoble, France) and the beamline NCD of synchrotron ALBA (Cerdanyola del Vallés, Spain). It is reported that the vesicular membrane have a thickness around 5 nm. Consequently we require a q-range around 1.2 nm^{-1} which is achieved by standard sample to detector distance between 1 to 3 m.

In all the experiments, standard silver behenate and polyethylene samples were used for the calibration of SAXS and WAXS diffraction spacing, respectively. Background correction was accomplished by subtracting the integrated images of buffer in the solution cell from that of the sample using a scaling factor to line up the higher q region. The powder rings arising from the random orientation of vesicles were integrated radially using the Fit2d [278] software resulting in the so-called I-q plot, a one dimensional profile of X-ray intensity $I(q)$ versus scattering vector q. Final one dimensional data was evaluated using the ATSAS [279] and SCATTER [280] software packages.

The scattering data of Chol-CTAB (W-US) quatsomes and Chol-CTAB (W10Et-DELOS) quatsomes at different temperatures were measured in the Beamline X33 of the EMBL. A sample to detector distance of 2.7 m was used for SAXS (q-range around 0.06-6 nm^{-1}) and of 1.2 m was used for WAXS (q-range around 3.8-17.5 nm^{-1}). The wavelength of the beamline was 1.5 Å. Small-angle X-ray scattering (SAXS) and wide-angle X-ray scattering (WAXS) patterns were simultaneously recorded using a 2D Photon counting Pilatus 1M-W and a 2D Photon counting Pilatus 300K-W detectors, respectively. 8 patterns of 30 s each were acquired per sample.

The scattering data of Chol-CTAB (W-US) quatsomes at different concentrations and Chol/Chol-VS/CTAB aqueous mixtures were measured in the Elettra Synchrotron of Trieste (Italy). The wavelength of the beamline was 1.54 Å (8 KeV). A sample to detector distance of 1.005 m was used (q-range around 0.1-6.6 nm^{-1}) and the small-angle X-ray scattering (SAXS) patterns were recorded using a PILATUS3 1M detector. 4 patterns of 30 s each were acquired per sample. All the experiments were done at 298 K.

The scattering data of Chol-DPPC (W-TFH100x21) liposomes and Chol-CTAB (W10Et-TFH800x1) quatsomes at different temperatures were measured in the beamline BM16 of the ESRF. The samples were exposed to polarized monochromatic X-rays of a wavelength of 0.979 Å (12.6 keV) for 120 s. The given scattering plot corresponds to an averaged over 5 identical sequences after verifying a precise reproducibility. Small-angle X-ray scattering (SAXS) patterns were recorded using a Mar CCD camera detector. A sample to detector distance of 1.4 m was used (q-range around 0.03-7 nm^{-1}). A Julabo chiller (Julabo GmbH, Germany) with a mineral oil refrigerator was used for controlling the temperature with a

± 0.1 °C precision. Samples were loaded into a fixed temperature controlled flat cell with mica windows and a beam path thickness of 3 mm.

The scattering data of Chol-CTAB (W10Et-US), Chol-CTAB (W10Et-DELOS), Chol-CTAB (W10Et-TFH800x1), Chol-CTAB (W10Et-TFH100x1) and Chol-CTAB (W10Et-TFH100x21) quatsomes were measured in the beamline NCD of the ALBA. The wavelength of the beamline was 1.0 Å (12.4 keV). A sample to detector distance of 2.584 m was used (q-range around 0.09-5 nm^{-1}) and the small-angle X-ray scattering (SAXS) patterns were recorded using a Quantum 210r CCD camera detector. 30 patterns of 30 s each were acquired per sample. All the experiments were done at 298 K.

6.3.12. Thermal gravimetric analysis (TGA)

Thermal gravimetric analysis (TGA) data were acquired on a Mettler Toledo TGA/DSC 1. SiNCs dispersed in chloroform were drop cast and dried into a 70 µl alumina crucible (Mettler Toledo). The sample was then heat under 50 ml per minute air flow at a rate of 10 °C per minute from 25 °C to 800 °C and then held at 800 °C for 30 minutes.

6.3.13. Transmission electron microscopy (TEM)

The morphology of the samples was analyzed using a JEOL JEM-2011 (Jeol LTD, Tokio, Japan) transmission electron microscope operating at 120 kV with samples placed in standard carbon Holey grids. Besides, in some cases negatively stained TEM (NS-TEM) using chemical fixation was performed. Briefly, a sample drop was adsorbed onto a carbon-supported film, excess solution was removed by blotting with filter paper, and the sample was fixed by adding uranyl acetate. Finally, the sample was air-dried and examined in the TEM at room temperature.

The SiNC and the AuNC TEM images (Chapter 4) were taken using an FEI Tecnai Biotwin TEM operated at 80 kV accelerating voltage, and acquired digitally. Samples were prepared by drop casting the nanocrystals from organic solvent dispersions onto 200 mesh carbon-coated copper grids (Electron Microscopy Science).

6.3.14. UV-Vis spectroscopy

Absorbance spectra were acquired on a Varian Cary 50 Bio ultraviolet-visible spectrophotometer, a Varian Cary 500 ultraviolet-visible-near infrared spectrophotometer (Agilent Technologies) or a Perkin-Elmer Lambda 2 UV/Vis spectrophotometer (Perkin-Elmer, USA).

6.3.15. Viscosity

Viscosity measurements were performed at 298 K using a rheometer HAAKE Rheostress 600 (Thermo Fisher Scientific, Madrid, Spain).

6.4. Phase behavior study of the different cholesterol/CTAB mixtures

6.4.1. Preparation of the different cholesterol/CTAB mixtures

The amounts of cholesterol and CTAB weighted in each Chol/CTAB mixtures are summarized in Table 6.2. For all preparations, the CTAB concentration was kept constant 10 times above its critical micelle concentration (cmc), at a theoretical value of 10 mM. In order to facilitate the description of each Chol/CTAB mixture in the performed study in Section 2.2 of the Chapter 2, it has been used a nominal *Q* value.

Table 6.2.: Amounts of cholesterol, CTAB and Chol/CTAB molar ratio *(Q)* of the different prepared mixtures.

Cholesterol (mg)	**CTAB (mg)**	X_{Chol}	***Q* = Chol/CTAB (mol/mol)**
0	36.27	0	0
0.04	36.35	0.001	1×10^{-3}
0.43	36.51	0.011	1.1×10^{-2} ($\approx 1 \times 10^{-2}$)
3.71	36.69	0.0870	0.0953 (≈ 0.1)
19.25	36.30	0.3333	0.4999 (≈ 0.5)
38.60	36.38	0.5001	1.000 (≈ 1)
58.71	36.21	0.6044	1.528 (≈1.5)
117.65	36.74	0.7512	3.019 (≈ 3)

6.4.2. Measurement of membrane thickness of vesicles

Various vesicles of different cryo-TEM images were analyzed for estimating the thickness of their membrane using the Digital Micrographs 3.9.2 (Gatan Inc.) software package specific for the analysis of transmission electron microscopy images. This analysis showed that the membrane thickness of vesicles prepared by sonication range between 4.0 and 5.0 nm, which according to the literature [281,282] is in the range of the thickness of a lipid bilayer. Therefore this fact indicates that these vesicles are unilamellar. It is important to remark that the width of the dark rim of the vesicle observed in cryo-TEM image is wider than the actual bilayer thickness because of the curvature of the vesicle.

6.5. Preparation of liposomal formulations for comparison purposes with quatsomes

6.5.1. Cholesterol-DPPC liposomes

6.5.1.1. By DELOS-SUSP

Chol-DPPC (W5Et-DELOS) liposomes (Table 6.4): 1.2 ml of an ethanolic solution of a mixture of 12.4 mg of cholesterol and 23.6 mg of DPPC, was loaded into a 7.5 ml high-pressure vessel (Section 6.2.1) at atmospheric pressure and the working temperature (T_w = 308 K). The solution was then volumetrically expanded with compressed CO_2 until achieving a molar fraction *(*X_{CO_2}*)* of 0.85, reaching a working pressure *(*P_w*)* of 10 MPa. The system was kept at 308 K for approximately 1 hour to achieve a complete homogenization and to attain thermal equilibration. Afterwards the depressurization of the volumetric expanded organic phase was performed over 24 ml Milli-Q water. In this step a flow of N_2 at the working pressure is used as a plunger to push down the CO_2-expanded solution and to maintain a constant pressure of P_w inside the vessel during the depressurization. The final concentration was 1.4 mg/ml, included 1.3 mM cholesterol and 1.3 mM DPPC, in high purity water containing 5% ethanol (vol. %). The obtained liposomes were stored at 277 K until their characterization.

On the other hand, it is important to note that the solubility behavior of DPPC in ethanol and CO_2 was explored previously in *Nanomol* as described in the PhD Thesis of Dr. Ingrid Cabrera [182]. In these studies, it was observed that DPPC is soluble in ethanol and CO_2 at molar fraction (X_{CO_2}) of 0.85, therefore Chol-DPPC liposomes can be prepared using these compositions.

6.5.1.2. By Thin Film Hydration (TFH)

Chol-DPPC (W-TFH100x21) liposomes (Table 6.4): 0.94 mg of DPPC and 0.49 mg of cholesterol were dissolved in chloroform. The solvent was slowly evaporated under N_2 flow to create a thin lipid film and the glass vials were placed in vacuum for at least 3 hours in order to remove any remaining solvent. The lipid films were then hydrated overnight using 1 ml of Milli-Q water, at room temperature. Next, the samples were taken through 10 rounds of freeze/thaw cycles by transferring they between liquid nitrogen and a water bath (313 K) and finally, the samples were extruded reducing the size of the vesicles by mechanical energy. In this extrusion-step, the suspensions are forced through a polycarbonate filter with a defined pore size to yield particles having a diameter near the pore size of the filter used. In this preparation, a filter with a pore size of 100 nm was used and the sample was passed through the extruder twenty-one times. The membrane components concentration was 1.4 mg/ml (1.3 mM cholesterol and 1.3 mM DPPC) in high purity water. The obtained liposomes were stored at 277 K until their characterization.

Usually in the hydration and extrusion steps of this method, the working temperature should be above the thermotropic phase transition *(T_m)* of membrane components, in order to hydrate and extrude in their fluid phase. This transition temperature was studied for preformed Chol-DPPC liposomes at equimolar ratio prepared by DELOS-SUSP method (the low content of ethanol was considered negligible) (Section 6.5.1.1). The measurements were conducted using a VP-DSC microcalorimeter equipment and are presented in Section 6.6. As explained in that Section, the Chol-DPPC liposomes at equimolar ratio adopted the liquid-ordered *(L_o)* phase and did not exhibit a thermotropic phase transition *(T_m)*, therefore all the steps of this vesicle preparation can be conducted at room temperature.

6.5.2. DOPC liposomes by DELOS-SUSP

DOPC (W17Et-DELOS) liposomes (Table 6.4): 35 mg of DOPC were dissolved in 1.9 ml of ethanol and loaded into a 7.5 ml high-pressure vessel (Section 6.2.1) at atmospheric pressure and 308 K. The solution was then volumetrically expanded with compressed CO_2, until reaching a molar fraction of CO_2 of X_{CO_2}= 0.76 at a working pressure of 10 MPa. The system was kept at 308 K and 10 MPa for approximately 1 hour to achieve complete homogenization and to attain thermal equilibration. Finally, the CO_2-expanded DOPC solution was depressurized over 9 ml of an aqueous solution to create the liposomes. The final concentration of DOPC in the liposomal system was 3.6 mM in high purity water containing 17% ethanol. The obtained liposomes were stored at 277 K until their characterization.

On the other hand, it is important to note that the solubility behavior of DOPC in ethanol and CO_2 was explored previously in *Nanomol* as described in the PhD Thesis of Dr. Elisa Elizondo [187]. In these studies, it was observed that DOPC is soluble in ethanol and CO_2 at molar fraction (X_{CO_2}) of 0.76, therefore DOPC liposomes can be prepared using these compositions.

6.5.3. DOPG liposomes by Thin Film Hydration (TFH)

DOPG (HEPES-TFH100x21) liposomes (Table 6.4): 7 µmol of DOPG were dried from chloroform into a film with a rotary evaporator for 15 minutes. Residual solvent was removed by placing the film in a vacuum oven for 2 hours. The film was then hydrated with 1 ml 10 mM HEPES, 10 mM NaCl and bath sonicated for 30 minutes. Finally, the suspension was extruded 21 times through a 100 nm pore size polycarbonate filter on an Avanti MiniExtruder (Avanti Polar Lipids). The thermotropic phase transition *(T_m)* of DOPG is -18 °C [283], thus as explained in Section 6.6, this vesicle preparation was conducted at room temperature. The final concentration of DOPG in the liposomal system was 7 mM. The obtained liposomes were stored at 277 K until their characterization.

6.6. Differential scanning calorimetry measurements of T_m for preformed vesicles by DELOS-SUSP

Usually, the hydration and extrusion steps in Thin Film Hydration method should be done at a temperature above the thermotropic phase transition *(T_m)* of the phospholipids used, to hydrate and extrude in their fluid phase (Figure 6.8).

In the gel phase ($L_{\beta'}$ or L_β), also called solid-ordered *(S_o)* phase, the lipids are arranged on a two-dimensional triangular lattice in the plane of the membrane. The hydrocarbon lipid chains display an all-trans configuration and are elongated at the maximum, giving rise to an extremely compact lipid network. In the fluid phase, also called liquid-disordered (L_α or L_d) phase, trans-gauche isomerisation occurs giving rise to much less extended lipid chains [284]. Moreover, the two-dimensional triangular lattice is completely lost. The transition between the gel and fluid phases occurs at a specific temperature called thermotropic phase transition *(T_m)*. For some membrane lipids, the lipid disordering occurs in two steps when increasing temperature. A first transition is observed a few degrees below the main transition T_m. For the lipids that exhibit a pretransition temperature, an additional lamellar phase exists. This phase, called the ripple phase *(P_β)*, is characterized by periodic one-dimensional undulations on the surface of the lipid bilayer [285]. In presence of cholesterol, lipid bilayers can adopt an extra lamellar phase, called the liquid-ordered *(L_o)* phase, which shares the characteristics of both gel and fluid phases. In other words, this phase resembles to the gel phase with less lateral packing order and at the same time to the fluid phase with more packing order [284, 286]. Therefore, as shown in Figure 6.8, a lipid bilayer in the liquid-ordered *(L_o)* phase, with a high concentration of cholesterol, do not exhibit thermotropic phase transition *(T_m)* [286].

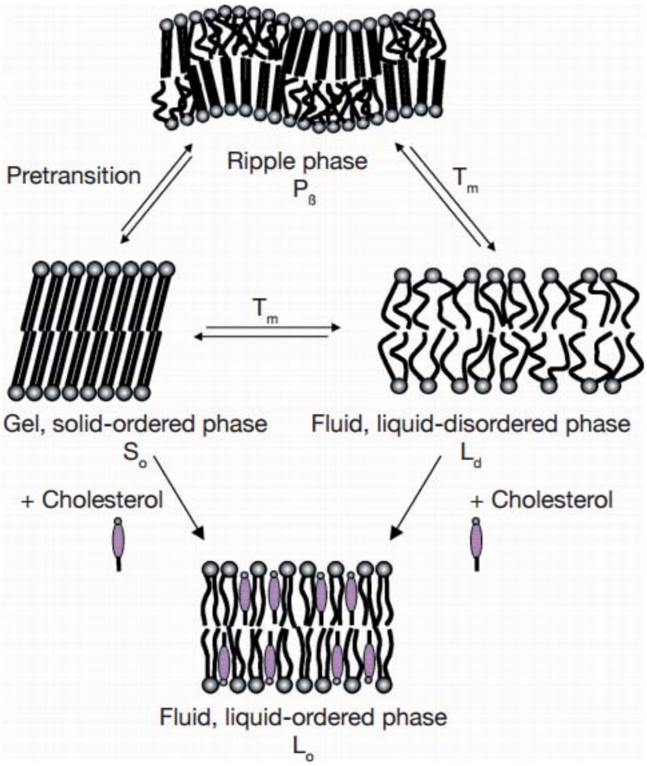

Figure 6.8.: Scheme illustrating the different physical states adopted by a lipid bilayer in aqueous medium. Obtained from [284].

The thermotropic phase transition *(T_m)* was studied for Chol-CTAB (W10Et-DELOS) quatsomes (Table 6.3) and Chol-DPPC (W5Et-DELOS) liposomes (Table 6.4), both at equimolar ratio, preformed by DELOS-SUSP method. Besides, plain DPPC liposomes without cholesterol were also prepared by DELOS-SUSP in order to study the influence of cholesterol content on the T_m. This last preparation was performed following the protocol described in Section 6.5.1.1 but using 36 mg of DPPC, 1.2 ml of ethanol and 24 ml of Milli-Q water.

The measurements were conducted by the differential scanning calorimetry technique. Specifically, a VP-DSC microcalorimeter equipment was employed with a heating rate of 1.5 °C/min. With the increase of temperature the thermotropic transitions should take place in the lipid bilayers [284, 286–288] (Figure 6.8).

As can be ascertained from Figure 6.9, the thermotropic phase transition *(T_m)* of plain DPPC liposomes (Figure 6.9a) was found around 40 °C. However, for Chol-DPPC (W5Et-DELOS) liposomes and Chol-CTAB (W10Et-DELOS) quatsomes (Figure 6.9b,c), no peak could be observed, suggesting the absence of transition using such vesicle formulations. Thus, due to the high content of cholesterol, both vesicle bilayers adopted the liquid-ordered *(L_o)* phase. Therefore, based on these measurements we can determine that the preparation of these cholesterol-rich vesicles by Thin Film Hydration can be performed at room temperature.

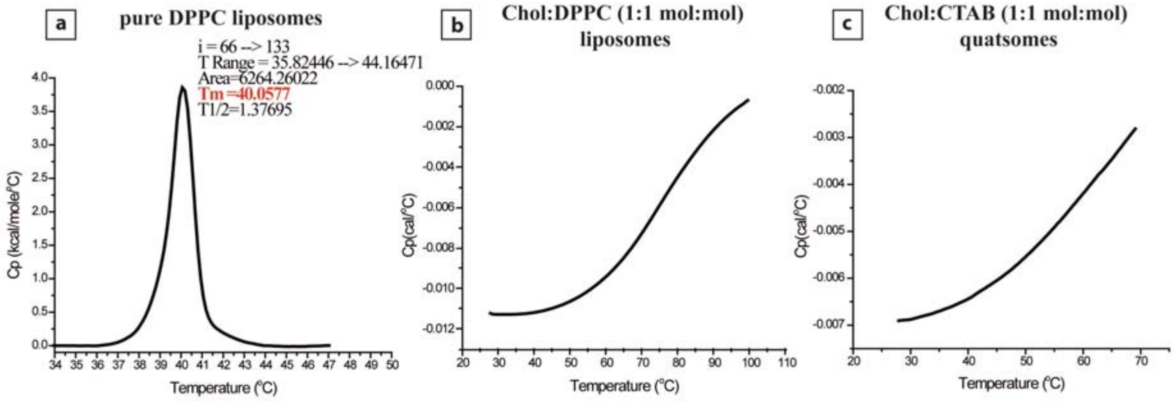

Figure 6.9.: VP-DSC measurements of (a) DPPC liposomes, (b) Chol-DPPC (W5Et-DELOS) liposomes and (c) Chol-CTAB (W10Et-DELOS) quatsomes.

6.7. Standard calibration curves for the quantification of 2-mercaptobenzothiazole by UV-Vis spectroscopy

Different quantities (0, 30, 150, 700, 1,000 and 1,450 µl) of 2-mercaptobenzothiazole (MBT) (5.14 x 10^{-5}M) in 25 mM $NaHCO_3$ buffer (pH = 8) were placed in dry glass vials. To all standards, 50 µl of the corresponding vesicles were added. Finally, all the samples were diluted into 25 mM $NaHCO_3$ buffer (pH = 8) until a final volume of 1,500 µl. The absorbance of the final standard samples was then measured using UV-Vis spectroscopy (Section 6.3.14).

Two standard calibration curves following the explained protocol were conducted, one for plain Chol-CTAB vesicles (*VS* ratio = 0) and another one for VS-functionalized vesicles (*VS* ratio = 0.25) (see Table 3.1 of the Chapter 3). Besides, when the linearity of each standard calibration curve was studied, the MBT (5.14 x 10^{-5}M) solution was prepared again 2 times. With these new MBT solutions, the last point of each standard calibration curve (1,450 µl MBT + 50 µl vesicles) was prepared again and the absorbance of these samples was measured. These new measurements were added to the initial standard calibration curves. By adjusting the absorbance experimental data to an equation $y = a + bx$ the following calibration curves were obtained:

- Plain Chol-CTAB vesicles (VS ratio = 0) , $y = 0.05881 + 14768.89071x$ ($R^2 = 0.9997$).
- VS-functionalized Chol-CTAB vesicles (VS ratio = 0.25), $y = 0.05387 + 14652.96721x$ ($R^2 = 0.9996$).

Figure 6.10 shows the obtained standard calibration curves for the quantification of MBT in plain and VS-functionalized Chol-CTAB vesicles.

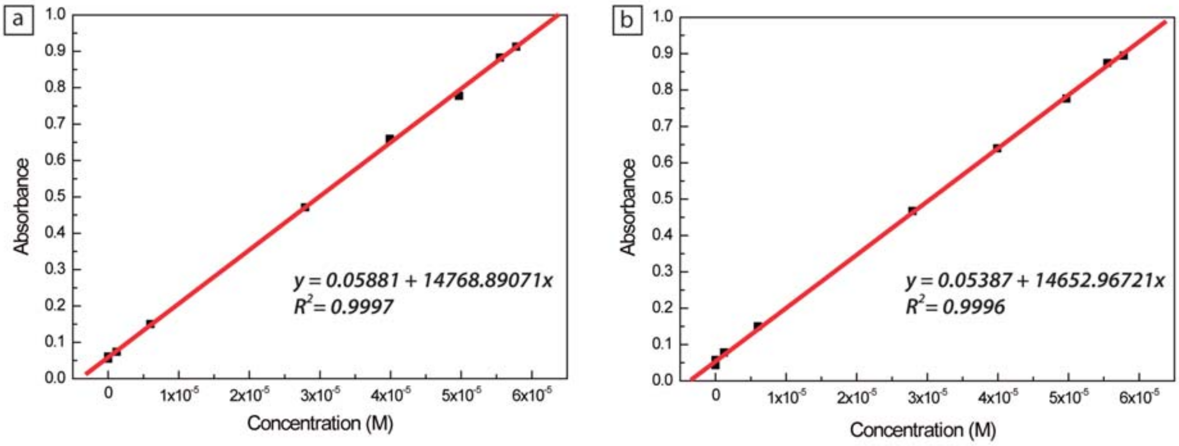

Figure 6.10.: Calibration curves for the quantification of 2-mercaptobenzothiazole (MBT) in (a) plain Chol-CTAB vesicles (λ_{max} = 312 nm) and (b)VS-functionalized Chol-CTAB vesicles (λ_{max} = 319 nm) by UV-Vis spectroscopy.

6.8. Synthesis and characterization of nanocrystals

6.8.1. Silicon nanocrystals (SiNCs)

Silicon nanocrystals were synthesized according to previously reported methods [256] (see Figure 6.11). Briefly, HSQ was degassed and then heat to 1100 °C for 60 minutes in a tube furnace under forming gas flow. The resulting brown material was then ground with a mortar and pestle, followed by further size reduction by mechanical shaking in a wrist action shaker with borosilicate beads for 9 hours. The final brown powder consists of crystalline silicon embedded in a SiO_2 matrix. To liberate the nanocrystals from the matrix, 0.6 g of SiNC powder was etched in the dark with 2 ml HCl and 20 ml HF for 3.5 hours. After etching, the material was precipitated by centrifugation for 5 minutes at 8000 rpm. The HF was removed and the precipitate was redispersed in ethanol, and then centrifuged again. This washing process was repeat once more with ethanol and then once with chloroform, resulting in –H terminated nanocrystals. Surface passivation was achieved by redispersing the precipitated nanocrystals with 20 ml of 1-octene and then injecting them into a 3-neck flask under vacuum. The solution was quickly frozen under vacuum, and then thawed under nitrogen flow. The freeze-thaw process was repeat three more times. Finally, the flask was left stirring at 400 rpm under nitrogen flow at 120 °C for 12 hours. Unpassivated nanocrystals were precipitated out using centrifugation at 8000 rpm for 5 minutes. The 1-octene solution was removed on a rotary evaporated at 760 mmHg, 60 °C and the nanocrystals were redispersed in hexanes. The SiNCs were then washed using ethanol as an antisolvent and hexanes as the solvent 4 times through centrifugation. The final SiNCs were dispersed in chloroform, and had a diameter of approximately 2.8 nm.

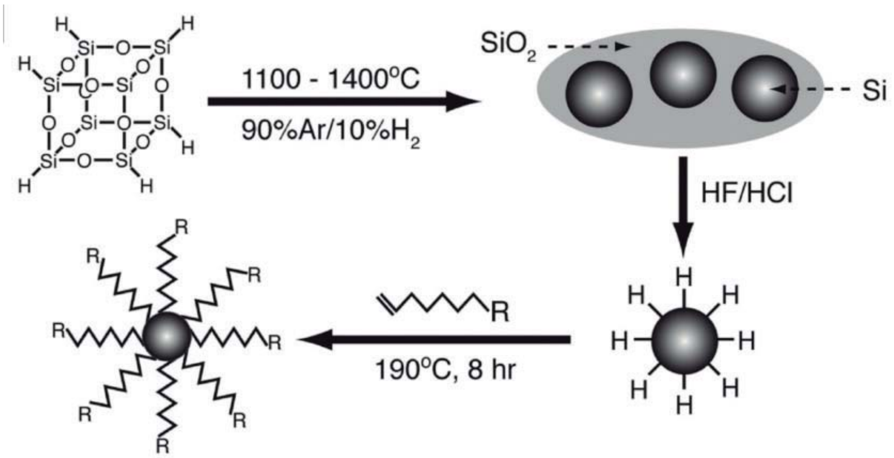

Figure 6.11.: Synthetic pathway from HSQ to alkyl passivated Si nanocrystals. Obtained from [256].

6.8.2. Gold nanocrystals (AuNCs)

Gold nanocrystals were synthesized using previously reported methods [263]. 328.4 g of gold(III) chloride trihydrate was dissolved in 20 ml of deionized water. Separately, 6 g of TOAB was added to 80 ml of toluene and stirred until dissolved. The gold solution was then added to the TOAB and toluene mixture and stirred for 1 hour, during which time the solution turned from yellow to red. After stirring, the gold remained in the toluene and a phase extraction was performed to remove the clear aqueous phase. 0.6 ml of 1-dodecanethiol was added to the mixture and the solution turned colorless as it was stirred for 15 minutes. 378 mg of sodium borohydride was then added to 20 ml of cold water before being added to the stirring flask. The solution turned dark brown as the nanoparticles stirred overnight. A phase extraction was conducted to remove the aqueous phase. Then, 5 ml of the gold solution was added to a glass centrifuge tube with

20 ml of ethanol and centrifuged for 5 minutes at 8000 rpm to precipitate out the gold nanocrystals. The supernatant was discarded and the precipitate was redispersed in toluene. This process was repeat until the entire gold solution had been washed with ethanol. Finally, the gold nanoparticles in toluene (approximately 3 ml) were centrifuged once more in the presence of 20 ml ethanol to precipitate out nanoparticles, and then redispersed in toluene for storage until use. Prior to using the gold nanocrystals for experiments with quatsomes, the nanocrystals were dried out of the toluene solution and then redispersed in chloroform. The final AuNCs dispersed in chloroform had a diameter of approximately 1.77 nm studied by TEM.

6.9. Synthesis and characterization of compounds

All the following compounds were synthesized and characterized by the group of Prof. Francisco Santoyo from the University of Granada.

6.9.1. Synthesis of N-(2-(2-(vinylsulfonyl)ethoxy)ethyl) dodecanamide (VS-1)

A solution of lauric acid (2.7 g, 13.2 mmol) in Cl_2SO (10 ml) was magnetically stirred for 1 h at room temperature. Evaporation and coevaporation with anhydrous toluene (3 x 15 ml) under reduced pressure gave a crude that was dissolved in anhydrous Cl_2CH_2 (30 ml). This solution was added dropwise to a solution of 2-amino ethanol (1.2 ml, 19.8 mmol) and Et_3N (3.75 ml, 26.4 mmol) in anhydrous Cl_2CH_2 (30 ml). The reaction mixture was kept at room temperature (15 min) and then evaporated under reduced pressure to give a crude that was purified by column chromatography (EtOAc) to give compound **1** as a solid (2.98 g, 93%).

(1)

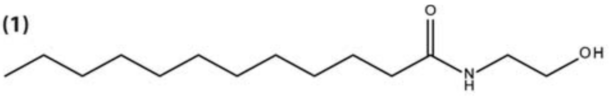

M.P. 89 – 91 °C; ν_{max} (KBr)/cm^{-1}: 3292, 2984, 2917, 1740, 1640, 1373, 1240 and 1046; ^{1}**H-NMR** ($CDCl_3$, 400 MHz): δ 6.18 (br s, 1 H), 3.69 (t, 2 H, *J* = 4.9 Hz), 3.39 (q, 2 H, *J* = 5.1 Hz), 2.20 (t, 2 H, *J* = 7.6 Hz), 1.60 (m, 2 H), 1.24 (m, 16 H), 0.86 (t, 3 H, *J* = 6.7 Hz); ^{13}**C-NMR** ($CDCl_3$, 100 MHz): δ 174.6, 62.3, 42.4, 36.7, 31.9, 29.6, 29.6, 29.5, 29.3, 29.3, 29.3, 25.7, 22.6, 14.1.

To a solution of compound **1** (500 mg, 2.1 mmol) in THF (50 ml) was added DVS (420 μl, 4 mmol) and t-BuOK (23 mg, 0.2 mmol). The reaction mixture was magnetically stirred

(25 min) at room temperature. Evaporation of the solvent under reduced pressure gave a crude that was purified by column chromatography (EtOAc:hexane 2:1 → EtOAc) to give compound **VS-1** as a solid (394 mg, 53%).

(VS-1)

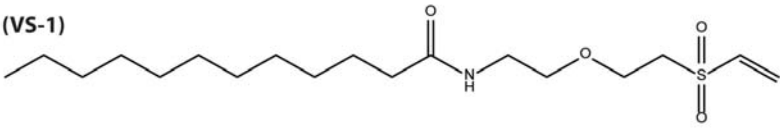

M.P. 64 – 66 °C; ν_{max} (KBr)/cm^{-1}: 3306, 3061, 2914, 2848, 1636, 1551, 1460, 1380, 1295, 1248, and 1123; ^{1}**H-NMR** (CDCl$_3$, 500 MHz): δ 6.70 (dd, 1 H, *J* = 16.6 and 9.9 Hz), 6.43 (d, 1 H, *J* = 16.6), 6.12 (d, 1 H, *J* = 9.9 Hz), 3.89 (t, 2 H, *J* = 5.5 Hz), 3.55 (t, 2 H, *J* = 5.1 Hz), 3.44 (q, 2 H, *J* = 5.2 Hz), 3.24 (t, 2 H, *J* = 5.5 Hz), 2.17 (t, 2 H, *J* = 7.6 Hz), 1.61 (m, 2 H), 1.24 (br s, 16 H), 0.87 (t, 3 H, *J* = 6.8 Hz); ^{13}**C-NMR** (CDCl$_3$, 125 MHz): δ 173.4, 137.6, 129.4, 70.0, 63.8, 54.6, 38.7, 36.7, 29.6, 29.6, 29.5, 29.3, 29.3, 25.7, 22.6, 14.1; HRMS (*m/z*) (NALDI-TOF) calcd. for $C_{18}H_{35}O_4SNa$ [M + Na]$^+$: 384.2184; found: 384.2189.

6.9.2. Synthesis of N-(2-(2-(vinylsulfonyl)ethoxy)ethyl)oleamide (VS-2)

A solution of oleic acid (1.9 g, 6.7 mmol) in Cl_2SO (15 ml) was magnetically stirred for 1 h at room temperature. Evaporation and coevaporation with anhydrous toluene (3 x 15 ml) under reduced pressure gave a crude that was dissolved in anhydrous Cl_2CH_2 (50 ml). This solution was added dropwise to a solution of 2-amino ethanol (0.608 ml, 10.1 mmol) and Et_3N (1.9 ml, 13.5 mmol) in anhydrous Cl_2CH_2 (50 ml). The reaction mixture was kept at room temperature (15 min) and then evaporated under reduced pressure to give a crude that was purified by column chromatography (EtOAc:hexane 2:1 → AcOEt) to give compound **2** as a solid (1.93 g, 88%).

(2)

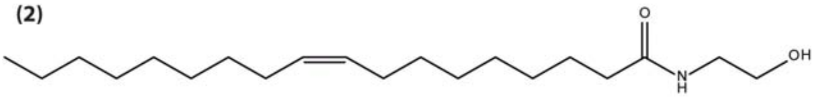

M.P. 59 – 61 °C; ν_{max} (KBr)/cm^{-1}: 3301, 1642, 1561, 1464, 1265, 1211, 1057, and 1035; ^{1}**H-NMR** (CDCl$_3$, 400 MHz): δ 6.15 (sa, 1 H), 5.35 (m, 2 H, CH=CH), 3.72 (t, 2 H, *J* = 5 Hz), 3.42 (c, 2 H, *J* = 5 Hz), 2.97 (sa, 1 H), 2.20 (t, 2 H, *J* = 7.5 Hz), 2.02 (m, 4 H), 1.62 (m, 2 H), 1.28 (several m, 20 H), 0.88 (m, 3H); ^{13}**C-NMR** (CDCl$_3$, 75 MHz): δ 174.7, 130.1, 129.8, 62.4, 42.5, 36.7, 32.0, 29.8, 29.8, 29.6, 29.4, 29.4, 29.3, 29.3, 29.2, 27.3, 27.2, 25.8, 22.7, 14.2.

To a solution of compound **2** (780 mg, 2.4 mmol) in THF (100 ml) was added DVS (497 µl, 4.8 mmol) and t-BuOK (30 mg, 0.27 mmol). The reaction mixture was magnetically stirred (15 min) at room temperature. Evaporation of the solvent under reduced pressure gave a crude that was purified by column chromatography (EtOAc:hexane 2:1 → EtOAc) gave compound **VS-2** as a syrup (538 mg, 51%).

(VS-2)

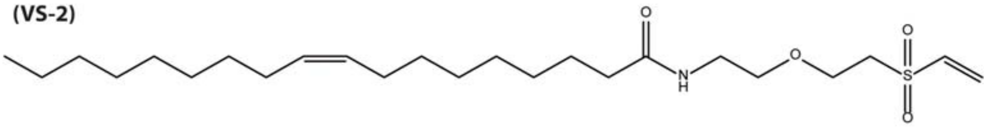

ν_{max} (KBr)/cm^{-1}: 3303, 1646, 1541, 1460, 1379, 1312, 1249, and 1124; ^{1}**H-NMR** ($CDCl_3$, 400 MHz): δ 6.71 (dd, 1 H, *J* = 16.4 and 9.7 Hz), 6.45 (d, 1 H, *J* = 16.4 Hz), 6.14 (d, 1 H, *J* = 9.6 Hz), 6.12 (br s, 1 H), 5.35 (m, 2 H), 3.91 (t, 2 H, *J* = 5.4 Hz), 3.57 (t, 2 H, *J* = 5.0 Hz), 3.46 (q, 2 H, *J* = 5.2 Hz), 3.26 (t, 2 H, *J* = 5.4 Hz), 2.18 (t, 2 H, *J* = 7.7 Hz), 2.01 (m, 4 H), 1.62 (m, 2H), 1.28 (several m, 20 H), 0.88 (m, 3H); ^{13}**C-NMR** ($CDCl_3$, 75 MHz): δ 173.5, 137.6, 130.0, 129.8, 129.5, 70.0, 63.9, 54.6, 38.8, 36.7, 32.0, 29.8, 29.8, 29.6, 29.4, 29.4, 29.2, 27.3, 27.3, 25.8, 22.8, 14.2; HRMS (*m/z*) (FAB+) calcd. for $C_{24}H_{45}NO_4SNa$ [M + Na]$^+$: 466.2967; found: 466.2968.

6.9.3. Synthesis of 1-(vinylsulfonyl)octadecane (VS-3)

To a solution of 2-thioethanol (200 mg, 2.56 mmol) in 30 ml DMSO-THF 1:1 was added 1-bromooctadecane (1.33 g, 3.84 mmol) and K_2CO_3 (531 mg, 3.84 mmol). The solution was magnetically stirred at room temperature until TLC showed complete disappearance of starting materials (24 h). The salt was vacuum filtered and the solvent removed under reduced pressure. To the crude they were added 60 ml of water and extracted with CH_2Cl_2 (2 x 60 ml). The combined organic extracts were then dried (Na_2SO_4) and the solvent removed under reduced pressure to give a crude that was purified by column chromatography (hexane:ether 1:1) to give compound **3a** as solid (775 mg, 92%).

(3a)

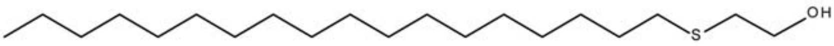

M.P. 60 – 61 °C; ν_{max} (KBr)/cm^{-1} : 3213, 2918, 2849, 1460, 1063 and 719; ^{1}**H-NMR** ($CDCl_3$, 400 MHz): δ 3.71 (t, 2 H, *J* = 6.0 Hz), 2.72 (t, 2 H, *J* = 5.6 Hz), 2.51 (t, 2 H, *J* = 7.4 Hz), 2.11 (s, 1 H), 1.58 (m, 2 H), 1.41 – 1.20 (m, 30 H), 0.87 (t, 3 H, *J* = 6.7 Hz); ^{13}**C-NMR** ($CDCl_3$, 100 MHz): δ 60.3, 35.5, 32.0, 31.8, 29.9, 29.8, 29.8, 29.7, 29.7, 29.6, 29.4, 29.3, 29.0, 22.8, 14.2.

To a solution of compond **3a** (425 mg, 1.29 mmol) in AcOH (6.4 ml) was added 33% H_2O_2 (2.6 ml). The solution was kept in the dark for 24 h. Evaporation of the solvent under reduced pressure gave a crude that was purified by column chromatography (EtOAc) to give **3b** as a solid (397 mg, 85%).

(3b)

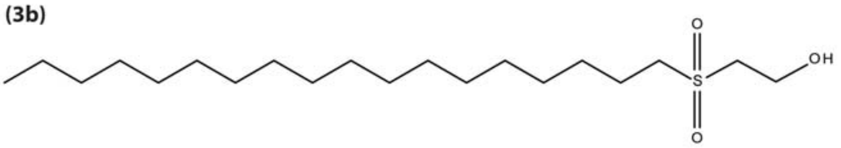

M.P. 93 – 94 °C; ν_{max} (KBr)/cm^{-1}: 3368, 2913, 2847, 1594, 1470, 1256, 1133 and 1059; ^{1}**H-NMR** ($CDCl_3$, 400 MHz): δ 4.13 (t, 2 H, *J* = 5.0 Hz), 3.19 (t, 2 H, *J* = 5.0 Hz), 3.07 (t, 2 H, *J* = 8.0 Hz), 1.85 (m, 2 H), 1.50 – 1.18 (m, 30 H), 0.88 (t, 3 H, *J* = 6.6 Hz); ^{13}**C-NMR** ($CDCl_3$, 100 MHz): δ 56.5, 54.9, 54.7, 32.0, 29.8, 29.7, 29.6, 29.5, 29.4, 29.2, 28.6, 22.8, 22.0, 14.2. HRMS (*m/z*) (FAB+) calcd. for $C_{20}H_{42}O_3SNa$ $[M + Na]^+$: 385.2752; found: 385.2755.

A solution of compond **3b** (173 mg, 0.48 mmol) in anhydrous CH_2Cl_2 (10 ml) was cooled by means of an ice bath. Et_3N (0.2 ml, 1.42 mmol) and mesyl chloride (0.57 ml, 0.73 mmol) were then added and the solution was left to warm to room temperature until TLC showed complete disappearance of starting materials (24 h). The solvent was removed under reduced pressure and the resulting crude was purified by column chromatography (hexane:ether 1:1) to give **VS-3** as a solid (133 mg, 81%).

(VS-3)

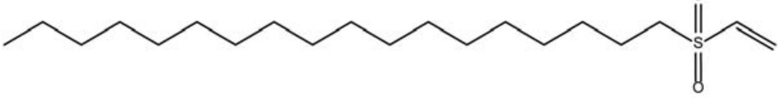

M.P. 61 – 62 °C; ν_{max} (KBr)/cm^{-1}: 3062, 2915, 2847, 1462, 1284, 1124, 908 and 730; ^{1}**H-NMR** ($CDCl_3$, 400 MHz): δ 6.62 (dd, 1 H, *J* = 16.6 and 9.8 Hz, CH =), 6.43 (d, 1 H, *J* = 16.6 Hz, = CH_2 trans), 6.15 (d, 1 H, *J* = 9.8 Hz, = CH_2 cis), 2.96 (t, 2 H, *J* = 8.0 Hz), 1.77 (m, 2 H), 1.46 – 1.20 (m, 30 H), 0.88 (t, 3 H, *J* = 6.7 Hz); ^{13}**C-NMR** ($CDCl_3$, 100 MHz): δ 136.3, 130.4, 54.4, 32.0, 29.8, 29.7, 29.7, 29.7, 29.6, 29.4, 29.3, 29.1, 28.5, 22.8, 22.4, 14.2. HRMS (*m/z*) (FAB+) calcd. for $C_{20}H_{40}O_2SNa$ $[M + Na]^+$: 367.2647; found: 367.2644

6.9.4. Synthesis of Cholest-5-ene, 3-[2-(ethenylsulfonyl)ethoxy]-, (3β)- (Chol-VS)

To a solution of cholesterol (300 mg, 0.77 mmol) in THF (20 ml) was added DVS (0.12 ml, 1.16 mmol) and t-BuOK (9 mg, 0.077 mmol). The reaction mixture was magnetically stirred at room temperature for 1 h. Amberlita IR 120H was then added and the magnetic stirring continued for additional 30 min. After filtration, the solvent was evaporated under reduced pressure. TLC of the crude showed the presence of cholesterol. Ac_2O (8 ml) and pyridine (4 ml) were added to the resulting crude and the new reaction mixture was kept at room temperature for 16 h. Acetylation of the crude reaction allowed the separation of compound **Chol-VS**. Evaporation under reduced pressure gave a crude that was purified by column chromatography (ether:hexane 1:2) yielding compound **Chol-VS** as a solid (204 mg, 52%).

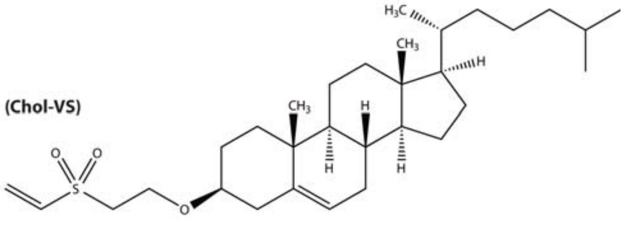

M.P. 133 – 135 °C; $[\alpha]_D$ - 19 (c 1, chloroform); ν_{max}(KBr)/cm^{-1} : 3409, 1461, 1373, 1319, 1115, and 1052; ^{1}**H-NMR** ($CDCl_3$, 400 MHz): δ 6.75 (dd, 1 H, J = 16.7 and 9.9 Hz), 6.40 (d, 1 H, J = 16.7 Hz), 6.07 (d, 1 H, J = 9.9 Hz), 5.35 (br s, 1 H), 3.88 (t, 2 H, J = 5.6 Hz), 3.23 (t, 2 H, J = 5.6 Hz), 3.19 (m, 1 H), 2.35 – 1.84 (several m, 7 H), 1.56 – 0.95 (several m, 21 H), 0.99 (s, 3 H), 0.92 (d, 3 H, J = 6.4 Hz), 0.86 (d, 6 H, J = 6.6 Hz), 0.67 (s, 3H); ^{13}**C-NMR** ($CDCl_3$, 125 MHz): δ 140.2, 138.0, 128.5, 122.1, 79.8, 61.5, 56.7, 56.1, 55.4, 50.1, 42.3, 39.7, 39.5, 38.8, 37.0, 36.8, 36.2, 35.8, 31.9, 31.8, 28.2, 28.1, 28.0, 24.3, 23.8, 22.9, 22.5, 21.0, 19.3, 18.7, 11.8; HRMS (m/z) (FAB+) calcd. for $C_{31}H_{52}O_3SNa$ $[M + Na]^+$: 527.3535; found: 527.3535.

6.9.5. Synthesis of ferrocenylmethyl cholesteryl ether (Chol-Fc)

To a solution of dimethylaminomethyl ferrocene (1.24 ml, 6.02 mmoles) in acetone (60 ml) was added cholesterol (2.61 g, 6.4 mmoles) followed by addition of methyl iodide (380 μL, 6.1 mmoles). The reaction mixture was magnetically stirred 24 h at 40 °C. Afterwards, the solvent was evaporated and the reaction crude diluted with water and extracted with CH_2Cl_2. The solvent was removed under reduced pressure and the resulting crude was purified by column chromatography (EtOAc:hexane 1:4) yielding compound **Chol-Fc** as a solid (15%).

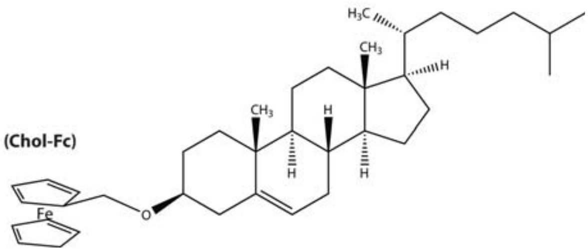

^{1}**H-NMR** ($CDCl_3$, 400 MHz): δ 5.35 (s, 1 H, =CH cholesterol), 4.31 (s, 2 H, ferrocene), 4.23 (s, 2 H, CH_2O ferrocene), 4.12 (s, 7 H, ferrocene), 3.23 (m, 1 H, CHOH cholesterol), 1.56 - 0.95 (several m, 21 H, cholesterol), 0.99 (s, 3 H), 0.92 (d, 3 H, $J = 6.4$ Hz), 0.86 (d, 6 H, $J = 6.6$ Hz), 0.67 (s, 3H); ^{13}**C-NMR** ($CDCl_3$, 100 MHz): δ 141.10, 121.41, 84.23, 78.10, 69.35, 68.40, 68.37, 66.10, 56.77, 56.13, 50.17, 42.31, 39.78, 39.50, 39.16, 37.27, 36.87, 36.17, 35.77, 31.94, 31.88, 30.93, 29.69, 28.47, 28.23, 28.01, 24.28, 23.81, 22.82, 22.56, 21.05, 19.38, 18.71, 11.85.

6.10. Tables summarizing the prepared vesicle systems

Quatsome-like systems and liposome-like systems prepared in this Thesis are summarized in Table 6.3 and Table 6.4, respectively.

Table 6.3.: Description of the quatsome-like systems prepared in this Thesis.

Vesicle[a] type	**Solvent vol. %[b] (v/v$_{total}$ x 100)**	**Membrane components[c] concentration (mM)**	**Methodology of preparation**
	QUATSOME-LIKE SYSTEMS		
Chol-CTAB (W-US)	100 % water	10 mM CTAB 10 mM Chol	Sonication
Chol-CTAB (W10Et-US)	90 % water 10 % EtOH	7.3 mM CTAB 7.3 mM Chol	Sonication
Chol-CTAB (W10Et-DELOS)	90 % water 10 % EtOH	7.3 mM CTAB 7.3 mM Chol	DELOS-SUSP
Chol-CTAB (W20Et-DELOS)	80 % water 20 % EtOH	6.4 mM CTAB 6.4 mM Chol	DELOS-SUSP
Chol-CTAB (PBS10Et-DELOS)	90 % PBS[f] 10 % EtOH	7.3 mM CTAB 7.3 mM Chol	DELOS-SUSP
Chol-CTAB (W10Et-TFH800x1)	90 % water 10 % EtOH	7.3 mM CTAB 7.3 mM Chol	TFH + extrusion 800 nm[e]x 1 time
Chol-CTAB (W10Et-TFH100x1)	90 % water 10 % EtOH	7.3 mM CTAB 7.3 mM Chol	TFH + extrusion 100 nm[e]x 1 time
Chol-CTAB (W10Et-TFH100x21)	90 % water 10 % EtOH	7.3 mM CTAB 7.3 mM Chol	TFH + extrusion 100 nm[e]x 21 times
Chol-SDS[d] (W10Et-DELOS)	90 % water 10 % EtOH	14.6 mM SDS 7.3 mM Chol	DELOS-SUSP
Chol-MKC[d] (W10Et-DELOS)	90 % water 10 % EtOH	7.3 mM MKC 3.65 mM Chol	DELOS-SUSP
Chol-CPC[d] (W10Et-DELOS)	90 % water 10 % EtOH	7.3 mM MKC 3.65 mM Chol	DELOS-SUSP
β-sitosterol-CTAB (W10Et-DELOS)	90 % water 10 % EtOH	7.3 mM CTAB 7.3 mM β-sitosterol	DELOS-SUSP

[a] Unless otherwise noted, equimolar ratio between membrane components are used.
[b] % of solvent volume in the obtained sample.
[c] Final concentration of membrane components in the obtained sample.
[d] Cholesterol:Surfactant at 1:2 molar ratio.
[e] Pore size of the membrane filter used in the extrusion process.
[f] PBS 100 mM, pH = 7.4.

Table 6.4.: Description of the liposome-like systems prepared in this Thesis.

Vesicle[a] type	Solvent vol. %[b] (v/v$_{total}$ x 100)	Membrane components[c] concentration (mM)	Methodology of preparation
LIPOSOME-LIKE SYSTEMS			
Chol-DPPC (W-US)	100 % water	1.3 mM DPPC 1.3 mM Chol	Sonication
Chol-DPPC (W-TFH100x21)	100 % water	1.3 mM DPPC 1.3 mM Chol	TFH + extrusion 100 nm[e]x 21 times
Chol-DPPC (W5Et-DELOS)	95 % water 5 % EtOH	1.3 mM DPPC 1.3 mM Chol	DELOS-SUSP
DPPC (W5Et-DELOS)	95 % water 5 % EtOH	1.9 mM DPPC	DELOS-SUSP
Chol-DOPC[d] (PBS10Et-DELOS)	90 % PBS[f] 10 % EtOH	2.4 mM DOPC 0.6 mM Chol	DELOS-SUSP
DOPC (W17Et-DELOS)	83 % water 17 % EtOH	3.6 mM DOPC	DELOS-SUSP
DOPG (HEPES-TFH100x21)	100 % HEPES[g]	7 mM DOPG	TFH + extrusion 100 nm[e]x 21 times

[a] Unless otherwise noted, equimolar ratio between membrane components are used.
[b] % of solvent volume in the obtained sample.
[c] Final concentration of membrane components in the obtained sample.
[d] Cholesterol:DOPC at 1:4 molar ratio.
[e] Pore size of the membrane filter used in the extrusion process.
[f] PBS 100 mM, pH = 7.4.
[g] 10 mM HEPES/10 mM NaCl.

A

Appendix

A.1. Molecular Dynamics simulations of cholesterol/CTAB mixtures in water

All the MD simulations were performed using the NAMD 2.9 and VMD programs [141, 142]. The model for the molecules was based on the CHARMM22/CMAP force field [289, 290], designed for biomolecular simulations. The standard CHARMM force-field parameters for water (TIP3P) and cholesterol was used, since they are known to correctly predict the solvation free energy of this molecule [291], a quantity of major importance in the hydrophobic self-assembly processes studied here. The CTAB molecule is composed of a cetyltrimethylammonium cation, modeled following the parameters given in reference [292], and a bromide (Br^-) counterion, modeled employing the parameters given in reference [293].

Simulations of several kinds of systems were performed. First, bilayer simulations were performed aimed at elucidating the molecular organization of CTAB and cholesterol in vesicles. Since the simulation of a whole vesicle with atomistic detail is impossible with current computer capabilities, the same methodology usually employed to simulate heterogeneous biological membranes containing phospholipids and cholesterol was employed [294]. It was considered a bilayer patch in the XY plane in its tensionless state in contact with water maintained at a pressure of 1 in the Z direction (perpendicular to the bilayer). Three different bilayers with different compositions were considered, as shown in Table A.1.

A second kind of simulation (bulk simulation) was also performed aimed at elucidating how cholesterol molecules are incorporated inside small micelles of CTAB. In this case (simulation S4 in Table A.1), it was considered diluted bulk conditions, that is, a single CTAB micelle with a certain amount of cholesterol molecules inside a large water box. Finally, several auxiliary simulations of simpler bulk systems were performed which were found to be useful for the interpretation of the results of the previous simulations

(simulations A1–A3 in Table A.1). In A1, it was considered the simplest possible mixed system, namely one CTAB and one cholesterol molecule in water. In A2, it was considered a small cluster of cholesterol molecules in water. In A3, it was considered a pure CTAB micelle in water. In some of the previously described simulations, it was computed the Gibbs free energy characterizing self-assembly by employing the adaptive biasing force (ABF) methodology [141]. In these calculations, one starts from the results of the previous, equilibrium MD simulations and obtains the free energy (potential of mean force) over a "reaction" coordinate by applying a biasing force to the system.

Table A.1.: Composition for each simulation described in the text (number of molecules of each species and total number of atoms) and equilibrium size of the simulation box (averaged over production runs). *Note: For bilayer simulations, it was considered a bilayer patch in the XY plane in its tensionless state in contact with water maintained at a pressure of 1 in the Z direction (perpendicular to the bilayer). For bulk simulations, it was considered diluted bulk conditions (certain amount of molecules inside a large water box).*

Simulation	Number of molecules Chol/CTAB/water	Atoms (total)	Eq. box size
S1 (Bilayer)	54/54/5,443	23,727	15.7 nm^2 × 14.5 nm
S2 (Bilayer)	30/60/5,443	22,329	11.9 nm^2 × 18.0 nm
S3 (Bilayer)	10/60/5,443	20,849	14.4 nm^2 × 14.0 nm
S4 (Bulk)	1/72/11,109	37,937	369.7 nm^3
A1 (Bulk)	1/1/6,434	19,445	194.0 nm^3
A2 (Bulk)	60/0/1,063	7,629	70.43 nm^3
A3 (Bulk)	0/72/21,176	68,064	667.3 nm^3

All the MD simulations were performed using the NAMD2 software [141] version 2.9 running in parallel using 32-64 Itanium Monvale processors at the Finisterrae Supercomputer (CESGA Supercomputing Center, Spain). The equations of motion were solved with a time step of 2 fs. Electrostatic interactions were computed using the particle mesh Ewald summation method (PME) with the standard settings in NAMD (1 Å spatial resolution and were updated each 2 time steps). Lennard- Jones interactions were truncated at 1.2 nm employing a switching function starting at 1.0 nm. In all our simulations, the temperature was maintained constant (298 K) using the Langevin thermostat with a relaxation constant of 1 ps^{-1}.

The pressure was adjusted to 1 atm employing the Nosé-Hoover-Langevin piston as implemented in NAMD2 with an oscillation period of 100 fs and a decay time of 50 fs. It was employed periodic boundary conditions in all directions. NAMD configuration, topology and forcefield files are available from the authors under request.

In all the simulated systems, it was followed the same sequence of build-up and equilibration. First, an initial configuration was built employing the VMD program [142] and/or the CHARM-GUI membrane builder [295]. The energy of the initial configuration was minimized for 10^4 steps following the combined conjugate gradient and line search procedure implemented in NAMD 2.9. Then the system was solvated and the energy of the resulting system was minimized again. After energy minimization, it was performed a short NVT run (i.e. the pressure constraint was not imposed). Finally a long simulation run was performed in each system under the conditions (normal pressure or bulk pressure) described before.

Several physical quantities (such as potential and kinetic energy, area per molecule in bilayer systems or volume in bulk systems) were monitored in order to discriminate between the initial, relaxation processes and the final equilibrium state. For example, in the S1 bilayer system (Table A.1) the equilibration/relaxation required 3 ns and the total simulation time was 30 ns with a cost of 3.7 hours of CPU per ns of simulation. The results presented correspond to averages over the production part of the MD trajectories, obtained after discarding the initial equilibration/relaxation period. All the snapshots and the monitoring of the simulation (evolution of energy, simulation box, temperature, pressure, etc.) was performed using the VMD program [142]. The atomic density profiles in the bilayer simulations were performed by a home-made python script running in VMD to read NAMD trajectories. The profiles were averaged over the XY coordinates and over the production (equilibrium) part of the trajectory.

A.1.1. Protocol for the build-up of the initial configurations and equilibration for our MD bilayer simulations (S1-S3 in Table A.1)

Generation of initial configurations for bilayer simulations is typically made generating random, initial positions for the molecules at a specified area per molecule, avoiding molecular overlap. In practice, one employs the algorithms implemented in the VMD or CHARMM-Gui programs. However, in our case, the CTAB molecules are not available in the libraries of these standard programs so we have to do it manually or by using home-made programs. To this end, it was first performed a preliminary simulation in order to build up a bilayer template containing a (initially) homogeneous mixture of CTAB and cholesterol.

We started with a pre-equilibrated water slab with dimensions 60x60x47 $Å^3$ inside a simulation box with dimensions 60x60x150 $Å^3$ generated with the solvate option of the

VMD program. Then, using VMD, we added 30 surfactant and 30 cholesterol molecules on top of each of the two water/vacuum interfaces with homogeneous distribution. The initial surface area was large enough (two surfaces with 36 nm^2 each) to ensure an expanded state, which makes easier to avoid overlaps between the initial positions of the molecules. After energy minimization, we performed a 16 ns MD simulation run using the NAMD2 program at fixed T, p and zero surface tension. During the simulation, the size of the simulation box in the dimension perpendicular to the water slab was reduced in order to put in contact the hydrophobic tails of the molecules of each monolayer. In this way, the two monolayers were merged, obtaining in this way a bilayer configuration to be employed in subsequent simulations.

The initial configuration for simulations S1 and S2 of Table A.1 was obtained from this preliminary bilayer configuration. In order to obtain the numbers of cholesterol and CTAB molecules for each simulation as indicated in Table A.1, we randomly removed cholesterol and/or surfactant (in equal numbers for each layer). The initial configuration for simulation S3 was with an identical method but in this case we started from the final configuration of simulation S2. The configurations obtained in this way were energy minimized and MD simulations were performed with the parameters and conditions described before.

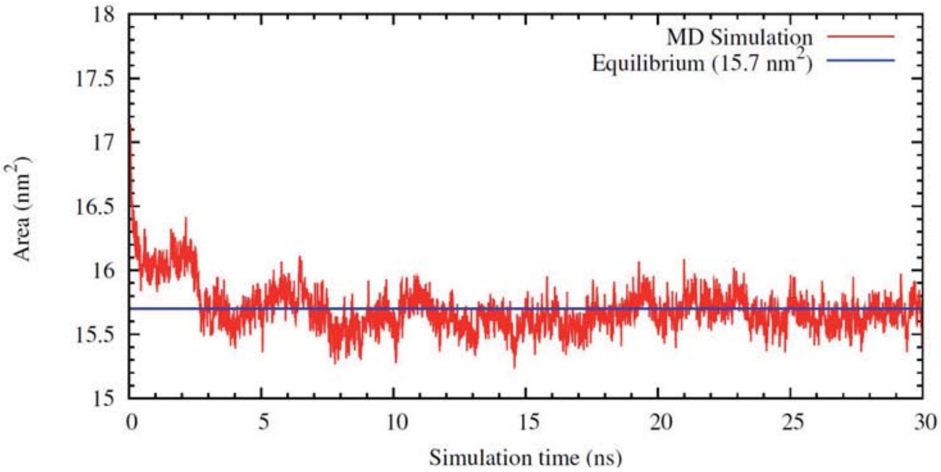

Figure A.1.: Evolution of bilayer area as a function of time in simulation S1. The equilibrium value reported in Table A.1 (calculated as an average over the last 10 ns) is also shown.

Because of the deletion method employed to generate the initial conditions for the S1-S3 simulations, we observe an initial, equilibration process in which the lateral are of the membrane rapidly decreases (in order to reach the correct equilibrium value). This is illustrated in Figure A.1, which corresponds to simulation S1. In this case, this equilibration period corresponds to 3 ns, which is a small portion of the total simulated time (30 ns). Similar equilibration times were observed for all simulations.

A.1.2. Protocol for the build-up of the initial configurations for our MD simulations A1-A3 and S4 in Table A.1

The initial condition for the A1 simulation in Table A.1 was simply a random placement of the two molecules (one surfactant with its counterion and one cholesterol molecule). A large amount of pre-equilibrated water was added to this initial configuration using the “solvate” option in VMD.

The initial condition for the A2 simulation (pure CTAB in water) in Table A.1 was obtained by generating (with a home-made tcl script) two layers with a periodic arrangement of surfactant molecules (the two layers had the hydrophilic heads pointing in opposite directions). The Br^- counterions were placed randomly and a large amount of water was added by using the solvate option of the VMD program. The obtained configuration was energy minimized with NAMD2. A short (1 ns), NVT equilibration run was performed and the CTAB system adopted a micellar configuration during this equilibration run. The obtained configuration was employed as initial condition for the subsequent NPT run described before.

The initial configuration for the A3 simulation (pure cholesterol) was obtained employing the CHARMM-GUI Membrane builder, since cholesterol is one of the molecules included in the lipid library of this program.

The initial configuration for the S4 simulation in Table A.1 was obtained by adding a cholesterol molecule to the A2 simulation.

A.1.3. Free Energy calculations

The Free Energy calculations were made employing the adaptive biasing force (ABF) methodology. The ABF calculations performed here were the following. First, the free energy of interaction between a surfactant and a cholesterol molecule was obtained using a 10 ns MD-ABF calculation starting from simulation A1. The reaction coordinate was the center of mass separation between the two molecules (0.2 Å resolution) and the employed force constant was the default value of 10 kcal/mol/Å^2. In a second calculation, we obtained the free energy of transfer of a cholesterol or a CTAB molecule between a 1:1 bilayer and water. In this case, the MD-ABF calculation starts from the result of simulation S1 in Table A.1. We choose as the reactions coordinate the distance between a tagged molecule (a cholesterol or a surfactant) and the center of the bilayer.

The force constant employed in these two cases was 50 kcal/mol/Å^2 and the total simulation time was 5.6 ns. Analogous calculations were performed for the calculation of the potential of mean force for the transfer of a cholesterol molecule (simulation S4) or a surfactant molecule (simulation A2) from a CTAB micelle to water or the extraction of a cholesterol molecule from a pure cholesterol nanoparticle to water (simulation A3). It has to be emphasized here that ABF-MD simulations are much more computationally expensive than typical MD runs. For example, for the system S1, a ABF-MD run costs about 1.5 days of CPU per ns of simulation to be compared with the 3.7 hours per ns required by unbiased MD simulations of the same system.

A.2. Molecular Dynamics simulations of Chol-VS

All the MD simulations were performed using the NAMD 2.9 and VMD programs [141, 142]. The model for the molecules was based on the CHARMM22/CMAP force field [289, 290], designed for biomolecular simulations. Extensive simulations of Chol-VS molecule in different situations were performed in Silvia Illa Master's Thesis [235]. It was simulated: one molecule of Chol-VS at water-chloroform interface, a monolayer of Chol-VS at water-chloroform interface and one molecule of Chol-VS with one molecule of CTAB in bulk water.

Additionally, the simulation S1-VS was performed to study the interaction between 64 molecules of CTAB and 64 molecules of Chol-VS in water. In this simulation, the temperature was maintained constant (298 K) and the pressure was adjusted to 1 atm. Table A.2 shows the composition used in such simulation.

Table A.2.: Composition of simulation S1-VS described in the text (number of molecules of each species and total number of atoms) and equilibrium size of the simulation box (average over production runs).

Simulation	**Number of molecules Chol-VS/CTAB/water**	**Atoms (total)**	**Eq. box size (Å^3)**
S1-VS (NPT)	64/64/9,176	37,128	50 x 50 x 111

A.3. Molecular Dynamics simulations of nanocrystals

A.3.1. Simulation protocol

The steps followed to prepare the system were the following: (i) MD simulations of NCs in vacuum (without capping molecules) (ii) addition of capping molecules (iii) addition of solvent (water or chloroform).

In the first step, we generated small clusters of Si atoms and NVT simulations (at 298 K) were performed. We started with a small number of atoms, adding more atoms until the required size (2.8 nm) was obtained. The obtained NC had 342 Si atoms. The same protocol was also applied to Au, obtaining a NC of 1.8 nm with 281 Au atoms. The obtained NCs are shown in Figure A.2.

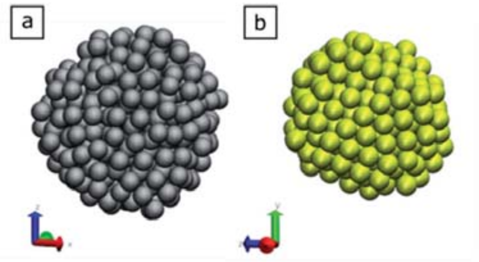

Figure A.2.: Nanocrystals of (a) Si and (b) Au generated for use in MD simulations (not to scale).

In the second step, we added the capping molecules. In order to obtain the configurations of the molecules, we prepared NVT simulations containing a single NC and randomly distributed molecules (1-octene for SiNC and 1-dodecanethiol for AuNC). In order to build the capping layer, we performed NVT simulations in the presence of a biasing force which induced an attraction between the capping molecule and the NC (a terminal C atom in the case of 1-octene and the S atom in the case of 1-dodecanethiol). The simulations were performed maintaining the NC atoms in fixed positions. The NVT runs were performed until all the terminal atoms of the capping molecules reached the NC surface. These final configurations were stored for further use in simulations with solvent. In the case of 1-dodecanethiol, the H atom of the thiol group was suppressed (since in the actual chemical reaction the H is released) and its partial charge was added to the S partial charge. We recall here that the number of added capping molecules was different for each case. In the case of Si NC, we added 242 molecules obtaining a coverage of 9.8 molecules/nm^2, very close to the estimate of 245 molecules (9.9 molecules/nm^2) obtained from the analysis of the TGA experimental data. In the case of the AuNC we added 65 capping molecules (1-dodecanethiol) corresponding to a surface coverage of 6.39 molecules/nm^2, which are identical to the values estimated experimentally in [264].

In the third step, we added the solvent (water or chloroform) using the solvate tool in VMD. In the case of chloroform the program required a pre-equilibrated solvent slab that was prepared from NPT simulations of pure chloroform at ambient T and p. The system containing the NC, the capping molecules and the solvent was further equilibrated using NPT simulations at 298 K and 1 atm. In these simulations, the atoms of the NC (Si or Au) were maintained at fixed positions. The terminal atoms (C or S) of the capping molecules were also fixed at their positions. A few ns of simulation were enough to obtain stable sizes for the simulation box. The obtained equilibrium sizes for the (cubic) simulation box were the following. For Si nanoparticles, the equilibrium sizes of the cubic simulation box were 69.1 Å in water and 68.6 Å in chloroform. For Au nanoparticles, the equilibrium sizes of the cubic simulation box were 67.9 Å in water and 66.5 Å in chloroform.

A.3.2. Computational details

The equations of motion were solved with a time step of 1 fs (NPT simulations of Si particles) and 2 fs time step (all other simulations). The temperature was kept constant at 298 K using the Langevin thermostat with a relaxation constant of 1 ps^{-1}. A constant pressure of 1 atm was applied using an isotropic Nosé-Hoover-Langevin piston with an oscillation period of 300 fs and decay time of 150 fs. Periodic boundary conditions in all directions were employed in all our simulations. Electrostatic interactions were computed using the particle mesh Ewald summation method (PME) with the standard settings in NAMD (1 Å spatial resolution and were updated each 2 time steps). Lennard-Jones interactions were truncated at 1.2 nm employing a switching function starting at 1.0 nm. In all production runs, we maintained the atoms of the NC (Si or Au) and the terminal atoms (C or S) of the capping molecules fixed at their positions. Statistics shown in the work were typically collected in production runs of 20 ns.

In Figure A.3, images of snapshots from the MD simulations are shown corresponding to the two kinds of particles considered in this work (SiNC and AuNC with their organic capping ligands) in the two different solvents involved in the experiments (water and chloroform). As shown, the structure of the capping layer of the two NCs is very different, thus the equilibrium lengths of capping molecules were studied.

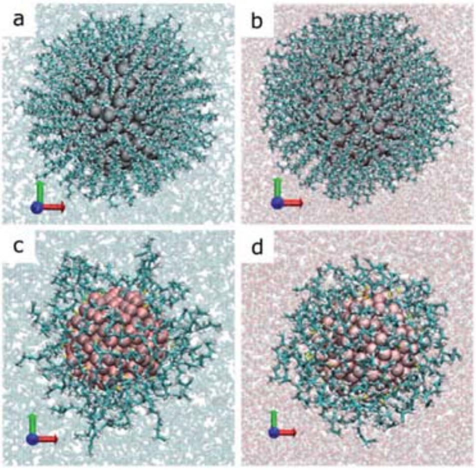

Figure A.3.: Snapshots from MD simulations using the Visual Molecular Dynamics (VMD) program [142]. A SiNC capped with 1-octene molecules in (a) chloroform and (b) water. An Au NC capped with 1-dodecanethiol in (c) chloroform and (d) water. Si and Au atoms are shown with their Van der Waals radius. Capping molecules are shown in bond representation. Solvent molecules are drawn translucent. The results show that SiNCs have denser packed ligand layers than the AuNCs, and that in chloroform the ligands are more extended.

The length *(l)* (see Figure A.4a) of the capping molecule was defined as the largest distance between the center of the adsorbed atom of the capping molecule and the center of any atom from the same molecule, averaged for all capping molecules of the NCs and averaged over time for all the production run. We obtained l = 0.84 nm for 1-octane, 1.07 nm for 1-dodecanethiol in water and 1.15 nm for 1-dodecanethiol in chloroform. These obtained distances were compared with the maximum values corresponding to fully extended molecules. For the case of 1-octane the distance between the center of two extreme C atoms is 0.89 nm (projecting all the carbon-carbon bond lengths onto the direction of the molecular axis) and for 1-dodecanethiol the distance between the center of the extreme C atom and the center of the thiol S atom is 1.55 nm. This means that the 1-octane molecules over the SiNC have an average length which is 94% of their maximum length and 1-dodecanethiol molecule are found to be at average lengths of 69% (in water) and 74% (in chloroform) of their maximum length. We also studied orientation angles for 1-octane, which is defined as the angle *(α)* (see Figure A.4a) between the unit vector normal to the nanocrystal surface at the point of adsorption of each molecule and the vector joining the adsorbed atom of the capping molecule and the atom from the same molecule situated farthest from the adsorption point. The 1-octane molecules were observed to form a well-defined angle (28°) with the direction normal to the surface of the SiNC. For each capping molecule we compute the *cos(α)* and the average *<cos2α>* over all capping molecules and simulation time.

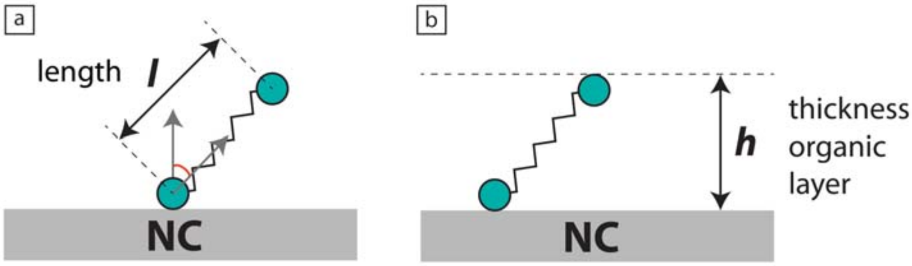

Figure A.4.: Schematic representation of (a) the length *(l)* of the capping molecule, defined as the largest distance between the center of the adsorbed atom of the capping molecule and the center of any atom from the same molecule, and the angle *(α)* between the unit vector normal to the nanocrystal surface at the point of adsorption of each molecule and the vector joining the adsorbed atom of the capping molecule and the atom from the same molecule situated farthest from the adsorption point. (b) Schematic representation of the thickness *(h)* of the organic layer covering the NC.

For all particles we also report the thickness h (see Figure A.4b) of the organic layer covering the NC. The thickness of the layer is related to both the length of the capping molecules and the angle α. In the simulations, the thickness is calculated as the distance measured perpendicular to the surface of the NC between the surface of the NC and the end of the farthest atom of the capping molecule. Note that in this calculation the size of these two extreme atoms is also accounted for. The obtained results were $h = 1.14$ nm for SiNCs in both solvents and $h = 0.89$ nm and 1.14 nm for AuNCs in water and chloroform respectively.

A.3.3. Simulation results for planar surfaces

In order to estimate the effects of curvature, we have performed MD simulations in the NPT ensemble of a small planar surface covered with 1-octane molecules. We considered three different coverages: 9.95 molecules/nm^2, 6.25 molecules/nm^2 and 2.8 molecules/nm^2. These values are similar to those found for the SiNCs, AuNCs, and a less dense coverage. Here, we consider only the case of water solvent. Our results show (Figure A.5) that capping molecules form a highly ordered layer for the coverages of 9.95 molecules/nm^2 and 6.25 molecules/nm^2 and a highly disordered layer for a coverage of and 2.8 molecules/nm^2. A comparison of these results with those reported in the main text for the NCs, demonstrate the importance of curvature in the state and ordering of the capping layer. The same coverage of capping molecules, which is highly disordered onto the highly curved AuNC, will be extremely ordered when adsorbed onto a planar surface.

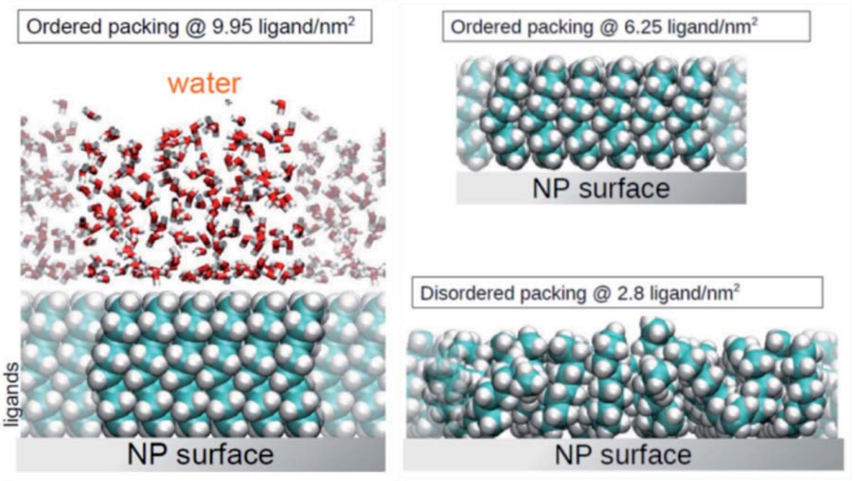

Figure A.5.: Simulation results for planar surfaces covered with different coverages of 1-octane molecules.

A.4. Theoretical model for SAXS data analysis of vesicles

In order to understand the experimental SAXS data, a mathematical model reported in the literature has been used. This theoretical model was studied by Dr. Evelyn Moreno from the *Nanomol* group (ICMAB-CSIC). This model describes the scattering of monodisperse systems, where the vesicles are equated to core-shell spheres and the composition of the cores are the same as the dispersant medium (hollow spheres).

The typical scattering pattern of a hollow sphere and other geometrical bodies with the same maximum size are represented in Figure A.6.

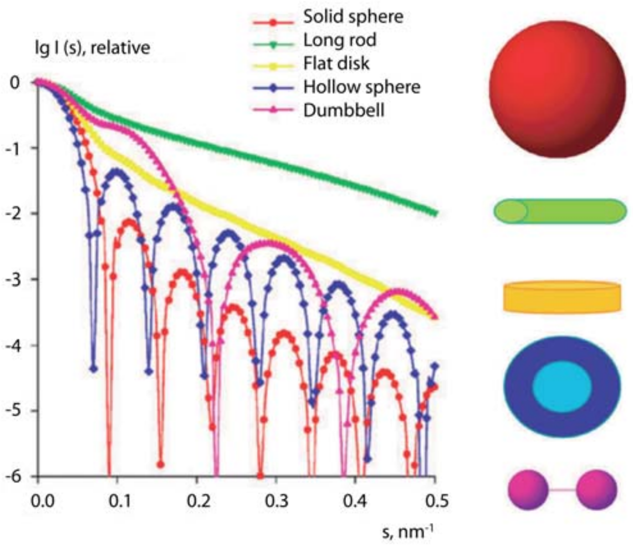

Figure A.6.: Typical scattering patterns of geometrical bodies with the same maximum size. Adapted from [175].

The background subtracted normalized scattered intensity of an object is directly related to the morphology and interactions between the objects in the scattering volume. The *I(q)* from a particulate suspension with random orientation can be expressed as:

$$I(q) = NV^2 \Delta\rho P(q) S(q) \tag{A.1}$$

Where N is the number density of particles, V their volume, $\Delta\rho$ the difference of scattering length density between the solvent and the particle, *P(q)* the form factor of the particle and *S(q)* the structure factor of interaction between particles. The form factor describes the morphology, shape and size, of the particle and the structure factor accounts for the interaction between them. As ideally the sample measurements are performed with diluted samples the interaction between particles can be neglected, thus the term $S(q) \approx 1$, over the q range of investigation. The factorization described in Equation A.1 is strictly applicable for monodisperse and spherically symmetric particles [133, 175]. This expression can be evaluated analytically in a few cases of defined geometrical shapes (cylinders, spheres, disks, etc.). Probably the easiest case to consider is a sphere of radius R, uniform in electron density. In this case, the form factor, $P(q)$, of an sphere of radius R can be readily calculated according to Equation A.2,

$$P(q,R) = F_0^2(q,R) = (\frac{3[sin(qR) - qRcos(qR)]}{(qR)^3})^2 \tag{A.2}$$

where F_0 (q,R) is the scattering amplitude of a sphere -of radius R- given by the Fourier Transform of the radial electron density [133, 175]. In the case of core-shell spheres with core and shell radii R_1 and R_2, respectively, the form factor depends on the contrast of both the core and the shell

$$\Delta\rho^2 V^2 P(q,R_1,R_2) = \left[\Delta\rho_2 V_2 F_0(qR_2) - \Delta\rho_1 V_1 F_0(qR_1)\right]^2 \tag{A.3}$$

where $\Delta\rho_1$ and $\Delta\rho_2$ are the difference of scattering length densities between the core and the shell and the solvent and the shell, respectively. For the case of unilamellar vesicles one can consider them as a core shell sphere in which the core is filled with water and consequently the resulting shell scattering function is given by:

$$V^2 P(q,R_1,R_2) = \frac{16\pi^2}{9}\left[R_2^3 F_0(qR_2) - R_1^3 F_0(qR_1)\right]^2 \tag{A.4}$$

For the analysis of the scattering of vesicles using Equation A.4 the following assumptions have been made:

1. The scattering length density is assumed to be uniform across the bilayer. This assumption will be reasonable in the cases in which the two membrane components mix well and no phase segregation of chains is expected (this is true for strongly synergistic mixtures).

2. The scattering contribution of the counter ions is neglected assuming they have low contrast.

3. The packing difference between the inner and the outer layers of the bilayers is unlikely to make a significant difference in the scattering function of unilamellar vesicles.

As an example, the theoretical scattering of three monodisperse vesicular systems was studied using two different vesicle sizes (50 and 100 nm) and two different thickness layers (4.4 and 10 nm) (Figure A.7). Origin Lab. was used to simulated the *q*-dependence X-ray scattering of these monodisperse solutions of vesicles. As evidenced by Figure A.7, at finite *q*, scattering curve of vesicular symmetric objects consists of a series of high frequency oscillations (according to the dimensions of the vesicle) modulated with a low frequency curve (according to the density profile or the membrane thickness).

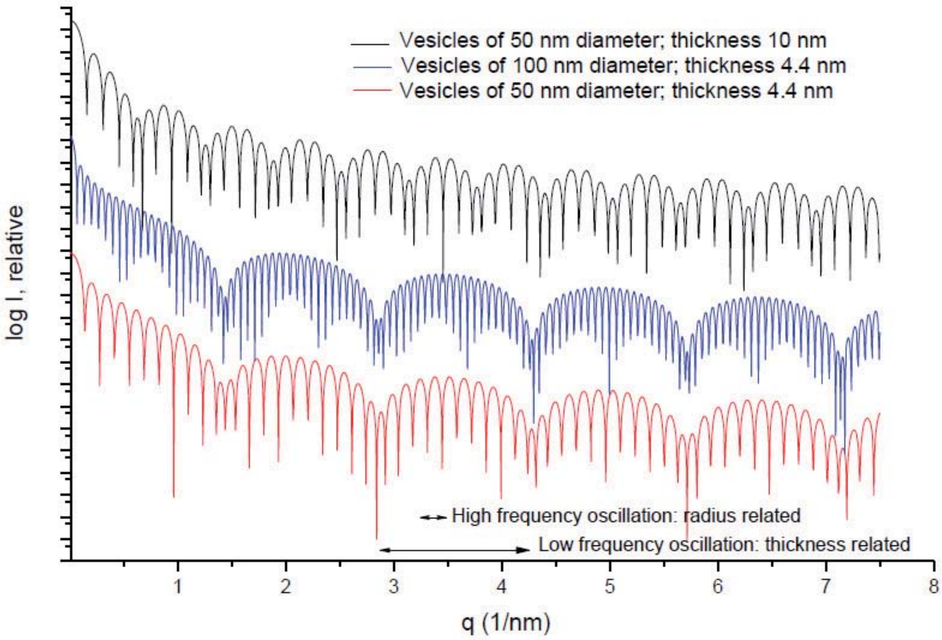

Figure A.7.: Scattering intensities of monodisperse vesicular bodies of different outer radius with different thickness.

Quantitative structural information can be derived from the analysis of the curve:

1. The period of the low frequency oscillations do not change with the shell radius but with the thickness of the bilayer. This period satisfies $d = 2\pi n/q$ and therefore the value of d provides the shell thickness.

2. The number of the high frequency oscillations is related with the object radius, the larger the radius, the more the number of oscillations. It is reported that for a spherical shell structure with radius R, the minima of the high frequency oscillations is related to the radii of the scattering object by $\Delta q = \pi/R$ [174].

The above expressions of scattering functions are applicable only to monodisperse systems. As we are aware, the experimental systems studied in this Thesis are not ideally monodisperse, thus we have simulated the effect in SAXS curves of discrete mixtures of vesicles with different sizes. As shown inFigure A.8, the introduction of polydispersity in the sample in the form of mixture of different populations leads to a rapid damping of the intensity oscillations.

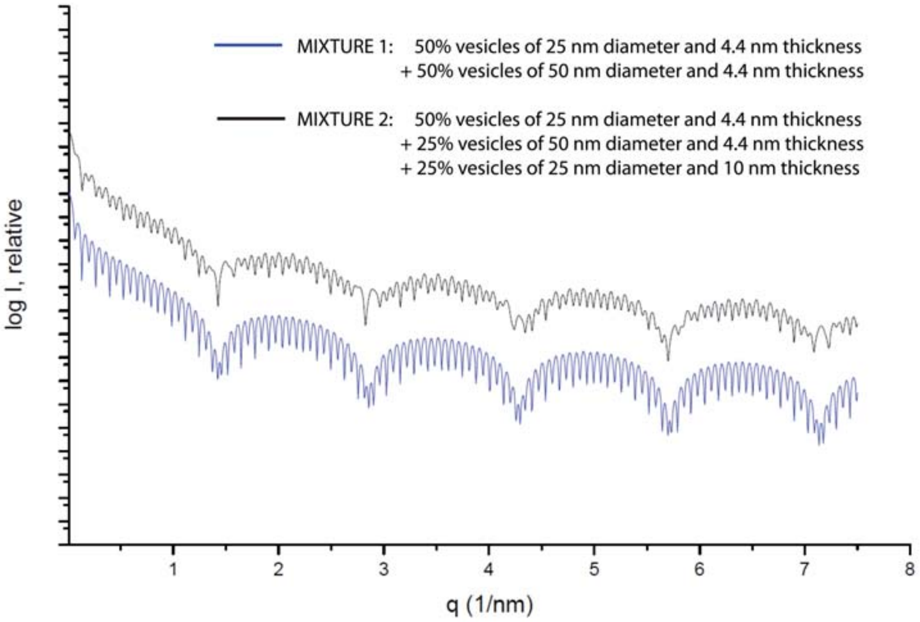

Figure A.8.: Calculated SAXS curves of (blue) an ensemble of vesicles of the same shell thickness and different radius according to the percentage of mixture 1 and, (black) and an ensemble of spheres with distinct radius and distinct shell thickness.

A more exactly route to quantify the vesicle polidispersion in SAXS curves was performed by Professor Jan Skov Pedersen (Aarhus University, Denmark) by fitting the experimental SAXS data to a vesicle model. This model was a vesicle with a cross section shell-core-shell structure with graded/smeared interfaces. This was implemented as the form factor of a three layer shell, in which the inner and outer layer (head groups) have the same thickness. The polydispersity of the radius of the central plane of the vesicle was taken as a Gaussian. Using this model, the quatsome diameter and the polydipersity index was estimated.

A.5. Viscoelastic properties of vesicles

The viscoelastic properties of Chol-CTAB (PBS10Et-DELOS) quatsomes and Chol-DOPC (PBS10Et-DELOS) liposomes were studied by Dr. Witold Tatkiewicz from the *Nanomol* group (ICMAB-CSIC) in his PhD work [188]. Using Quartz Crystal Microbalance with Dissipation (QCM-D) and Surface Plasmon Resonance (SPR) techniques, the thickness of vesicles deposited over gold surfaces, forming vesicular layers, and the viscosity of such vesicles were calculated.

QCM-D measurements were performed in the Laboratory of Biosurfaces at the Centre for Cooperative Research in Biomaterials-CIC biomaGUNE, located in San Sebastian (Spain) under the supervision of Dr. Ralf Richter.

A.5.1. Quartz Crystal Microbalance with Dissipation technique

Quartz Crystal Microbalance with Dissipation (QCM-D) enables measurements of mass of material adhering to an acoustic sensor and have emerged as another technique useful in this field. Mass is directly calculated from changes of its frequency (ΔHz) using the Sauerbrey relation [296]. Dissipation factor (also measured in Hz) can be related with viscoelastic properties of the deposited material [297] and by applying an appropriate model (e.g. Voigt model) physically meaningful properties of the material, such as shear stress and viscosity, can be determined. Schematic cartoon of the QCM-D principle is presented in Figure A.9.

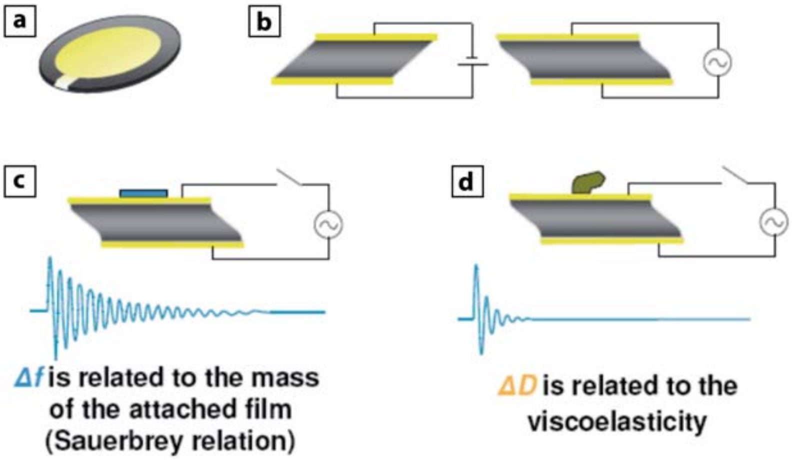

Figure A.9.: QCM-D principle. (a) View of the sensor: circular tile of quartz with deposited gold. (b) Upon electrical stimuli the quartz crystal undergoes a share deformation. (c) Resonance frequency *(Δf)* of crystal oscillation under alternating stimuli depends on the total mass of material absorbed on the sensor. (d) Dissipation *(ΔD)* depends on the viscoelastic properties of the absorbed material. Image adapted from [298].

A.5.2. Surface Plasmon Resonance

Electromagnetic waves that propagate at the metal/dielectric interface in a direction parallel to this surface are called surface plasmon polaritons (surface plasmons). These oscillations are very sensitive to any change on the boundary of the metal and the external medium (e.g. liquid or gaseous medium) such as the adsorption of material to the metal surface, refractive index changes of medium or temperature changes.

SPR quantifies changes in direct proximity of the sensor's surface (up to ~300 nm) using an optic sensor (Figure A.10). For a given laser incidence angle to the conductor-dielectric surface, a resonance between the laser photons and plasmons occurs leading to decrease of reflected laser light intensity. The angle of minimum intensity of reflected laser can quantified and used to study phenomena occurring on the sensor surface, such as vesicle or protein absorption. These phenomena change its local refractive index and it influences the electric field called evanesced wave that is formed close to the sensor surface by surface plasmons. As the evanesced field decays exponentially with distance from the sensor, SPR is extremely sensitive to small and local changes on the properties of the metal-liquid interface. It changes the angle of incident light at which the resonance of plasmons occurs and therefore it can be quantified. By measuring changes of resonant angle we are able to gain insight into local changes of refractive index at close proximity of the sensor surface. Schematic illustration of the used setup is presented in Figure A.10.

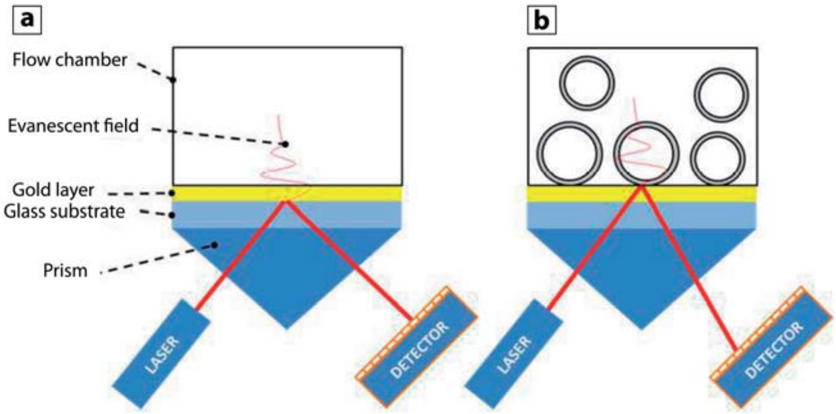

Figure A.10.: Schematic view of SPR setup based on a continuous flow system. (a) The device consists of a monochromatic light source (LASER), an optical detector, a prism of controlled refractive index, a gold coated glass slide and a flow chamber. (b) In the case of interaction of the sensor with an analyte, the variations of the local refraction index, change the incidence angle that is monitored while the solution is pumped over the gold layer.

The number of phenomena able to generate an SPR response is quite numerous, from conformational changes, to modifications of the colorimetric or fluorescent properties of the substrate, nevertheless the adsorption of molecules is the most common of all of them. This technique is therefore used as a tool to study kinetic and affinity of binding events.

Bibliography

[1] J. W. Steed, D. R. Turner, and K. Wallace, *Core concepts in supramolecular chemistry and nanochemistry.* John Wiley & Sons, Ltd, 2007.

[2] K. Rajagopal and J. P. Schneider, "Self-assembling peptides and proteins for nanotechnological applications," *Current opinion in structural biology*, vol. 14, no. 4, pp. 480–6, 2004.

[3] G. M. Whitesides and M. Boncheva, "Beyond molecules: self-assembly of mesoscopic and macroscopic components," *Proceedings of the National Academy of Sciences of the United States of America*, vol. 99, no. 8, pp. 4769–74, 2002.

[4] G. M. Whitesides and B. Grzybowski, "Self-assembly at all scales," *Science (New York, N.Y.)*, vol. 295, no. 5564, pp. 2418–21, 2002.

[5] G. R. Desiraju, *Crystal Engineering: The Design of Organic Solids*. New York: Elsevier, 1989.

[6] D. Fennell Evans and H. Wennerström, *The colloidal domain: Where physics, chemistry, biology, and technology meet.* 1999.

[7] M. N. Jones and D. Chapman, *Micelles, monolayers, and biomembranes.* New York: Wiley-Liss, 1995.

[8] E. L. Thomas, "Materials science: Enhanced: The ABCs of self-assembly," *Science*, vol. 286, no. 5443, p. 1307, 1999.

[9] A. Kumar, N. L. Abbott, H. A. Biebuyck, E. Kim, and G. M. Whitesides, "Patterned self-assembled monolayers and meso-scale phenomena," *Accounts of Chemical Research*, vol. 28, no. 5, pp. 219–226, 1995.

[10] V. Grantcharova, E. J. Alm, D. Baker, and A. L. Horwich, "Mechanisms of protein folding," *Current Opinion in Structural Biology*, vol. 11, no. 1, pp. 70–82, 2001.

[11] S. Neidle, *Oxford handbook of nucleic acid structure.* Oxford, U.K: Oxford Univ. Press, 1999.

[12] R. S. Tu and M. Tirrell, "Bottom-up design of biomimetic assemblies," *Adv Drug Deliv Rev*, vol. 56, no. 11, pp. 1537–1563, 2004.

[13] P. Ekwall, L. Mandell, and K. Fontell, "Solubilization in Micelles and Mesophases and the Transition from Normal to Reversed Structures," *Molecular Crystals*, vol. 8, no. 1, pp. 157–213, 1969.

[14] H. Wennerström, "Micelles. Physical chemistry of surfactant association," *Physics Reports*, vol. 52, no. 1, pp. 1–86, 1979.

[15] Y. Chevalier and T. Zemb, "The structure of micelles and microemulsions," *Reports on Progress in Physics*, vol. 53, no. 3, pp. 279–371, 1990.

[16] C. Tanford, *The hydrophobic effect: Formation of micelles and biological membranes*, vol. 18. 1980.

[17] B. W. Ninham and P. L. Nostro, *Molecular forces and self assembly: in colloid, nano sciences and biology*. 2010.

[18] J. N. Israelachvili, D. J. Mitchell, and B. W. Ninham, "Theory of self-assembly of hydrocarbon amphiphiles into micelles and bilayers," *Journal of the Chemical Society, Faraday Transactions 2*, vol. 72, pp. 1525–1568, 1976.

[19] E. Elizondo, E. Moreno, I. Cabrera, A. Córdoba, S. Sala, J. Veciana, and N. Ventosa, "Liposomes and other vesicular systems: structural characteristics, methods of preparation, and use in nanomedicine," *Progress in molecular biology and translational science*, vol. 104, pp. 1–52, 2011.

[20] K. Kita-Tokarczyk, J. Grumelard, T. Haefele, and W. Meier, "Block copolymer vesicles using concepts from polymer chemistry to mimic biomembranes," *Polymer*, vol. 46, no. 11, pp. 3540–3563, 2005.

[21] S. Svenson, "Self-assembly and self-organization: Important processes, but can we predict them?," *Journal of Dispersion Science and Technology*, 2008.

[22] J.-H. Ryu, D.-J. Hong, and M. Lee, "Aqueous self-assembly of aromatic rod building blocks.," *Chemical communications (Cambridge, England)*, no. 9, pp. 1043–54, 2008.

[23] M. S. Brown and J. L. Goldstein, "A receptor-mediated pathway for cholesterol homeostasis," *Science (New York, N.Y.)*, vol. 232, no. 4746, pp. 34–47, 1986.

[24] L. Hosta-Rigau, Y. Zhang, B. M. Teo, A. Postma, and B. Städler, "Cholesterol–a biological compound as a building block in bionanotechnology," *Nanoscale*, vol. 5, no. 1, pp. 89–109, 2013.

[25] T.-H. Chou, C.-W. Chen, C.-H. Liang, L.-H. Yeh, and S. Qian, “Simple synthesis, self-assembly, and cytotoxicity of novel dimeric cholesterol derivatives,” *Colloids and surfaces. B, Biointerfaces*, vol. 116, pp. 153–9, 2014.

[26] S. R. Naik, S. K. Desai, P. D. Shah, and S. M. Wala, “Liposomes as potential carrier system for targeted delivery of polyene antibiotics,” *Recent patents on inflammation & allergy drug discovery*, vol. 7, no. 3, pp. 202–14, 2013.

[27] D. S. Chung, G. B. Benedek, F. M. Konikoff, and J. M. Donovan, “Elastic free energy of anisotropic helical ribbons as metastable intermediates in the crystallization of cholesterol,” *Proceedings of the National Academy of Sciences of the United States of America*, vol. 90, no. 23, pp. 11341–11345, 1993.

[28] F. M. Konikoff, D. S. Chung, J. M. Donovan, D. M. Small, and M. C. Carey, “Filamentous, helical, and tubular microstructures during cholesterol crystallization from bile. Evidence that cholesterol does not nucleate classic monohydrate plates,” *The Journal of Clinical Investigation*, vol. 90, no. 3, pp. 1155–1160, 1992.

[29] F. M. Konikoff, D. E. Cohen, and M. C. Carey, “Filamentous Crystallization of Cholesterol and Its Dependence on Lecithin Species in Bile,” *Molecular Crystals and Liquid Crystals Science and Technology. Section A. Molecular Crystals and Liquid Crystals*, vol. 248, no. 1, pp. 291–296, 1994.

[30] B. Smith, Y. V. Zastavker, and G. B. Benedek, “Tension-induced straightening transition of self-assembled helical ribbons,” *Physical review letters*, vol. 87, no. 27 Pt 1, p. 278101, 2001.

[31] W. D. Nes, “Biosynthesis of Cholesterol and Other Sterols,” 2011.

[32] Y. V. Zastavker, N. Asherie, A. Lomakin, J. Pande, J. M. Donovan, J. M. Schnur, and G. B. Benedek, “Self-assembly of helical ribbons,” *Proceedings of the National Academy of Sciences of the United States of America*, vol. 96, no. 14, pp. 7883–7887, 1999.

[33] H.-A. Klok, J. J. Hwang, S. N. Iyer, and S. I. Stupp, “Cholesteryl-(L-Lactic Acid)n Building Blocks for Self-Assembling Biomaterials,” *Macromolecules*, vol. 35, no. 3, pp. 746–759, 2002.

[34] K. Sugiyama, R. Hanamura, and M. Sugiyama, "Assembly of poly[N-(2-hydroxypropyl)methacrylamide] having cholesteryl moiety as terminal groups," *Journal of Polymer Science Part A: Polymer Chemistry*, vol. 38, no. 18, pp. 3369–3377, 2000.

[35] Y. Zhou, V. A. Briand, N. Sharma, S.-k. Ahn, and R. M. Kasi, "Polymers Comprising Cholesterol: Synthesis, Self-Assembly, and Applications," *Materials*, vol. 2, no. 2, pp. 636–660, 2009.

[36] A. Ajayaghosh, C. Vijayakumar, R. Varghese, and S. J. George, "Cholesterol-Aided Supramolecular Control over Chromophore Packing: Twisted and Coiled Helices with Distinct Optical, Chiroptical, and Morphological Features," *Angewandte Chemie International Edition*, vol. 45, no. 3, pp. 456–460, 2006.

[37] S. L. Veatch and S. L. Keller, "Separation of liquid phases in giant vesicles of ternary mixtures of phospholipids and cholesterol," *Biophysical journal*, vol. 85, no. 5, pp. 3074–83, 2003.

[38] S. Kulin, R. Kishore, K. Helmerson, and L. Locascio, "Optical manipulation and fusion of liposomes as microreactors," *Langmuir*, vol. 19, no. 20, pp. 8206–8210, 2003.

[39] P. Y. Bolinger, D. Stamou, and H. Vogel, "Integrated nanoreactor systems: Triggering the release and mixing of compounds inside single vesicles," *Journal of the American Chemical Society*, vol. 126, no. 28, pp. 8594–8595, 2004.

[40] G. Gregoriadis, "Carrier potential of liposomes in biology and medicine 0.1," *New England Journal of Medicine*, vol. 295, no. 13, pp. 704–710, 1976.

[41] G. Gregoriadis, "Engineering liposomes for drug delivery: progress and problems," *Trends in biotechnology*, vol. 13, no. 12, pp. 527–37, 1995.

[42] T. Lian and R. J. Ho, "Trends and developments in liposome drug delivery systems," *Journal of pharmaceutical sciences*, vol. 90, no. 6, pp. 667–80, 2001.

[43] Y. Malam, M. Loizidou, and A. M. Seifalian, "Liposomes and nanoparticles: nanosized vehicles for drug delivery in cancer," *Trends Pharmacol Sci*, vol. 30, no. 11, pp. 592–599, 2009.

[44] R. R. Sawant and V. P. Torchilin, "Liposomes as 'smart' pharmaceutical nanocarriers," *Soft Matter*, vol. 6, no. 17, pp. 4026–4044, 2010.

[45] G. M. Whitesides and B. Grzybowski, “Self-assembly at all scales,” *Science*, vol. 295, no. 5564, pp. 2418–2421, 2002.

[46] V. Guida, “Thermodynamics and kinetics of vesicles formation processes,” *Advances in Colloid and Interface Science*, vol. 161, no. 1-2, pp. 77–88, 2010.

[47] A. Bangham and R. Horne, “Negative staining of phospholipids and their structural modification by surface-active agents as observed in the electron microscope,” *Journal of Molecular Biology*, vol. 8, no. 5, pp. 660–668, 1964.

[48] A. Bangham, M. Standish, and J. Watkins, “Diffusion of univalent ions across the lamellae of swollen phospholipids,” *Journal of Molecular Biology*, vol. 13, no. 1, pp. 238–IN27, 1965.

[49] V. P. Torchilin, “Recent advances with liposomes as pharmaceutical carriers,” *Nat Rev Drug Discov*, vol. 4, no. 2, pp. 145–160, 2005.

[50] D. Papakostas, F. Rancan, W. Sterry, U. Blume-Peytavi, and A. Vogt, “Nanoparticles in dermatology,” *Archives of dermatological research*, vol. 303, no. 8, pp. 533–50, 2011.

[51] M. Fathi, M. Mozafari, and M. Mohebbi, “Nanoencapsulation of food ingredients using lipid based delivery systems,” *Trends in Food Science & Technology*, vol. 23, no. 1, pp. 13–27, 2012.

[52] H. Barani and M. Montazer, “A Review on Applications of Liposomes in Textile Processing,” *Journal of Liposome Research*, 2008.

[53] Z. K. Cui, A. Bouisse, N. Cottenye, and M. Lafleur, “Formation of pH-Sensitive Cationic Liposomes from a Binary Mixture of Monoalkylated Primary Amine and Cholesterol,” *Langmuir*, vol. 28, no. 38, pp. 13668–13674, 2012.

[54] L. Sercombe, T. Veerati, F. Moheimani, S. Y. Wu, A. K. Sood, and S. Hua, “Advances and Challenges of Liposome Assisted Drug Delivery.,” *Frontiers in pharmacology*, vol. 6, p. 286, Jan. 2015.

[55] J. M. Metselaar and G. Storm, “Liposomes in the treatment of inflammatory disorders,” *Expert Opinion on Drug Delivery*, 2005.

[56] G. A. Koning and G. Storm, “Targeted drug delivery systems for the intracellular delivery of macromolecular drugs,” *Drug Discovery Today*, vol. 8, no. 11, pp. 482–483, 2003.

[57] A. S. Ulrich, “Biophysical aspects of using liposomes as delivery vehicles,” *Bioscience reports*, vol. 22, no. 2, pp. 129–50, 2002.

[58] R. Duncan and R. Gaspar, “Nanomedicine(s) under the microscope,” *Molecular pharmaceutics*, vol. 8, no. 6, pp. 2101–41, 2011.

[59] Y. Malam, M. Loizidou, and A. M. Seifalian, “Liposomes and nanoparticles: nanosized vehicles for drug delivery in cancer.,” *Trends in pharmacological sciences*, vol. 30, pp. 592–9, Nov. 2009.

[60] O. C. Farokhzad and R. Langer, “Impact of nanotechnology on drug delivery.,” *ACS nano*, vol. 3, no. 1, pp. 16–20, 2009.

[61] R. A. Petros and J. M. DeSimone, “Strategies in the design of nanoparticles for therapeutic applications,” *Nature reviews. Drug discovery*, vol. 9, no. 8, pp. 615–27, 2010.

[62] S. Hussain, A. Plückthun, T. M. Allen, and U. Zangemeister-Wittke, “Antitumor activity of an epithelial cell adhesion molecule targeted nanovesicular drug delivery system,” *Molecular cancer therapeutics*, vol. 6, no. 11, pp. 3019–27, 2007.

[63] T. M. Allen and P. R. Cullis, “Drug delivery systems: entering the mainstream,” *Science (New York, N.Y.)*, vol. 303, no. 5665, pp. 1818–22, 2004.

[64] “http://ncl.cancer.gov/.”

[65] M. Dubois and T. Zemb, “Phase behavior and scattering of double-chain surfactants in diluted aqueous solutions,” *Langmuir*, vol. 7, no. 7, pp. 1352–1360, 1991.

[66] F. Caboi and M. Monduzzi, “Didodecyldimethylammonium bromide vesicles and lamellar liquid crystals. A multinuclear NMR and optical microscopy study,” *Langmuir*, vol. 12, no. 15, pp. 3548–3556, 1996.

[67] Z. Drulis-Kawa and A. Dorotkiewicz-Jach, “Liposomes as delivery systems for antibiotics,” *Int J Pharm*, vol. 387, no. 1-2, pp. 187–198, 2010.

[68] C. Kirby, J. Clarke, and G. Gregoriadis, “Effect of the cholesterol content of small unilamellar liposomes on their stability in vivo and in vitro,” *The Biochemical journal*, vol. 186, no. 2, pp. 591–8, 1980.

[69] G. Gregoriadis and C. Davis, “Stability of liposomes in vivo and in vitro is promoted by their cholesterol content and the presence of blood cells,” *Biochemical and biophysical research communications*, vol. 89, no. 4, pp. 1287–93, 1979.

[70] M. Antonietti and S. Förster, “Vesicles and liposomes: a self-assembly principle beyond lipids,” *Advanced Materials*, vol. 15, no. 16, pp. 1323–1333, 2003.

[71] C. LoPresti, H. Lomas, M. Massignani, T. Smart, and G. Battaglia, “Polymersomes: nature inspired nanometer sized compartments,” *Journal of Materials Chemistry*, vol. 19, no. 22, pp. 3576–3590, 2009.

[72] B. M. Discher, “Polymersomes: Tough Vesicles Made from Diblock Copolymers,” *Science*, vol. 284, no. 5417, pp. 1143–1146, 1999.

[73] L. Zhang and A. Eisenberg, “Multiple morphologies of "crew-cut" aggregates of polystyrene-b-poly(acrylic acid) block copolymers,” *Science (New York, N.Y.)*, vol. 268, no. 5218, pp. 1728–31, 1995.

[74] H. Kukula, H. Schlaad, M. Antonietti, and S. Förster, “The formation of polymer vesicles or "peptosomes" by polybutadiene-block-poly(L-glutamate)s in dilute aqueous solution,” *Journal of the American Chemical Society*, vol. 124, no. 8, pp. 1658–1663, 2002.

[75] A. Shioi and T. A. Hatton, “Model for formation and growth of vesicles in mixed anionic-cationic (SOS-CTAB) surfactant systems,” *Langmuir*, vol. 18, no. 20, pp. 7341–7348, 2002.

[76] Y. Xia, I. Goldmints, P. W. Johnson, T. A. Hatton, and A. Bose, “Temporal evolution of microstructures in aqueous CTAB/SOS and CTAB/HDBS solutions,” *Langmuir*, vol. 18, no. 10, pp. 3822–3828, 2002.

[77] H.-T. Jung, S. Y. Lee, E. W. Kaler, B. Coldren, and J. A. Zasadzinski, “Gaussian curvature and the equilibrium among bilayer cylinders, spheres, and discs,” *Proceedings of the National Academy of Sciences of the United States of America*, vol. 99, no. 24, pp. 15318–15322, 2002.

[78] E. F. Marques, “Size and stability of catanionic vesicles: effects of formation path, sonication, and aging,” *Langmuir*, vol. 16, no. 11, pp. 4798–4807, 2000.

[79] E. W. Kaler, K. L. Herrington, A. K. Murthy, and J. A. N. Zasadzinski, “Phase behavior and structures of mixtures of anionic and cationic surfactants,” *The Journal of Physical Chemistry*, vol. 96, no. 16, pp. 6698–6707, 1992.

[80] H. Fukuda, K. Kawata, H. Okuda, and S. L. Regen, “Bilayer-forming ion pair amphiphiles from single-chain surfactants,” *Journal of the American Chemical Society*, vol. 112, no. 4, pp. 1635–1637, 1990.

[81] T. Bramer, N. Dew, and K. Edsman, “Pharmaceutical applications for catanionic mixtures,” *The Journal of pharmacy and pharmacology*, vol. 59, no. 10, pp. 1319–34, 2007.

[82] Y. C. Liu, A. L. Le Ny, J. Schmidt, Y. Talmon, B. F. Chmelka, and C. T. Lee Jr., “Photo-assisted gene delivery using light-responsive catanionic vesicles,” *Langmuir*, vol. 25, no. 10, pp. 5713–5724, 2009.

[83] E. J. Danoff, X. Wang, S.-H. Tung, N. A. Sinkov, A. M. Kemme, S. R. Raghavan, and D. S. English, “Surfactant vesicles for high-efficiency capture and separation of charged organic solutes,” *Langmuir : the ACS journal of surfaces and colloids*, vol. 23, no. 17, pp. 8965–71, 2007.

[84] I. P. Kaur, A. Garg, A. K. Singla, and D. Aggarwal, “Vesicular systems in ocular drug delivery: an overview,” *Int J Pharm*, vol. 269, no. 1, pp. 1–14, 2004.

[85] I. F. Uchegbu and A. T. Florence, “Non-ionic surfactant vesicles (niosomes): physical and pharmaceutical chemistry,” *Advances in Colloid and Interface Science*, vol. 58, no. 1, pp. 1–55, 1995.

[86] I. F. Uchegbu and S. P. Vyas, “Non-ionic surfactant based vesicles (niosomes) in drug delivery,” *International Journal of Pharmaceutics*, vol. 172, no. 1-2, pp. 33–70, 1998.

[87] A. Manosroi, P. Wongtrakul, J. Manosroi, H. Sakai, F. Sugawara, M. Yuasa, and M. Abe, “Characterization of vesicles prepared with various non-ionic surfactants mixed with cholesterol,” *Colloids and Surfaces B: Biointerfaces*, vol. 30, no. 1-2, pp. 129–138, 2003.

[88] “The Rules Governing Medicinal Products in the European Union, Vol 4: EU Guidelines to Good Manufacturing Practice, Medicinal Products for Human and Veterinary Use,” 2005.

[89] "ICH Harmonished tripartite guideline. Impurities: Guideline for Residual Solvents Q3C(R4), International conference on harmonisation of technical requirements for registration of pharmaceuticals for human use," 2009.

[90] R. C. C. New, *Preparation of liposomes.* New York: Oxford University Press, 1990.

[91] A. Bangham, M. Standish, and G. Weissmann, "The action of steroids and streptolysin S on the permeability of phospholipid structures to cations," *Journal of Molecular Biology*, vol. 13, no. 1, pp. 253–IN28, 1965.

[92] F. Szoka, F. Olson, T. Heath, W. Vail, E. Mayhew, and D. Papahadjopoulos, "Preparation of unilamellar liposomes of intermediate size (0.1-0.2 μm) by a combination of reverse phase evaporation and extrusion through polycarbonate membranes," *Biochimica et Biophysica Acta (BBA) - Biomembranes*, vol. 601, pp. 559–571, 1980.

[93] A. A. Smirnov, "Preparation of liposomes by reverse-phase evaporation and by freezing and thawing," *Bulletin of Experimental Biology and Medicine*, vol. 98, no. 2, pp. 1146–1149, 1984.

[94] A. A. Elzainy, X. Gu, F. E. R. Simons, and K. J. Simons, "Hydroxyzine- and Cetirizine-Loaded Liposomes: Effect of Duration of Thin Film Hydration, Freeze-Thawing, and Changing Buffer pH on Encapsulation and Stability," *Drug Development and Industrial Pharmacy*, 2008.

[95] D. J. Woodbury, E. S. Richardson, A. W. Grigg, R. D. Welling, and B. H. Knudson, "Reducing liposome size with ultrasound: Bimodal size distributions," *Journal of Liposome Research*, vol. 16, no. 1, pp. 57–80, 2006.

[96] M. Hope, M. Bally, G. Webb, and P. Cullis, "Production of large unilamellar vesicles by a rapid extrusion procedure. Characterization of size distribution, trapped volume and ability to maintain a membrane potential," *Biochimica et Biophysica Acta (BBA) - Biomembranes*, vol. 812, no. 1, pp. 55–65, 1985.

[97] N. Berger, A. Sachse, J. Bender, R. Schubert, and M. Brandl, "Filter extrusion of liposomes using different devices: comparison of liposome size, encapsulation efficiency, and process characteristics," *International Journal of Pharmaceutics*, vol. 223, no. 1-2, pp. 55–68, 2001.

[98] R. C. MacDonald, R. I. MacDonald, B. P. Menco, K. Takeshita, N. K. Subbarao, and L.-r. Hu, “Small-volume extrusion apparatus for preparation of large, unilamellar vesicles,” *Biochimica et Biophysica Acta (BBA) - Biomembranes*, vol. 1061, no. 2, pp. 297–303, 1991.

[99] D. Bachmann, M. Brandl, and G. Gregoriadis, “Preparation of liposomes using a Mini-Lab 8.30 H high-pressure homogenizer,” *International Journal of Pharmaceutics*, vol. 91, no. 1, pp. 69–74, 1993.

[100] E. Pupo, A. Padron, E. Santana, J. Sotolongo, D. Quintana, S. Duenas, C. Duarte, M. C. de la Rosa, and E. Hardy, “Preparation of plasmid DNA-containing liposomes using a high-pressure homogenization-extrusion technique,” *J Control Release*, vol. 104, no. 2, pp. 379–396, 2005.

[101] J. T. Buboltz and G. W. Feigenson, “A novel strategy for the preparation of liposomes: rapid solvent exchange,” *Biochimica et Biophysica Acta (BBA) - Biomembranes*, vol. 1417, no. 2, pp. 232–245, 1999.

[102] E. Elizondo, J. Larsen, N. S. Hatzakis, I. Cabrera, T. Bjø rnholm, J. Veciana, D. Stamou, and N. Ventosa, “Influence of the preparation route on the supramolecular organization of lipids in a vesicular system.,” *Journal of the American Chemical Society*, vol. 134, no. 4, pp. 1918–21, 2012.

[103] L. A. Meure, N. R. Foster, and F. Dehghani, “Conventional and dense gas techniques for the production of liposomes: a review,” *AAPS PharmSciTech*, vol. 9, no. 3, pp. 798–809, 2008.

[104] M. A. W. Eaton, “Improving the translation in Europe of nanomedicines (a.k.a. drug delivery) from academia to industry,” *Journal of Controlled Release*, vol. 164, no. 3, pp. 370–371, 2012.

[105] J. Jennings, M. Beija, A. P. Richez, S. D. Cooper, P. E. Mignot, K. J. Thurecht, K. S. Jack, and S. M. Howdle, “One-pot synthesis of block copolymers in supercritical carbon dioxide: a simple versatile route to nanostructured microparticles,” *Journal of the American Chemical Society*, vol. 134, no. 10, pp. 4772–81, 2012.

[106] I. Pasquali and R. Bettini, “Are pharmaceutics really going supercritical?,” *Int J Pharm*, vol. 364, no. 2, pp. 176–187, 2008.

[107] E. Reverchon and R. Adami, “Nanomaterials and supercritical fluids,” *The Journal of Supercritical Fluids*, vol. 37, no. 1, pp. 1–22, 2006.

[108] C. A. Eckert, B. L. Knutson, and P. G. Debenedetti, “Supercritical fluids as solvents for chemical and materials processing,” *Nature*, vol. 383, no. 6598, pp. 313–318, 1996.

[109] E. Elizondo, J. Veciana, and N. Ventosa, “Nanostructuring molecular materials as particles and vesicles for drug delivery, using compressed and supercritical fluids,” *Nanomedicine*, vol. 7, no. 9, pp. 1391–1408, 2012.

[110] F. Cansell and C. Aymonier, “Design of functional nanostructured materials using supercritical fluids,” *The Journal of Supercritical Fluids*, vol. 47, no. 3, pp. 508–516, 2009.

[111] E. Reverchon, R. Adami, S. Cardea, and G. D. Porta, “Supercritical fluids processing of polymers for pharmaceutical and medical applications,” *The Journal of Supercritical Fluids*, vol. 47, no. 3, pp. 484–492, 2009.

[112] M. Perrut and J.-Y. Clavier, “Supercritical Fluid Formulation: Process Choice and Scale-up,” *Industrial & Engineering Chemistry Research*, vol. 42, no. 25, pp. 6375–6383, 2003.

[113] K. Otake, T. Shimomura, T. Goto, T. Imura, T. Furuya, S. Yoda, Y. Takebayashi, H. Sakai, and M. Abe, “Preparation of liposomes using an improved supercritical reverse phase evaporation method,” *Langmuir : the ACS journal of surfaces and colloids*, vol. 22, no. 6, pp. 2543–50, 2006.

[114] L. A. Meure, R. Knott, N. R. Foster, and F. Dehghani, “The depressurization of an expanded solution into aqueous media for the bulk production of liposomes,” *Langmuir : the ACS journal of surfaces and colloids*, vol. 25, no. 1, pp. 326–37, 2009.

[115] L. Lesoin, C. Crampon, O. Boutin, and E. Badens, “Development of a continuous dense gas process for the production of liposomes,” *Journal of Supercritical Fluids*, vol. 60, pp. 51–62, 2011.

[116] C. C. Beh, R. Mammucari, and N. R. Foster, “Lipids-based drug carrier systems by dense gas technology: A review,” *Chemical Engineering Journal*, vol. 188, pp. 1–14, Apr. 2012.

[117] S. Sala, A. Córdoba, E. Moreno-Calvo, E. Elizondo, M. Muntó, P. E. Rojas, M. A. Larrayoz, N. Ventosa, and J. Veciana, “Crystallization of Microparticulate Pure Polymorphs of Active Pharmaceutical Ingredients Using CO2-Expanded Solvents,” *Crystal Growth & Design*, vol. 12, no. 4, pp. 1717–1726, 2012.

[118] S. Sala, E. Elizondo, E. Moreno, T. Calvet, M. A. Cuevas-Diarte, N. Ventosa, and J. Veciana, “Kinetically Driven Crystallization of a Pure Polymorphic Phase of Stearic Acid from CO2 -Expanded Solutions,” *Crystal Growth & Design*, vol. 10, no. 3, pp. 1226–1232, 2010.

[119] N. Ventosa, S. Sala, J. Veciana, J. Torres, and J. Llibre, “Depressurization of an Expanded Liquid Organic Solution (DELOS): A New Procedure for Obtaining Submicron- or Micron-Sized Crystalline Particles,” *Crystal Growth & Design*, vol. 1, no. 4, pp. 299–303, 2001.

[120] N. Ventosa, S. Sala, and J. Veciana, “DELOS process: a crystallization technique using compressed fluids,” *The Journal of Supercritical Fluids*, vol. 26, no. 1, pp. 33–45, 2003.

[121] M. Cano-Sarabia, N. Ventosa, S. Sala, C. Patino, R. Arranz, and J. Veciana, “Preparation of uniform rich cholesterol unilamellar nanovesicles using CO2-expanded solvents,” *Langmuir*, vol. 24, no. 6, pp. 2433–2437, 2008.

[122] I. Cabrera, E. Elizondo, O. Esteban, J. L. Corchero, M. Melgarejo, D. Pulido, A. Córdoba, E. Moreno, U. Unzueta, E. Vazquez, I. Abasolo, S. Schwartz, A. Villaverde, F. Albericio, M. Royo, M. F. García-Parajo, N. Ventosa, and J. Veciana, “Multifunctional Nanovesicle-Bioactive Conjugates Prepared by a One-Step Scalable Method Using CO2-Expanded Solvents,” *Nano Lett*, vol. 13, no. 8, pp. 3766–3774, 2013.

[123] I. Cabrera et al., “DOI:10.1002/adhm.201500746,” *Adv. Healthcare Mater*, 2016.

[124] H. Santana, L. Ventosa, E. Martínez, J. Berlanga, I. Cabrera, and J. Veciana, “Vesicles comprising epidermal growth factor and compositions thereof. WO2014/019555 (extension to all PCT countries under reference PCT REF: PCT/CU2013/000004 and also to Argentina, Venezuela, Saudi Arabia, Kuwait, Jordania, Lebanon),” 2012.

[125] A. M. Cano-Sarabia, *Preparación de materiales moleculares nanoparticulados y dispersos -vesículas y microemulsiones- empleando fluidos comprimidos.* PhD thesis, 2009.

[126] G. F. Catá, H. C. Rojas, A. P. Gramatges, C. M. Zicovich-Wilson, L. J. Álvarez, and C. Searle, “Initial structure of cetyltrimethylammonium bromide micelles in aqueous solution from molecular dynamics simulations,” *Soft Matter*, vol. 7, no. 18, pp. 8508–8515, 2011.

[127] P. S. Goyal, B. A. Dasannacharya, V. K. Kelkar, C. Manohar, K. Srinivasa Rao, and B. S. Valaulikar, “Shapes and sizes of micelles in CTAB solutions,” *Physica B: Condensed Matter*, vol. 174, pp. 196–199, 1991.

[128] M. Gradzielski, “Vesicles and vesicle gels - structure and dynamics of formation,” *Journal of Physics: Condensed Matter*, vol. 15, no. 19, pp. R655–R697, 2003.

[129] D. Danino, “Cryo-TEM of soft molecular assemblies,” *Current Opinion in Colloid & Interface Science*, vol. 17, no. 6, pp. 316–329, 2012.

[130] T. M. Weiss, T. Narayanan, C. Wolf, M. Gradzielski, P. Panine, S. Finet, and W. I. Helsby, “Dynamics of the self-assembly of unilamellar vesicles,” *Physical Review Letters*, vol. 94, no. 3, pp. 038303 (1) – (4), 2005.

[131] D. R. Fattal, D. Andelman, and A. Ben-Shaul, “The vesicle-micelle transition in mixed lipid-surfactant systems: A molecular model,” *Langmuir*, vol. 11, no. 4, pp. 1154–1161, 1995.

[132] P. Fromherz, “Lipid-vesicle structure: Size control by edge-active agents,” *Chemical Physics Letters*, vol. 94, no. 3, pp. 259–266, 1983.

[133] J. Gummel, M. Sztucki, T. Narayanan, and M. Gradzielski, “Concentration dependent pathways in spontaneous self-assembly of unilamellar vesicles,” *Soft Matter*, vol. 7, no. 12, pp. 5731–5738, 2011.

[134] J. Leng, S. U. Egelhaaf, and M. E. Cates, “Kinetics of the micelle-to-vesicle transition: Aqueous lecithin-bile salt mixtures,” *Biophysical Journal*, vol. 85, no. 3, pp. 1624–1646, 2003.

[135] A. J. O’Connor, T. A. Hatton, and A. Bose, “Dynamics of micelle-vesicle transitions in aqueous anionic/cationic surfactant mixtures,” *Langmuir*, vol. 13, no. 26, pp. 6931–6940, 1997.

[136] R. Podgornik, “Statistical thermodynamics of surfaces, interfaces, and membranes,” *Journal of Statistical Physics*, vol. 78, no. 3, pp. 1175–1177, 1995.

[137] M. Ollivon, S. Lesieur, C. Grabielle-Madelmont, and M. Paternostre, “Vesicle reconstitution from lipid-detergent mixed micelles,” *Biochimica Et Biophysica Acta-Biomembranes*, vol. 1508, no. 1-2, pp. 34–50, 2000.

[138] E. Feitosa, N. M. Bonassi, and W. Loh, “Vesicle-micelle transition in mixtures of dioctadecyldimethylammonium chloride and bromide with nonionic and zwitterionic surfactants,” *Langmuir : the ACS journal of surfaces and colloids*, vol. 22, no. 10, pp. 4512–7, 2006.

[139] K. Kuperkar, L. Abezgauz, K. Prasad, and P. Bahadur, “Formation and growth of micelles in dilute aqueous CTAB solutions in the presence of NaNO3 and NaClO3,” *Journal of Surfactants and Detergents*, vol. 13, no. 3, pp. 293–303, 2010.

[140] P. Schurtenberger, N. Mazer, and W. Kanzig, “Micelle to vesicle transition in aqueous solutions of bile salt and lecithin,” *Journal of Phyical Chemistry*, vol. 89, no. 6, pp. 1042–1049, 1985.

[141] J. C. Phillips, R. Braun, W. Wang, J. Gumbart, E. Tajkhorshid, E. Villa, C. Chipot, R. D. Skeel, L. Kalé, and K. Schulten, “Scalable molecular dynamics with NAMD,” *Journal of Computational Chemistry*, vol. 26, no. 16, pp. 1781–1802, 2005.

[142] W. Humphrey, A. Dalke, and K. Schulten, “VMD: Visual molecular dynamics,” *Journal of Molecular Graphics & Modelling*, vol. 14, no. 1, pp. 33–38, 1996.

[143] J.-h. Lee, Y. J. Choi, and Y.-b. Lim, “Self-assembled filamentous nanostructures for drug/gene delivery applications,” *Expert opinion on drug delivery*, vol. 7, no. 3, pp. 341–51, 2010.

[144] S. E. Feller, R. M. Venable, and R. W. Pastor, “Computer simulation of a DPPC phospholipid bilayer: Structural changes as a function of molecular surface area,” *Langmuir*, vol. 13, no. 24, pp. 6555–6561, 1997.

[145] D. P. Tieleman, S. J. Marrink, and H. J. Berendsen, “A computer perspective of membranes: molecular dynamics studies of lipid bilayer systems,” *Biochimica et biophysica acta*, vol. 1331, no. 3, pp. 235–70, 1997.

[146] A. Martín-Molina, C. Rodríguez-Beas, and J. Faraudo, “Effect of calcium and magnesium on phosphatidylserine membranes: Experiments and all-atomic simulations,” *Biophysical Journal*, vol. 102, no. 9, pp. 2095–2103, 2012.

[147] A. Martín-Molina, C. Rodríguez-Beas, and J. Faraudo, “Charge reversal in anionic liposomes: Experimental demonstration and molecular origin,” *Physical Review Letters*, vol. 104, no. 16, pp. 168103(1)–(4), 2010.

[148] W. F. D. Bennett, J. L. MacCallum, M. J. Hinner, S. J. Marrink, and D. P. Tieleman, "Molecular view of cholesterol flip-flop and chemical potential in different membrane environments.," *Journal of the American Chemical Society*, vol. 131, no. 35, pp. 12714–20, 2009.

[149] S. J. Marrink, A. H. de Vries, T. A. Harroun, J. Katsaras, and S. R. Wassall, "Cholesterol shows preference for the interior of polyunsaturated lipid membranes.," *Journal of the American Chemical Society*, vol. 130, no. 1, pp. 10–1, 2008.

[150] P. Tarazona, E. Chacón, and F. Bresme, "Thermal fluctuations and bending rigidity of bilayer membranes.," *The Journal of chemical physics*, vol. 139, no. 9, p. 094902, 2013.

[151] M. C. A. Stuart and E. J. Boekema, "Two distinct mechanisms of vesicle-to-micelle and micelle-to-vesicle transition are mediated by the packing parameter of phospholipid-detergent systems," *Biochimica et Biophysica Acta (BBA) - Biomembranes*, vol. 1768, no. 11, pp. 2681–2689, 2007.

[152] H. J. Watzke, *Reaction-controlled self-assembly of amphiphilic membranes*, vol. 93. Publ by Springer-Verlag GmbH & Company KG, 1993.

[153] R. Laughlin, "Equilibrium vesicles: fact or fiction?," *Colloids and Surfaces A: Physicochemical and Engineering Aspects*, vol. 128, no. 1-3, pp. 27–38, 1997.

[154] W. Helfrich, "Elastic properties of lipid bilayers: theory and possible experiments," *Zeitschrift für Naturforschung. Teil C: Biochemie, Biophysik, Biologie, Virologie*, vol. 28, no. 11, pp. 693–703, 1972.

[155] S. A. Safran, P. Pincus, and D. Andelman, "Theory of spontaneous vesicle formation in surfactant mixtures," *Science (New York, N.Y.)*, vol. 248, no. 4953, pp. 354–6, 1990.

[156] S. A. Safran, P. A. Pincus, D. Andelman, and F. C. MacKintosh, "Stability and phase behavior of mixed surfactant vesicles," *Physical Review A*, vol. 43, no. 2, pp. 1071–1078, 1991.

[157] B. D. Simons and M. E. Cates, "Vesicles and onion phases in dilute surfactant solutions," *Journal de Physique II*, vol. 2, no. 7, pp. 1439–1451, 1992.

[158] P. Hervé, D. Roux, A.-M. Bellocq, F. Nallet, and T. Gulik-Krzywicki, "Dilute and concentrated phases of vesicles at thermal equilibrium," *Journal de Physique II*, vol. 3, no. 8, pp. 1255–1270, 1993.

[159] H. T. Jung, B. Coldren, J. A. Zasadzinski, D. J. Iampietro, and E. W. Kaler, "The origins of stability of spontaneous vesicles," *Proceedings of the National Academy of Sciences*, vol. 98, no. 4, pp. 1353–1357, 2001.

[160] M. M. A. E. Claessens, B. F. van Oort, F. A. M. Leermakers, F. A. Hoekstra, and M. A. Cohen Stuart, "Bending rigidity of mixed phospholipid bilayers and the equilibrium radius of corresponding vesicles," *Physical Review E*, vol. 76, p. 011903, July 2007.

[161] N. D. Denkov, H. Yoshimura, T. Kouyama, J. Walz, and K. Nagayama, "Electron Cryomicroscopy of Bacteriorhodopsin Vesicles: Mechanism of Vesicle Formation," *Biophysical Journal*, vol. 74, no. 3, pp. 1409–1420, 1998.

[162] R. van Zanten and J. A. Zasadzinski, "Using cryo-electron microscopy to determine thermodynamic and elastic properties of membranes," *Current Opinion in Colloid & Interface Science*, vol. 10, pp. 261–268, Dec. 2005.

[163] M. Bergström, "Thermodynamics of Vesicle Formation from a Mixture of Anionic and Cationic Surfactants," *Langmuir*, vol. 12, no. 10, pp. 2454–2463, 1996.

[164] C. Caillet, M. Hebrant, and C. Tondre, "Sodium octyl sulfate/cetyltrimethylammonium bromide catanionic vesicles: Aggregate composition and probe encapsulation," *Langmuir*, vol. 16, no. 23, pp. 9099–9102, 2000.

[165] H. Hoffmann, C. Thunig, P. Schmiedel, and U. Munkert, "Surfactant Systems with Charged Multilamellar Vesicles and Their Rheological Properties," *Langmuir*, vol. 10, pp. 3972–3981, Nov. 1994.

[166] S. Segota and D. Tezak, "Spontaneous formation of vesicles," *Advances in colloid and interface science*, vol. 121, no. 1-3, pp. 51–75, 2006.

[167] B. A. Coldren, H. Warriner, R. van Zanten, J. A. Zasadzinski, and E. B. Sirota, "Flexible bilayers with spontaneous curvature lead to lamellar gels and spontaneous vesicles," *Proceedings of the National Academy of Sciences of the United States of America*, vol. 103, no. 8, pp. 2524–9, 2006.

[168] S. B. Lioi, X. Wang, M. R. Islam, E. J. Danoff, and D. S. English, "Catanionic surfactant vesicles for electrostatic molecular sequestration and separation," *Physical chemistry chemical physics : PCCP*, vol. 11, no. 41, pp. 9315–25, 2009.

[169] E. Kaler, A. Murthy, B. Rodriguez, and J. Zasadzinski, “Spontaneous vesicle formation in aqueous mixtures of single-tailed surfactants,” *Science*, vol. 245, no. 4924, pp. 1371–1374, 1989.

[170] M. Gradzielski, “Kinetics of morphological changes in surfactant systems,” *Current Opinion in Colloid & Interface Science*, vol. 8, pp. 337–345, Nov. 2003.

[171] K. Morigaki, P. Walde, M. Misran, and B. H. Robinson, “Thermodynamic and kinetic stability. Properties of micelles and vesicles formed by the decanoic acid/decanoate system,” *Colloids and Surfaces A: Physicochemical and Engineering Aspects*, vol. 213, no. 1, pp. 37–44, 2003.

[172] M. Rosoff, *Vesicles.* New York: Marcel Dekker Inc, 1996.

[173] B. Heurtault, “Physico-chemical stability of colloidal lipid particles,” *Biomaterials*, vol. 24, pp. 4283–4300, Oct. 2003.

[174] V. O. Glatter and O. Kratky., *Small angle x-ray scattering.* London: Academic Press Inc. Ltd., 1982.

[175] D. I. Svergun and M. H. J. Koch, “Small-angle scattering studies of biological macromolecules in solution,” *Reports on Progress in Physics*, vol. 66, no. 10, pp. 1735–1782, 2003.

[176] G. Pabst, R. Koschuch, B. Pozo-Navas, M. Rappolt, K. Lohner, and P. Laggner, “Structural analysis of weakly ordered membrane stacks,” 2003.

[177] L. Ferrer-Tasies, E. Moreno-Calvo, M. Cano-Sarabia, M. Aguilella-Arzo, A. Angelova, S. Lesieur, S. Ricart, J. Faraudo, N. Ventosa, and J. Veciana, “Quatsomes: vesicles formed by self-assembly of sterols and quaternary ammonium surfactants,” *Langmuir*, vol. 29, no. 22, pp. 6519–6528, 2013.

[178] F. Olson, C. Hunt, F. Szoka, W. Vail, and D. Papahadjopoulos, “Preparation of liposomes of defined size distribution by extrusion through polycarbonate membranes,” *Biochimica et Biophysica Acta (BBA) - Biomembranes*, vol. 557, no. 1, pp. 9–23, 1979.

[179] Y. Liu, M. Li, R. Bansil, and M. Steinhart, “Kinetics of Phase Transition from Lamellar to Hexagonally Packed Cylinders for a Triblock Copolymer in a Selective Solvent,” *Macromolecules*, vol. 40, no. 26, pp. 9482–9490, 2007.

[180] E. Touitou, N. Dayan, L. Bergelson, B. Godin, and M. Eliaz, “Ethosomes - novel vesicular carriers for enhanced delivery: characterization and skin penetration properties,” *Journal of Controlled Release*, vol. 65, no. 3, pp. 403–418, 2000.

[181] E. Touitou, B. Godin, and C. Weiss, “Enhanced delivery of drugs into and across the skin by ethosomal carriers,” *Drug Development Research*, vol. 50, no. 3-4, pp. 406–415, 2000.

[182] I. Cabrera Puig, *Nanovesicle-bioactive conjugates to be used as nanomedicines, prepared by a one-step scalable method using CO2-expanded solvents.* PhD thesis, 2013.

[183] M. R. Wenk, “The emerging field of lipidomics,” *Nature reviews. Drug discovery*, vol. 4, no. 7, pp. 594–610, 2005.

[184] S. Ganta, H. Devalapally, A. Shahiwala, and M. Amiji, “A review of stimuli-responsive nanocarriers for drug and gene delivery,” *J Control Release*, vol. 126, no. 3, pp. 187–204, 2008.

[185] P. Janmey and P. Kinnunen, “Biophysical properties of lipids and dynamic membranes,” *Trends in Cell Biology*, vol. 16, no. 10, pp. 538–546, 2006.

[186] M. Radmacher, M. Fritz, C. M. Kacher, J. P. Cleveland, and P. K. Hansma, “Measuring the viscoelastic properties of human platelets with the atomic force microscope.,” *Biophysical journal*, vol. 70, no. 1, pp. 556–67, 1996.

[187] E. Elizondo Sáez de Vicuña, *New molecule based nanostructured drug carriers prepared using compressed fluids.* PhD thesis, 2010.

[188] Witold Ireneusz Tatkiewicz, *Two-dimensional engineering of molecular nanoparticles for biological applications.* PhD thesis, 2014.

[189] E. Tellechea, D. Johannsmann, N. F. Steinmetz, R. P. Richter, and I. Reviakine, “Model-independent analysis of QCM data on colloidal particle adsorption.,” *Langmuir : the ACS journal of surfaces and colloids*, vol. 25, no. 9, pp. 5177–84, 2009.

[190] E. Reimhult, C. Larsson, B. Kasemo, and F. Höök, “Simultaneous surface plasmon resonance and quartz crystal microbalance with dissipation monitoring measurements of biomolecular adsorption events involving structural transformations and variations in coupled water.,” *Analytical chemistry*, vol. 76, no. 24, pp. 7211–20, 2004.

[191] X. C. Tang and M. J. Pikal, “Design of Freeze-Drying Processes for Pharmaceuticals: Practical Advice,” *Pharmaceutical Research*, vol. 21, no. 2, pp. 191–200, 2004.

[192] H. Talsma, M. J. van Steenbergen, P. J. Salemink, and D. J. Crommelin, “The cryopreservation of liposomes. 1. A differential scanning calorimetry study of the thermal behavior of a liposome dispersion containing mannitol during freezing/thawing.,” *Pharmaceutical research*, vol. 8, no. 8, pp. 1021–6, 1991.

[193] K. Tanaka, T. Takeda, K. Fuji, and K. Miyajima, “Cryoprotective mechanism of saccharides on freeze-drying of liposome,” *CHEMICAL & PHARMACEUTICAL BULLETIN*, vol. 40, no. 1, pp. 1–5, 1992.

[194] J. Bauer, S. Spanton, R. Henry, J. Quick, W. Dziki, W. Porter, and J. Morris, “Ritonavir: an extraordinary example of conformational polymorphism,” *Pharmaceutical Research*, vol. 18, no. 6, pp. 859–866.

[195] S. L. Morissette, S. Soukasene, D. Levinson, M. J. Cima, and O. Almarsson, “Elucidation of crystal form diversity of the HIV protease inhibitor ritonavir by high-throughput crystallization.,” *Proceedings of the National Academy of Sciences of the United States of America*, vol. 100, no. 5, pp. 2180–4, 2003.

[196] E. Elizondo, J. Larsen, N. S. Hatzakis, I. Cabrera, T. Bjornhorn, J. Veciana, D. Stamou, and N. Ventosa, “Influence of the Preparation Route on the Supramolecular Organization of Lipids in a Vesicular System,” *Journal of the American Chemical Society*, vol. 134, no. 4, pp. 1918–1921, 2012.

[197] M. Valcárcel and A. I. López-Lorente, *Gold Nanoparticles in Analytical Chemistry*. Elsevier Science, 2014.

[198] “http://www.accessdata.fda.gov/scripts/cder/iig/index.cfm.”

[199] E. F. Marques, O. Regev, A. Khan, M. da Graça Miguel, and B. Lindman, “Vesicle formation and general phase behavior in the catanionic mixture SDS-DDAB-Water. The anionic-rich side,” *The Journal of Physical Chemistry B*, vol. 102, no. 35, pp. 6746–6758, 1998.

[200] T. Asakawa, H. Kitano, A. Ohta, and S. Miyagishi, “Convenient estimation for counterion dissociation of cationic micelles using chloride-sensitive fluorescence probe,” *Journal of Colloid and Interface Science*, vol. 242, no. 2, pp. 284–287, 2001.

[201] J. Ouimet and M. Lafleur, “Hydrophobic match between cholesterol and saturated fatty acid is required for the formation of lamellar liquid ordered phases,” *Langmuir : the ACS journal of surfaces and colloids*, vol. 20, no. 18, pp. 7474–81, 2004.

[202] G. F. Santoyo, C. De Albornoz Antonio Osuna, S. J. Morales, F. A. Megía, B. T. Cruz, and G. G. M. González, “Vinyl sulphone functionalised lipid systems. Synthesis and uses,” 2011.

[203] G. Su, H. Zhou, Q. Mu, Y. Zhang, L. Li, P. Jiao, G. Jiang, and B. Yan, “Effective Surface Charge Density Determines the Electrostatic Attraction between Nanoparticles and Cells,” *The Journal of Physical Chemistry C*, vol. 116, no. 8, pp. 4993–4998, 2012.

[204] R. Kanasty, J. R. Dorkin, A. Vegas, and D. Anderson, “Delivery materials for siRNA therapeutics.,” *Nature materials*, vol. 12, no. 11, pp. 967–77, 2013.

[205] R. B. Campbell, D. Fukumura, E. B. Brown, L. M. Mazzola, Y. Izumi, R. K. Jain, V. P. Torchilin, and L. L. Munn, “Cationic Charge Determines the Distribution of Liposomes between the Vascular and Extravascular Compartments of Tumors,” *Cancer Res.*, vol. 62, no. 23, pp. 6831–6836, 2002.

[206] E. Fröhlich, “The role of surface charge in cellular uptake and cytotoxicity of medical nanoparticles.,” *International journal of nanomedicine*, vol. 7, pp. 5577–91, Jan. 2012.

[207] K. Romø ren, B. J. Thu, N. C. Bols, and O. y. Evensen, “Transfection efficiency and cytotoxicity of cationic liposomes in salmonid cell lines of hepatocyte and macrophage origin,” *Biochimica et biophysica acta*, vol. 1663, no. 1-2, pp. 127–34, 2004.

[208] C. Srinivasan and D. J. Burgess, “Optimization and characterization of anionic lipoplexes for gene delivery,” *Journal of controlled release : official journal of the Controlled Release Society*, vol. 136, pp. 62–70, May 2009.

[209] H. Liang, D. Harries, and G. C. L. Wong, “Polymorphism of DNA-anionic liposome complexes reveals hierarchy of ion-mediated interactions.,” *Proceedings of the National Academy of Sciences of the United States of America*, vol. 102, no. 32, pp. 11173–8, 2005.

[210] S. Ghosh, A. Roy, D. Banik, N. Kundu, J. Kuchlyan, A. Dhir, and N. Sarkar, “How does the surface charge of ionic surfactant and cholesterol forming vesicles control

rotational and translational motion of rhodamine 6G perchlorate (R6G ClO4)?," *Langmuir : the ACS journal of surfaces and colloids*, vol. 31, no. 8, pp. 2310–20, 2015.

[211] P. L. Felgner, T. R. Gadek, M. Holm, R. Roman, H. W. Chan, M. Wenz, J. P. Northrop, G. M. Ringold, and M. Danielsen, "Lipofection: a highly efficient, lipid-mediated DNA-transfection procedure," *Proceedings of the National Academy of Sciences of the United States of America*, vol. 84, pp. 7413–7, Nov. 1987.

[212] Y. Ma, Y. Zhuang, X. Xie, C. Wang, F. Wang, D. Zhou, J. Zeng, and L. Cai, "The role of surface charge density in cationic liposome-promoted dendritic cell maturation and vaccine-induced immune responses.," *Nanoscale*, vol. 3, no. 5, pp. 2307–14, 2011.

[213] S. Mandal, J. Kuchlyan, S. Ghosh, C. Banerjee, N. Kundu, D. Banik, and N. Sarkar, "Vesicles formed in aqueous mixtures of cholesterol and imidazolium surface active ionic liquid: a comparison with common cationic surfactant by water dynamics," *The journal of physical chemistry. B*, vol. 118, no. 22, pp. 5913–23, 2014.

[214] S. Ghosh, J. Kuchlyan, S. Roychowdhury, D. Banik, N. Kundu, A. Roy, and N. Sarkar, "Unique influence of cholesterol on modifying the aggregation behavior of surfactant assemblies: investigation of photophysical and dynamical properties of 2,2'-bipyridine-3,3'-diol, BP(OH)2 in surfactant micelles, and surfactant/cholesterol forming vesicl," *The journal of physical chemistry. B*, vol. 118, no. 31, pp. 9329–40, 2014.

[215] N. Thomas, D. Dong, K. Richter, M. Ramezanpour, S. Vreugde, B. Thierry, P.-J. Wormald, and C. A. Prestidge, "Quatsomes for the treatment of Staphylococcus aureus biofilm," *J. Mater. Chem. B*, vol. 3, no. 14, pp. 2770–2777, 2015.

[216] M. R. Mozafari, "Liposomes: an overview of manufacturing techniques," *Cellular & molecular biology letters*, vol. 10, no. 4, pp. 711–9, 2005.

[217] European Medicines Agency, "Reflection paper on the data requirements for intravenous liposomal products developed with reference to an innovator liposomal product," 2013.

[218] B. L. Krister Holmberg, Bo Jonsson, Bengt Kronberg, *Surfactants and polymers in aqueous solution.* 2003.

[219] T. Kubo, T. Sugita, S. Shimose, Y. Nitta, Y. Ikuta, and T. Murakami, “Targeted delivery of anticancer drugs with intravenously administered magnetic liposomes in osteosarcoma-bearing hamsters,” *International journal of oncology*, vol. 17, no. 2, pp. 309–15, 2000.

[220] S. Azarmi, W. H. Roa, and R. Löbenberg, “Targeted delivery of nanoparticles for the treatment of lung diseases,” *Advanced drug delivery reviews*, vol. 60, no. 8, pp. 863–75, 2008.

[221] S. r. T. Larsen, H. Verder, and G. D. Nielsen, “Airway effects of inhaled quaternary ammonium compounds in mice.,” *Basic & clinical pharmacology & toxicology*, vol. 110, no. 6, pp. 537–43, 2012.

[222] J. M. López-Pinto, M. L. González-Rodríguez, and A. M. Rabasco, “Effect of cholesterol and ethanol on dermal delivery from DPPC liposomes.,” *International journal of pharmaceutics*, vol. 298, no. 1, pp. 1–12, 2005.

[223] L. Ventosa, J. Veciana, I. Cabrera, E. Elizondo, M. Melgarejo, M. Royo, F. Albericio, D. Pulido, S. Sala, J. Corchero, S. Schwartz, I. Abasolo, and A. Villaverde, “Functionalized liposomes useful for the delivery of bioactive compounds. PCT/EP2013/063646,” 2012.

[224] J. Hartgerink, “Supramolecular one-dimensional objects,” *Current Opinion in Solid State and Materials Science*, vol. 5, no. 4, pp. 355–361, 2001.

[225] D. P. Nair, M. Podgórski, S. Chatani, T. Gong, W. Xi, C. R. Fenoli, and C. N. Bowman, “The Thiol-Michael Addition Click Reaction: A Powerful and Widely Used Tool in Materials Chemistry,” 2013.

[226] J. W. Bae, E. Lee, K. M. Park, and K. D. Park, “Vinyl Sulfone-Terminated PEG-PLLA Diblock Copolymer for Thiol-Reactive Polymeric Micelle,” *Macromolecules*, vol. 42, no. 10, pp. 3437–3442, 2009.

[227] M. S. Masri and M. Friedman, “Protein reactions with methyl and ethyl vinyl sulfones,” *Journal of protein chemistry*, vol. 7, no. 1, pp. 49–54, 1988.

[228] U. Kauscher, K. Bartels, I. Schrader, V. A. Azov, and B. J. Ravoo, “Metastable oxidation states of tetrathiafulvalenes on the surface of liposomes,” *J. Mater. Chem. B*, vol. 3, no. 3, pp. 475–480, 2015.

[229] K. Wang and G. W. Gokel, “Redox-switched amphiphiles: oxidized ferrocene derivatives form stable vesicles when either one or two alkyl tails are present,” *Journal of Physical Organic Chemistry*, vol. 10, no. 5, pp. 323–334, 1997.

[230] L. Ziserman, H.-Y. Lee, S. R. Raghavan, A. Mor, and D. Danino, “Unraveling the mechanism of nanotube formation by chiral self-assembly of amphiphiles.,” *Journal of the American Chemical Society*, vol. 133, pp. 2511–7, Mar. 2011.

[231] A. Sorrenti, O. Illa, and R. M. Ortuño, “Amphiphiles in aqueous solution: well beyond a soap bubble,” *Chemical Society reviews*, vol. 42, no. 21, pp. 8200–19, 2013.

[232] L. C. Palmer and S. I. Stupp, “Molecular self-assembly into one-dimensional nanostructures.,” *Accounts of chemical research*, vol. 41, pp. 1674–84, Dec. 2008.

[233] W. Li, M. Zhang, J. Zhang, and Y. Han, “Self-assembly of cetyl trimethylammonium bromide in ethanol-water mixtures,” *Frontiers of Chemistry in China*, vol. 1, no. 4, pp. 438–442, 2006.

[234] L. F. Uchegbu, *Synthetic Surfactant Vesicles: Niosomes and Other Non-Phospholipid Vesicular Systems (Drug Targeting and Delivery)*. 2000.

[235] S. Illa, “Atomistic simulation of amphiphilic molecules. Application to functionalized cholesterol,” *IQS School of Engineering Master’s Thesis*, 2014.

[236] G. A. Jeffrey, *An Introduction to Hydrogen Bonding*. Oxford University Press, 1 edition ed., 1997.

[237] S. Chatani, D. P. Nair, and C. N. Bowman, “Relative reactivity and selectivity of vinyl sulfones and acrylates towards the thiol-Michael addition reaction and polymerization,” *Polym. Chem.*, vol. 4, no. 4, pp. 1048–1055, 2013.

[238] F. B. Li, X. Z. Li, and K. H. Ng, “Photocatalytic Degradation of an Odorous Pollutant: 2-Mercaptobenzothiazole in Aqueous Suspension Using Nd 3+ -TiO2 Catalysts,” *Industrial & Engineering Chemistry Research*, vol. 45, no. 1, pp. 1–7, 2006.

[239] X. Hou and B. T. Jones, “Inductively Coupled Plasma-Optical Emission Spectrometry,” 2008.

[240] N. Neghmouche and T. Lanez, “Electrochemical properties of ferrocene in aqueous and organic mediums at glassy carbon electrode,” *Recent Trends in Physical Chemistry: An International Journal*, vol. 1, pp. 1–3, 2013.

[241] A. Brizard, R. Oda, and I. Huc, “Chirality Effects in Self-assembled Fibrillar Networks,” *Topics in current chemistry*, vol. 256, pp. 167–218, 2005.

[242] A. Brizard, R. K. Ahmad, and R. Oda, “Control of nano-micrometric twist and helical ribbon formation with gemini?oligoalanine via interpeptidic ?-sheet structure formation,” *Chemical Communications*, no. 22, p. 2275, 2007.

[243] L. Ziserman, A. Mor, D. Harries, and D. Danino, “Curvature Instability in a Chiral Amphiphile Self-Assembly,” *Physical Review Letters*, vol. 106, no. 23, p. 238105, 2011.

[244] R. Oda, I. Huc, M. Schmutz, S. J. Candau, and F. C. MacKintosh, “Tuning bilayer twist using chiral counterions,” *Nature*, vol. 399, no. 6736, pp. 566–9, 1999.

[245] N. G. Tsierkezos, “Cyclic Voltammetric Studies of Ferrocene in Nonaqueous Solvents in the Temperature Range from 248.15 to 298.15 K,” *Journal of Solution Chemistry*, vol. 36, no. 3, pp. 289–302, 2007.

[246] M. Reches and E. Gazit, “Casting metal nanowires within discrete self-assembled peptide nanotubes,” *Science (New York, N.Y.)*, vol. 300, no. 5619, pp. 625–7, 2003.

[247] M. S. Lamm, N. Sharma, K. Rajagopal, F. L. Beyer, J. P. Schneider, and D. J. Pochan, “Laterally Spaced Linear Nanoparticle Arrays Templated by Laminated β-Sheet Fibrils,” *Advanced Materials*, vol. 20, no. 3, pp. 447–451, 2008.

[248] I. L. Medintz, H. T. Uyeda, E. R. Goldman, and H. Mattoussi, “Quantum dot bioconjugates for imaging, labelling and sensing,” *Nature materials*, vol. 4, no. 6, pp. 435–46, 2005.

[249] A. Miyawaki, “Visualization of the spatial and temporal dynamics of intracellular signaling,” *Developmental cell*, vol. 4, no. 3, pp. 295–305, 2003.

[250] E. Schröck, S. du Manoir, T. Veldman, B. Schoell, J. Wienberg, M. A. Ferguson-Smith, Y. Ning, D. H. Ledbetter, I. Bar-Am, D. Soenksen, Y. Garini, and T. Ried, “Multicolor spectral karyotyping of human chromosomes.,” *Science (New York, N.Y.)*, vol. 273, no. 5274, pp. 494–7, 1996.

[251] N. O’Farrell, A. Houlton, and B. R. Horrocks, “Silicon nanoparticles: applications in cell biology and medicine.,” *International journal of nanomedicine*, vol. 1, no. 4, pp. 451–72, 2006.

[252] X. Michalet, F. F. Pinaud, L. A. Bentolila, J. M. Tsay, S. Doose, J. J. Li, G. Sundaresan, A. M. Wu, S. S. Gambhir, and S. Weiss, “Quantum dots for live cells, in vivo imaging, and diagnostics.,” *Science (New York, N.Y.)*, vol. 307, no. 5709, pp. 538–44, 2005.

[253] M. V. Kovalenko, L. Manna, A. Cabot, Z. Hens, D. V. Talapin, C. R. Kagan, V. I. Klimov, A. L. Rogach, P. Reiss, D. J. Milliron, P. Guyot-Sionnnest, G. Konstantatos, W. J. Parak, T. Hyeon, B. A. Korgel, C. B. Murray, and W. Heiss, “Prospects of Nanoscience with Nanocrystals,” *ACS Nano*, vol. 9, no. 2, p. 150122081035000, 2015.

[254] M. Bruchez Jr., “Semiconductor Nanocrystals as Fluorescent Biological Labels,” *Science*, vol. 281, no. 5385, pp. 2013–2016, 1998.

[255] A. P. Alivisatos, “Semiconductor Clusters, Nanocrystals, and Quantum Dots,” *Science*, vol. 271, no. 5251, pp. 933–937, 1996.

[256] C. M. Hessel, D. Reid, M. G. Panthani, M. R. Rasch, B. W. Goodfellow, J. Wei, H. Fujii, V. Akhavan, and B. A. Korgel, “Synthesis of Ligand-Stabilized Silicon Nanocrystals with Size-Dependent Photoluminescence Spanning Visible to Near-Infrared Wavelengths,” *Chemistry of Materials*, vol. 24, no. 2, pp. 393–401, 2012.

[257] J.-H. Park, L. Gu, G. von Maltzahn, E. Ruoslahti, S. N. Bhatia, and M. J. Sailor, “Biodegradable luminescent porous silicon nanoparticles for in vivo applications.,” *Nature materials*, vol. 8, no. 4, pp. 331–6, 2009.

[258] E. J. Henderson, A. J. Shuhendler, P. Prasad, V. Baumann, F. Maier-Flaig, D. O. Faulkner, U. Lemmer, X. Y. Wu, and G. A. Ozin, “Colloidally stable silicon nanocrystals with near-infrared photoluminescence for biological fluorescence imaging,” *Small (Weinheim an der Bergstrasse, Germany)*, vol. 7, no. 17, pp. 2507–16, 2011.

[259] L. T. Canham, “Silicon quantum wire array fabrication by electrochemical and chemical dissolution of wafers,” *Applied Physics Letters*, vol. 57, no. 10, p. 1046, 1990.

[260] A. G. Cullis, L. T. Canham, and P. D. J. Calcott, “The structural and luminescence properties of porous silicon,” *Journal of Applied Physics*, vol. 82, no. 3, p. 909, 1997.

[261] Y. Yu, C. M. Hessel, T. D. Bogart, M. G. Panthani, M. R. Rasch, and B. A. Korgel, “Room Temperature Hydrosilylation of Silicon Nanocrystals with Bifunctional Terminal Alkenes,” *Langmuir*, vol. 29, no. 5, pp. 1533–1540, 2013.

[262] F. Erogbogbo, K.-t. T. Yong, I. Roy, G. X. Xu, P. N. Prasad, and M. T. Swihart, “Biocompatible luminescent silicon quantum dots for imaging of cancer cells,” *ACS nano*, vol. 2, no. 5, pp. 873–878, 2008.

[263] M. R. Rasch, E. Rossinyol, J. L. Hueso, B. W. Goodfellow, J. Arbiol, and B. A. Korgel, “Hydrophobic gold nanoparticle self-assembly with phosphatidylcholine lipid: membrane-loaded and janus vesicles.,” *Nano letters*, vol. 10, no. 9, pp. 3733–9, 2010.

[264] M. R. Rasch, Y. Yu, C. Bosoy, B. W. Goodfellow, and B. A. Korgel, “Chloroform-enhanced incorporation of hydrophobic gold nanocrystals into dioleoylphosphatidylcholine (DOPC) vesicle membranes.,” *Langmuir : the ACS journal of surfaces and colloids*, vol. 28, no. 36, pp. 12971–81, 2012.

[265] C. M. Hessel, M. R. Rasch, J. L. Hueso, B. W. Goodfellow, V. A. Akhavan, P. Puvanakrishnan, J. W. Tunnel, and B. A. Korgel, “Alkyl passivation and amphiphilic polymer coating of silicon nanocrystals for diagnostic imaging.,” *Small (Weinheim an der Bergstrasse, Germany)*, vol. 6, no. 18, pp. 2026–34, 2010.

[266] F. Erogbogbo, K.-T. Yong, I. Roy, R. Hu, W.-C. Law, W. Zhao, H. Ding, F. Wu, R. Kumar, M. T. Swihart, and P. N. Prasad, “In vivo targeted cancer imaging, sentinel lymph node mapping and multi-channel imaging with biocompatible silicon nanocrystals.,” *ACS nano*, vol. 5, no. 1, pp. 413–23, 2011.

[267] H. Jang, L. E. Pell, B. A. Korgel, and D. S. English, “Photoluminescence quenching of silicon nanoparticles in phospholipid vesicle bilayers,” *Journal of Photochemistry and Photobiology A: Chemistry*, vol. 158, no. 2-3, pp. 111–117, 2003.

[268] L. Paasonen, T. Laaksonen, C. Johans, M. Yliperttula, K. Kontturi, and A. Urtti, “Gold nanoparticles enable selective light-induced contents release from liposomes.,” *Journal of controlled release : official journal of the Controlled Release Society*, vol. 122, no. 1, pp. 86–93, 2007.

[269] W. T. Al-Jamal and K. Kostarelos, “Liposomes: from a clinically established drug delivery system to a nanoparticle platform for theranostic nanomedicine.,” *Accounts of chemical research*, vol. 44, no. 10, pp. 1094–104, 2011.

[270] B. Dubertret, P. Skourides, D. J. Norris, V. Noireaux, A. H. Brivanlou, and A. Libchaber, “In vivo imaging of quantum dots encapsulated in phospholipid micelles.,” *Science (New York, N.Y.)*, vol. 298, no. 5599, pp. 1759–62, 2002.

[271] Y. Yu, *Surface Functionalization and Self-Assembly of Ligand-Stabilized Silicon Nanocrystals.* PhD thesis, The University of Texas at Austin, 2015.

[272] R. Alenaizi, S. Radiman, I. Abdul Rahman, and F. Mohamed, “Zwitterionic betaine-cholesterol system: Effects of sonication duration and aging on vesicles stability,” *Colloids and Surfaces A: Physicochemical and Engineering Aspects*, vol. 482, pp. 662–669, 2015.

[273] K. Vanommeslaeghe, E. Hatcher, C. Acharya, S. Kundu, S. Zhong, J. Shim, E. Darian, O. Guvench, P. Lopes, I. Vorobyov, and A. D. Mackerell, “CHARMM general force field: A force field for drug-like molecules compatible with the CHARMM all-atom additive biological force fields.,” *Journal of computational chemistry*, vol. 31, no. 4, pp. 671–90, 2010.

[274] A. Sánchez-Iglesias, M. Grzelczak, T. Altantzis, B. Goris, J. Pérez-Juste, S. Bals, G. Van Tendeloo, S. H. Donaldson, B. F. Chmelka, J. N. Israelachvili, and L. M. Liz-Marzán, “Hydrophobic Interactions Modulate Self-Assembly of Nanoparticles,” *ACS Nano*, vol. 6, no. 12, p. 121205123934003, 2012.

[275] D. Marsh, *Handbook of Lipid Bilayers, Second Edition.* CRC Press, 2013.

[276] F. Szoka and D. Papahadjopoulos, “Comparative properties and methods of preparation of lipid vesicles (liposomes),” *Annual review of biophysics and bioengineering*, vol. 9, pp. 467–508, 1980.

[277] R. Pecora (Ed.), *Dynamic light scattering: applications of photon correlation spectroscopy.* New York; Plenum Press, 1985.

[278] A. P. Hammersley, “FIT2D: An introduction and overview,” *ESRF Internal Report ESRF97HA02T*, 1997.

[279] P. V. Konarev, V. V. Volkov, A. V. Sokolova, M. H. J. Koch, and D. I. Svergun, “PRIMUS : a Windows PC-based system for small-angle scattering data analysis,” *Journal of Applied Crystallography*, vol. 36, no. 5, pp. 1277–1282, 2003.

[280] S. Förster, L. Apostol, and W. Bras, “Scatter : software for the analysis of nano- and mesoscale small-angle scattering,” *Journal of Applied Crystallography*, vol. 43, no. 3, pp. 639–646, 2010.

[281] E. Amstad, J. Kohlbrecher, E. Müller, T. Schweizer, M. Textor, and E. Reimhult, “Triggered release from liposomes through magnetic actuation of iron oxide

nanoparticle containing membranes.," *Nano letters*, vol. 11, no. 4, pp. 1664–70, 2011.

[282] W.-C. Lin, C. D. Blanchette, T. V. Ratto, and M. L. Longo, "Lipid asymmetry in DLPC/DSPC-supported lipid bilayers: a combined AFM and fluorescence microscopy study.," *Biophysical journal*, vol. 90, no. 1, pp. 228–37, 2006.

[283] Silvius JR, "Thermotropic Phase Transitions of Pure Lipids in Model Membranes and Their Modifications by Membrane Proteins," in *Lipid-Protein Interactions* (P. Jost and O. Griffith, eds.), pp. 239–281, New York: John Wiley & Sons, Inc., 1982.

[284] M. Eeman and M. Deleu, "From biological membranes to biomimetic model membranes," 2010.

[285] M. J. Janiak, D. M. Small, and G. G. Shipley, "Temperature and compositional dependence of the structure of hydrated dimyristoyl lecithin," *The Journal of biological chemistry*, vol. 254, no. 13, pp. 6068–78, 1979.

[286] D. Pentak, W. W. Sulkowski, and A. Sulkowska, "Calorimetric and EPR studies of the thermotropic phase behavior of phospholipid membranes," *Journal of Thermal Analysis and Calorimetry*, vol. 93, no. 2, pp. 471–477, 2008.

[287] E. Urbán, A. Bóta, B. Kocsis, and K. Lohner, "Distortion of the lamellar arrangement of phospholipids by deep rough mutant lipopolysaccharide from Salmonella minnesota," *Journal of Thermal Analysis and Calorimetry*, vol. 82, no. 2, pp. 463–469, 2005.

[288] I. Hatta, "Temperature scanning X-ray diffraction at phase transitions of biologically related lipid assemblies," *Journal of Thermal Analysis and Calorimetry*, vol. 82, no. 1, pp. 189–192, 2005.

[289] A. D. MacKerell, D. Bashford, M. Bellott, R. L. Dunbrack, J. D. Evanseck, M. J. Field, S. Fischer, J. Gao, H. Guo, S. Ha, D. Joseph-McCarthy, L. Kuchnir, K. Kuczera, F. T. K. Lau, C. Mattos, S. Michnick, T. Ngo, D. T. Nguyen, B. Prodhom, W. E. Reiher, B. Roux, M. Schlenkrich, J. C. Smith, R. Stote, J. Straub, M. Watanabe, J. Wiorkiewicz-Kuczera, D. Yin, and M. Karplus, "All-atom empirical potential for molecular modeling and dynamics studies of proteins," *Journal of Physical Chemistry B*, vol. 102, no. 18, pp. 3586–3616, 1998.

[290] A. D. Mackerell, M. Feig, and C. L. Brooks, “Extending the treatment of backbone energetics in protein force fields: Limitations of gas-phase quantum mechanics in reproducing protein conformational distributions in molecular dynamics simulations,” *Journal of Computational Chemistry*, vol. 25, no. 11, pp. 1400–1415, 2004.

[291] Z. Cournia, A. C. Vaiana, G. M. Ullmann, and J. C. Smith, “Derivation of a molecular mechanics force field for cholesterol,” *Pure and Applied Chemistry*, vol. 76, no. 1, pp. 189–196, 2004.

[292] B. Minisini, S. Chavand, R. Barthelery, and F. Tsobnang, “Calculations of the charge distribution in dodecyltrimethylammonium: a quantum chemical investigation,” *Journal of Molecular Modeling*, vol. 16, no. 6, pp. 1085–1092, 2010.

[293] T. P. Lybrand, I. Ghosh, and J. A. McCammon, “Hydration of chloride and bromide anions: determination of relative free energy by computer simulation,” *Journal of the American Chemical Society*, vol. 107, no. 25, pp. 7793–7794, 1985.

[294] S. Jo, J. B. Lim, J. B. Klauda, and W. Im, “CHARMM-GUI Membrane Builder for mixed bilayers and its application to yeast membranes,” *Biophysical journal*, vol. 97, no. 1, pp. 50–8, 2009.

[295] J. Huang and G. W. Feigenson, “A microscopic interaction model of maximum solubility of cholesterol in lipid bilayers,” *Biophysical journal*, vol. 76, no. 4, pp. 2142–57, 1999.

[296] G. Sauerbrey, “Verwendung von Schwingquarzen zur Wägung dünner Schichten und zur Mikrowägung,” *Zeitschrift für Physik*, vol. 155, no. 2, pp. 206–222, 1959.

[297] M. Rodahl, F. Höök, A. Krozer, P. Brzezinski, and B. Kasemo, “Quartz crystal microbalance setup for frequency and Q-factor measurements in gaseous and liquid environments,” *Review of Scientific Instruments*, vol. 66, no. 7, p. 3924, 1995.

[298] “http://soft.ifs.hr/procurement-contract-signed/ 29/09/2014.”

Nomenclature

1-D	One-dimensional
ABF	Adaptive Biasing Force methodology
API	Active Pharmaceutical Ingredient
AuNCs	Gold nanocrystals
CF	Compressed Fluid
Chol	cholesterol
Chol-Fc	ferrocenylmethyl cholesteryl ether
Chol-VS	Cholest-5-ene, 3-[2-(ethenylsulfonyl)ethoxy]-, (3β)-
cmc	critical micelle concentration
CPC	cetylpyridinium chloride
Cryo-TEM	Cryogenic Transmission Electron Microscopy
CTAB	hexadecyltrimethyl ammonium bromide
CV	Cyclic Voltammetry
DDS	Drug Delivery Systems
DELOS-SUSP	Depresurization of an Expanded Organic Solution-suspension
DLS	Dynamic Light Scattering
DOPC	1,2-Dioleoyl-sn-glycero-3-phosphocholine
DOPG	1,2-dioleoyl-sn-glycero-3-(1'-rac-glycerol)
DPPC	1,2-dipalmitoyl-sn-glycero-3-phosphocholine
DSC	Differential Scanning Calorimetry
Fc	ferrocene
FDA	Food and Drug Administration

GMP	Good Manufacturing Practice
GUVs	Giant Unilamellar Vesicles
ICP-OES	Inductively Coupled Plasma Optical Emission Spectrometry
LS	Light Scattering
LUVs	Large Unilamellar Vesicles
MBT	2-mercaptobenzothiazole
MD	Molecular Dynamics
MKC	myristalkonium chloride
MLVs	Multilamellar vesicles
MM	Mixed Micelles
MVVs	Multivesicular vesicles
NS-TEM	Negatively Stained-Transmission Electron Microscopy
OD	Optical Density
PL	Photoluminescence
PLE	Photoluminescence excitation
PXRD	Powder X-ray diffraction
QCM-D	Quartz Crystal Microbalance with Dissipation technique
QUATs	quaternary ammonium surfactants
SDS	Sodium Dodecyl Sulfate
SiNCs	Silicon nanocrystals
SPR	Surface Plasmon Resonance
SUVs	Small Unilamellar Vesicles
SWAXS	Small and Wide-Angle X-ray Scattering
TEM	Transmission Electron Microscopy

TFH	Thin Film Hydration method
TGA	Thermal Gravimetric Analysis
VS	Vinyl Sulphone
VS-1	N-(2-(2-(vinylsulfonyl) ethoxy)ethyl) dodecanamide
VS-2	N-(2-(2-(vinylsulfonyl) ethoxy)ethyl) oleamide
VS-3	1-(vinylsulfonyl) octadecane

Patents and Publications

- L. Ferrer-Tasies, E.Moreno-Calvo, M. Cano-Sarabia, M. Aguilella-Arzo, A. Angelova, S. Lesieur, S. Ricart, J. Faraudo, N. Ventosa, and J. Veciana, “Quatsomes: vesicles formed by self-assembly of sterols and quaternary ammonium surfactants,” Langmuir, vol. 29, no. 22, pp. 6519–6528, 2013.
- D. A. Silbaugh, L. Ferrer-Tasies, J. Faraudo, J. Veciana, N. Ventosa and B. A. Korgel, “Highly fluorescent silicon nanocrystals stabilized in water using quatsomes,” *submitted.*
- D. A. Silbaugh, L. Ferrer-Tasies, J. Veciana, N. Ventosa and B. A. Korgel, “Silicon nanocrystal quatsome assemblies.” *WO Patent Application submitted.*
- W. I. Tatkiewicz, L. Ferrer-Tasies, E. Moreno-Calvo, N. Ventosa, I. Ratera, R. Richter and J. Veciana, “Quatsomes versus liposomes: influence of internal structure on vesicular rigidity by a combined SPR and QCM-D approach,” *submitted.*

Papers in preparation:

- “Quatsomes: new thermodynamically stable vesicles with spontaneous curvature.”
- “Formation of quatsomes by different preparation routes.”
- “From quatsomes to nanoribbons.”